UNIVERSITY OF NOVA GORICA
GRADUATE SCHOOL

SYNTHESIS AND ELECTRONIC PROPERTIES OF COMPOUNDS FROM A $Bi_2O_3-Nd_2O_3-VO_x$ SYSTEM

DISSERTATION

Mirela Dragomir

Mentor: Prof. dr. Matjaž Valant

Nova Gorica, 2013

UNIVERZA V NOVI GORICI
FAKULTETA ZA PODIPLOMSKI ŠTUDIJ

SINTEZA IN ELEKTRONSKE LASTNOSTI SPOJIN IZ SISTEMA $Bi_2O_3-Nd_2O_3-VO_x$

DISERTACIJA

Mirela Dragomir

Mentor: Prof. dr. Matjaž Valant

Nova Gorica, 2013

"Mystery is a very necessary ingredient in our lives. Mystery creates wonder, and wonder is the basis for man's desire to understand. Who knows what mysteries will be solved in our lifetime and what new riddles will become the challenge of new generations?"

-Neil Armstrong, 1969

Ad astra per aspera

Acknowledgments

During my Ph.D. studies in Slovenia, I have been supported and encouraged by several people without whom it would not be possible to complete the work presented in this thesis. Therefore, I would like to express my gratitude to the following people and institutions:

Prof. dr. Matjaž Valant, my supervisor, thank you for giving me the chance to be a part of your new group and to conduct my Ph.D. studies in Slovenia. Your passion and enthusiasm for research has been contagious and highly motivating. Thank you for the confidence and freedom you have given to my research.

Prof. dr. Iztok Arčon has played an important role for the work conducted in this thesis and thus, I would like to thank him for his advices, expertise, and help with the X-ray absorption spectroscopy analyses.

I extend my sincere thanks and gratitude to my committee members, prof. dr. Urška Lavrenčič, prof. dr. Steve Dunn, and prof.dr. Slavko Bernik.

I would also like to express my very great appreciation to prof. dr. Daniela Berger and conf. dr. Cristian Matei from Politechnica University of Bucharest (Romania) for their scientific advices, constant friendship, and continuous support.

I would like to thank doc. dr. Mattia Fanetti for the help with the SEM measurements and doc. dr. Sandra Gardonio for the initiation into fluorescence spectroscopy technique.

I am also very grateful to Aleš Štefančič and doc. dr. Gašper Tavčar from the Department of Inorganic Chemistry and Technology – K1 at Jožef Stefan Institute, Ljubljana (Slovenia) for all their help with the vacuum line experiments.

Thanks to Ms. Tea Stibilj Nemec from University of Nova Gorica, the administrative issues of my arrival and stay in this beautiful country have been always solved really fast.

I would also like to acknowledge the financial support from the Slovenian Research Agency.

I am thankful to my colleagues from campus Ajdovščina (Iuliia Mikulska, Metka Benčina, Michael Pitcher, Saim Emin, Mattia Fanettti, Sandra Gardonio, Egon Pavlica, Miro Zdvoc, Mojca Vrčon, Sasa Badalič, Tina Mavrič, Artem Badasyan,

Abstract

The scientific contribution presented in this thesis comprises research on new phases in the $Bi_2O_3-Nd_2O_3-VO_x$ system. Firstly, I report on the solid-state synthesis and optoelectronic properties of phases from the $BiVO_4-NdVO_4$ system (**Chapter II**). Using EXAFS analysis, I show that Bi can substitute Nd in tetragonal $NdVO_4$ up to 49 ± 1 mol%, while Nd cannot enter the monoclinic $BiVO_4$ structure without the ability for hybridization. Doping with Bi allowed the decrease of the $NdVO_4$ band gap to below 3.1 eV and the apparition of new emissions in the PL spectra. The observed properties were explained on the basis of the hybridization of Bi $6s^2$ and O $2p$ orbitals. The dynamics of the photoluminescence of the $Bi_xNd_{1-x}VO_4$ powders were found to depend on the composition: the lifetime values of the photogenerated charges in $NdVO_4$ decreased with Bi doping. Since $Bi_xNd_{1-x}VO_4$ samples showed visible light absorption, it was also interesting to further investigate their photocatalytic properties. In this sense, I prepared Bi-doped $NdVO_4$ nanoparticles by aqueous precipitation reactions (**Chapter III**). The Raman studies showed that with the Bi doping, the $NdVO_4$ Raman modes shift continuously to lower wavenumbers together with an increase in their FWHM values. Also, the calculated V−O bond length in $NdVO_4$ becomes longer with the Bi concentration. The as prepared Bi-$NdVO_4$ nanoparticles can absorb light up to 410 nm (3.03 eV) depending on the Bi content. A quenching effect of the PL emissions with the Bi concentration was also observed. As these findings suggested that $BiNdVO_4$ nanoparticles could show good photocatalytic properties, their photocatalytic activity was further evaluated for the degradation of the Rhodamine B (RhB) dye under UVA light irradiation (**Chapter IV**). Confronting their photocatalytic activities with the composition and the pH of the reaction, I found that at a pH of 6.5, the photoactivity of $NdVO_4$ decreases with the Bi content, while at a pH of 5 and in presence of H_2O_2, the photoactivity increased with the Bi content. The $Bi_{0.48}Nd_{0.52}VO_4/H_2O_2$ system showed the highest photodegradation activity: 87% of the RhB was degraded after 60 min of UVA irradiation.

Later, I investigated the synthesis and stability of a new possible perovskite with the $BiVO_3$ chemical formula (**Chapter V**). Firstly, I estimated its structural stability and further on, several approaches to synthesize it were described. I found out that $BiVO_3$

could adopt a stable perovskite-type structure, but its synthesis is facing a big challenge: $BiVO_3$ cannot be obtained by high-temperature synthesis methods due to a reduction-oxidation reaction between Bi^{3+} and V^{3+}. In the end, I propose that the stability of $BiVO_3$ or the possibility of its formation can be at lower temperatures, for which the activation energy for the redox reaction is not exceeded.

Keywords: Orthovanadates, $BiVO_3$, oxide photocatalysts, X-ray methods, optical spectroscopy.

Povzetek

Znanstveni prispevek, predstavljen v tej disertaciji, sestavljajo raziskave novih faz v sistemu $Bi_2O_3-Nd_2O_3-VO_x$. Najprej poročam o sintezi v trdnem stanju in o optoelektronskih lastnostih faz, ki obstajajo v sistemu $BiVO_4-NdVO_4$ (**II. Poglavje**). Z uporabo EXAFS analize sem pokazala, da Bi lahko do 49 ± 1 mol% nadomesti Nd v tetragonalnem $NdVO_4$, medtem ko se Nd, pri katerem ne prihaja do hibridizacije s kisikovimi orbitalami, ne more vključiti v monoklinsko strukturo $BiVO_4$. Dopiranje z Bi povzroči znižanje prepovedanega pasu pod 3,1 eV in pojav novih emisij v PL spektru. Razlaga opaženih lastnosti temelji na hibridizaciji Bi $6s^2$ in O $2p$ orbital. Fotoluminiscenčna dinamika $Bi_xNd_{1-x}VO_4$ je odvisna od sestave: hitrost rekombinacije svetlobno generiranih nosilcev naboja se povečuje pri dopiranju z Bi. Ker vzorci $Bi_xNd_{1-x}VO_4$ kažejo absorpcijo vidne svetlobe, je bilo zanimivo raziskati njihove fotokatalitične lastnosti. Z obarjanjem iz vodnih raztopin sem pripravila z bizmutom dopirane $NdVO_4$ nanodelce (**III. Poglavje**). Ramanska spektroskopija je pokazala, da se z dopiranjem Ramanski vrhovi $NdVO_4$ zvezno pomikajo proti nižjim valovnim številom, obenem pa se jim povečujejo FWHM vrednosti. Tudi izračunana V–O vezna razdalja v strukturi $NdVO_4$ postaja daljša z naraščajočo koncentracijo Bi. Tako pripravljeni Bi-$NdVO_4$ nanodelci absorbirajo svetlobo do 410 nm (3,03 eV). Opazila sem tudi zmanjšanje PL emisij ob naraščanju vsebnosti Bi. Ker ta opažanja nakazujejo potencialne fotokatalitične lastnosti $BiNdVO_4$ nanodelcev, sem raziskala njihovo fotokatalitsko aktivnost za razkroj barvila Rodamin B (RhB) z UVA svetlobo (**IV. Poglavje**). Pri analizi fotokatalitske aktivnosti v odvisnosti od sestave in pH sem ugotovila, da pri pH 6,5 fotoaktivnost $NdVO_4$ pada s povečevanjem koncentracije Bi, obratno pa le-ta raste pri pH 5 in ob prisotnosti H_2O_2. Sistem $Bi_{0.48}Nd_{0.52}VO_4/H_2O_2$ kaže največjo aktivnosti za fotodegradacijo: 87 % RhB se je razkrojilo po 60 min obsevanja z UVA svetlobo.

V drugem delu sem raziskovala sintezo in stabilnost novega potencialnega perovskita s kemijsko sestavo $BiVO_3$ (**V. Poglavje**). Najprej sem ocenila stabilnost strukture in nato preizkusila več sinteznih pristopov. Ugotovila sem, da bi $BiVO_3$ lahko imel stabilno perovskitno strukturo, a je njegova sinteza zelo težavna. Spojine $BiVO_3$ ni mogoče pripraviti z reakcijo pri višji temperaturi, kajti poteče redoks reakcija med Bi^{3+} in V^{3+}. Na osnovi te študije lahko sklepam, da bi spojina $BiVO_3$ lahko bila

stabilna venda bi jo bilo potrebno sintetizirati pri nižjih temperaturah, pri katerih ni presežena aktivacijska energija za omenjeno redoks reakcijo.

Ključne besede: Ortovanadati, $BiVO_3$, oksidni fotokatalizatorji, Rentgenske metode, optična spektroskopija.

Contents

x

List of figures

xviii

List of tables

List of symbols and abbreviations

AOPs	Advanced oxidation processes
E_g	Band gap
Bi-NdVO$_4$	Bi-doped NdVO$_4$
CASTEP	Cambridge Serial Total Energy Package
CB	Conduction band
CBM	Conduction band minimum
CTAB	Cetyltrimethylammonium bromide
CR	Congo Red
CV	Crystal Violet
DFT	Density Functional Theory
DRS	Diffuse Reflectance Spectroscopy
SDBS	Sodium Dodecylbenzene Sulfonate
DMP	Dimethyl phosphonate
m^{eff}	Effective masses of the charge carriers
e_{CB}^-	Electrons in the CB
EG	Ethylene glycol
EXAFS	Extended X-ray Absorption Fine Structure
E$_F$	Fermi level
h_{VB}^+	Holes in the VB
·OOH	Hydroperoxyl radical
·OH	Hydroxyl radicals
JT	Jahn-Teller effect
Ln	Lanthanide

Lys	L-lysine
MOFs	Metal-organic frameworks
MO	Methyl orange
MB	Methylene blue
m-BiVO$_4$	Monoclinic BiVO$_4$
O$_2^{\cdot-}$	Superoxide anion radical
–OH	Hydroxyl group
OA	Oleic acid
PL	Photoluminescence spectroscopy
PEG	Polyethylene glycol
QSE	Quantum size effects
RhB	Rhodamine B
RBL	Rhodamine Blue
TEA	Triethanolamine
UV	Ultraviolet irradiation
VASP	Vienna Ab initio simulation package
VB	Valence band
VBM	Valence band maximum
XAS	X-ray absorption spectroscopy
XRD	X-ray diffraction
XPS	X-ray photoemission spectroscopy

1   Introduction

Bismuth is the heaviest element of the group 15 with the [Xe] $4f^{14}5d^{10}6s^26p^3$ electronic configuration. Bismuth-based compounds have been extensively studied in the last decades. These compounds show many interesting and unique properties originating from the electronic and/or steric influences of the $6s^2$ lone pair of Bi^{3+}. Restrictions on the use of toxic materials in electronics products have accelerated the development of new ecologically friendly materials based on Bi such as piezoelectrics, but the broad spectrum of applications of Bi-based compounds ranges from pigments, cosmetic products, biocompatible additives in medicine, superconductors, sensors, ion conducting solid electrolytes, luminescent materials, ferroelectric materials, to thermoelectric and photocatalytic materials. In photocatalysis, the Bi-based compounds are very important narrow band gap semiconductors with visible light absorption.

In this thesis, I report on studies of phases in the Bi_2O_3–Nd_2O_3–VO_x system. Besides the interesting properties that Bi^{3+} contributes (e.g., ferroelectricity, multiferroicity, ionic conductivity, low band gap, fluorescence, thermoelectricity, superconductivity, etc.), the interest in the Bi_2O_3–Nd_2O_3–VO_x system is further amplified by the presence of Nd, the lanthanide with the [Xe] $4f^4 6s^2$ configuration, and V from the group 5 with an [Ar] $3d^3 4s^2$ electronic configuration. Nd^{3+} is an important constituent of optical materials, while V is considered a good constituent element for the modulation of the conduction band minima of semiconductor photocatalysts. Vanadium is also a constituent of pigments.

The Bi_2O_3–Nd_2O_3 binary system has been investigated so far [1,2,3,4] and several compounds are known, e.g., $Bi_3Nd_5O_{12}$, $Bi_2Nd_4O_9$, $Bi_{0.55}Nd_{0.45}O_{1.5}$, $Bi_{0.8}Nd_{0.2}O_{1.5}$, etc. Solid solutions also form, but with a small solubility limit of both Nd_2O_3 in Bi_2O_3 and of Bi_2O_3 in Nd_2O_3. The Bi-rich region has been the most studied due to high ionic conductivity of the δ-Bi_2O_3 and Bi_2O_3-based phases. On the other side, the Nd-rich part of the system was expected to show magnetic ordering at low temperatures.

The Bi_2O_3–V_2O_5 phase diagram is rich in Bi compounds with attractive properties. This system was studied by Smolyaninov and Belyaev in 1964 [5], Blinoskov and Fotiev in 1987 [6], Touboul and Vacon in 1988 [7], and many others.

Many crystalline compounds were identified: $BiVO_4$, $Bi_{14}V_2O_{26}$, $Bi_6V_4O_{19}$, $Bi_2V_8O_{23}$, Bi_5VO_{10}, $Bi_7V_3O_{18}$, $Bi_{14}V_4O_{31}$, $Bi_8V_2O_{17}$, $Bi_{12}V_2O_{23}$, $Bi_8V_2O_{17}$, $Bi_4V_2O_{11}$, $Bi_4V_6O_{21}$, BiV_3O_9, etc. From all these compounds, the most investigated was the orthovanadate $BiVO_4$, particularly due to its photocatalytic properties, and $Bi_4V_2O_{11}$- the parent compound of BIMEVOX ($Bi_4V_{2-2x}Me_{2x}O_{11-\delta}$) phases, as a solid electrolyte. Only little attention has been paid to the other phases in this binary system.

The Bi_2O_3–VO_2 system has also been studied and phases such as $(Bi_2O_2)_2V_{2y}O_{4y+2}$ ($1 \leq y \leq 4$) are already known [8].

The binary Nd_2O_3–V_2O_5 system contains several known compounds: $4Nd_2O_3 \cdot V_2O_5$, $6Nd_2O_3 \cdot V_2O_5$, $NdVO_4$, $2Nd_2O_3 \cdot V_2O_5$, $Nd_2O_3 \cdot 2V_2O_5$ [9,10]. $NdVO_4$ is an important ABO_4-type compound and one of the most studied orthovanadates with applications ranging from optics to catalysis and photocatalysis.

In the Nd_2O_3–V_2O_3 system, only $NdVO_3$ has been found [11]. This system has been investigated [12] but with difficulty because of the instability of V_2O_3 in air. $NdVO_3$ is an ABO_3-type perovskite with magnetic and photocatalytic properties.

No information about the binary Bi_2O_3–V_2O_3 system is available in the literature so far. But an interest in a $BiVO_3$ perovskite has often been expressed in the scientific community. $BiVO_3$ has never been synthesized but, if stable, it can exhibit interesting photocatalytic and/or multiferroic properties.

After an introduction into the main ABO_4 and ABO_3–type compounds of the Bi_2O_3–Nd_2O_3–VO_x system, the general objectives of this thesis are:

- to investigate the phase relations in the $BiVO_4$–$NdVO_4$ binary system and to analyse the phase relations, structural, and optoeletronic properties of the new compounds and solid solutions with several techniques such as: X-ray diffraction (XRD), extended X-ray absorption fine structure (EXAFS), Raman spectroscopy, diffuse reflectance (DRS), and photoluminescence (PL) spectroscopy techniques.
- to understand the factors that govern the stability and synthesis of the new possible perovskite in the binary Bi_2O_3–V_2O_3 system with the $BiVO_3$ chemical formula. Even if this compound has never been synthesized, yet it has gained considerable interest at an international level as it could exhibit promising photocatalytic and/or multiferroic properties.

2

1.1 Review of the ABO_4−type compounds from the Bi_2O_3−Nd_2O_3−VO_x system

ABO_4 compounds display very interesting physical properties, which make them suitable for a large range of technological applications. Therefore, significant efforts have been made to understand their crystal chemistry. The A and B ionic radii control the diversity of the ABO_4 compounds and according to the valences of the A and B cations, they can be classified in I-VII, II-VI, III-V and IV-IV compounds, with the valence of the A cation less than or equal to the B. ABO_4 compounds crystallize in different structures such as: scheelite, monazite, zircon, fergusonite, wolframite, barite, anhydrite, rutile, stiobiotantalite, and other.

Compounds adopting the zircon ($I4_1/amd$ space group, Fig. 1) and scheelite ($I4_1/a$ space group, Fig. 2) structures are technically important materials in the fields related to optoelectronic devices, lasers, bio-imaging phosphors, and catalysis. In these structures, the smaller cation (B) prefers a tetrahedral coordination, while the larger one (A) adopts an eightfold coordination. Both zircon and scheelite structures are built from BO_4 tetrahedra and AO_8 bisphenoids. Differences between them are in the way how the polyhedra are connected. The symmetry of the A-site cation in the scheelite type is S_4, while in zircon is D_{2d}.
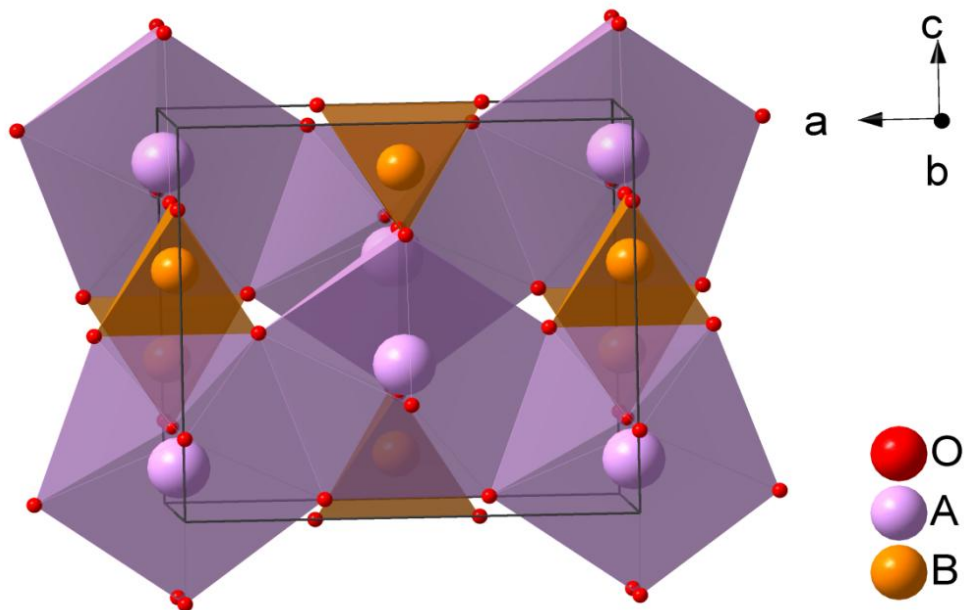
Fig. 1 Crystal structure of ABO_4 zircon structure.
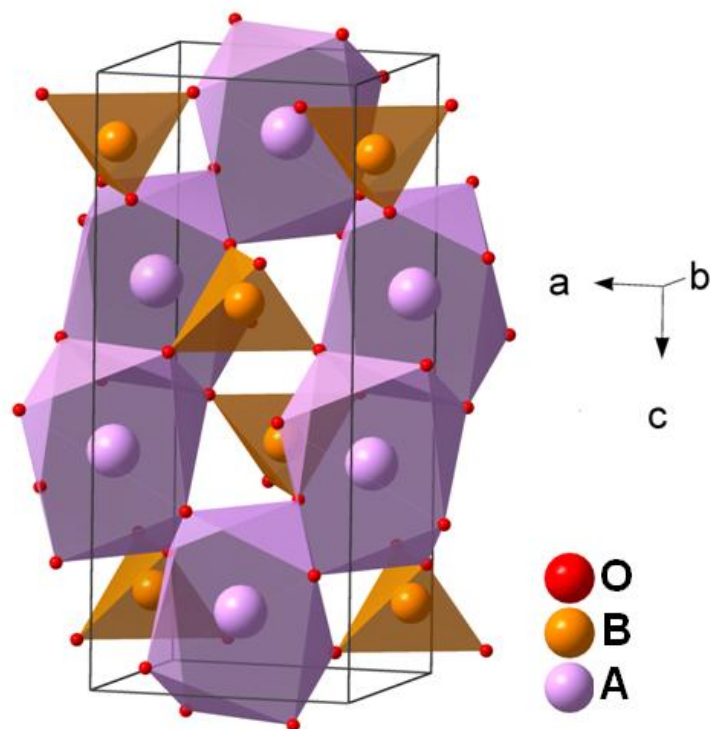
Fig. 2 Crystal structure of the tetragonal scheelite ABO$_4$ compounds.

1.1.1 BiVO$_4$

One important ABO$_4$ compound from the Bi$_2$O$_3$–Nd$_2$O$_3$–VO$_x$ system is bismuth vanadate, BiVO$_4$. BiVO$_4$ has attracted considerable attention in the last years due to its interesting properties such as pigmentation, ferroelasticity, acusto-optical, ionic conductivity and, maybe the most important, visible-light photocatalytic activity for the degradation of organic pollutants and oxygen evolution at the water splitting reaction. A series of factors control the physico-chemical properties of BiVO$_4$ such as the crystal structure, particle size, surface area, morphology or degree of crystallinity.

1.1.1.1 Crystal structure

BiVO$_4$ occurs naturally in the mineral pucherite that has an orthorhombic crystal structure. But synthetic methods of preparation do not give this structural modification. Low temperature methods give a tetragonal dreyerite (zircon-type structure, space group I4$_1$/*amd*), while higher temperature methods yield a monoclinic (distorted scheelite) structure, also called *fergusonite* (space group I2/*b*) with the lattice parameters *a = 5.195 Å, b = 5.092 Å, c = 11.701 Å, β = 90.38°*,

JCPDS No. 14-0688. At about 255 °C, the monoclinic scheelite phase undergoes a reversible second-order transition to the tetragonal scheelite structure (space group $I4_1/a$) [13,14,15]. The metastable tetragonal zircon-type $BiVO_4$ phase undergoes an irreversible transformation to the monoclinic scheelite-type on heating at 397–497 °C [15], or by mechanical stress [13].
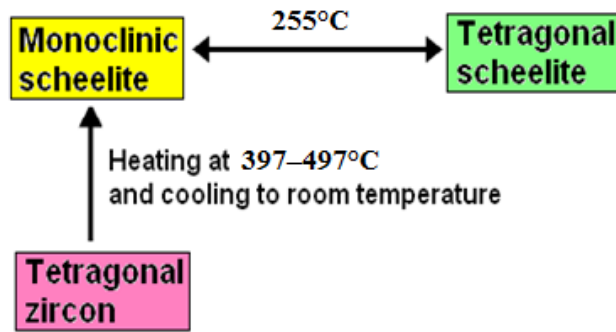
Fig. 3 Phase transitions of $BiVO_4$.

In the monoclinic structure (Fig. 4), the BiO_8 dodecahedra form chains that are parallel to the $(1\bar{1}0)$ direction by sharing an edge. The VO_4 tetrahedron does not come in contact with the next VO_4 tetrahedron; the VO_4 and BiO_8 structural units are connected through an apex O atom. While the VO_4 tetrahedron contains 2 types of V−O bond lengths of 1.69 and 1.77 Å, the BiO_8 dodecahedron is surrounded by eight isolated VO_4 tetrahedra with a wider range of Bi−O distances: 2×2.416 Å, 2×2.418 Å, 2×2.446 Å, and 2×2.449 Å, respectively [16]. The site symmetry (C_2) of the Bi^{3+} ions is lower than in the tetragonal forms (D_{2d} and S_4, respectively), and this is believed [14] to allow an off-centering of the Bi^{3+} to produce the distorted environment.
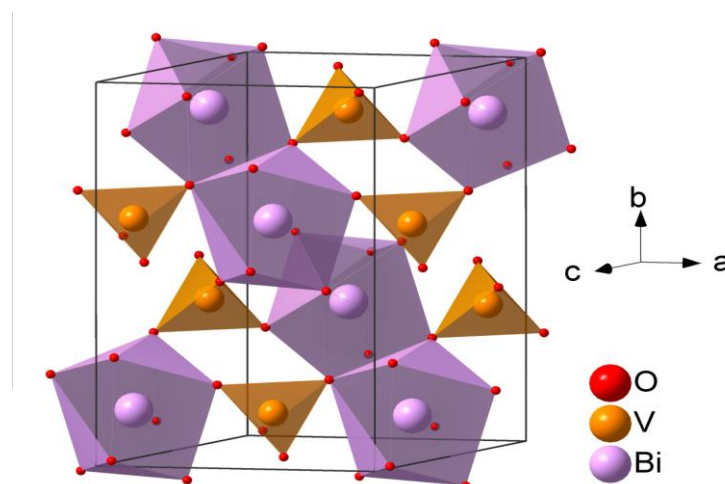
Fig. 4 The crystal structure of monoclinic scheelite $BiVO_4$.

5

The tetragonal scheelite $BiVO_4$ also consists of the VO_4 tetrahedra and BiO_8 dodecahedra but the BiO_8 dodecahedra are connected through the edges. Here the polyhedra alternate along the c axis (Fig. 5). In this crystal form, only one type of V–O bond exists with a length of 1.72 Å and eight nearly equivalent Bi–O distances: 4×2.45 Å and 4×2.49 Å [17]. The Bi ion is located at a site with S_4 symmetry.
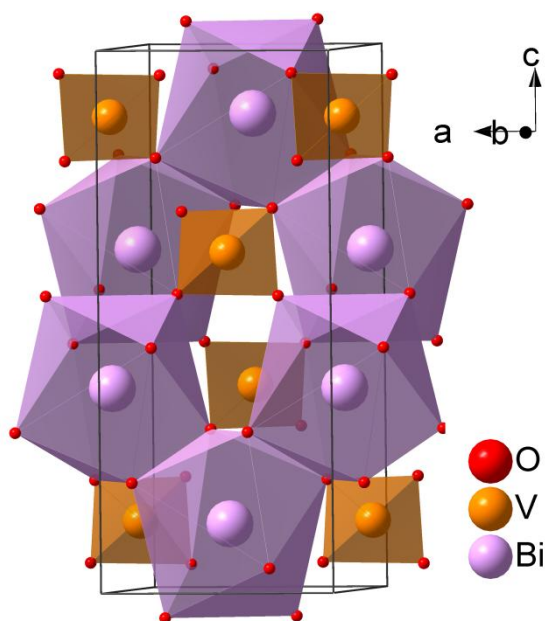
Fig. 5 The crystal structure of the tetragonal scheelite $BiVO_4$.

In the tetragonal zircon structure (Fig. 6), isolated VO_4 tetrahedra share corners and edges with BiO_8 dodecahedra.
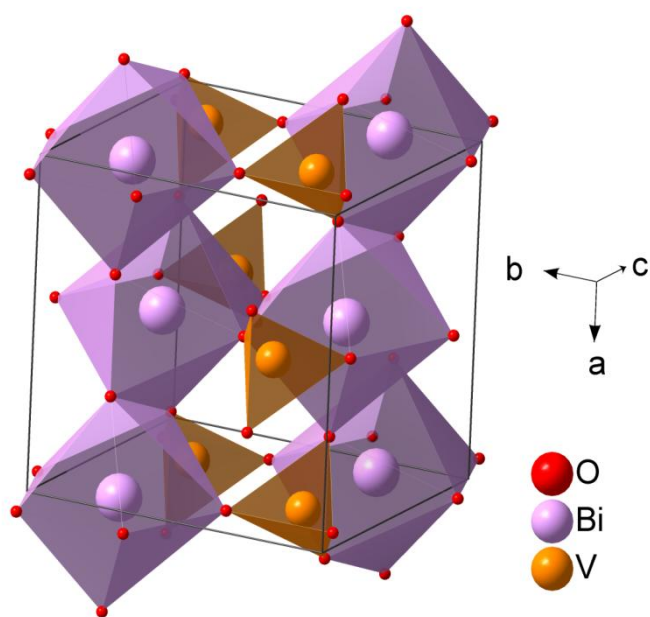
Fig. 6 Crystal structure of the tetragonal zircon $BiVO_4$.

6

The BiO_8 dodecahedra share edges with eachother to form chains parallel to a-axis. These 'chains' are crosslinked by sharing corners with VO_4 tetrahedra. The Bi and V polyhedra also form an edge-connected chain of alternating BiO_8 and VO_4 polyhedra parallel to c-axis, between which lie unoccupied channels, also parallel to the c-axis. The Bi cation occupies a site with the D_{2h} symmetry and forms 2 types of Bi−O bonds with the lengths: 4×2.41 Å and 4×2.55 Å, while the V−O bond length is 4×1.70 Å [14].

1.1.1.2 Electronic structure of BiVO₄

With the n-type conductivity, band gap (E_g) of 2.4 eV [18,19], and capability for visible light absorption, the monoclinic $BiVO_4$ (m-$BiVO_4$) is the most important polymorph. It exhibits superior optical and photocatalytic properties over the tetragonal zircon form that has a band gap of 2.9 eV and an absorption band in the near UV (ultraviolet irradiation) [18]. Kudo et al. [18] studied the optical properties of these two polymorphs and proposed a scheme of the band structures of tetragonal zircon and m-$BiVO_4$ (Fig. 7).
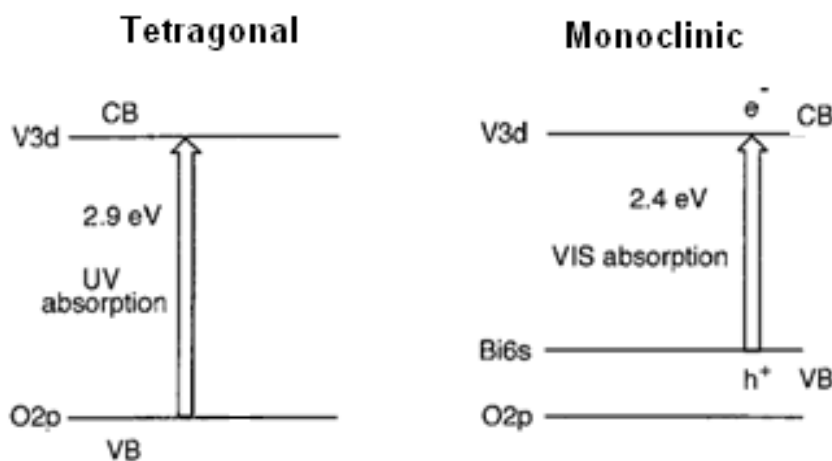
Fig. 7 The scheme of the $BiVO_4$ tetragonal and monoclinic band structures proposed by Kudo et al. [18].

As was mentioned earlier, both tetragonal zircon and monoclinic scheelite structures are constructed from the same structural units but interconnected in different ways. The site symmetry of the Bi cation in tetragonal zircon is D_{2d}, while in the monoclinic sheelite is C_2. According to Stolfuz et al. [14], only the C_2 symmetry allows the mixing of the Bi $6s^2$ and O $2p$ orbitals. This mixing further

results in a decrease of the band gap due to an up-shift of the VB (valence band) level of the monoclinic form, while the VB level in tetragonal form remains low due to their O $2p$ character. Kudo et al. [18] observed differences in the optical absorption spectra of the two polymorphs and attributed them to the differences in their band structures. They proposed that at the top of the VB of m-$BiVO_4$ orbitals are located antibonding Bi $6s^2$ – O $2p$ orbitals, while at the bottom of the CB (conduction band) are positioned the V $3d$ orbitals. In the tetragonal structure, the top of the VB is formed solely by O $2p$ orbitals, at a more positive potential than the Bi $6s^2$ [18]. Therefore, the charge transfer from Bi $6s^2$ – $O2p$ to V $3d$ occurs at a lower energy than the charge transfer in VO_4^{3-}.

A number of researchers have studied the electronic structure of $BiVO_4$ and confirmed or disagreed with the proposed structure of Kudo et al. [18]. In 2009, Walsh et al. [20] reported their DFT (density functional theory) calculations (using the VASP (Vienna Ab initio simulation package) code) on 3 k points: Γ, A, and M, in which they found that $BiVO_4$ is a direct band gap semiconductor because the VBM (valence band maximum) and CBM (conduction band minimum) are located at the same position on the $\overline{AM}$ line. Their calculated E_g is 2.18 eV. In their proposed $BiVO_4$ band structure, the coupling between the Bi $6s^2$ and O $2p$ orbitals results in an upward dispersion of the top of the VB and consequently, reduction of the band gap with 0.4 eV. The CB was found to be dominated by V $3d$ states plus a contribution from O $2p$ and Bi $6p$ orbitals. They also found relatively light effective masses for both electrons and holes (0.3 m^{eff}) which is very important for separation of the photoexcited charge carriers.

Further analyses of Payne et al. [21], using X-ray absorption spectroscopy (XAS), X-ray emission and photoemission spectroscopy (XPS), confirmed the direct band gap of $BiVO_4$ (2.48 eV) and the claim that the Bi $6s^2$ orbitals hybridize with O $2p$ ones to form antibonding states at the top of the VB. They concluded that the visible light absorption in m-$BiVO_4$ originates from the transition from the Bi $6s^2$ – O $2p$ electrons to the empty $3d$ orbital of V, as the scheme of Kudo et al. [18] shows.

However, the study of Zhao et al. [16] disagreed with these previous findings. Their DFT calculations (performed along 6 high symmetry directions of the Brillouin zone: L, M, A, Γ, Z, V) showed a different band structure for m-$BiVO_4$ and a band gap of 2.174 eV. In their band gap calculations, the VBM and CBM are located at

different positions on the $\overline{LM}$ line, which suggest that $BiVO_4$ is an indirect band gap semiconductor. They found nonbonding O 2π states at the top of the VB and nonbonding V $3d$ states at the bottom of the CB. They also argued that the non-bonding O 2π states at the top of the VB are a result of the crystal distortion that pushes the O $2p$ orbitals upwards. In this way, the band gap is reduced. In conclusion, the authors argue that the visible light absorption will excite the electrons in these O $2p$ states towards the unoccupied V $3d$ states, and not from Bi $6s^2$ states as previous studies suggested.

1.1.1.3 Optical properties of monoclinic BiVO₄

In the last years, $BiVO_4$ have attracted an increasing interest in the pigment industry because of its interesting coloristic properties. Due to the high toxicity, the use of lead and chromate pigments has been reduced and new materials have been searched to replace them. With its greenish-yellow colour, m-$BiVO_4$ is non-toxic, and this makes the $BiVO_4$–based pigments a good alternative to lead chromate ($PbCrO_4$) and cadmium sulphide (CdS) pigments.

Despite the fact that the m-$BiVO_4$ displays these interesting optical properties, not much research has been done to understand the relationship between its structure and optical properties. In 1980, Waring et al. [22] have reported on the optical properties of $BiVO_4$ but their studies have not provide enough data. In 1992, Li et al. [23] reported the temperature dependence of the refractive indices of $BiVO_4$ crystals orientated along (100), (110), and (001) planes, investigated by spectroscopic ellipsometry.

A calculated optical absorption spectrum, in which they summed over all possible VB–CB transitions, was reported in 2009 by Walsh et al. [20] For the DFT calculations, they used the VASP code. Their calculated optical absorption spectrum shows an absorption that begins at 2.1 eV plus an absorption peak at about 2.4 eV followed by a continued ascent of absorption at higher photon energies. All the band-edge transitions were considered dipole allowed. Their calculated spectrum is in a good agreement with the experimental spectrum of Luo et al. [24].

In 2011, Zhao et al. [16] have also explored the relationship between the structure and optical properties of $BiVO_4$. They performed DFT calculations using the Cambridge Serial Total Energy Package (CASTEP) code. Their calculated optical

absorption spectrum showed two shoulders: one at 330 nm and one at 440 nm. The first peak was argued to originate from photon absorption on the b axis (E‖b) while the other peak at 440 nm was probably due to photon absorption of polarization direction on the a and c axis (E‖a and E//c). These different absorption properties along the a, b, and c axes were explained based on the bond arrangements in the monoclinic structure; the bond types along the b axis are different than on the a and c axis, but of the same kind on the a and c axis. As a result, the electron transition from the top of the VB to the bottom of the CB are forbidden along the polarization directions E//b due to the arrangement of the V–O bonds, but are allowed for the E//a and E//c polarization directions. The authors suggest that this optical anisotropy is beneficial for the pigmentary properties of m-$BiVO_4$, and also for the photocatalytic ones. Furthermore, the authors believe that the $BiVO_4$ particles with exposed facets on (100) and (001) planes could absorb more visible light than the other orientations, which could contribute to an improvement of the photocatalytic properties. Experimental results of Xi et al. [25] and Zhang et al. [26] confirmed the findings of Zhao et al. $BiVO_4$ with exposed (001) or (010) crystal facets show the enhanced photocatalytic activity due to a higher absorption of visible light.

1.1.1.4 Ferroelasticity in BiVO$_4$

Bierlin and Sleight [27] were the first who showed the existence of ferroelasticity in $BiVO_4$. Their study showed that the m-$BiVO_4$ transforms to the tetragonal scheelite form above 255 $^{\circ}$C through the continue phase transition. More details about the ferroelasticity of $BiVO_4$ can be found in ref [28,29].

1.1.1.5 Synthesis and photocatalytic properties of BiVO$_4$

Bi-based semiconductors have a special band structure which makes them suitable for photocatalytic applications. Their special character comes from the hybrid O 2p-Bi 6s orbitals that shift the VB upward (to lower energies) due to a repulsion between the two orbitals (Fig. 8-b), while the other metal oxides have the VB composed mainly of O 2p orbitals and thus are located at a more positive potential versus the RHE (Fig. 8-a).
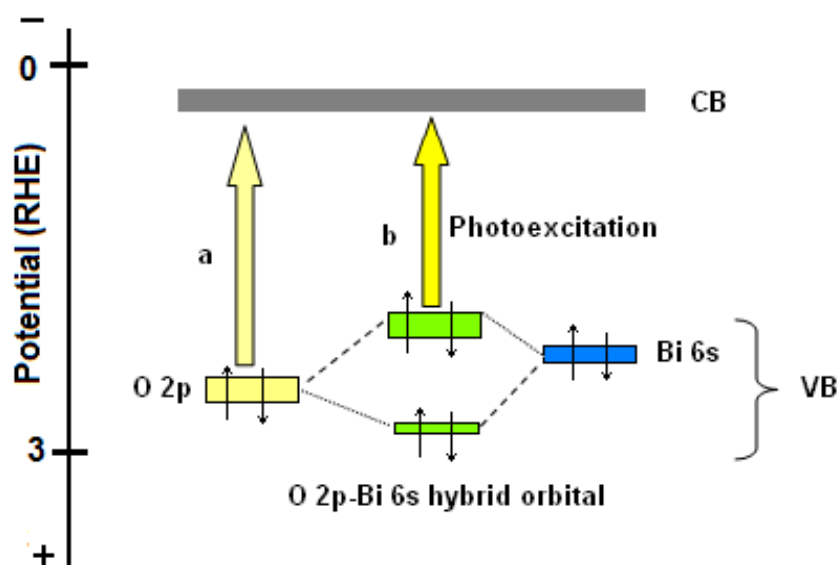
Fig. 8 The positions of VB and CB levels of BiVO$_4$. Adapted from ref [30].

From all the three BiVO$_4$ crystalline forms, the m-BiVO$_4$ shows the highest photocatalytic activity under visible light irradiation. Furthermore, the low effective mass of electrons and holes [19,20] and high energy dispersion in the band structure of m-BiVO$_4$ [16] significantly improve separation and transport properties of the photoexcited charges. Moreover, it is said that the distortion of a Bi–O polyhedron by a $6s^2$ lone pair of Bi^{3+} also facilitates the charge separation and delocalization of photogenerated electrons and holes [15].

Several other factors are playing important roles determining the photocatalytic activity of m-BiVO$_4$ such as: morphology, particle size, crystal defects, surface area, dopants, impurities, surface modification (addition of co-catalysts), etc. M-BiVO$_4$ prepared by the solid-state reaction exhibits few orders of magnitude lower photocatalytic activity than the one prepared by aqueous processes. Therefore, numerous aqueous processes for the monoclinic BiVO$_4$ have been reported during the last decade, such as: hydrothermal synthesis [25,26,31,32,33,34,35,36], co-precipitation [37,38], sol-gel [39,40], ultrasound assisted [41] and microwave assisted synthesis [42], flame spray method [43], microemulsion [44], molten-salt [45], solution combustion synthesis [46], and other.

Room temperature processing techniques such as precipitation from Bi(NO$_3$)$_3$ nitric acid solution and aqueous NH$_4$VO$_3$ solution will generally yield tetragonal BiVO$_4$ while processing techniques at high temperatures result in the monoclinic

phase. After calcination at temperatures around 200 °C or simply by crushing the powder [13], the tetragonal phase transforms to the monoclinic. Kudo et al. [18] reported that polycrystalline samples of monoclinic and/or tetragonal (zircon) $BiVO_4$ can be obtained selectively in aqueous media from a reaction between layered potassium vanadates ($K_3V_5O_{14}$ and KV_3O_8) with $Bi(NO_3)$ in presence of Na_2CO_3 or $NaHCO_3$, by adjusting the preparation time. Pure tetragonal zircon resulted after 4.5 h, tetragonal scheelite after 9–24 h, while monoclinic scheelite after 46 h.

Hydrothermal method is a convenient approach for synthesis of m-$BiVO_4$, because it is offering numerous advantages: is a technologically facile process, is it conducted at low temperatures, it gives the possibility to choose from a large range of precursors, highly crystalline products can be obtained, it allows a good control over the crystal size and morphology, etc. More details about the hydrothermal synthesis can be obtained from the reference [47].

In 2009, Wang et al. [32] prepared uniform m-$BiVO_4$ nanoribbons (with a width ranging from 60 to 80 nm and a thickness from 15 to 20 nm) by a hydrothermal method without using any surfactants. $BiCl_3$ and NH_4VO_3 were used as precursors, while the pH was adjusted to 10 with NaOH solution. After 2h of hydrothermal treatment, BiOCl spheres are initially obtained. But if the reaction time is increased to 8 h, many short and thin ribbons begin to form from the spheres, while after 14 h, the nanoribbons grow longer, wider and thicker. The crucial factor in forming the m-$BiVO_4$ nanoribbons is in the use of $BiCl_3$ and the pH value. $BiCl_3$ hydrolyzes fast to form BiOCl particles and initially slowing down the reaction rate so that large-scale and long uniform nanoribbons can further form. On the other side, a high pH value accelerates the hydrolyzation of $BiCl_3$ that results in a lower Bi^{3+} concentration, which is beneficial for the nucleation and growth of $BiVO_4$ nanoribbons. The as obtained m-$BiVO_4$ nanoribbons exhibited high photocatalytic activity for the degradation of eosin Y dye aqueous solution (with a concentration $5.0 \cdot 10^{-5}$ mol·L^{-1}) under visible light irradiation, being able to degrade 98.8% of the dye in 40 min, while the commercial $BiVO_4$ degraded only 19.2% in 80 min. The high photocatalytic activity was attributed to several factors: the high surface area of the nanoribbons, larger atom density on the (001) lattice plane of the exposed surfaces, the distortion of the Bi–O polyhedron, and the free surfaces (no surfactants adsorbed onto the surface) of the nanoribbons which allowed a direct contact with dye molecules.

By a surfactant-free hydrothermal method, Ren et al. [48] obtained $BiVO_4$ particles with controlled morphology, i.e., 200 nm nanotubes with a hexagonal cross section. The precursors ($Bi(NO_3)_3$ and NH_4VO_3) were dissolved in an ethanol–water mixture, and the pH was adjusted to 4 with nitric acid solution. Under visible light irradiation, the as-synthesized nanotubes showed more than two times higher photocatalytic activity for O_2 evolution than that of bulk $BiVO_4$. The authors explained these results with a higher oxidation capacity of this nanostructure due to their higher valence band potential.

But surfactant-free hydrothermal method cannot result in a large variety of morphologies. In addition, the appearance of large crystals with low surface area is a drawback of this approach which limits the use of as-obtained $BiVO_4$ in photocatalytic processes. On the other side, the surfactant-assisted hydrothermal synthesis brought forward $BiVO_4$ materials with a larger range of morphologies and high surface area. Xi et al. [25] used a surfactant-assisted hydrothermal process to synthesize $BiVO_4$ particles with exposed (001) facets from $BiCl_3$ and NH_4VO_3 precursors and ethanolamine ($H_2NCH_2CH_2OH$). The pH of the solution played an important role in the formation of the nanoplates. At low pH values (1.0, 2.0, and 3.0) particles with irregular shapes were obtained, while with an increase in pH up to 5.0 the particles started to shape into microcrystals and further grew in the well-defined nanoplates at a pH = 6.15. The increase in pH favoured the hydrolization of $BiCl_3$ into BiOCl. With a very low solubility, BiOCl provided a low concentration of Bi^{3+} ions in the solution and thus, lowered the rate of nucleation of $BiVO_4$ crystals, allowing the formation of the particles with the desired shapes. The as-obtained nanoplates showed a very good enhancement of the photocatalytic degradation of rhodamine B (RhB) and photocatalytic oxidation of water under the visible light ($\lambda >$ 420 nm) irradiation compared to m-$BiVO_4$ nanorods. After 30 min of the visible light irradiation, the m-$BiVO_4$ nanoplates almost completely degraded the RhB solution ($12\ mg \cdot L^{-1}$). The authors suggested that the enhanced photocatalytic activity of these nanoplates occurs due to a high hydrophilic character and/or high surface energy of the (001) planes. But another important reason could also be the optical anisotropy that leads to a higher absorption of visible light and better separation of the electron-hole pairs.

Cetyltrimethylammonium bromide (CTAB) has been widely used as a surfactant agent in syntheses of the monoclinic $BiVO_4$ with different morphologies. Ke at al.

[33] used the CTAB-assisted hydrothermal method to prepare lamellar m-BiVO$_4$ particles at a temperature of 200 °C, through a 'microsphere mediated process'. At 160 °C, microspheres consisting of tetragonal and m-BiVO$_4$ were obtained, while at 200 °C, only m-BiVO$_4$ lamellae resulted. The addition of CTAB (with a 0.3 M concentration) and a further increase of the temperature to 200 °C were the principal factors that controlled the tetragonal to monoclinic phase transformation and adjusted the morphology. These lamellar particles presented good photocatalytic activity for the evolution of O$_2$, being able to evolve around 1600 µmol O$_2$ in the presence of Fe(NO$_3$)$_3$ solution and under visible-light irradiation ($\lambda > 420$ nm).

Li et al 2009 [34] also reported on the synthesis of 200−300 nm cubes and flower-like BiVO$_4$ particles by a CTAB-assisted hydrothermal process. In the absence of CTAB, and at a pH of 9, irregular BiVO$_4$ particles resulted. But at a pH of 7 and in presence of CTAB, cuboid-like particles formed (E$_g$ = 2.39 eV). In the presence of CTAB and at a pH of 9, sheet-like crystals with width of around 3 µm and thickness of around 500 nm resulted (E$_g$ = 2.40 eV). If the pH was further increased to 11, from simultaneous collective self-assembly of 2D BiVO$_4$ nanosheets, flower-like structures with a diameter of about 1−2 µm resulted (E$_g$ = 2.46 eV). These findings could indicate that both pH value and CTAB play crucial roles in the morphology evolution of the BiVO$_4$ nanoparticles. CTAB was preferentially adsorbed on certain facets and thus, decreased the growth rate of the adsorbed crystal faces inducing compression along the axis perpendicular to those facets and determining the product geometry. The adsorption of CTAB on certain facets was enhanced at a higher pH through electrostatic forces and this resulted in other morphologies. The photocatalytic activity of these BiVO$_4$ particles (cubes, sheets and flower-like particles) were tested for the photodegradation of methyl orange (MO) 10 mg·L^{-1} under sunlight irradiation. As a reference, the photocatalytic activity of P25 was also tested in the same conditions. The results of the photocatalytic tests showed that the flower like morphology degraded 56% of the MO after 240 min, while TiO$_2$ had the lowest degradation rate of only 12%. Higher specific surface area, lower band gap and plate like morphology were assumed to be the reasons of the higher photocatalytic activity of the flower-like BiVO$_4$ particles.

Zhang et al. [26] also reported the preparation of BiVO$_4$ nanosheets by using a hydothermal synthesis with sodium dodecylbenzenesulfonate (SDBS) as surfactant

and $Bi(NO_3)_3 \cdot 5H_2O$ and NH_4VO_3 as raw materials. At an optimal concentration of 0.72 mmol (0.25 g) SDBS, m-$BiVO_4$ with nanosheet morphology was preferred instead of tetragonal particles that resulted when lower SDBS concentrations were employed. The photocatalytic activity of such $BiVO_4$ nanosheets was estimated for the degradation of RhB ($2.09 \cdot 10^{-4}$ mol$\cdot$L^{-1}) under natural sunlight. Over 60% of RhB was degraded after 180 min in the presence of $BiVO_4$ nanosheets, while bulk $BiVO_4$ was able to degrade less than 20%. The superior photocatalytic activity of the nanosheets compared to the bulk $BiVO_4$ was somehow related to the higher surface area of the nanosheets and a higher photocatalytic reaction at the nanostructure surface.

Han et al. [35] have also reported the use of SDBS assisted hydrothermal synthesis to produce single crystal $BiVO_4$ octahedra with size from 5–200 mm. The size of the octahedra was found to vary with the reaction time, when all other parameters such as acid concentration and temperature were kept constant at 1.2 M and 150 ºC, respectively. For comparison, m-$BiVO_4$ particles were also synthesized in the same conditions, but without SDBS. In this later case, irregular shaped particles with non-uniform particle size resulted, suggesting that the addition of SDBS surfactant plays an important role in the morphology of the m-$BiVO_4$ particles. The photocatalytic performance of the octahedral m-$BiVO_4$ crystals with different crystal sizes was evaluated by the degradation of RhB ($15 \cdot 10^{-3}$ mol$\cdot$L^{-1}) under visible light irradiation. For comparison, the samples composed of irregular $BiVO_4$ particles were also evaluated for the degradation of RhB, in identical conditions. $BiVO_4$ octahedral crystals showed better photocatalytic performance than the $BiVO_4$ particles with irregular morphology obtained by a SDBS free synthesis. Moreover, the smaller sized octahedra (0.2–0.3 µm) showed the highest photoactivity, being able to degrade all RhB in 10 h under visible light irradiation. The higher photocatalytic activity of the smaller octahedrons (200−300 nm size) was attributed to their larger specific surface area of ca. 4 m^2/g compared to the specific surface area of the larger octahedrons (5 µm) of ca. 0.2 m^2/g.

Another surfactant encountered in the synthesis of $BiVO_4$ nanoparticles is L-lysine (Lys). Chen et al. [36] reported the first hollow peanut-like synthesis of m-$BiVO_4$ particles. After 24 h of hydrothermal treatment at 120 or 160 ºC in the presence of SDBS, and further subjected to thermal treatment at 550 ºC, the $BiVO_4$

particles self assembled into particles with a peanut-like morphology. The photocatalytic activity of the peanut-like $BiVO_4$ particles was tested for the degradation of crystal violet (CV) and methylene blue (MB) aqueous solutions ($2 \cdot 10^{-5}$ mol$\cdot L^{-1}$) under solar light irradiation. The samples prepared at 160 ºC and heated at 550 ºC showed the highest photocatalytic activity; after 60 min of solar light irradiation, they were able to degrade all the CV. Similar results was observed for the degradation of the other dye, MB being able to degrade all the MB solution after 60 min of artificial solar light irradiation. In contrast, the irregular-shaped $BiVO_4$ particles showed almost 2 times lower photocatalytic activity. The good photocatalytic activity of the peanut-like m-BVO_4 was related to their large specific area, high crystallinity and special morphology.

The use of NaF in the synthesis of m-$BiVO_4$ has recently been reported by Liu et al. [49]. A hydrothermal treatment at 180 ºC for 24 h of an aqueous solution containing $Bi(NO_3)_3$, V_2O_5, and NaF resulted in surface fluorinated m-$BiVO_4$ particles composed of irregular and large polyedra grown along the [040] direction. The NaF dosage played an important role in both the nucleation dynamics and the surface chemistry of $BiVO_4$ nuclei, directing the crystal evolution and the morphology of the final fluorinated $BiVO_4$ crystals. It was also observed that the absorption edge for the fluorinated $BiVO_4$ samples exhibited slight redshift relative to unflorinated samples. Photocatalytic tests for the degradation of RhB (10^{-5} mol$\cdot L^{-1}$) under visible light irradiation showed that the as prepared particles degraded all RhB after 60 min through two distinctive photochemical pathways: direct semiconductor excitation and indirect dye sensitization. Was also found that fluorinated $BiVO_4$ sample synthesized with moderate NaF dosage facilitates the mineralization process, but fluorinated $BiVO_4$ sample synthesized with excess NaF dosage retards the mineralization process. Excess NaF in the synthesis system not only eliminated the highly active (040) facets, but also reduced the specific surface areas, which leaded to a decrease of the photocatalytic activity.

Li et al. [50] used dimethyl phosphonate (DMP) in a microwave assisted hydrothermal process to prepare m-$BiVO_4$ nanosheets, starting from $Bi(NO_3)_3$ $5H_2O$ and NH_4VO_3 solutions at a pH of 5. The photocatalytic activities of the as prepared m-$BiVO_4$ particles (with the E_g = 2.38 eV) have been measured for the degradation of 0.008 g$\cdot L^{-1}$ MB aqueous solution under visible light irradiation and found to be

much higher than for TiO_2 P25 (Degussa). These results have been attributed to the small particle thickness (10 nm) which could suppress the recombination of the photogenerated charge carriers by an increase in the charge transfer to the particle surface, but as well to their high surface to volume ratio and good dispersity.

Another soft route for the synthesis of $BiVO_4$ is by coprecipitation method. In comparison with the other methods, the co-precipitation offers a number of advantages such as: simplicity, low cost, large scale production, easy control of particle size, low contamination with organic compounds etc. The products are obtained directly in the form of a precipitate that should be further heated to improve crystallinity. In general, lower heating temperatures are desired in order to avoid the growth of the particles and to keep high surface areas. The size and morphology of these particles can be influenced by: a choice of the precursor solutions and their concentrations, the precipitation agent, pH, maturation process and stabilizers. More details about this method can be obtained in references [51,52]. On the other side, the co-precipitation method has few disadvantages such as difficult control of product stoichiometry.

The synthesis of $BiVO_4$ by the co-precipitation method has so far been reported by several authors such as de la Cruz and Perez [37] and Yu et al [38]. De la Cruz and Perez [37] prepared 250–300 nm m-$BiVO_4$ particles by the co-precipitation method at pH of 9 starting from solutions of $Bi(NO_3)_3 \cdot 5H_2O$ in HNO_3 and NH_4VO_3 in NH_4OH. The resulted precipitate was further heated at 200 ^{o}C for 61 h. Yu et al. [38] reported a similar procedure, but even for higher calcination temperature (300 ^{o}C) they obtained $BiVO_4$ particles with a poorer crystallinity. The reason why de la Cruz and Perez obtained the m-$BiVO_4$ particles with higher crystallinity is due to a lower pH of their precursor solution compared with the one of Yu et al. The higher concentration of HNO_3 and therefore lower pH induced faster supersaturation and crystallization of the m-$BiVO_4$. The photocatalytic activity of $BiVO_4$, as prepared by de la Cruz and Perez, was evaluated on the photodegradation of RhB dissolved in aqueous solution (20 mg·L^{-1}) under visible light irradiation. The material exhibited a good capacity to degrade the dye solution, but it was somehow dependent on the pH of the solution and the O_2 flow during the photocatalytic test. At a pH = 10 and after 300 min of visible light irradiation, the solution was bleached by 99%.

1.1.2 NdVO$_4$

1.1.2.1 Crystal and electronic structure

Another important compound from the Bi_2O_3–Nd_2O_3–VO_x system is NdVO$_4$. NdVO$_4$ belongs to the rare earth orthovanadates family, RVO$_4$ (R = Y, Sc, La–Lu), with ABO$_4$-type structure. The rare earth elements refer to the lanthanide family (La–Lu) together with Sc and Y. Lanthanide (Ln) compounds has been extensively studied in the last years. The technological importance and theoretical interest in these compounds rises from the [Xe] $4f^n$ electronic configurations (n = 0–14) of the Ln^{3+}. The energy levels of Ln^{3+} are well-defined because of the shielding of the $4f$ orbitals by the filled $5s^2 5p^6$ subshells and so they are less affected by the chemical (micro)surroundings. Due to their excellent optical properties (wide optical transparency and large birefringence), the rare earth orthovanadates have been used in optical polarizers, lasers host matrices, thermophosphorus sensors, solar cells, phosphors, as scintillators for γ-rays detection, in nuclear waste storage, as ionic conductors, in catalysis for oxidative dehydrogenation, and photocatalysis [53,54,55,56].

At the ambient conditions, the RVO$_4$ compounds exist in two polymorphs: a monazite-type (monoclinic) with space group $P/2_1n$ (Z = 4) and a zircon-type (tetragonal) structure with $I4_1/amd$ (Z = 4) space group. The phase stability of the RVO$_4$ compounds depends upon the R cation size. La, as the larger rare earth element, prefers the monazite structure with La located in a polyhedron where it is coordinated with nine oxygen ions (has nine unique La–O bond distances). The LaO$_9$ polyhedra are edge-shared with VO$_4$ tetrahedra along the c axis [57]. Monoclinic LaVO$_4$ is easily obtained by conventional solid-state reaction or solution process, while tetragonal LaVO$_4$ can only be prepared by solution process with a careful control of the reaction conditions [58]. All the other orthovanadates crystallize (at ambient conditions) in a zircon-type structure (ZrSiO$_4$) where the rare earth ions are located in a polyhedron, in which they are coordinated with eight oxygen ions (see Fig. 1). At the boundary between these monazite and zircon structures lies CeVO$_4$, which also crystallizes prefers the zircon structure but undergoes a phase transition to a monoclinic structure at relatively low pressures compared to the other rare earth orthovanadates. On further increase of pressure, monoclinic CeVO$_4$ transforms to a

tetragonal scheelite structure. However, metastable monazite $PrVO_4$ and $NdVO_4$ can also be obtained but at high pressures.

At ambient conditions, $NdVO_4$ adopts the zircon structure (Fig. 9) but under applied pressures of 6 GPa, it undergoes a phase transformation to monazite. At around 11.4 GPa, $NdVO_4$ further transforms to a scheelite phase and so a denser packing [59]. All these phase transformations are accompanied by a decrease in the band gap of the material for approximatly 0.5 eV (measured on a single crystal) [59].
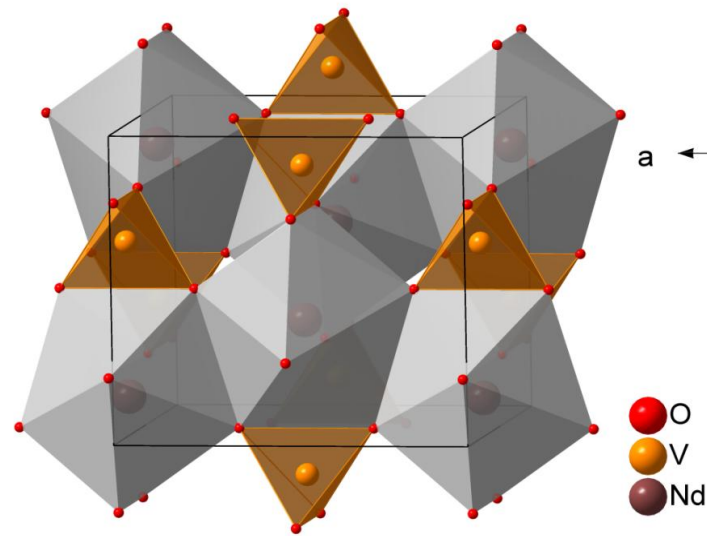
Fig. 9 The zircon structure adopted by $NdVO_4$ at ambient conditions.

The electronic structure of zircon $NdVO_4$ has been investigated by Panchal et al [59]. They observed that $NdVO_4$ shows a similar band shapes as $LuVO_4$ and YVO_4. The upper part of the valence band and the lower part of the conduction band is mainly comprised of the V $3d$ and O $2p$ states, while the Nd $6s$ states contributes to a decrease in the band gap due to their hybridization with the antibonding CB states.

1.1.2.2 Synthesis, optical, and photocatalytic properties of $NdVO_4$

Zircon $NdVO_4$ is one of the most studied orthovanadate. Numerous investigations have been made on optical materials based on $NdVO_4$ [55,60,61] due to their good laser properties. For example, Y-doped $NdVO_4$ is a well known laser material with a 5 times higher absorption coefficient at 808 nm (the standard wavelength of the currently available laser diodes) than in the Nd:YAG laser diodes [60].

The catalytic properties of $NdVO_4$ have been investigated for oxidative dehydrogenation of propane [54] but recently it has been found that $NdVO_4$ exhibits

a photocatalytic activity for degradation of dyes and organic pollutants comparable [62] or even higher than that of the commercial TiO_2 [63]. A study of Mahapatra et al. [56] indicates that Mo-doped $NdVO_4$ shows a higher photocatalytic activity for the degradation of different dyes (such as MB, RhB, remazol briliant blue (RBBR) than $NdVO_4$, under both UV and solar light irradiation.

Besides the solid-state reactions, various other methods have been developed for synthesis of 0D, 1D or 2D $NdVO_4$ nanostructures such as: microwave [64], co-precipitation [62], hydrothermal [65,66], methathesis reactions [67], sonochemical synthesis [68], and other. The synthesis of monodisperse nanoparticles with controllable morphologies is a challenge for the synthetic chemist.

The hydrothermal synthesis is often used for obtaining $NdVO_4$ particles with controllable morphologies. For example, Wu et al. [55] employed the hydrothermal method to obtain, at 180 $^{\circ}$C, single crystalline $NdVO_4$ nanoroads of ~60 nm diameter. The precursors used were Nd_2O_3 and $(NH_4)_{0.5}V_2O_5$ nanowires and an optimal pH of 5−6. The $NdVO_4$ nanowires formed according to the reactions [55]:

$$2 \cdot (NH_4)_{0.5}V_2O_5 + 4 \cdot Nd^{3+} + 6 \cdot H_2O \rightarrow NH_4^+ + 4 \cdot NdVO_4 + 12 \cdot H^+ \tag{1}$$

A 24 h hydrothermal treatment of $NaVO_3$ and $Nd(NO_3)$ aqueous solutions at 180 $^{\circ}$C and in NaOH media with pH ~5 also gives $NdVO_4$ nanorods with diameters of 10−50 nm and lengths of 50−200 nm as reported by Fan et al. [69].

By a hydrothermal treatment at 180 $^{\circ}$C for 24 h starting from $NdCl_3$ and Na_3VO_4 as precursors and with organic trisodium citrate, results $NdVO_4$ nanoparticles of 20−50 nm, as reported by Xu et al. [66].

Also Liu et al. [65] reported on the synthesis of colloidal $NdVO_4$ nanocrystals by a hydrothermal method using oleic acid (OA). The reaction was carried out for 8 h at 140 $^{\circ}$C, starting from $Nd(NO_3)_3$ aqueous solution and Na_3VO_4 as precursors and using NaOH as a mineralizer. In this synthesis, OA reacted with NaOH to form sodium oleate. Sodium oleate had two roles: first, to limit the growth of the particles through interactions with the Nd^{3+} ions, and, second, to prevent the agglomeration of the colloids through electrostatic (via the COO^- groups) and steric repulsions. The as prepared nanocrystals exhibited strong emissions in the visible light range, at 592 nm and at 752 nm, which can be attributed to the $^4I_{9/2}$ to $^4G_{5/2}$ and $^4F_{7/2}$ transitions of the Nd^{3+} ion.

Molten salt method has also been used for the synthesis of $NdVO_4$ nanowires. Xu et al. [70] prepared crystalline 100 nm long $NdVO_4$ nanowires (with $E_g = 2.95$ eV) by a 24 h heat treatment at 200 ^{o}C of $NdCl_3 \cdot 6H_2O$ and V_2O_5 in a $LiNO_3/KNO_3$ 1:2 mixture. The as-obtained nanowires exhibited a selective photoactivity activity for the RhB under solar light irradiation. After 6 h of irradiation, $NdVO_4$ degraded ~75% of a RhB solution (0.01 $mol \cdot L^{-1}$), while only ~29% of MO (0.01 $mol \cdot L^{-1}$) was degraded.

1.2 Review on ABO_3 compounds from the $Bi_2O_3{-}Nd_2O_3{-}VO_x$ system

A general classification of the ABO_3 compounds can be made according to the valence of the constituent ions. There are known compounds of the $A^{2+}B^{4+}O_3$, $A^{3+}B^{3+}O_3$, or $A^{1+}B^{5+}O_3$-type [71]. Ionic or semi-ionic materials with ABO_3 composition tend to adopt either a high-coordination cubic perovskite structure or a low-coordination sesquioxide structure. The two common sesquioxide structures are the ilmenite and the lithium niobate structures.

Materials adopting the ABO_3 perovskite structure are very important from both technological and application point of view. Due to the versatility of their structure and chemical composition, the ABO_3 perovskites exhibit a broad diversity of properties such as: (ferro)electricity, (ferro)magnetism, multiferroicity, superconductivity, metal to insulator transitions, interesting optical properties, and (photo)catalytic activity. The use of the perovskite-based materials in photocatalytic applications is based on their reduced band gap energy and good separation of the photogenerated holes and electrons. Materials like $SrTiO_3$, $BiFeO_3$, $NaTaO_3$, $LaFeO_3$ or $YFeO_3$ have shown a good photocatalytic activity for water splitting and degradation of organic pollutants (dyes).

In the $Bi_2O_3{-}Nd_2O_3{-}VO_x$ system so far has been synthesized only one perovskite type compound, namely $NdVO_3$. By analogy to similar $BiFeO_3$ and $BiMnO_3$ systems, a new Bi-based perovskite with the chemical formula $BiVO_3$ is raising interest but was not synthesized yet. The design and synthesis of new perovskites such as $BiVO_3$ is important not only for understanding their fundamental physics but

also for their great potential for applications in the area of spintronics, lead-free piezoelectrics, acoustics, sensors or photocatalysis.

1.2.1 The perovskite structure

The name 'perovskite' comes from a mineral with the composition of $CaTiO_3$ that was discovered in 1939 and was named after the Russian mineralogist L. A. Perovski. Its unique electronic structure leads to a strong coupling between the structural, electronic and magnetic properties and results in very diverse properties that are extremely important in modern electronic devices. The physical properties of the perovskite compounds are mainly determined by factors such as the chemical composition, cation ordering, defects, synthesis method, particle size and morphology, purity, temperature, strain, applied fields, etc.

Almost 90% of the metallic elements are known to be stable in a perovskite-type structure [72]. Therefore, there is a large number of multicomponent perovskite structures where both A and B cations can be substituted. By choosing different A or B cations, and consequently, altering the band width, the band filling and the electronic correlations in the system, a diversity of electric and magnetic properties can be obtained [73]: catalysts, piezoelectrics, pyroelectrics, superconductors, insulators, multiferroics, etc. For an ideal perovskite structure, the B cation (which can also be a transition metal) occupies a cubic lattice and it is surrounded by octahedra of oxygen anions. The A cation (non-transition metal) occupies the space between the octahedra, being surrounded by twelve oxygen atoms.
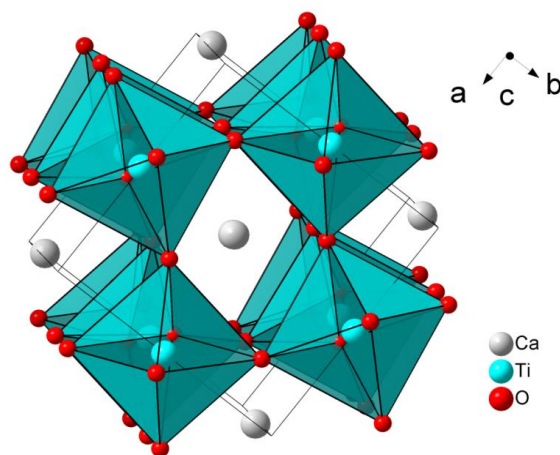
Fig. 10 The perovskite structure – view along the c axis.

The first who has proposed a relationship between ionic radii of the cations and anions in the perovskite structure was Goldschmidt, in 1926 [74]. He treated the lattice as a closed packed array of spheres (ions), where the A cation must be surrounded by as many anions as it can touch. If the ionic radii have the right size to pack perfectly, then:

$$r_A + r_O = \sqrt{2}(r_B+r_O) \tag{2}$$

In words, twice the A–O distance is equal to the length of a face diagonal and twice the B–O distance is equal to the cell edge.

The distortion of the structure can be measured through t, the Goldschmidt tolerance factor:

$$t = r_A+r_O \, / \, \sqrt{2}(r_B+r_O) \tag{3}$$

If $t < 1$, the A cation is too small for its site and this results in a tilting of the BO_6 octahedra, lowering of the symmetry. The tolerance factor for a stable perovskite structure should be in the range 1.05–0.78 [75] for ionic radii reported by Shannon [76]. For $t > 1$, the structure results in hexagonal polytypes.

Another empiric relation to study the stability of the perovskites, as much as important as the tolerance factor, is the octahedral factor, r_B/r_O. A stable perovskite structure should have the r_B/r_O value between 0.414 and 0.732 [77].

As it was mentioned earlier, the symmetry of an ideal perovskite structure is cubic with the $Pm\bar{3}m$ space group. But in the real perovskite structure, this relation is not satisfied; even the Perovskite mineral $CaTiO_3$ is orthorhombic rather than cubic. Known crystal symmetries of the perovskites are tetragonal, orthorhombic ($GdFeO_3$-type structure), rhomohedral, monoclinic and triclinic perovskites. These distortions lead to dramatic changes of their properties. Reasons for structural distortions are

- Ionic radii of the A and B cations, which are related to octahedron tilting,
- First and Second order Jahn-Teller effect (FOJT and SOJT) in BO_6 octahedra,
- A cations off-center displacements which are linked to feerroelectricity or antiferroelectricity.

Many studies have been focused on classifying the perovskites based on the deformations that occur, but the most important study belongs to Glazer [78] who proposed in 1972 a classification of perovskites based on octahedral tilting. The

Glazer tilt notations specify the rotations of the octahedra around each of the Cartesian axes. The Jahn-Teller effect (JT) was first stated in 1937 by Jahn and Teller [79] and it states that *any polyatomic non-linear molecular system in a degenerate state will not be stable and will undergo geometrical distortions that removes the degeneracy and lowers the total energy of the system*. JT effects are grouped into two categories with quite different physical bases. The first (FOJT) arises from incomplete shells of degenerate orbitals - first-order Jahn-Teller effect, and the pseudo(second) Jahn-Teller effect (SOJT) - arises from filled and empty molecular orbitals that are close in energy [80]. The FOJ effect is typical for the transition metal cations with an odd number of d-electrons in the e_g orbitals, *i.e.* d^4, d^7, and d^9 in a crystal with the perovskite structure, surrounded by six O^{2-}. The FOJT effect lifts the degeneracy of the e_g orbitals of the B-cations in an anion crystal field by the distortion of the BO_6 octahedra. The most common type of the BO_6 distortion in perovskites is when two opposite B–O bonds are elongated, two other opposite B–O bonds are shortened and the remaining two 2 stay intact.

1.2.2   NdVO$_3$

In the Bi_2O_3–Nd_2O_3–VO_x system, only one ABO_3-type perovskite is known so far, i.e., $NdVO_3$.

1.2.2.1   Crystal structure and magnetic properties of NdVO$_3$

$NdVO_3$ belongs to the RVO_3 type of compounds. At room temperature, the RVO_3 compounds adopt a *Pbnm* orthorhombic structure with the lattice parameters which can be found in ref [81,82,83] but they undergo structural changes as a function of temperature and R ionic radii. There are two types of JT distortion with the corresponding types for orbital ordering (OO) for the RVO_3 compounds: *G-type OO* and *C-type OO* (Fig. 11). From the two t_{2g} electrons in V^{3+}, one electron always occupies the d_{xy} orbital (due to the orthorhombic distortion) and is coupled ferromagnetically to the other electron in either d_{yz} or d_{zx} orbital, forming a spin $S = 1$. The spins are arranged ferromagnetically along the c axis and antiferromagnetically in the ab plane (C-type). This gives rise to four V–O bonds (two short and two long) for each vanadium atom. This pattern is 'in phase' in adjacent planes along c axis. In the G-type OO, the d_{yz}/d_{zx} OO is alternating in all

three directions, so the V–O bonding pattern in successive *ab* planes is arranged 'out of phase' (Fig. 12).
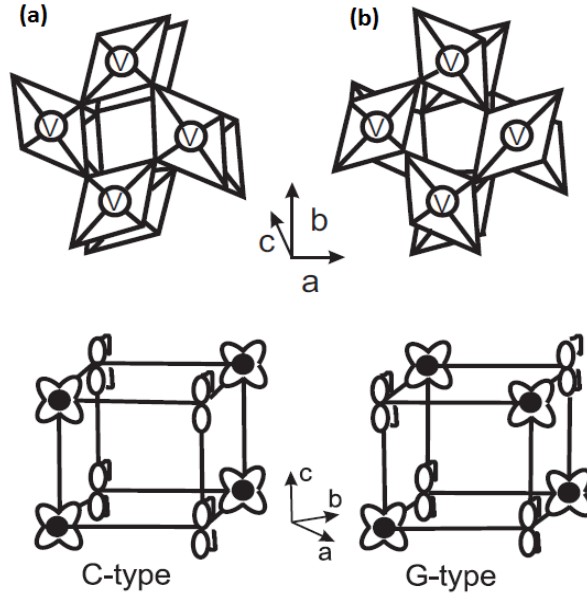
Fig. 11 Top: scheme of the JT distortion associated with C type (a) and G-type orbital ordering (b); bottom: Scheme of the occupied zx and yz orbitals for the C-type (orthorhombic) and G-type (monoclinic) orbital orderings. Adopted from ref [84].
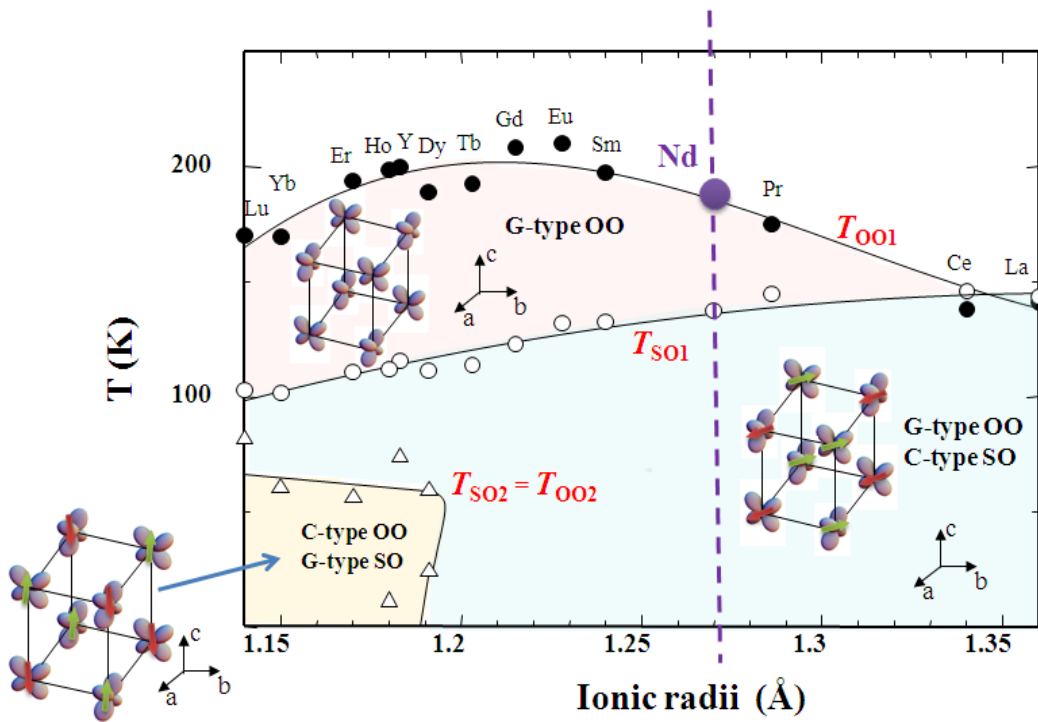
Fig. 12 The spin-orbital phase diagram for RVO$_3$ compounds. Adapted from ref [85].

The type of the orbital ordering that RVO_3 perovskite exhibits, depends on the ionic size of the R cation. The compounds with the smallest R (Lu–Pr) undergo an orthorhombic to monoclinic structural phase transition, simultaneously with a G-type orbital ordering at a temperature T_{OO1} (orbital ordering temperature) which is above the T_{SO1} (the spin ordering temperature). As the ionic radii increases, the T_{OO1} and T_{SO1} cross in between Pr and Ce. For $LaVO_3$ and $CeVO_3$, the T_{SO1} is below T_{OO1} (of the *G*-type OO), which indicates that the C-type orbital ordering induces the G-type one.

For the R cations with ionic radii smaller than the ionic radius of Tb (so with larger octahedral tilting) a second crystallographic and magnetic transition to C-type orbital ordering and G-type spin ordering occurs at T_{OO2} which is equal to T_{SO2}.

At room temperature, $NdVO_3$ (Fig. 13) is distorted from the cubic to the orthorhombic *Pnma* perovskite structure (isostructural with $GdFeO_3$, with the lattice parameters: $a = 5.451$ Å, $b = 5.575$ Å, $c = 7.740$ Å, $\alpha = \beta = \gamma = 90°$ [12]) by cooperative rotation of the VO_6 units around the $\bar{1}10$ axis of the ideal cubic cell.
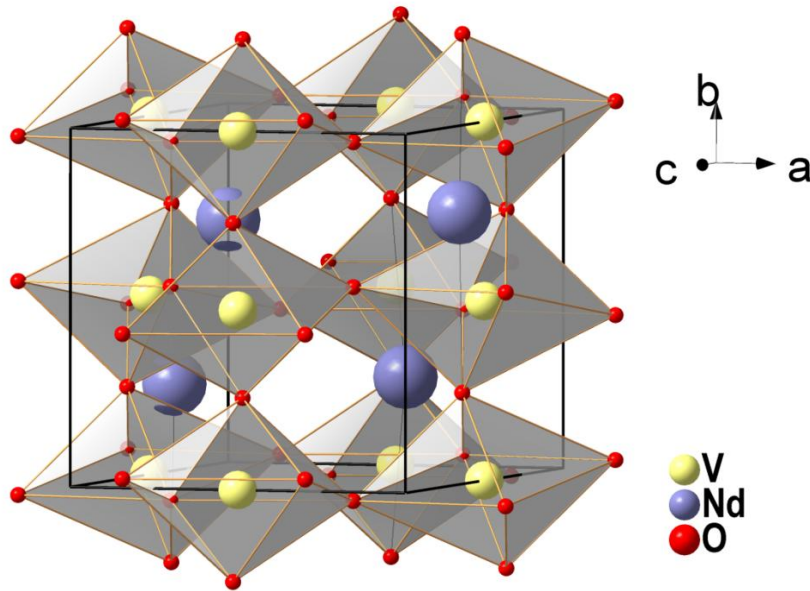
Fig. 13 Schematic representation of the orthorhombic $NdVO_3$ crystal structure.

With the decreasing of the temperature, at $T_{OO} \approx -88$ °C [12,84,86], the orthorhombic symmetry changes to monoclinic $P2_1/a$ and undergoes the G-type orbital ordering and antiferromagnetic coupling. Besides the structural phase transition, this compound undergoes a magnetic transition at $T_{SO1} = -135$ °C to the

C-type antiferromagnetic state where the magnetic moments are ordered antiferromagnetically in the ab plane and ferromagnetically along the *c* axis.

The magnetic properties of $NdVO_3$ were studied by Bozorth et al. [87], Kimishima et al. [88], Tung et al. [89]. $NdVO_3$ shows N-type ferrimagnetism (ferrimagnetism arising from the imbalance of the quenching rate of the orbital moments of V^{3+} ions) (with the magnetic transition temperature at 138 K) and magnetization reversal (MR) with a single MR temperature, T_O, at -260 °C. MR and is a very important phenomenon for both fundamental physics as well as for the application point of view for magnetic data storage and implies a 180 degree 'switching' of the magnetization vector from one stable direction to the opposite one.

The magnetization reversal can be achieved by a large applied magnetic field in the opposite direction of the aligned moments, by changing the temperature or by circularly polarized light. It was discovered in 1948 by Néel on spinels [90], but it was recently studied on transitional metal perovskites, e.g. RVO_3 perovskites, which are an example of compounds which show temperature induced MR. While the MR (for example) in $LaVO_3$ was attributed to the combined effects of Dzyaloshinsky-Moriya interaction, the temperature induced MR in $NdVO_3$ is still an open question. Different mechanisms were developed in order to explain this phenomenon in $NdVO_3$. Kimishima et al [88] explained it based on the N-type ferrimagnetism of $NdVO_3$, while Tung et al [89] suggest that the physics behind MR in $NdVO_3$ may be linked to inhomogenieties caused by a (very) small amount of defects in the quasi one-dimensional orbital systems.

1.2.2.2   Synthesis of NdVO₃

Polycrystalline RVO_3 compounds (with V in +3 oxidation state) are only obtained in a two step synthesis. The first step involves the synthesis of RVO_4 compounds (where V is in +5 oxidation state) with methods such as microwave irradiation, co-precipitation, microemulsion, hydro(solvo)thermal synthesis, etc. The second step is a reduction of RVO_4 for 10–20 hours at high temperatures, e.g., 1000 °C under H_2/N_2 (or H_2/Ar) gas mixture. The thermal reduction leads to the formation of RVO_3 compounds with V in +3 oxidation state. Single crystals of RVO_3 compounds can be grown by a floating zone technique.

The synthesis of $NdVO_3$ has been reported by Sage et al. [84], Tung et al. [89], Kimishima et al. [88], Martinez-Lope at al. [91], and others. Sage et al. [84] prepared polycrystalline orthorhombic $NdVO_3$ by chemical reduction of $NdVO_4$ at 1400 °C in a H_2/N_2 atmosphere. Tung at al. [89] grew single crystals of $NdVO_3$ by the floating zone technique, using a high-temperature xenon arc furnace. At first, $NdVO_4$ was obtained through solid-state reactions from Nd_2O_3 and V_2O_5 at temperatures of 950–1100 °C for 48 hours. Subsequently, $NdVO_4$ powders were reduced in a H_2 flow, at 1000 °C to obtain $NdVO_3$.

Kimishima et al. [88] prepared $NdVO_3$ and Ca-doped $NdVO_3$ by an arc melting method at 1527 °C, and subsequent quenching in Ar atmosphere. Martinez-Lope et al. [91] prepared polycrystalline $NdVO_3$ using a chemical reduction technique of V +5 to V in +3 oxidation state The $NdVO_4$ sample was prepared by a soft chemistry method, using citrates as precursors, while the reducing conditions used were a gas flow containing 15% H_2 and 85% N_2.

No direct method (such as solid-state reactions) for obtaining such RVO_3 compounds has been reported till to date.

1.2.2.3   Photocatalytic properties of $NdVO_3$

$NdVO_3$ was only recently investigated as a photocatalyst for the degradation of organics and dyes. Saha et al. [92] reported on the photocatalytic activity of $NdVO_3$ and Ti-doped $NdVO_3$ samples for different classes of dyes. Their results indicate that $NdVO_3$ had a preferential degradation of chloro-substituted dyes such as Rhodamine Blue (RBL), while the Ti-doped $NdVO_3$ samples are also able to degrade azo-dyes such as: sulfonated azo dye (orange G), heteropolyaromatic dye (MB), sulfonated antroquinoic dye (remazol briliant blue), etc. $Nd_{0.9}Ti_{0.1}VO_3$ powder showed a photocatalytic activity for the degradation of 2 nitro-substituted phenols upon irradiation with an Hg lamp, which is comparable to that of Degussa P-25.

1.2.3 $BiVO_3$

1.2.3.1   Review on the synthesis of Bi-based ABO_3 perovskites

The design and synthesis of Bi-based ABO_3 perovskites (e.g., $BiFeO_3$, $BiMnO_3$, $BiCrO_3$, etc.) are important not only for understanding their fundamental physics but

also for their great potential for applications in the area of spintronics, lead-free piezoelectrics, acoustics, sensors or photocatalysis. The coexistence of ferroelectricity and magnetic order (i.e., multiferroic properties) in $BiFeO_3$ and $BiMnO_3$ has attracted considerable attention on these compounds. Only few materials exhibit the multiferroic behavior in the same phase because the mechanisms inducing the ferroelectricity and ferromagnetism are mutually exclusive due to their different origins [93,94]. In addition, the multiferroics, discovered by now, exhibit very weak coupling at room temperature.

$BiFeO_3$ is the most studied Bi-based ABO_3 perovskites due to the promising room temperature multiferroic properties. Since the first synthesis in the 1950's [95], many of the early studies have focused on its physical and structural characterisation. Below ~827 °C, bulk $BiFeO_3$ has a distorted rhombohedral structure with the $R3c$ space group [96,97]. The stereochemically active Bi ions are responsible for the ferroelectricity by the displacement from their center position towards the [111] direction [98]. This displacement is also encountered in other Bi-based perovskites [99,100]. $BiFeO_3$ also possesses a G-type antiferromagnetic order with the Néel temperature of ~377 °C [101]. Fe magnetic moments are coupled ferromagnetically within the pseudocubic (111) planes and antiferromagnetically between adjacent planes.

Thin films of $BiFeO_3$ have different crystal structure than bulk or single crystals. Grown on $SrTiO_3$ substrates, thin films of $BiFeO_3$ adopt a monoclinic structure, which, below a critical thickness, become tetragonal [102,103,104] due to strain-induced effects.

$BiMnO_3$ is a more controversial compound [105] despite the fact that a large number of studies were devoted to the understanding of its crystal symmetry, ferroelectricity and bulk versus film behaviour. The ferromagnetic order in $BiMnO_3$ is established to occur below −173 °C [107], while the ferroelectricity in $BiMnO_3$ is still a subject of many studies. There are two structural models that researchers try to use for explaining the crystal structure of $BiMO_3$: the $C2$ [106] and the $C2/c$ [107,108]. Only the $C2$ structure permits the ferroelectricity. On the other side, thin films clearly show ferroelectric properties [109]. In bulk form, $BiMnO_3$ can be synthesized using high pressure techniques at ~3–6 GPa. The first successful synthesis was reported in 1960s [110]. Some new studies [111] report the synthesis

of $BiMnO_3$ at atmospheric pressure, but the real composition of the obtained phase has been questioned by other researchers [105].

1.2.3.1.1 Synthesis of $BiFeO_3$ by the classical ceramic route (solid-state synthesis)

The solid-state synthesis of $BiFeO_3$ involves heating a stoichiometric mixture of Bi_2O_3 and Fe_2O_3 at temperatures between 800 and 880 ^oC. Because of the high volatility of Bi and chemical incompatibility of Bi and Pt, Pt crucibles are not recommended to use for the $BiFeO_3$ synthesis [112]. A peculiarity of the solid-state synthesis of $BiFeO_3$ is that regardless of the method employed, secondary phases such as $Bi_2Fe_4O_9$ or $Bi_{24}Fe_2O_{39}$ nucleate at the grain boundaries. The narrow temperature stability range of the $BiFeO_3$ phase, the volatility of Bi, or the presence of impurities in the starting materials may be the reasons for appearance of these competing phases [113]. A process that avoids their formation requires a careful control of the molar ratios and a high purity of the starting materials [113], good control of the cooling rates and gaseous environment (some argue that $BiFeO_3$ may be instable in air [114]). Sometimes, at the end, the 'parasitic' phases are separated from $BiFeO_3$ via a number of different dissolution procedures (i.e., using acetic, nitric or other acids).

The fast-growing interest in nanosized perovskites has motivated researchers to develop other approaches for the synthesis of nanostructured Bi-based ABO_3 materials. When used for ferroelectric data storage applications [115] where the miniaturization of the portable devices became crucial, the reduction of the size of $BiFeO_3$ particles, is a necessity. With the reduction in the size, these materials show distinct properties (e.g., enhanced magnetization, superparamagnetism [116]) as a result of the interplay between surface properties, strain effects from substrates, and quantum size effect [117,118]. Therefore, the size and morphology need to be carefully controlled.

For using $BiFeO_3$-based materials in photocatalytic applications, the understanding of the synthesis process of nanoparticles with a high volume to surface ratio is very important. Since the solid-state method requires high temperatures and yields particles with large size and high defects concentration (that will act as recombination centers for the photogenerated charge carriers and therefore, lead to a

decrease in the photocatalytic activity), we will now discuss the synthesis methods that are used for preparation of nano-BiFeO$_3$ materials for applications in photocatalysis. Several methods are employed for the production of nano-sized BiFeO$_3$ such as hydrothermal [119,120,121,122,123,124], microwave [125], sol.-gel [126,127,128,129], combustion [130] or polyacrylamide gel route [131].

1.2.3.1.2 Hydrothermal synthesis of BiFeO$_3$

This method involves reaction of the aqueous solution of reagents within a pressurized reactor (autoclave) at low temperatures (usually $< 300\,°C$) in the presence of aqueous solvents or mineralizers. The reaction takes place in the presence of aqueous solvents under high-pressure-high temperature conditions to dissolve and recrystallize materials that are insoluble at normal conditions. The autogenous pressure that develops within the autoclave depends on the hydrothermal temperature, the filling rate of the reactor, and the type of the solvent used. A processing time of 6–24 hours is usually sufficient for formation and crystallization of the desired compound. This method has the advantage of a low process temperature, good dispersion and is suitable for both bulk or nanocrystals. A precise control over characteristics such as morphology, size, crystallinity, and porosity can be achieved by utilizing a wider range of precursors or/and by changing the experimental parameters such as solvent type, temperature, reaction time, etc. Other varieties similar to hydrothermal synthesis are known, depending on the solvent used such as solvothermal, ionothermal, alcothermal, glycothermal, ammonothermal, and other.

Well crystallized BiFeO$_3$ with various morphologies (microspheres, microcubes, plates, spindle-like) can be hydrothermally synthesized from a precursor solutions usually containing Bi(NO$_3$) and Fe(NO$_3$)$_3$ in a mineralizer solution (NaOH or KOH) at a pH of 8−14, with surfactants such as Polyethylene glycol (PEG), CTAB or not, at temperatures of ~200 ºC for 24 to 72 hours. The concentration of the mineralizer solution and the presence of the additives play important role in the control of the morphology and the E$_g$ value. The use of PEG was reported [119] to be a suitable way to decrease the particle size from ~5 μm cubes (E$_g$ = 2.12 eV) to ~500 nm (E$_g$ = 2.27 eV) ones. Xiaomeng et al. [122] also observed a similar trend for a CTAB-assisted hydrothermal synthesis. Here, CTAB was added to direct the

morphology of the particles and to decrease their size. In the absence of CTAB, irregularly shaped $BiFeO_3$ particles with an average size of 3 μm were obtained. However, when the hydrothermal synthesis was performed in the presence of CTAB, uniform plates of 2 μm diameter and ~ 300 nm thickness resulted.

During the hydrothermal process, the size of the synthesized particles depends on the competition between crystal nucleation and crystal growth, which are further influenced by the inherent crystal structure and the pH value of the precursor solution. When the rate of nucleation is greater than the rate of crystal growth, the crystals will be small. A fast crystal growth will give large crystals and with a high aspect ratio along preferential directions [124]. According to the results of Li et al. [119], a moderate alkaline medium (8 M KOH) results in a fast crystal growth and large $BiFeO_3$ microspheres (with an E_g of 1.82 eV), while a high alkaline medium (12 M KOH) produces microcubes (with E_g = 2.12 eV).

The addition of additives such as PEG has been found to be also beneficial for reducing the particle size [119]. Han et al. [124] reported that the synthesis (at 200 °C) of pure phase spindle-like $BiFeO_3$ particles, can be facilitated by the addition of a small amount of H_2O_2 in a very alkaline pH (14). Without H_2O_2 at pH of 8-12, another phase, $Bi_{12}Fe_{0.63}O_{18.945}$, was obtained [124]. Temperatures as low as 130 °C can be employed for the synthesis of nano-$BiFeO_3$ [132] but only in presence of triethanolamine (TEA). Such 24-hour hydrothermal treatment of a suspension, obtained by precipitating a solution of the Bi and Fe precursors with a mixture of TEA and KOH, yielded $BiFeO_3$ nanopowders [132].

1.2.3.1.3 Synthesis of BiFeO$_3$ by sol-gel method

The sol-gel synthesis is a soft chemistry method to obtain (nano)oxide materials at low temperatures. The basic idea is that a sol (a stable suspension of colloidal solid particles within a liquid) containing the precursors (metallic salts or alkoxides) undergoes hydrolysis-polycondensation reactions to create an oxide network. The first step occurs in the sol phase and involves the hydrolysis of the precursors, where the alkoxyl groups (OR^-) are replaced by hydroxyl (OH^-) groups. A gel further results through the polycondensation reactions. A condensation reaction can take different patways: it can go through the reaction of the hydroxyl groups with other alkoxyl groups to generate a M−O−M network and an alcohol molecule (ROH),

and/or through the reaction of the hydroxyl groups with other hydroxyl groups to produce the M–O–M network and H_2O. During the gelification, the viscosity of the solution increases dramatically. After the *aging period* – a process through which the gel is transformed into a solid mass, the gel is further dried at temperatures that depend on the synthesis conditions of the gel. In a process of drying, the water and other volatile liquids are removed from the gel network and the gel densificates. Usually, the formation of new phases (oxides) do not occur at these low temperatures and the termodynamically stable product will be obtained only at high temperatures, when the thermal energy will be enough for the reconstruction of the oxygen packing.

Several factors are affecting the sol-gel process: the type of precursors, type of solvent, temperature, pH, concentrations of the reactants, presence of additives, agitation time, use of catalysts, etc. In a typical procedure for synthesis of single phase $BiFeO_3$ nanoparticles with the size from 100 to 150 nm, the precursors – usually $Bi(NO_3)_3$ and $Fe(NO_3)_3$, are dissolved in 2-methoxyethanol. The reaction can be performed either by adding different amounts of acid catalyst (HNO_3) until a pH of 4–5, or not. Usually citric acid (in 1:1 molar ratio with respect to the metal nitrates) is used as a complexant, while ethylene glycol (EG) or PEG are employed as dispersants. The resulted mixture is stirred for ~30–60 min at 60–80 °C to form the gel. Then the gel is further processed by heating at ~500 °C for 2 h and a fine powder is obtained.

1.2.3.2 Photocatalytic properties of Bi-based ABO_3 perovskites

It is known that ABO_3 perovskite-type oxides are important heterogeneous catalysts in industrial reactions. As one of ABO_3, $BiFeO_3$ (E_g ~2.2 eV) also poses interesting catalytic and photocatalytic properties of interest in certain oxidation and reduction processes [119–131,132,133] in addition to the applications in the information storage, spintronics, sensors, etc.

The applications of $BiFeO_3$ in solar energy conversion technologies such as photocatalysis and photovoltaics started with the recent studies of Gao et al. [126], Joshi et al. [125], and Yang et al. [134]. Usually, the main advantage of a Bi-based photocatalyst is the low band gap due to the hybridization between Bi $6s$ and O $2p$ orbitals. This increases the VB level compared to other metal oxides. In this case, not

only the low band gap is responsible for the good photocatalytic activity of $BiFeO_3$ but also the internal polarization of the material [130].

$BiFeO_3$ is a ferroelectric material characterized by a nonzero polarization in the absence of an electric field, also called *spontaneous polarization* that can be switched with an applied electric field of the opposite sign. The direction of the polarization varies from region to region inside the material. A region with a local uniform polarization is called a *domain*. The domains are separated from each other by *walls* (or '*domain walls*'). These domain walls are often referred to the angle between the polarization vectors on the two sides of the wall. The band bending [135] will transport the electrons on the surface of the domains where the electric dipole is aligned with its positive end, creating spatially selected sites for reduction reactions. The holes will be directed towards the surfaces where the electric dipole is aligned in the opposite direction, creating positively charge surfaces that will act as active sites for oxidation reactions. This effect is called '*dipolar field effect*'. Because the charge carriers are separated by the internal polarization, they are less likely to recombine, and this can lead to an increase in the photocatalytic efficiency of the material.

In Fig. 14, the domains in a ferroelectric sample and the effect of the dipolar field on a photochemical reaction are schematically illustrated.
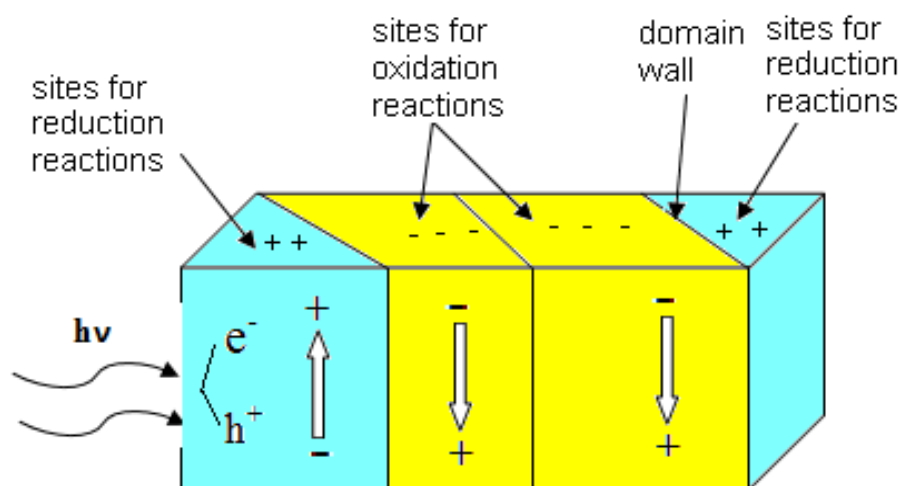
Fig. 14 Domain walls and the effect of the dipolar field on photochemical reactions.

Due to a higher local electric field than in the bulk, a more efficient separation of the photo-generated excitons can occur when the light is incident to the domain wall.

The photoexcited electron–hole pairs are separated and drift to either side of the domain wall, resulting in an excess of charge: see Fig. 15.
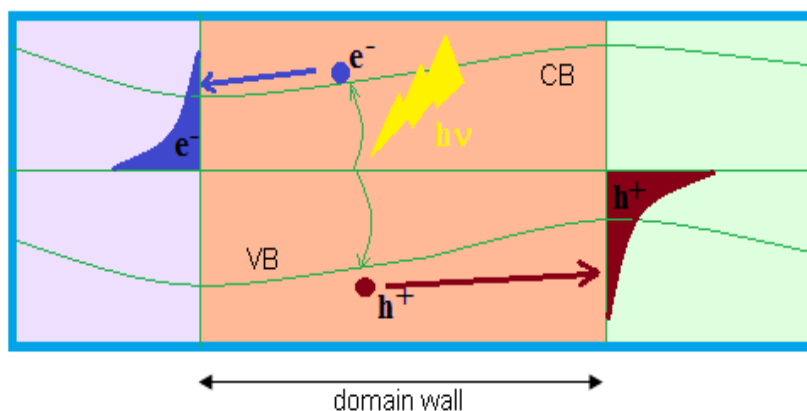
Fig. 15 Scheme representing the band bending and the evolution of the photoexcited charge carriers at the domain wall.

The photocatalytic properties of ferroelectric/ferromagnetic $BiFeO_3$ have been studied in the form of bulk, nanoparticles, nanowires, or thin films, in pure phase or doped, in form of heterostuctures with other photocatalysts (TiO_2, $SrTiO_3$). The organic dyes usually degraded by $BiFeO_3$ are: RhB [127,128,130,123], MO [126,131], Congo Red (CR) [119] and orange II [122].

Hengky at al. [130] tested the photocatalytic activity of 20 nm $BiFeO_3$ nanoparticles towards the degradation of RhB dye under simulated solar light and at different pH values. They found that at an optimal pH of 2.0 the $BiFeO_3$ nanoparticles were able to totally degrade the dye in 30 min.

The visible light photocatalytic activity (for the degradation of CR) of the $BiFeO_3$ microspheres synthesized by Li et al. [119] by a hydrothermal method was found to be negligible, but $BiFeO_3$ cubes < 1μm posses a good photocatalytic performance, degrading 40% of the dye after 3 hours.

The $BiFeO_3$ nanoparticles (80–120 nm, E_g of 2.18 eV) obtained by Gao et al. [126] through a sol-gel technique were able to decompose almost 90% of the MO under 16 h of visible light irradiation.

Xian et al. [131] reported that there is a dependence of the photoctalytic performace of $BiFeO_3$ on the particle size and morphology. They have compared the visible light activity as well as UV photocatalytic activity of $BiFeO_3$ nanoparticles with different particle size, i.e., 52, 70, 95 and 110 nm. The photocatalytic activity exhibited a rising trend with the decrease of the particle size. The 52-nm size

particles showed the highest activity for degradation of MO for both visible and UV light. The small size and the high surface-to-volume ratio of the 52 nm particles could be the reasons of the observed increase in the photocatalytic activity. The smaller the particle size, the lower the recombination of the photogenerated charge carriers, and the higher the number of the active sites available.

The influence of morphology on the photocatalytic activity of $BiFeO_3$ was studied by Xiaomeng et al. [122]. Two dimensional plates with the dimensions of about 2 µm and 300 nm showed a much higher activity for the degradation of orange II under visible light than the irregularly shaped $BiFeO_3$ particles with an average size of 2 µm.

Other ways to improve the photocatalytic activity of $BiFeO_3$ is by doping. Guo et al. [128] reported that doping $BiFeO_3$ with Gd increases the efficiency for the degradation of RhB under visible light irradiation. The highest photocatalytyic activity was at a doping concentration x of 0.1. The reasons may be an increase in the E_g (for 0.1 Gd doping the E_g increased from 2.03 to 2.2 eV) and a larger space charge region at the interface of the particle and solution helped the separation of the photogenerated electrons and holes [128].

$BiFeO_3$ can also be used as a 'coating' for large band gap semiconductors like $SrTiO_3$ [121]. The photocatalytic activity of $BiFeO_3$ coated $SrTiO_3$ for the water splitting process (under visible light radiation was 129 $\mu mol \cdot h^{-1} \cdot g^{-1}$ of produced H_2. No H_2 can be produced under such conditions with uncoated $SrTiO_3$. The authors claim that $BiFeO_3$ sensitized the $SrTiO_3$ shell to visible light.

1.3 Photocatalysis

In 2011 the world population of our planet reached 7 billion [136] and it continues to grow by about 80 million each year [137]. Some of the biggest problems associated with the increasing number of people are the environmental pollution and the high energy demands. The present time welfare of the continuously growing population is built upon fossil fuels. But coal, oil, or natural gas (which provides us with around 87% of the total energy supply) are estimated to only last for about next 100 years. Nowadays, only 6.5% of the total energy consumed comes from renewable sources [138]. What is more to worry about is that the energy crisis will start long before the fossil fuels will disappear and these reserves are hard to recover.

Another serious concern is the global warming. Among other greenhouse gases such as methane or nitrous oxide, carbon dioxide is the gas most responsible for the warming. CO_2 is the main residue of the energy production through the burning of fossil fuels in cars, factories, or for electricity production. Therefore, the use of fossil fuels makes a serious contribution to the CO_2 emission in the atmosphere causing the so-called 'greenhouse effect'[1]. The level of the greenhouse gases has been quite constant in the last two thousand years, but now the changes are happening over the course of decades. Since then, the industrial revolution and the expanding human population have increased the amount of CO_2 in the atmosphere by more than a third. Hoffert et al. [139] estimated that the CO_2 level has increased from 250 to 370 ppm, and it is currently rising by about 2 ppm/year. Consequences of levels > 400 ppm could be dramatic: the ecosystems could change, the ice could melt worldwide (especially at the Earth's poles), the sea levels could rise, less fresh water could be available, some diseases could spread, etc. A concentration of 450 ppm would increase the temperature by 3 degrees, while at a level of 550 ppm, the effect of the global warming could be comparable in magnitude (but with opposite sign) with the Ice Age [139]. An international goal [140] is to stabilize the carbon dioxide to levels that will not induce climate changes (<350 ppm). To reduce and keep the CO_2 level at the low concentration, we have to find new green (renewable) energy sources that do not emit CO_2. But this is a very challenging task if we consider the economical issues associated with the new technologies.

With the growing population, we are also facing environmental problems related to the remediation of contaminated groundwater, hazardous wastes or toxic air contaminants. The contaminated industrial water is the first source of contact between the population and toxic wastes such as: phenols, halogenated hydrocarbons, biocide compounds from the pharmaceutical companies, organic dyes from textile industry, etc. In order to prevent the contact, and before their release in the environment, these compounds must be oxidized to inert species such as CO_2, water, NO_3^-, or SO_4^{2-}. Because the traditional treatment of water in wastewater treatment plants is not successful, more powerful processes are necessary to oxidize these compounds.

---

[1] The 'greenhouse effect' is the warming that happens when certain gases in the Earth's atmosphere trap heat. These gases let in light but keep heat from escaping, like the glass walls of a greenhouse.

All these concerns of the modern world opened the use of solar energy for chemical transformations. Photocatalysis[2] can provide solutions for pollution control of the air or water, and can also be applied to the production of the fuel of the future–hydrogen.

1.3.1 Solar hydrogen production

Among other green energy projects that are underway (such as photovoltaic cells), collecting and storing solar energy in form of chemical bonds is a promising and desirable solution to the future high energy demands. Hydrogen is a prime candidate for a future energy carrier, but introducing hydrogen as a fuel into the world still dependent on oil is a very challenging task. The most important for so-called *hydrogen economy* is to achieve a low cost of hydrogen production from renewable energy sources. To be competitive with other renewable sources an optimum price for hydrogen is set at \$2–4/kg [141]. Another big problem of the hydrogen economy is storage of H_2. H_2 has a low volumetric density compared with hydrocarbons, so it requires larger tanks to store. This disadvantage can be overcome by compression, liquid-cryo storage, physiosorption on metal-organic frameworks (MOFs), by forming chemical bonds in the metal hydrides, or by making chemical fuels with CO_2.

Many routes for producing hydrogen are nowadays adopted such as different energy–conversion processes from other sources of energy like fossil fuels (natural gas, coal, petroleum), renewable resources (like biomass), etc. But the most straightforward method is to produce hydrogen from water. Water is an available and abundant source of hydrogen and the only residual product of its burning. There are many ways to convert water to hydrogen: electrolysis, thermochemically, photobiologicaly, artificial photosynthesis, using coupled photovoltaic-electrolysis systems, by photoelectrochemical water splitting, or photocatalytic water splitting. All of these methods have advantages and disadvantages, but the most promising ways to obtain hydrogen from water are the photoelectrochemical water splitting and photocatalytic water splitting using sunlight–the most abundant, renewable and free energy. The solar energy is an inexhaustible natural resource, more energy from

---

[2] Photocatalysis defines a catalytic process under light irradiation.

sunlight strikes our planet in one hour (4.3×10^{20} J) than all the energy consumed in a year: 4.1×10^{20} J [142].

The water splitting reaction that yields H_2 and O_2 is accompanied by a positive change in the Gibbs free energy with $+ 237$ kJ/mol (1.23 eV).

$$2H_2O \xrightarrow{Sunlight} 2H_2 + O_2 \qquad\qquad \Delta G = +237 \text{ kJ/mol} \qquad\qquad (4)$$

The reduction reaction is a two electron transfer reaction, while the oxidation of water to form oxygen involves four electrons:

$$2H_2O \quad\rightarrow\quad O_2 + 4H^+ + 4e^- \tag{5}$$

$$4H^+ + 4e^- \rightarrow 2H_2 \tag{6}$$

$$2H_2O \xrightarrow{h\nu} 2H_2 + O_2 \tag{7}$$

The photoelectrochemical and photocatalytic water splitting are very similar concepts. The schematic representations of the two types of processes are illustrated in the Fig. 16.

(a)   (b)
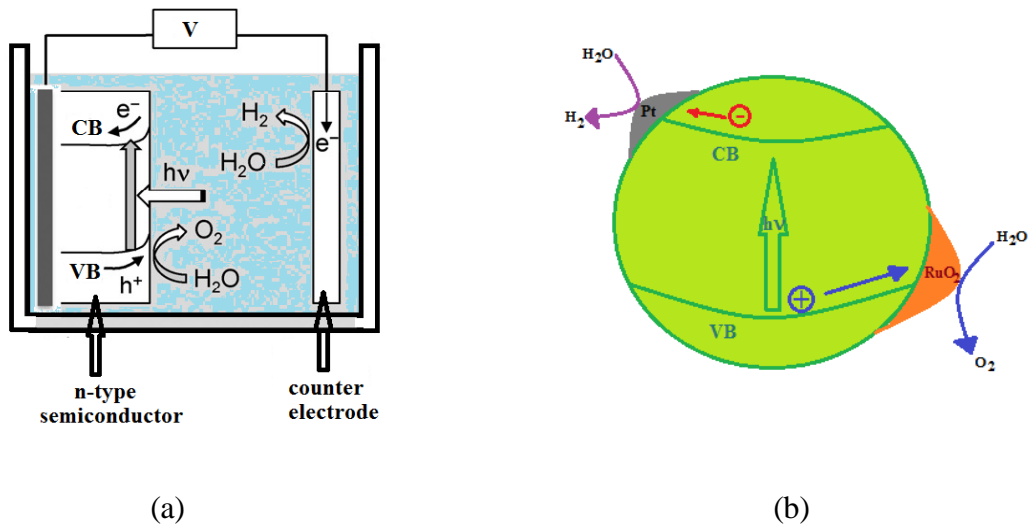
Fig. 16 Schematic representation of a photoelectrochemical cell (a) and the water splitting at a photocatalyst particle with two co-catalysts (b).

A photoelectrochemical cell (Fig. 16a) consists of a n-type semiconductor (photoanode) and a counter electrode immersed in an electrolyte. The electrodes are connected through an external bias. When the anode is illuminated, electron-hole

39

pairs are generated. The photogenerated electrons migrate to the counter electrode (such as Pt) where they can reduce water to form H_2, while the holes left behind can oxidize the water to form O_2. Water splitting at a photocatalyst particle is represented in Fig. 16b. After photoexcitation, the electron and hole generated will travel to the surface where they are involved in reduction and oxidation reactions. For the reactions to take place (oxidizing H_2O to O_2, and reducing H_2O to H_2), the photocatalyst has to provide active sites (co-catalysts). If the active sites do not exist, then the photogenerated charge carriers will not initiate any reactions and will recombine.

1.3.2 Photocatalysis for environmental remediation

Conventional water treatment methods such as filtration, sedimentation, or adsorption, do not completely succeed to destroy the pollutants, include high operating cost, or can generate high secondary pollutants in the ecosystem. Therefore, new technologies have been developed for chemical treatment of industrial wastewater, contaminated ground water, drinking water and air, namely the *advanced oxidation processes* (AOPs). AOPs involve in-situ generated highly powerful oxidants such as hydroxyl radicals ($\cdot$OH), to accelerate the oxidation and, thus, the mineralization of recalcitrant organic compounds, water pathogens and other wastewater contaminants. Some of the processes include: UV iradiation [direct irradiation or mediated by hydrogen peroxide (UV/H_2O_2), or ozone (UV/O_3)], heterogeneous photocatalysis (UV/TiO_2), electron beam irradiation, ultrasonic irradiation, Fenton's treatment, etc [143]. While all the processes described above can destroy recalcitrant species, the best choice for a particular system depends on several factors such as: nature of the polluted medium, total load of oxidizable species, the number of pre-treatments available, temperature, pH, and other.

An AOP process can be divided in three parts:

1. The formation of $\cdot$OH radicals (it depends on the type of AOP used).
2. The attack of $\cdot$OH on the target molecules, breaking them into less stable by-products.
3. Complete mineralization.

Heterogeneous photocatalysis has been proved to be an efficient method for the elimination of toxic organic and inorganic compounds from the aqueous phase

through the ability of some semiconductors to oxidize certain organic and inorganic substances at ambient temperature [144]. The main difference from other AOPs is the use of a photocatalyst instead of ozone or H_2O_2 that are considered expensive.

In most of experiments with semiconductor photocatalysts, oxygen dissolved in water acts as a primary electron acceptor via the mechanism described in the reactions 8–11. At first, oxygen dissolved in water can trap the photogenerated electron and form the $O_2^{\cdot-}$ (superoxide anion radical) that oxidizes the pollutants, but not as effective as $\cdot OH$ radicals. The $O_2^{\cdot-}$ radical can also transform into H_2O_2. H_2O_2 can act as a direct electron acceptor and further transform in $\cdot OH$ radicals [145]:

$$(O_2)_{aq} + e_{CB}^- \rightarrow O_2^{\cdot-} \tag{8}$$

$$O_2^{\cdot-} + H^+ \rightarrow \cdot OOH \tag{9}$$

$$\cdot OOH + H^+ + e_{CB}^- \rightarrow H_2O_2 \tag{10}$$

$$H_2O_2 + O_2^{\cdot-} \rightarrow \cdot OH + OH^- + O_2 \tag{11}$$

To summarize the processes that take place in the photocatalytic reaction for water remediation, the following (simplified) reactions can be written:

Photoexcitation (charge carrier generation): $SC + h\nu\ (\geq E_g) \rightarrow h_{VB}^+ + e_{CB}^-$ (12)

Electron-hole recombination: $h_{VB}^+ + e_{CB}^- \rightarrow heat$ (13)

Charge carrier trapping:

    Hole trapping: $h_{VB}^+ + >SC\text{-}OH \rightarrow \{>SC\text{-}OH^\bullet\}^+$ (14)

    Electron trapping: $e_{CB}^- + >SC\text{-}OH \rightarrow \{>SC\text{-}OH/e_{tr}^-\}$ (15)
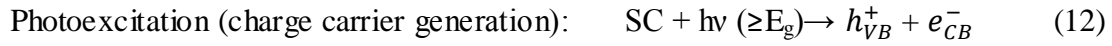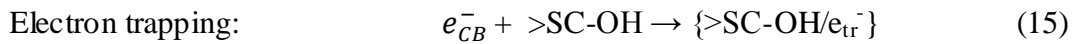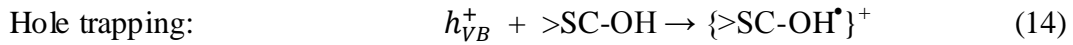
Interfacial charge transfer:

    Hole transfer: $\{>SC\text{-}OH^\bullet\}^+ + Red. \rightarrow >SC\text{-}OH + Red^{\bullet+}$ (16)

    Electron transfer: $\{>SC\text{-}OH/e_{tr}^-\} + Ox. \rightarrow >SC\text{-}OH + Ox^{\bullet-}$ (17)
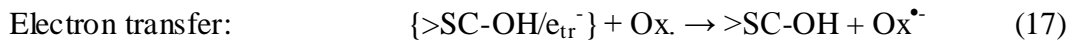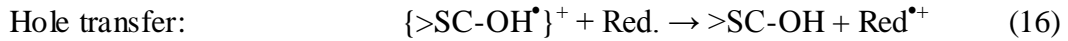
The notations used denote:

SC = semiconductor,

>SC-OH = primary hydrated surface of the semiconductor,

e_{CB}^- = photoexcited electron in CB,

h_{VB}^+ = photoexcited electron in VB,

>SC-OH/e_{tr}^- = surface trapped CB electron,

>SC-OH$^{\bullet+}$ = the surface trapped VB hole (the surface-bound hydroxyl radical),

Red. = electron donor,

Ox. = electron acceptor.

1.3.3 Main processes at a semiconductor particle upon band gap illumination

The main processes that take at a semiconductor particle upon band gap illumination are:

1. Absorption of the photons in the photocatalyst with the creation of the electron-hole pairs.
2. Migration of the electrons and holes to the surface.
3. Electron transfer reactions according to the redox potentials of the adsorbate (the electron is transferred to the acceptor molecules, while the donor molecule transfer an electron to the hole created in the photocatalyst).

1. Absorption of light (photons) to form electron-hole pairs ('excitons')

Electrons in a crystal are arranged in energy bands that are filled with electrons with increasing energies. The highest filled band is called VB, while the lower empty band is called CB. The VB and CB are separated by a forbidden region called 'energy gap' E_g or simply 'band gap'. The E_g is defined as the difference between the lowest point of the conduction band and the highest point of the valence band (Fig. 17). In a semiconductor crystal, the electrons can be promoted from VB to CB by electromagnetic ($h\nu$) excitation, only if $h\nu \geq E_g$. The threshold of continuous optical absorption gives the E_g.

There are two types of absorption processes: direct and indirect. In an electronic transition, the electric dipole momentum must be conserved, that is, the electric dipole momentum of the semiconductor in the final state must be equal to the sum of the electric dipole momentum of the solid in the initial state plus that of the absorbed photon. In a direct absorption process (as described in Fig. 17 left), a photon is absorbed by a crystal with the creation of an electron and a hole (the transition is vertical, with no change in the electric dipole momentum). In the case of an indirect absorption process (Fig. 17 right), a phonon can be absorbed or withdrawn by the lattice to ensure that the total electric dipole moment remains unchanged while an electron is promoted with a variation of its momentum.

So, only when a semiconductor is illuminated with photons that exhibit energy equal or greater than the E_g of the semiconductor, the electrons from the VB excite to the CB, generating holes in the VB (h_{VB}^+) and electrons in the CB (e_{CB}^-). The process is called 'photoexcitation'. The e_{CB}^- can act as a reductant, while the h_{VB}^+ is able to oxidize certain molecules. Their redox ability depends on the chemical potentials of the semiconductor relative to the normal hydrogen electrode (NHE).
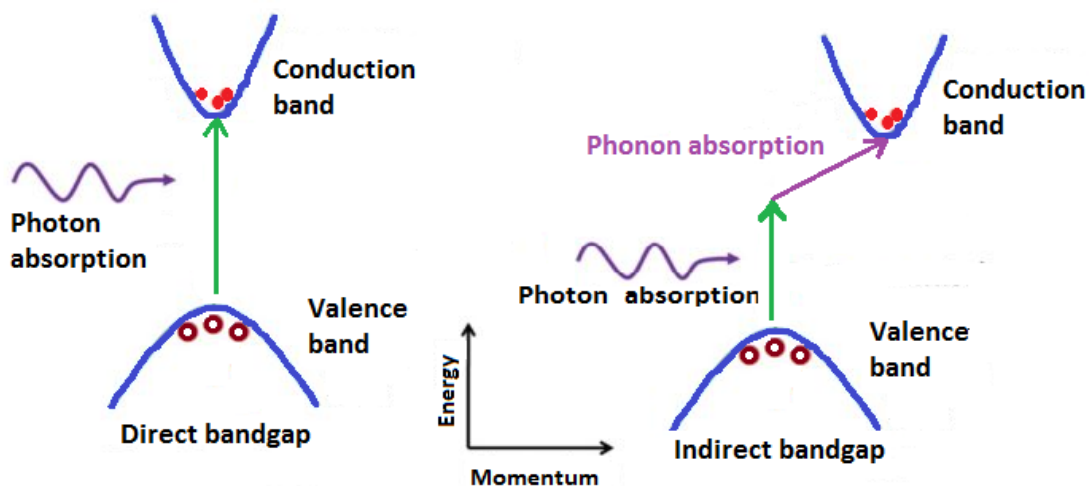
Fig. 17 A photon absorption process in the direct and the indirect band gap semiconductors.

2. *The charge separation and migration of the photogenerated carriers to the surface.*

The electron-hole pairs that are generated upon photoexcitation can dissociate and migrate to the surface where they can be trapped in surface states causing reduction and/or oxidation reactions. The ones that stay in the bulk recombine at the boundaries or defects (Fig. 18) dissipating heat or light.

The recombination of the photogenerated carriers is one of the biggest problems encountered in photocatalysis. A large proportion of excitons is recombining and thus, dissipate the input energy in form of heat or emitted light, resulting in a decrease of the photocatalytic efficiency. Because crystal structure and the crystallinity strongly affect the fate of the charge carriers, one way to overcome this problem is by increasing the crystallinity. The higher the crystallinity, the lower is the number of defects. Loading co-catalysts on the semiconductor's surface creates active sites. At the interface between the co-catalyst and the semiconductor, an electric field is formed which facilitates the separation of the electron-hole pairs,

induces a faster carrier migration and can also lower an overpotential. Some examples of the co-catalysts are: Pt, Pd, Ag, Au, NiO or RuO_2.
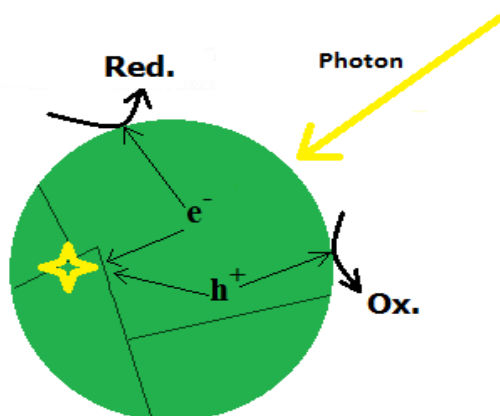
Fig. 18 Fate of the charge carriers at a semiconductor particle.

Another solution to avoid recombination is to decrease the particle size. With decreasing the dimension of the particle the distance that the photogenerated electrons and holes have to travel becomes shorter and the recombination probability decreases (the photogenerated charge carriers will easier reach the surface before they recombine). By decreasing the particle size, also the specific surface area becomes larger which increases the possibility of the charge carriers to find surface traps.

1. *Electron transfer reactions / The surface chemical reactions*

In this step, very important is the number of active sites available for the redox reactions. If the sites are not present, the photogenerated electrons and holes will recombine. A full description of surface chemical reactions that can take place is given in section 1.3.2 of this chapter.

1.3.4 Basic properties of the semiconductor/liquid interfaces

A semiconductor is characterized by energy of the VB, CB and the Fermi level (E_F) - Fig. 19. The energy levels of the semiconductor are referenced to the energy of an electron in vacuum, $E_{vac} = 0$. The Fermi level is the energy level, for which the probability of occupation is ½. For an intrinsic semiconductor, the Fermi level lies in the middle of the E_g, while for the doped ones, E_F lies below the CB (for the n-type

semiconductor) or close to the VB (for the p-type semiconductor). Another parameter is the electron affinity, χ, defined as energy required to excite an electron from the bottom of the CB to the vacuum level.
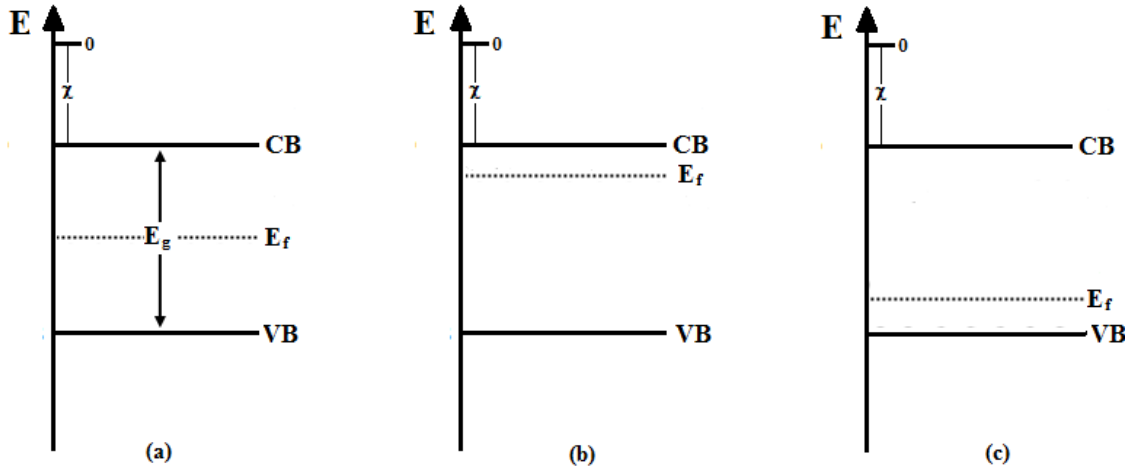
Fig. 19 Energy level diagrams of an intrinsic semiconductor (a), n-type semiconductor (b), and p-type semiconductor (c).

When a metal oxide semiconductor is exposed to humid air, then water molecules can adsorb and dissociate at the surface resulting in –OH (hydroxyl group)surface termination. The –OH groups form electronic surface states below the CB and these levels will be filled by free electrons from the bulk which leave behind a positive space charge. An electric field will form and the charge transfer from the surface will continue until a dynamic equilibrium establishes.

When a metal oxide semiconductor is immersed in an aqueous solution (electrolyte), the situation is more complicated. The semiconductor/liquid interface is similar with the metal/semiconductor junction or Schottky-type junction. Depending on pH of the solution, protons or hydroxide species affect the charge distribution at the interface and, consequently, the potential distribution. Inevitably, three different double layers are formed each involving space charge layers: the *space charge region* (or the depletion region, of ~1000 Å), the *Helmholtz region* (*D*, of ~2–5 Å), and an outer diffuse layer called the *Gouy-Chapman region* (~100 Å) - Fig. 20. These layers are very important as they control both, physical and chemical properties of the surface. Helmholtz [146] was first to describe the interfacial behaviour of a metal and an electrolyte as a capacitor, or the 'electrical double layer'

represented by the excess surface charge on the metallic electrode separated from the ionic counter charge in the electrode by the thickness of the solvation shell. Later, Gouy and Chapman [147,148] further developed the diffuse ionic double layer model where the potential decreases exponentially away from the surface to the bulk solution [149].
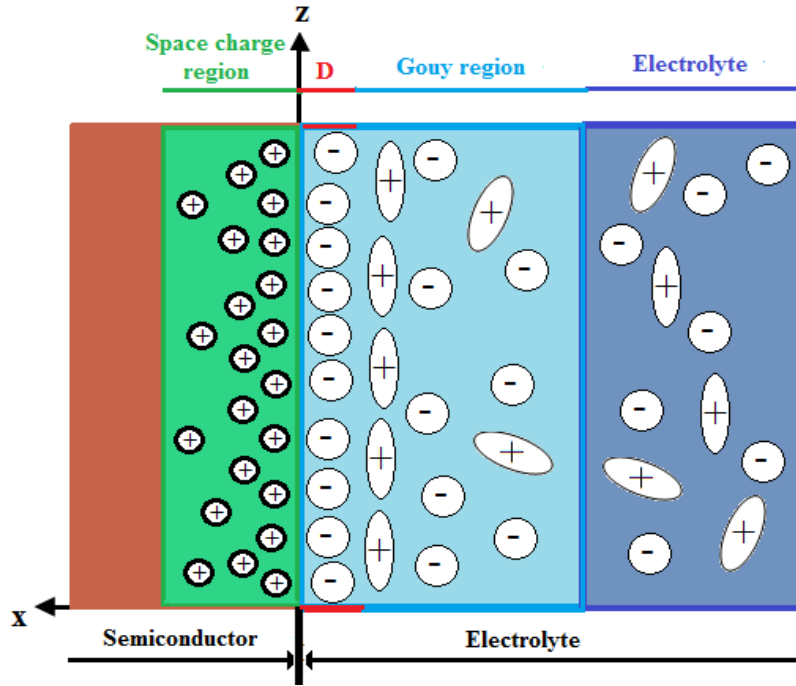
Fig. 20 A schematic representation of the structure of (n-type) semiconductor/liquid interface. z and x are space coordinates.

The electrochemical potential of the solution, $E_F, A/A^-$, is related to the reduction potential through the Nernst equation:

$$E_F, A/A^- = qE^0(A/A^-) \tag{18}$$

where the E^0 is the Nernst potential of the redox pair (A/A^-), and the Fermi level of a semiconductor (E_F) gives the electrochemical potential of the semiconductor. Equilibrium between these two phases at the interface can be achieved only if $E_F = E_F, A/A^-$ (Fig. 21), that is, the electrochemical potentials of the semiconductor and liquid should be the equal. In order to reach the equilibrium (when no charge transfer will be possible) an electron transfer from the semiconductor to the liquid takes place, leaving a positive charge behind which is compensated by an accumulation layer of negative excess charges from the electrolyte.

46
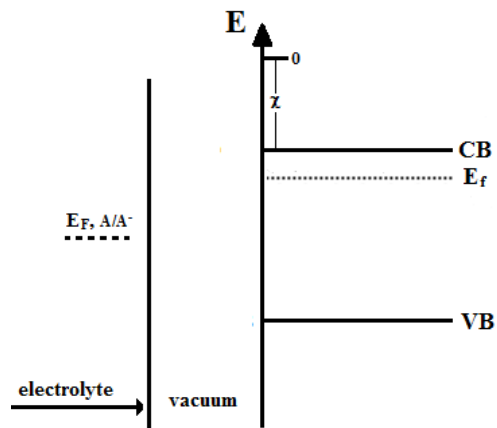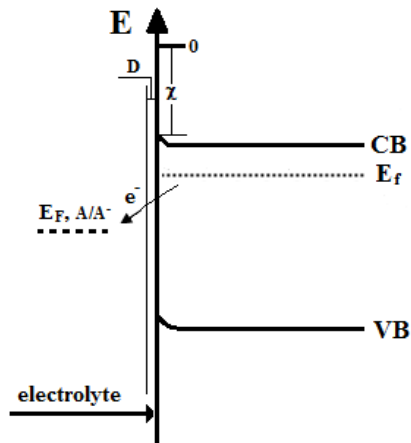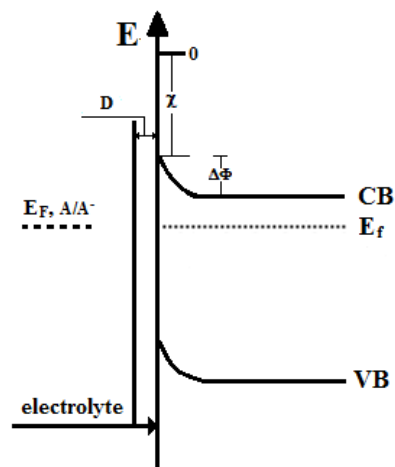
Fig. 21 Energy level diagram of an n-type semiconductor before (a), after partial chemisorption of the solution on the surface (b), and in equilibrium with an A/A⁻ redox couple (c).

47

Inevitably, the Fermi levels of the semiconductor and the solution will adjust at the same level. Only little movement to smaller values of the $E_{F,A/A^-}$ is expected, while, due to its limited charge carrier concentration in the semiconductor, the Fermi level of the semiconductor will become more positive as the electrons are injected in the solution.

The region in the semiconductor with the electron concentration lower than in the bulk is the *space charge region*. A negative charge counter region will also form in the solution (the *Helmholtz region* (D)). As a result of the charge transfer, an electric field will exist in the depletion region which will cause a change in the electrostatic potential towards the surface. The difference between the surface potential relative to some reference level and the bulk potential is called the *band bending* and it is further denoted in this thesis with $\Delta\phi$ (Fig. 21 c).

The Fermi level of the semiconductor and, therefore, the band edge positions can be shifted by the application of an external potential. At a certain applied potential, there will be no net excess charge on the semiconductor and no band bending. In order words, the applied voltage that leads to the flat bands in the semiconductor is called the *flat band potential*, V_{FB}. The V_{FB} is the difference between the Fermi level of the semiconductor and the Fermi level of the reference electrode.

The equations 19 and 20 below, give the approximate position of the CB of an n-type semiconductor and the valence band of the p-type semiconductor, respectively, with reference to the vacuum level, and the band gap of the semiconductor [150]:

$$E_F = E_{CB} - kTln\frac{N_{CB}^*}{n} \tag{19}$$

$$E_F = E_{VB} + kTln\frac{N_{VB}^*}{p} \tag{20}$$

Where the E_{CB} and E_{VB} are the energy levels of the conduction and valence band edges, respectively, k is Boltzman constant ($1.38*10^{-23}$ J/K), T is the temperature in Kelvin. Here, n and p are the intrinsic electron and hole concentrations, respectively. N_{CB}^* and N_{VB}^* are the effective density of states function in the conduction and valence bands:

$$N_{CB}^* = 2\left[\frac{2\pi m_e^* kT}{h^2}\right]^{3/2} \tag{21}$$

$$N_{VB}^* = 2 \left[\frac{2\pi m_h^* kT}{h^2} \right]^{3/2} \tag{22}$$

Where h is the Planck's constant, and m_e^* and m_h^* are the effective masses of holes and electrons that takes into account their ability to move through the atomic lattice. [150]. The acidic or basic character of the semiconductor surface makes possible the interaction with the solution by accepting or by donating protons:

$$\text{M-OH} \rightleftharpoons \text{MO}^- + \text{H}^+_{aq} \tag{23}$$

$$\text{M-OH} + \text{H}^+_{aq} \rightleftharpoons \text{M-(OH)}_2^+ \rightleftharpoons \text{M-OH}_2^+ \tag{24}$$
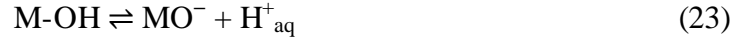
where M represents the metal ion.

Since the charge balance across the solid-liquid interface is potential dependent, the potential drop at the Helmholtz's layer (i.e., the potential difference between the surface of the semiconductor and the bulk of electrolyte), $\Delta\phi_H$, varies with the pH of the solution:

$$\Delta\phi_H = \text{const.} -0.059 \text{ pH} \tag{25}$$

In Fig. 22, the effect of the pH on the Helmoltz's potential drop can be seen. $\Delta\phi_H$ varies with the pH of the solution, but the band bending is independent of pH.

When the semiconductor is illuminated with an energy equal or greater than the E_g of the semiconductor, electron-hole pairs are generated, by means of the direct or indirect momentum transitions. If the semiconductor is an n-type one, than the holes will be driven to the surface, while the electrons will travel to the bulk.

If the excitation does not take place in the depletion layer, but it takes place in the diffuse region, behind the depletion layer, the electrons and holes will recombine because there is no field to separate them. Thus, the excitation in the depletion layer is an effective way to separate the photogenerated charges that will further take place in the redox reactions.

If the holes at the surface will not be involved in any oxidation reaction, this will result in a decrease of the band bending and a change of the E_F towards its initial flat-band position, E_F^* (Fig. 23).
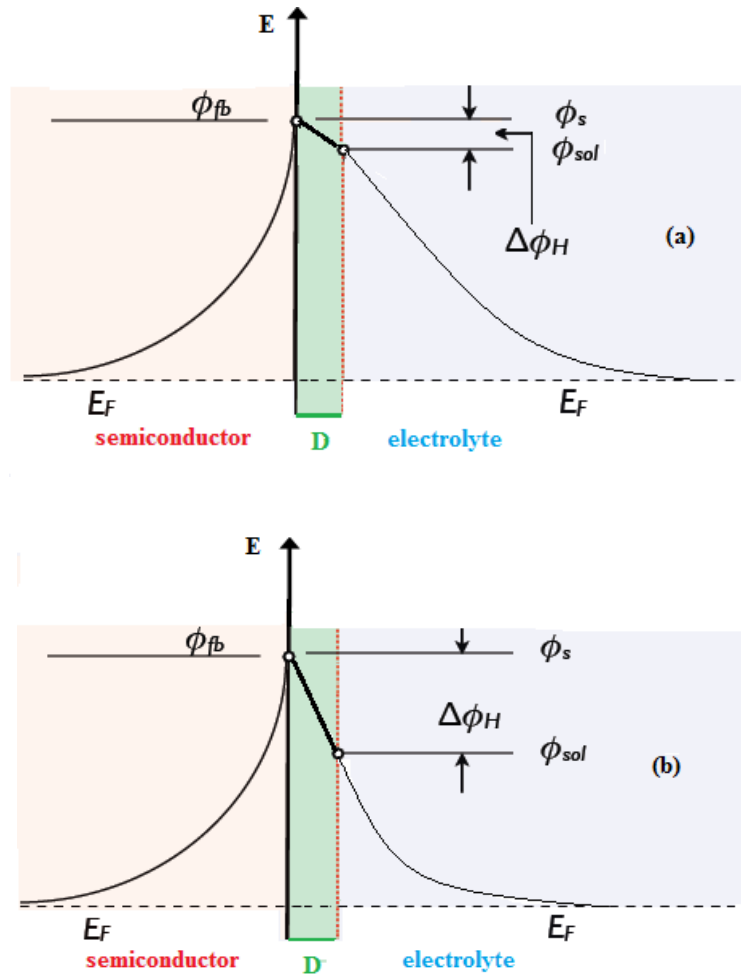
Fig. 22 The effect of pH on the Helmholtz potential drop, $\Delta\phi_H$. $(pH)_a < (pH)_b$. D represents the Helmholtz layer.
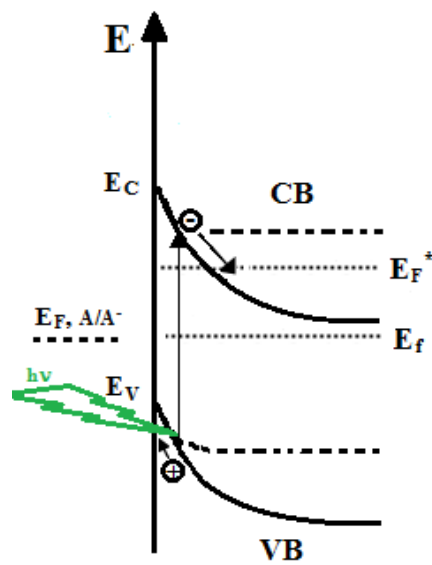
Fig. 23 Energy level diagram of an n-type semiconductor in contact with an electrolyte and upon illumination.

1.3.5 Quantum size effects (QSE)

One of the most important feature of the catalyst is its active centers, on which the reactions take place. Nanosized particles are desirable for photocatalytic applications because, the surface to volume ratio is high, and, therefore, more active centers for the reaction are available. The higher number of the active centers, the greater the photocatalytic efficiency. But below a critical size of the particle, a gradual transition from the bulk to molecular properties occurs. The effect known since the 80's as *the quantum size effect* occurs when the Bohr radius of the first exciton in the semiconductor becomes similar or larger than the particle. In the bulk material, the photoexcited electron finds a high density of states in the conduction band. But in the case of the nanoparticle with a size equal or smaller than that of the first excited state, the electron must assume a state of higher kinetic energy. The charge carriers are spatially confined within a potential well ('particle in a box') and thus behave quantum mechanically (the bands split in quantized levels). This phenomenon has been described by Brus [151] with the effective-mass model.

By solving the Schrödinger equation, the energy of the first excitonic state (E) of the semiconductor can be obtained [152]:

$$E(R) = E_g\,(R = \infty) + \frac{h^2 \cdot \pi^2}{2R^2}\left[\frac{1}{m_e^-} + \frac{1}{m_h^+}\right] - \frac{1.8e^2}{\varepsilon R} \tag{26}$$

The first term in the equation, E_g, is the band gap of the bulk material, the second term is the sum of the confinement energies for the electron and hole, while the last term is their Coulomb interaction energy.

The confinement of the valence electrons to small orbits determine the change of many important physical and chemical properties (related to the electronic properties) compared to the bulk material. As approaching the nanometer size, a point is reached when the band gap increases (Fig. 24). In the quantized particles, the electrons and holes have a higher reduction and oxidation potentials, respectively; the valence band shifts to higher oxidation potentials, while the conduction band shifts to more reducing potentials (with respect to the Nernst potential of the solution). The nanosized semiconductor particles that exhibit the size dependent optical properties are called *quantum dots* [152,153].
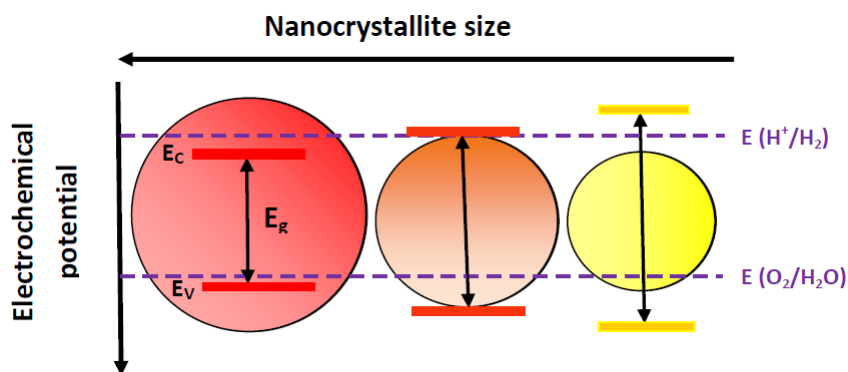
Fig. 24 Quantum size effect in nanocrystals (adapted from ref. [154]).

There are controversies regarding the critical size at which QSE appears. Many different values have been reported in the literature for the same semiconductor nanoparticles. There are also discrepancies between the calculated critical diameter and the experimental diameters, at which the quantization effects are observed. These predictions depend critically on the m^{eff} [151]; usually m^{eff} is small if R is small. To precisely determine the quantum size effect, the band gap should be measured on colloidal suspensions with a very narrow size distribution.

One example is TiO_2 for which different size for the apparition of the QSE have been claimed. Kornman et al. [155] reported the QSE in TiO_2 particles with the size of 2–4 nm, for which the E_g increased by ~0.15 eV relative to the bulk value of 3.18 eV. Anpo et al. [156] observed that QSE appears for TiO_2 NPs with the diameters between 5.5–200 nm, while Howe et al. [157] proposed that a critical size of QSE in TiO_2 of 10 nm.

The increase in E_g with decreasing particle size can have positive consequences for the the photocatalytic activity. Besides the high surface to volume ratio the shift of the band gap to larger redox potentials increases the rate constants for charge transfer at the surface and thus can lead to higher photocatalytic efficiency compared to their bulk counterparts. Some studies [156,158] reported the increase in the photocatalytic efficiency for size-quantized TiO_2. But some other studies [159] found that quantized TiO_2 particles were less photoactive than their bulk counterparts. The decrease in the photocatalytic activity can be due to a decrease in the band bending of the semiconductor [160], due to the surface defect sites on the size-quantized semiconductor particle (higher recombination) which can off-set the positive effects of increased overpotentials [145], and due to a larger band gap value. Nevertheless, the photocatalytic activity is not simply controlled by the particle size; additional

factors have to be taken into account such as: microstructure, impurities, agglomeration, specific surface area, etc. Several researchers [161,162] have found that the optimal particle size for TiO_2 exists, for which the photocatalytic efficiency is maximum. This value has been reported to be around 10–11 nm.

1.3.6 Photon efficiency/quantum yield

Diverse experimental conditions are reported for the evaluation of the photocatalytitc activity, such as different illumination systems, different reaction cells, etc. Therefore, the results of the photocatalytic activity tests cannot be directly compared with each other. To compare the experimental results of different researchers, the *'quantum yield'* was introduced. The quantum yield, ϕ, is defined as the ratio of the reactant molecules consumed or molecules formed to the absorbed photons at a given wavelength [163]. The quantum yield can be written as:

$$\Phi\ (\%) = I_r/I_a \cdot 100 \tag{27}$$

Where I_r = the number of reacted molecules and I_a represents the number of the absorbed photons. I_a can be obtained from the following relation:

$$I_a = I_0 \cdot F \tag{28}$$

Where I_0 is the incident photon flux and F is the integrated absorption fraction in the system over the useful wavelength range:

$$F = \frac{\int_{\lambda 1}^{\lambda 2} I_\lambda T_\lambda^F f_\lambda\ d\lambda}{\int_{\lambda 1}^{\lambda 2} I_\lambda T_\lambda^F\ d\lambda} \tag{29}$$

Where I_λ represents the relative incident photon flux in the wavelength band (dλ), T_λ^F is the transmittance of the filter used in the experiment, and f_λ is the fraction of photons absorbed at the wavelength λ:

$$f_\lambda = 1 - T_\lambda = 1 - 10^{-A_\lambda} \tag{30}$$

Here T_λ and A_λ are the transmittance and absorbance respectively, of the photocatalytic system at the wavelength λ. I_0 can be determined by actinometry (ferrioxalate actinometry) while F can be determined by spectrophotometry.

1.3.7 Requirements for a good photocatalyst

The semiconductor suitable for a photoelectrode or a particulate photocatalyst has to fulfill the following requirements:

1.   Sufficiently high (visible) light absorption

The optical absorption is an essential property of a semiconductor and it is related to its electronic band structure. The spectral region that the semiconductor absorbs is determined by its band gap. Most of the semiconductors have a large bandgap and absorb in the UV part of the solar spectrum. To utilize the maximum solar light irradiation and, therefore, to account for a higher efficiency, the photocatalyst must be also active under visible light irradiation. E.g., a visible light responsive photocatalyst for water splitting should have a narrow band gap of 1.9 (~650 nm) – 3.1 eV (~400 nm), which covers the visible part of the solar spectrum (Fig. 25) and their E_{CB} and E_{VB} edges should straddle the proton reduction potential (H/H$^+$ =0, pH =0, −0.41 at pH of 7) V and the oxidation potential of water (OH$^-$/O$_2$ = 1.23 V, at pH =0, 0.82 at pH =7).
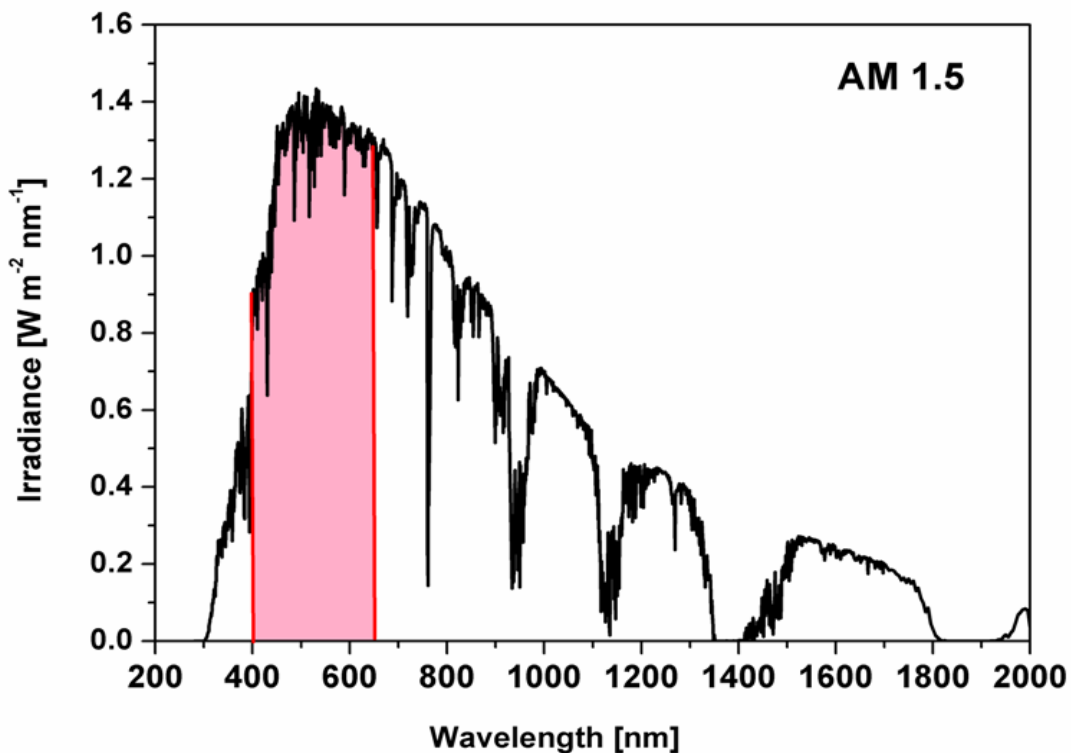
Fig. 25 The intensity of the sunlight versus wavelength for AM 1.5. The marked area represents the visible part of the spectrum that should be absorbed by a photocatalyst [164].

Therefore, the theoretical minimum band gap for a semiconductor to split water at a pH of 7 is 1.23 eV. Reduction and oxidation potentials of water vary with -0.59 mV per pH unit. Most of semiconductors have also a variation in the flatband potential −59 mV per pH unit [165]. Also the thermodynamic losses (0.2–0.4 eV) and an overpotential of 0.4–0.6 eV is needed to ensure fast reaction kinetics must be taken into consideration, so that the energy required to split water into H_2 and O_2 is reported to be around 1.6 eV.

2.   *High chemical stability in the dark and under illumination*

Find a visible-light active photocatalyst that is chemically stable is a challenge, because most of non-oxide semiconductors that are visible-light active (e.g., CdS, GaAs, ZnO, Fe_2O_3) dissolve in water solutions or form a thin film that makes the electron transfer across the interface $(2h^+_{vb} + CdS \rightarrow Cd^{2+} + S)$ impossible.
There is a trend that suggests an increase of the stability against photo corrosion as the band gap value increases.

3.   *Suitable band edge positions to enable the reduction/oxidation reactions*
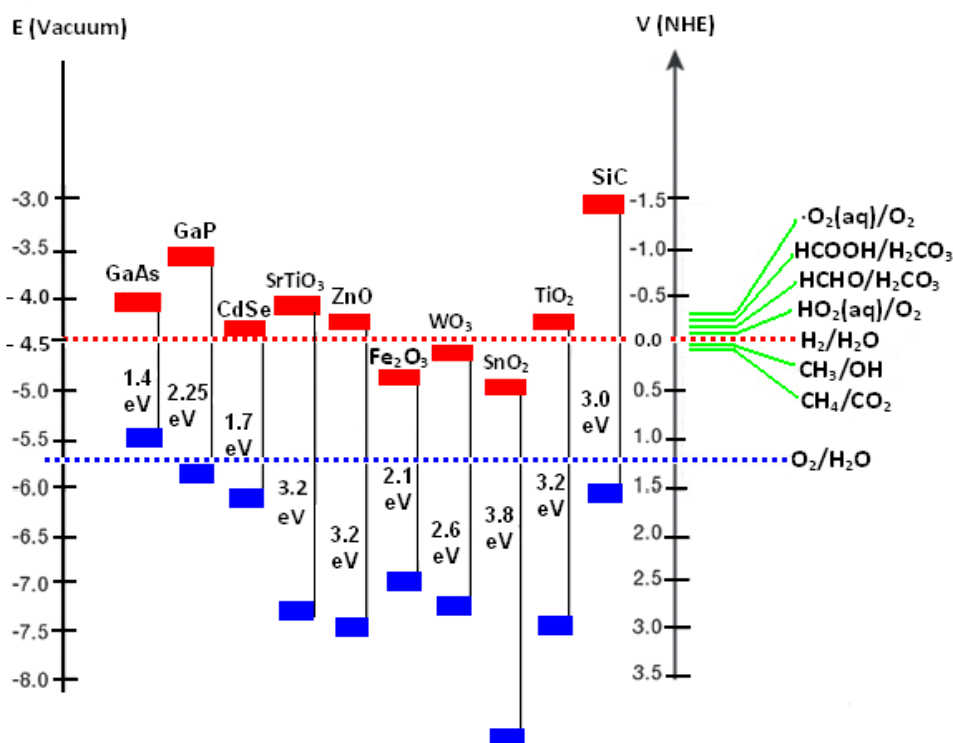
Fig. 26 Scheme of band-edge positions of several semiconductors relative to the energy levels of various redox couples in water (pH = 0).

E.g., for the H_2O to be splitted into H_2 and O_2 a semiconductor should have the bottom level of the CB positioned at lower potential than the redox potential of H^+/H_2 while for O_2 evolution, the top level of the CB has to be more positive than the redox potential of $O_2/H_2O(E_C > E_{red} (H^2/H^+); E_V < E_{ox} (OH^-/O_2))$. Most non-oxide semiconductors are able to reduce but not to oxidize water, while most oxide semiconductors are able to oxidize but not reduce water. A few materials such as for instance $SrTiO_3$ or TiO_2 are able to evolve both H_2 and O_2, but with very low efficiency (less than 1%) under solar light irradiation due to their large band gaps. A scheme of band-edge positions of several semiconductors relative to the energy levels of various redox couples in water at $pH = 0$ is shown in Fig. 26.

4.   Efficient charge transport in the semiconductor

This is an important criterion strongly affected by the crystal structure, crystallinity, and particle size. With improving the crystallinity the number of defects that act as recombination centers will also decrease.

The distribution of the photogenerated charge carriers in a semiconductor is determined by the intensity of light at a certain location. If the charge carriers are produced in the depletion region (space charge region), then they will be separated by the band bending due to the near surface electric field. Thus, the band bending (magnitude and direction) plays an important role in the electron/hole transfer and recombination, and thus influences the efficiency of the photoreaction [160].

If the charge carriers are generated at the center of the particle, then they have to travel to the surface and recombination may happen during the charge transport. For an efficient charge transport either minority carrier diffusion length longer than the particle size or high carrier life time is necessary. By decreasing the particle size, the diffusion length will also decrease and, so, most of the charge carriers will be able to reach the surface before recombination. Lifetime of the photogenerated charge carriers is an important metric of the photocatalytic efficiency.

Fe_2O_3, for example, is an ideal material from the point of view of availability, non-toxicity, chemical stability in aqueous environment and visible light absorption. However, the reduced lifetime of the charge carriers limits its utilization in the photocatalytic water splitting [166].

5.   Low overpotentials for the reduction/oxidation reaction (high catalytic activity)

This requirement implies that the charge transfer across the semiconductor/liquid interface must be fast enough to compete with the accumulation charge carriers which could lead to the decomposition of the semiconductor. Unfortunately, the stability against photocorrosion decreases with the decrease of the band gap. Accumulation of holes at the surface contribute to the decrease in the electric field and therefore in the electron-hole recombination.

The lack of an efficient photocatalyst for water splitting is due to the impossibility of finding a material that meets all these requirements.

1.3.8 Photocatalytic materials: general considerations

The discovery of water photolysis on TiO_2 electrode by Fujishima and Honda in 1972 has been recognized as a landmark event in the research of photocatalytic materials [167], although the history of photocatalysis can be traced back to the 1960's [168].

In the last 40 years, a big number of TiO_2 based-systems (supported thin films or unsupported in the form of powder) have been investigated for photonic energy conversion by photocatalytic methods. The good properties of TiO_2 such as high photostability, low cost, and non-toxicity enables a wide area of applications such as water, air treatment, H_2 generation from water, photocatalytic degradation of bacteria, viruses , etc. But unfortunately, TiO_2 is not an ideal photocatalyst due to its poor efficiency under solar light irradiation. With a band gap of 3.2 eV [169], anatase can utilize maximum 5% of the solar spectrum. Therefore, different attempts to increase the efficiency by modifying the material in order to absorb visible-light have been reported: band gap engineering by doping with N, C, S, sensitization, formation of metal/semiconductor junctions, solid solutions, etc [169].

Other materials such as WO_3 [170] or $SrTiO_3$ [171] have received a lot of attention as possible alternatives for TiO_2, but they also possess large band gaps.

Another approach is to develop new materials that are visible light active. To design new materials, for a specific photocatalytic process, the factors that determine the photocatalytic properties must be taken into account, such as:

a) The electronic band structures,

b) The symmetry of the metal-oxygen (octahedral/tetrahedral) coordination,

c) The polarization fields which are present in ferroelectric oxide materials.

Fig. 27 shows the elements that are able to form suitable band structure of photocatalytic materials and elements that are suitable as co-catalysts.

Red: d^0 group

Blue: d^{10} group

Green: co-catalysts

Fig. 27 Principal elements that construct the photocatalytic materials.

The electronic band structure is an important factor because the behaviour of the photogenerated charge carriers (closely associated with the photocatalytic activity) is determined by the band levels and dispersions. Most of the photocatalysts developed so far consist of metal oxides containing d^0 and d^{10} cations, usually in their highest oxidation states, e.g., Ti^{4+}, V^{5+}, Nb^{5+}, Ta^{5+}, W^{6+}, In^{3+}, Ge^{4+}, Sn^{4+}, Sb^{5+}. From the point of view of the electronic band structure, the photocatalysts containing d^{10} cations are more convenient than the d^0 ones. While usually the top of the valence band is composed of O $2p$ orbitals, the top of the conduction band of the oxides of d^{10} cations consists of hybridized s and p orbitals. The hybridized s and p orbitals have a large dispersion which leads to high mobility of the photogenerated electrons and, consequently, to a high photocatalytic activity. In the case of the d^0 oxides, the top of the conduction band is composed of empty d orbitals which form flat

conduction bands. Photocatalysts containing d^0 metal cations include: TiO_2, $SrTiO_3$, $K_4Nb_6O_{17}$, $Rb_4Nb_6O_{17,}$ $BiVO_4$, $ATaO_3$ (A = Li, Na, K), Ta_2O_5, WO_3, $Ca_2Nb_2O_{7,}$ $Sr_2Nb_2O_7$, $Sr_2Ta_2O_7$, etc. Examples of photocatalysts consisting of d^{10} cations are: ZnO, $AInO_2$ (A = Li, Na), In_2O_3, $In_2O_3(ZnO)_3$, $CaIn_2O_4$, $LaInO_3$, $NaSbO_3$, Ga_2O_3, Zn-doped Ga_2O_3, and others.

Not only the metal oxides containing d^0 and d^{10} cations, but also metal calcogenides, nitrides, oxynitrides are used for photocatalytic applications such asfor example, CdS and CdSe. These materials have suitable band gap for visible light absorption, but they are not stable in H_2O due to a self oxidation to S and Se. Nitrides such as Ge_3N_4 have a high ability for water reduction/oxidation when decorated with RuO_2 and in an alkaline pH but only under UV light irradiation [172]. Another photoactive nitride is GaN, a large band semiconductor (E_g = 3.4 eV [173]). For tuning the absorption of the GaN into the visible region of the solar spectrum GaN-ZnO solid solutions were formed [174]. Although both GaN and ZnO have large band gaps, the oxynitride that forms between them shows a narrow band gap and a visible light activity due to a special band structure (the repulsion between the N $2p$ and Zn $3d$ orbitals lifts the top of the valence band, while the conduction band minimum is not affected) [174].

Besides the electronic structure, also the geometric configuration plays an important role in the efficiency of a photocatalyst. The distortion of the polyhedral which can contain d^0, d^{10}, or none of these two plays an important role in the enhancement of the photocatalytic water splitting. Kudo et al. [175] argued that the distortion of the polyhedron in the perovskite-type structures influences the bond angles which have further influence on band gap and on the degree of delocalization of the electron-hole pairs. When the bond angle approaches 180°, excited energy or $e^-–h^+$ pairs in the crystal migrate more easily and the band gap becomes narrower.

It was found that the dipole moments have a significant effect on the photoexcitation; they are considered to enhance the charge separation separation [176,177]. Distortion of the polyhedra gives rise to internal polarization fields that have positive effects on the photocatalysis by controlling the behavior of photoexcited charges. The magnitude of the dipole moment increases with the distortion of the polyhedra, which can further positively affect the photocatalytic activitiy. Examples of materials for which the dipole moment lead to a good photocatalytic performance are: $BaTi_4O_9$ with a tunnel structure [178], $Na_2Ti_3O_7$

with a zigzag layer structure [179], $SrNb_2O_7$ with a layered perovskite structure [180], etc.

The effect of the electric fields of ferroelectrics on the photocatalytic activity was discussed in detail in section 1.2.3.2 of this chapter.

2   Phase relations in the BiVO$_4$─NdVO$_4$ system

2.1 Background and motivation

Even if it is one of the most promising visible light photocatalyst for the degradation of organic dyes [25] and for water oxidation (in the presence of sacrificial electron acceptors such as Ag$^+$) [181,182], m-BiVO$_4$ is catalytically inactive for hydrogen evolution due to its too low conduction band position relative to the proton reduction potential. But it can still be used in tandem (Z-scheme) with a separate hydrogen evolution catalyst to achieve the overall water splitting reaction [181]. In addition, the photocatalytic efficiency of m-BiVO$_4$ is still not high enough for practical applications. This is mainly due to a low electron transport and high charge recombination. Thus, several ways to improve the photocatalytic efficiency of BiVO$_4$ have been reported so far.

It is well known that the photocatalytic reactions take place on the surface of the particles and a shaped-controlled synthesis of BiVO$_4$ particles is an efficient way to increase its photocatalytic activity [35,183]. Xi et al. [25] prepared BiVO$_4$ particles with exposed (001) facets which showed, under the visible light irradiation, an enhanced photocatalytic degradation of RhB and photocatalytic oxidation of water compared to BiVO$_4$ nanorods. The photocatalytic activity of the nanoplates was better than that of the nanorods due to:

- the optical anisotropy of m-BiVO$_4$ on the (001) and (100) crystallographic planes which leadead to a higher absorption of visible light on that planes,
- a highly hydrophilic character and/or high surface energy of the (001) planes,
- a better separation of the electron-hole pairs.

Han et al. [35] also observed that m-BiVO$_4$ nanocrystals with octahedral geometry present better photocatalytic performance (evaluated for the degradation of RhB solution under visible light irradiation) than the m-BiVO$_4$ particles with irregular morphologies.

Another way to enhance the photocatalytic performance of m-BiVO$_4$ is by doping or metal loading. Loading with noble metals such as Pt [184], Pd [184], Au [185], Ag [186] or with transitional metals, such as Co [186,187], Ni [186], Fe [188] or Cu [189] increased the photocatalytic activity of m-BiVO$_4$ by a better electron-hole

separation near the metal-semiconductor junctions, i.e., it reduced the electron-hole recombination rate.

A moderate B-site doping with Mo [190], W [191] or P [192] can improve the electron transport in m-BiVO$_4$, while a recent study [193] reported that doping BiVO$_4$ with Al is another efficient way to suppress the recombination of the excitons. No successful A-site doping of the m-BiVO$_4$ has been reported so far with an exception of co-substitution of Bi and V with Ca and Mo [194] respectively, but which converted the monoclinic unit cell to a tetragonal one. Based on similarities between their ionic radii, Nd^{3+} could enter at the A site in the BiVO$_4$ structure. However, the synthesis of Nd-doped BiVO$_4$ and the effect of Bi-doping on the structure and, consequently, on the electronic properties of m-BiVO$_4$ has not yet been reported. Besides photocatalytic ones, Nd-doped BiVO$_4$ may also exhibit interesting luminescent properties due to the Nd^{3+} ion which is a luminescent center.

The other ABO$_4$ compound from the Bi$_2$O$_3$–Nd$_2$O$_3$–VO$_x$ system is NdVO$_4$. Usually, Nd^{3+} based compounds are important optical materials, but yet recently it has been reported that NdVO$_4$ exhibits a photocatalytic activity for degradation of dyes and organic pollutants, which is comparable [195] or even higher than that of the commercial TiO$_2$ [63]. But due to its wide band gap (> 3 eV), NdVO$_4$ is active under UV light [196]. Reports on doped-NdVO$_4$ have shown that the photocatalytic activity of NdVO$_4$ can be improved by B-site doping, e.g., Mo-doping [197]. Such doping reduces the band gap and broadens the distribution of the density of states in the conduction band. A-site doping of NdVO$_4$ with Bi could also be an efficient way to narrow its band gap for visible light absorption, due to Bi $6s^2$ − O $2p$ hybrid orbital. Modulation of the electronic structure by valence band adjustment through the Bi $6s^2$ − O $2p$ hybrid orbital has been often encountered e.g., in Bi-based compounds such as BiVO$_4$, CaBi$_2$O$_4$, BiFeO$_3$, Bi$_2$Ti$_2$O$_7$, etc. These compounds are a good choice for photocatalytic applications because the Bi $6s^2$ − O $2p$ hybridization results in an increase of the valence band level and contributes to a higher dispersion of the valence band.

A continuous modulation of both the valence and conduction band could be achieved by forming solid solutions with BiVO$_4$, but yet no information about the BiVO$_4$–NdVO$_4$ system was reported till to date. An example of continuous band gap adjustment is in the BiVO$_4$–CaWO$_4$ system. Ca$_{(1-x)}$Bi$_x$V$_x$Mo$_{1-x}$O$_4$ solid solutions

[194] exhibit band gaps between 2.4 and 2.7 eV depending on x. The continuous adjustment of the conduction band and valence band was realized by varying the V $3d$ to Mo $4d$ ratio and Bi $6s$ to O $2p$ states, respectively. A high Bi concentration allowed a bigger decrease in the band gap through a continuously upper-shift of the valence band maximum due to the more Bi $6s^2$ states.

Although the above discussions suggest that $NdVO_4$−$BiVO_4$ system is worth to be investigated, there were no reports about it at the beginning of this work. Therefore, the aim of this study was to obtained insights on the phase relations between $NdVO_4$ and $BiVO_4$.

In this chapter, I will first focus on the solid-state synthesis of selected compositions from the $NdVO_4$−$BiVO_4$ system:

- Bi-doped $NdVO_4$ with a nominal stoichiometry of $Bi_xNd_{1-x}VO_4$ where $x = 0$, 0.10, 0.20, 0.30, 0.40, 0.45, 0.48, 0.50, and 0.60;
- Nd-doped $BiVO_4$ with a nominal stoichiometry of $Nd_yBi_{1-y}VO_4$ where $y = 0$, 0.05, 0.08, and 0.10.

Further, I will describe their structure and optoelectronic properties analyzed using several different techniques such as: X-ray diffraction (XRD), extended X-ray absorption fine structure (EXAFS), diffuse reflectance spectroscopy (DRS), and photoluminescence spectroscopy (PL) techniques.

2.2 Experimental part

2.2.1 Sample preparation

Bi-doped $NdVO_4$ with a nominal stoichiometry of $Bi_xNd_{1-x}VO_4$ ($x = 0$, 0.10, 0.20, 0.30, 0.40, 0.45, 0.48, 0.50, and 0.60) and Nd-doped $BiVO_4$ with a nominal stoichiometry of $Nd_yBi_{1-y}VO_4$ ($y = 0$, 0.05, 0.08, and 0.10) were prepared by the solid-state method. Stoichiometric amounts of Bi_2O_3 (Alfa Aesar, 99.975% purity), V_2O_5 (Alfa Aesar, 99.6% purity) and Nd_2O_3 (Alfa Aesar, 99.6% purity) were homogenized in a planetary mill using ethanol as a homogenizing medium. The powders were dried and pressed into pellets. The $Bi_xNd_{1-x}VO_4$ samples were calcined in air in two steps, at 700 °C for 3 h and 800 °C for 3 h, with intermediate grinding. The $Nd_yBi_{1-y}VO_4$ samples were fired in air at 800 °C for 10 h.

2.2.2 X-ray powder diffraction characterisation

The discovery of X-rays in 1895 and the finding of Max von Laue in 1912 that he could observe atoms in a crystal with high precision by means of X-ray diffraction enabled scientists to probe crystalline structures at the atomic level [198].

The X-rays mostly used in crystallography are in the range of 0.5–2.5 Å, of the same order of magnitude as the shortest atomic spacing observed in most organic and inorganic materials and can be produced in most laboratories. When an X-ray is shined on a crystalline material, it diffracts in a pattern characteristic to the structure of the material which may be used as a 'fingerprint' for its identification.

A diffraction pattern is a plot of intensity as a function of the diffraction angle, 2θ. X-rays which are generated by a cathode ray tube are filtered to produce monochromatic radiation (usually Cu $K\alpha_1$ radiation), collimated and then directed on the sample. Possible interactions between X-ray photons and electrons in a material are the coherent elastic scattering, Compton or incoherent scattering, and absorption of X-rays. For diffraction, only the coherent elastic scattering is important since only coherent scattering results in the diffraction from a periodic lattice. The X-rays make the electronic cloud of the atom move and the movement re-radiates waves with the same frequency so that in a coherent scattered beam that energy of the photons remains unchanged compared to that in the primary beam. The interaction of the incident rays with the sample produces coherent elastic scattering only when the Bragg's law is satisfied [199]:

$$n\lambda = 2d_{hkl} \sin \theta_{hkl} \qquad (31)$$

where n is an integer, λ is the wavelength of the incident beam, and d_{hkl} represents the interplanar distance.

If we consider the incident waves as parallel propagation vectors which will form an angle θ with the crystallographic planes (hkl), then, in a mirror reflection, the reflected waves will also form the same angle θ with the planes.

Δ, the path differences between a pair of waves before and after they are reflected by the neighboring planes is given by the interplanar distance d_{hkl} as: $\Delta = d_{hkl} \sin\theta$. The constructive interference is observed only when $2\Delta = n\lambda$ (Bragg's law) [199] - Fig. 28. The diffracted X-rays are then detected, processed and counted. Powder and single crystal diffraction vary in instrumentation. In a X-ray powder diffraction

measurement, by scanning the sample through a range of 2θ angles, all possible diffraction directions of the lattice should be attained due to the random orientation of the powdered material. The identification of the material is made by the conversion of the diffracted peaks to d spacings and comparing with the d spacings of standard reference patterns.
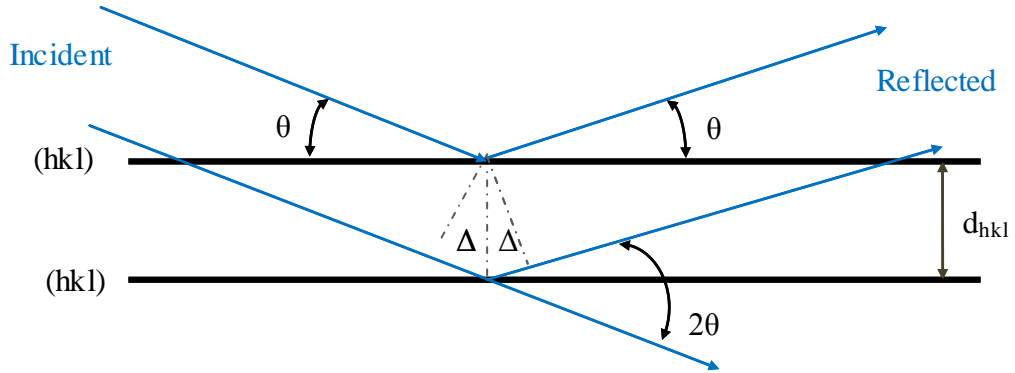
θ, 2θ – Bragg angles
$2\Delta = 2\,d_{hkl}\,\sin\theta$
$2\Delta = n\lambda$ – constructive interference

Fig. 28 Illustration of the Bragg's law.

In the present study, the crystallographic characterisation of the obtained phases was carried out by X-ray powder diffraction using a PANalytical X-ray diffractometer with Cu K$_\alpha$ radiation ($\lambda = 0.154$ nm), a step size of 0.017° and scan step time of 25.8 s. The diffraction patterns were recorded in the range $2\theta = 5–80°$. The average crystallite size was determined by the Scherrer's formula:

$$D = k\lambda/\beta\cos\theta \tag{32}$$

where D is the crystallite size, λ is the wavelength of the X-ray radiation ($\lambda = 0.154$ nm), k is a shape factor related to crystallite shape (0.9), β is the peak width at half maximum height, corrected for instrumental broadening. Crystallites were assumed to be spherical and the crystal distortions are not assumed in the calculation. The refinement of the unit cell was performed using the PANalytical X'pert HighScore Plus software.

2.2.3 X-ray absorption spectroscopy study

X-ray absorption spectroscopy (XAS) has been employed in this study to obtain more information about the structure of the resulted phases.

XAS is a powerful technique for the investigation of materials since it enables the identification of the local structure around selected atoms in a sample [200,201]. In an XAS experiment, the X-ray absorption coefficient of a material is measured as a function of energy, that is $\mu(E)$. Absorption coefficient increases like Z^5 with atomic number and decreases monotonically with increasing photon energy as E^α, where α ~3.5. In a basic experiment, the intensities of the incident beam and transmitted one are measured in a stepwise progression as a function of photon energy in a monochromatic beam. The energy calibration is established with simultaneous absorption measurements on a reference metal foil.
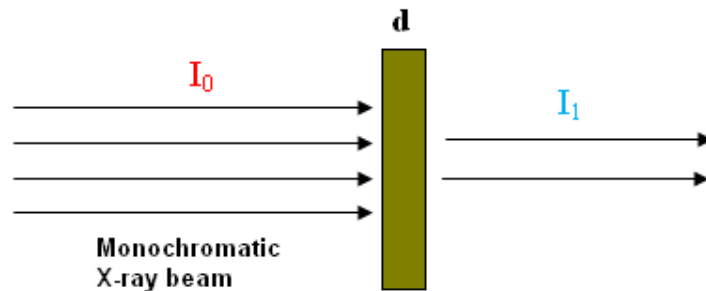
$$I_1 = I_0 - \mu d$$

Fig. 29 Schematic representation of X-ray absorption spectroscopy (in transmission mode).

For diluted samples (samples that contain low amount of the investigated element), and for thin films, the fluorescence photons (fluorescence mode) or emitted electrons from the sample are monitored instead of the transmitted beam. In this case, the emitted signal is proportional with the absorption coefficient of the investigated element.

The photoelectric effect is the phenomenon which dominates the interaction of X-rays (with energies between 1−100 keV) with a material. In a photoelectric effect, a photon (with energy below 100 keV) is absorbed and its energy is transferred to an inner shell electron that will be ejected as a photoelectron. If the incident X-ray has a higher energy than the inner-shell binding energy of the atom in a sample, then a

sharp absorption edge results, followed by an additional photoabsorption channel. The shape and position of the absorption edge and the spectrum that follows immediately contain important structural information. Through XANES (X-ray Absorption Near Edge Structure), the resulting pre-edge and edge structure within about 30 eV of the threshold gives structural information such as the valence state of the selected type of the atom in the sample and the local symmetry of its unoccupied orbitals. The portion above the absorption edge arises from the wavelike nature of the final photoelectron state. It appears immediately above the absorption edge, in a range up to about 1000 eV, whenever an absorbing atom is closely surrounded by other atoms. This rich fine structure called EXAFS (Extended X-ray Absorption Fine Structure) is superposed unto the smooth energy dependence. Important information can be extracted from this oscillatory part: number and species of neighbour atoms, their distance from the selected (absorbing) atom, and the thermal or structural disorder of their positions.

When the inner shell electron is ejected as a photoelectron, it can be regarded as an outgoing spherical wave centred at the excited atom. This wave is scattered by neighbour atoms, and the scattered wave is superimposed onto the initial outgoing wave. With increasing photon energy, the wavevector of the photoelectron wave increases, leading to alternating constructive and destructive interference. If we consider the contribution of single scattering of the photoelectron from the surrounding atoms, then EXAFS signal can be described by a sum of sine terms as a function of the wavevector k. Each term represents a contribution of a spherical shell of equivalent atoms at a distance R_i from the neighbouring atom [202]:

$$\chi(k) = \sum_i A_i(k) \sin(2KR_i + \delta_i) \qquad (33)$$

where:

$$A_i(k) = \frac{N_i}{kR_i^2} S_0^2 F_i(k) e^{(-2k^2\sigma_i^2)} e^{-R_i\lambda_i} \qquad (34)$$

$A_i(k)$ is the amplitude factor, δ_i is the phase shift, N_i is the number of atoms in the shell, $F_i(k)$ is the corresponding magnitude of the photoelectron backscattering amplitude, σ_i^2 is the Debye-Waller factor (it measures the thermal and structural disorder in the i-th shell), λ_i is the mean free path of the photoelectron. S_0^2 is the

amplitude reduction factor (describes the effects of multielectron photoexcitation that accompanies the photoeffect in the inner shell).

The relative K or L contribution in the total absorption spectra measured in transmission detection mode is obtained by removing the atomic absorption background, μ_0, which is approximated by a best fit spline function, and normalized by a unit edge jump, μ_k. By the Fourier transformation (FT) of the measured EXAFS structure, the contributions of individual shells are separated visually. Each peak in FT magnitude spectra corresponds to one sine term in the measured EXAFS signal, so that FT EXAFS can be considered as a radial distribution of the neighbours. The quantitative structural information can be obtained by a quantitative EXAFS analysis in which a model EXAFS function is fitted to the measured EXAFS spectra. Model EXAFS function can be constructed *ab initio* with a very used code, FEFF6 program, from a set of scattering pats of the photoelectron obtained in a tentative special distribution of the neighbour atoms.

In this study, Bi L_3-edge Nd L_3-edge and V K-edge EXAFS spectra were measured at C beamline of HASYLAB (Hamburg, Germany) in a transmission detection mode at room temperature, using a Si(311) double-crystal monochromator with ~1.5 eV resolution at the Bi L_3-edge (13419 eV), and Si(111) double-crystal monochromator with 1 eV resolution at the Nd L_3-edge (6208 eV) and V K-edge (5465 eV). The higher-order harmonics were efficiently eliminated by detuning the monochromator crystals to 60% of the rocking curve maximum using a stabilization feedback control. The intensity of the X-ray beam was measured by three consecutive 10 cm long ionization detectors, the first filled with 190 mbar of Ar, and the second and third with 1000 mbar of Kr, for the Bi L_3-edge EXAFS, while for the Nd L_3-edge and V K-edge EXAFS the cells were filled with 520 mbar of N_2, 250 mbar of Ar, and 400 mbar of Ar, respectively. The samples were placed between the first two detectors. The exact energy calibration was obtained by an absorption measurement on Pb metal foil (Pb L_3-edge 13035 eV), or Bi metal foil and Ti metal foil (Ti K-edge 4966 eV) or V metal foil, inserted between the second and the third ionization detector. The samples were prepared in the form of homogeneous pellets with an absorption thickness of about 2 above the investigated absorption edge, prepared from micronized powder homogeneously mixed with micronized BN powder. The absorption spectra were measured within the interval from –250 eV to 1000 eV relative to the absorption edge. In the edge region the equidistant energy

steps of 0.3 eV were used, while for the EXAFS region the equidistant k-steps (Δk $\approx$ 0.03 Å^{-1}) were used with an integration time of 1 s/step. The EXAFS spectra were further analysed with the IFEFFIT program package [203].

2.2.4 Diffuse reflectance analysis

Measurement of diffuse reflectance spectroscopy (DRS) with a UV-Vis spectrophotometer is a technique used for determination of absorption properties of materials.

Properties that can be estimated from the DRS measurements are the band gap energy and the absorption coefficient. The band gap is an important feature of semiconductors as it determines their applications in optoelectronics. For the determination of the band gap of powdered materials, the sample has to be thick enough so that all incident light is absorbed or scattered before it reaches the back surface of the sample (typically, a thickness of 1−3 mm is required).

The theory than can make possible to use DRS spectra for the band gap determination was proposed by Kubelka and Munk in 1931 [204]. They proposed a model for describing the behaviour of light inside a light-scattering sample, based on the equations:

$$-di = -(S+K)i dx + Sj dx \qquad (35)$$

$$-dj = -(S+K)j dx + Si dx \qquad (36)$$

where:
- i and j are the intensities of light inside the sample towards the luminated and un-illuminated surfaces,
- dx is the differential segment along the light path,
- S and K are the so called *Kubelka–Munk* scattering and absorption coefficients, respectively. They represent portions of light scattered and absorbed respectively, per vertical length.

For an infinitely thick sample, the Kubelka-Munk equation at any wavelength becomes:

$$\frac{K}{S} = \frac{(1-R_\infty)^2}{2 R_\infty} \equiv F(R_\infty) \qquad (37)$$

Where $F(R_\infty)$ is the Kubelk-Munk function, and R_∞ is $R_{sample}/Rs_{tandard}$ (R = reflectance).

According to the Kubelka-Munk theory [204], the diffuse reflectance data were converted to absorbance coefficients, $F(R_\infty)$.

The E_g energies and absorption coefficients are related through the following relation [205]:

$$\alpha h\nu = A(h\nu - E_g)^{n/2} \tag{38}$$

where α, $h\nu$, and A are the linear absorption coefficient, photon energy and proportionality constant, respectively. $n = 1$ for a direct band gap semiconductor or $n = 4$ for an indirect band gap semiconductor.

To obtain the band gap excitation profiles and the band gap energies, diffuse reflectance spectra of our samples were recorded in the range from 250 to 800 nm with a UV-Vis spectrophotometer (Perkin Elmer, model λ 650S) equipped with a 150 mm integrated sphere and using spectralon as a reference material. Both $NdVO_4$ and $BiVO_4$ are considered direct band gap semiconductors so $n = 1$. Plotting the $[F(R_\infty)h\nu]^{2/n}$ against excitation energy allowed us to evaluate their band gap energies (the extrapolation of the linear part of the absorption edge on the photon energy axis gives the band gap energy).

2.2.5 Fluorescence spectroscopy analysis

2.2.5.1 Steady-State Photoluminescence Spectroscopy

Among other techniques, such as electron paramagnetic resonance, transient absorption spectroscopy, or time-resolved infrared spectroscopy, fluorescence spectroscopy is one of the most powerful techniques for studying the carrier dynamics [206]. The competition between the recombination, trapping and transfer of the electron-hole pair determines the overall efficiency of a semiconductor photocatalyst. The PL emission spectra are useful in determining the efficiency of charge carrier trapping, the migration and transfer, as well as in understanding the evolution of electron-hole pairs in semiconductors. PL refers to the emission of light which results upon an optical stimulation of a material [207]. When a semiconductor absorbs light with a suitable energy, the electron from the conduction band travels

from the ground state to an excited state with the creation of an exciton (lifetime of the excitons is system-dependent and may be of the order of picoseconds to even seconds). Then the system undergoes a nonradiative internal relaxation and the electron moves to a lower, more stable excited level. After internal relaxation, the electron returns to the ground state, releasing energy. In luminescent materials, this energy is in form of light with the wavelength longer (lower energies) than that of the incident light. This emitted light is detected as PL. The intensity and spectral distribution of this PL is a direct measure of various important material properties.

In this study, the PL emission spectra were collected with a FLS920 Spectrometer of Edinburgh Instruments, using a steady state 450 W Xenon arc lamp. The experimental set-up was equipped with a blue sensitive high speed photomultiplier (Hamamatsu H5773-03 detector).

The emission spectra were collected at room temperature, within 400–700 nm with an excitation wavelength of 371 nm.

2.2.5.2 Dynamic Photoluminiscence Spectroscopy – Exciton Lifetime

By monitoring the PL intensity at a specific wavelength as a function of time delay after an exciting laser pulse, information on the electron relaxation and recombination mechanisms can be obtained. Recombination processes are crucial factors that influence the photocatalytic performances of a material. Therefore, understanding the dynamics of the photogenerated charge carriers in a photocatalyst is very important.

In this study, time-resolved photoluminescence spectra were recorded at room temperature, using a Pico-second diode laser EPL 375 with an excitation wavelength of 371 nm (λ_{em} = 522 nm and 524 nm respectively), and a blue sensitive high speed photomultiplier detector – Hamamatsu H5773-03. The time range was 0–50 ns. The analysis of the fluorescence decays were performed using the F900 analysis software.

Theoretically, the decay processes of powders with $Bi_xNd_{1-x}VO_4$ and $Nd_yBi_{1-y}VO_4$ nominal compositions were described by the following equation [208]:

$$R(t) = A + \sum_{i=1}^{4} \beta_i e^{-\frac{t}{\tau i}} \tag{39}$$

Where:

71

- β_i are pre-exponential factors (or the 'shape factors') which include technical (instrumental) and sample parameters like efficiency of the system, geometric conditions of the sample, intensity of the excitation source, etc.
- τ_i are the characteristic lifetimes,
- A is an additional background, and
- $R(t)$ is the sample decay model.

$R(t)$ expresses the theoretical fluorescence decay of the samples, but does not account for the statistical noise of the data and the optical pulse of the laser source that are present in the measured fluorescence decay. The initial part of the decay can be broadened by the finite pulse width of the excitation source, the transit time spread of the detector plus other potential optical and electronic contributions. Taking these into account, the actual measured time dependent fluorescence intensity becomes a convolution of the instrumental response function and the theoretical sample decay. The mathematical relationship between the sample response function $F(t)$, the instrumental response function $f(t')$, and the sample decay model $R(t)$ is the convolution integral [208]:

$$F(t) = \int_0^t R(t - t') f(t') dt' \qquad (40)$$

In this study, the measured (convoluted) data was fitted using the 'Reconvolution Fit method' [209]. This method fits the sample response to the data over the rising edge, to match the theoretical sample response, $R(t)$. The Reconvolution Fit procedure extracts the raw data (fluorescence decay) and eliminates both the noise and the effects of the exciting light pulse.

2.3 Results and discussion

2.3.1 $Bi_xNd_{1-x}VO_4$

2.3.1.1 Crystal structure and phase composition

The XRD patterns in Fig. 30 show the formation of tetragonal $Bi_xNd_{1-x}VO_4$ solid solution for x between 0 and 0.48. When $x > 0.48$, two phase mixtures were obtained,

which contained tetragonal $Bi_xNd_{1-x}VO_4$ and m-$BiVO_4$. This suggests that the solubility limit of Bi in $NdVO_4$ is between $x = 0.48$ and 0.50.
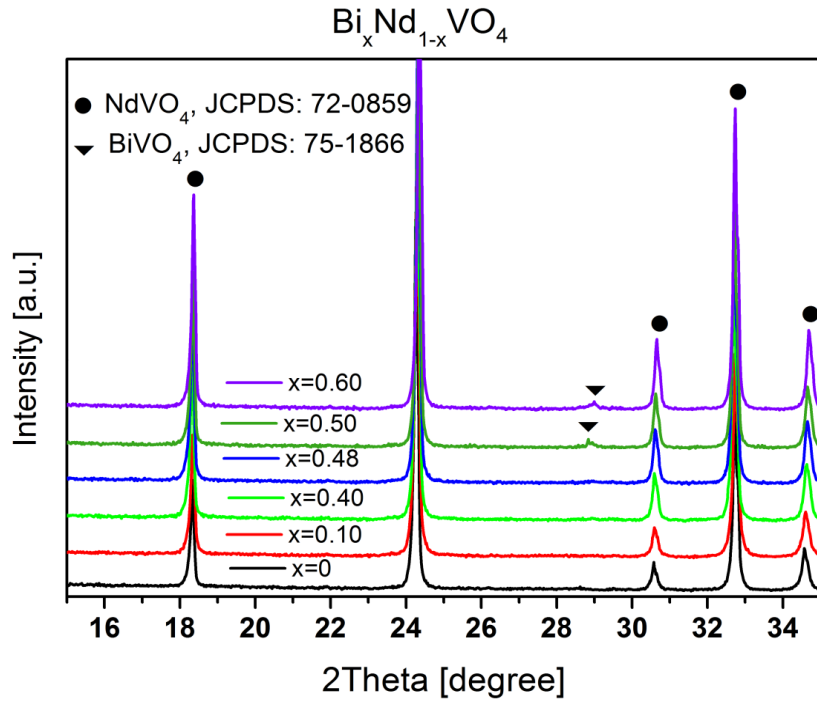
Fig. 30 X-ray diffraction patterns of Bi-doped $NdVO_4$ samples with the nominal stoichiometry $Bi_xNd_{1-x}VO_4$. The filled circles denote the tetragonal $NdVO_4$ phase (space group $I4_1/amd$), while the filled triangles represent the monoclinic $BiVO_4$ phase.
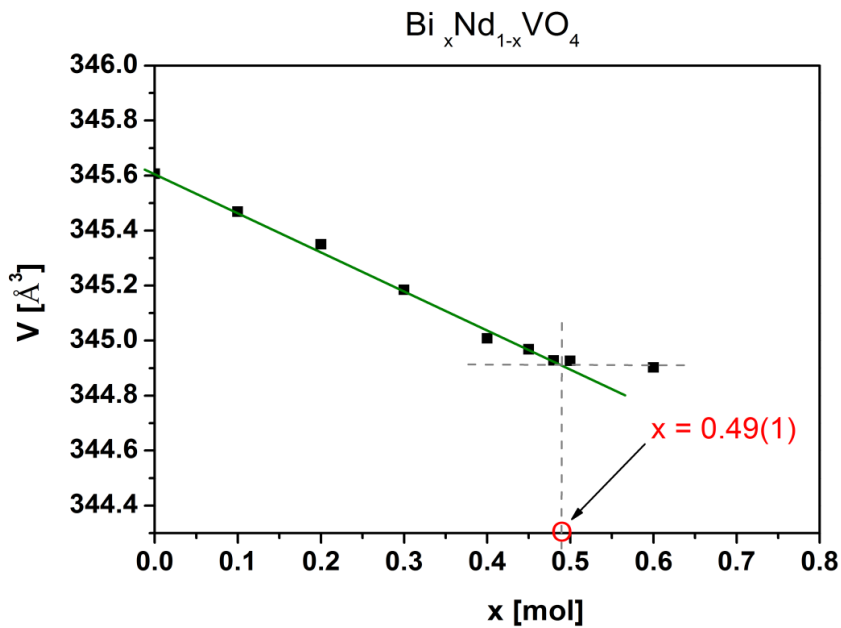
Fig. 31 Unit cell variation of $Bi_xNd_{1-x}VO_4$ samples as a function of Bi concentration (x).

The crystallographic details of the $Bi_xNd_{1-x}VO_4$ samples, obtained after refinement of the unit cell, are shown in Fig. 31. The standard deviation of the calculated unit cell parameters was $\pm$ 0.0002 Å.

As the composition of the solid solution changes, the lattice constant also changes. We observed that the $NdVO_4$ unit cell volume decreased according to Vegard's law with the dopant concentration up to $x = 0.48$, while for higher concentrations, the unit cell volume remained constant. Thus, the solid solubility limit was found to be at $x = 0.49(1)$[3].

2.3.1.2   EXAFS studies

The XRD analysis on the Bi-doped $NdVO_4$ sample with $Bi_{0.2}Nd_{0.8}VO_4$ composition only showed the presence of tetragonal $NdVO_4$-based structure (space group $I4_1/amd$). To study the distortion of the $NdVO_4$ local structure with the Bi-doping, we used EXAFS analysis, a chemically selective method that enables to study the crystallographic environment around Bi ions. Distinctive peaks in the FT magnitude of the EXAFS spectra are contributions of the photoelectron backscattering on the near neighbor shells around the central atom and represent the approximate radial distribution of the atoms surrounding the investigated central atom. The FT magnitude of k^2-weighted EXAFS spectra for Nd, Bi, and V that were calculated over the range of $k = 4$–11 A^{-1} are compared in Fig. 32.

Errors in FT magnitude EXAFS spectra due to the random noise in $\chi(k)$ are estimated at high R values (in the interval from 8–15 Å) and are of the order of $\pm$ $6 \cdot 10^{-3}$ for the Bi, $\pm$ $2 \cdot 10^{-2}$ for the Nd, and $\pm$ $4 \cdot 10^{-2}$ for the V spectrum. The qualitative comparison between the measured EXAFS signals shows that the Bi spectrum exhibits similar distribution of neighbour peaks as the Nd spectrum, and significantly different from the V one, suggesting that Bi ions in $Bi_{0.2}Nd_{0.8}VO_4$ have similar environment as Nd ions in $NdVO_4$. Such result was expected because the ionic radius of Bi^{3+} (1.17 Å) is similar to that of Nd^{3+} (1.11 Å), and much larger than that of V^{5+} (0.54 Å) [76]. It is therefore most unlikely that Bi^{3+} would replace V^{5+} in the $NdVO_4$ crystal lattice.

The quantitative structural information on the local Bi neighbourhood in $Bi_{0.2}Nd_{0.8}VO_4$ and of Nd in $NdVO_4$ (type and average number of neighbour atoms and their distances from the selected atom, as well as the thermal or structural

---

[3] Uncertainity of the last digit is given in parantheses.

disorder of their positions-Debye-Waller factors) was obtained by Bi L_3-edge and Nd L_3-edge EXAFS analysis in which the model EXAFS function was fitted to the measured EXAFS spectrum.
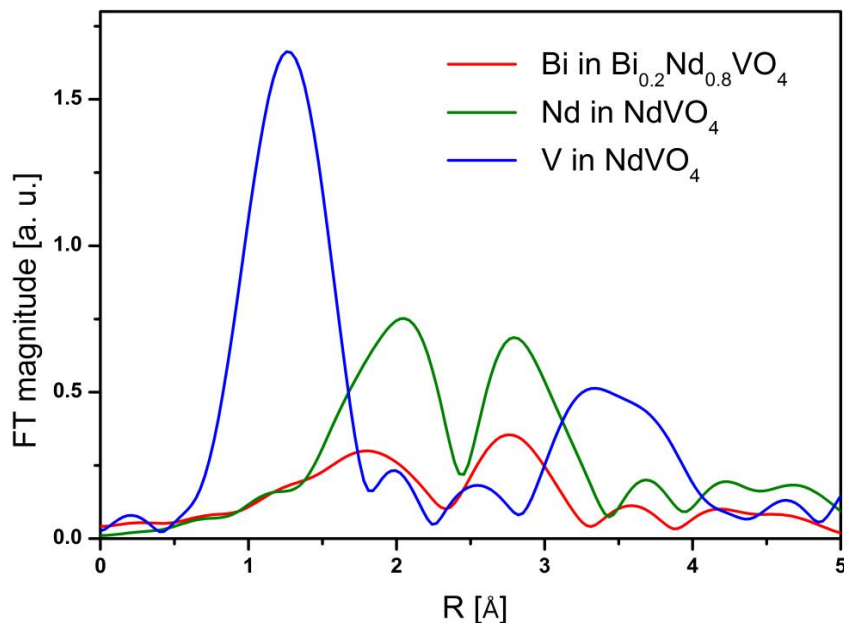
Fig. 32 Magnitude of Fourier transforms of the k^2-weighted Bi L_3-edge EXAFS of $Bi_{0.2}Nd_{0.8}VO_4$, Nd L_3-edge of $NdVO_4$ and V K-edge in $NdVO_4$ calculated in the k range of 4–11 $Å^{-1}$.

For that purpose, we used FEFF6 computer code [210] to construct Nd model EXAFS functions *ab initio* from a set of scattering paths of the photoelectron, built from crystallographic data for $NdVO_4$ with $I4_1/amd$ space group ($a = b = 7.33$Å, $c = 6.43$ Å, $α = β = γ = 90°$ [211]. In this crystal structure, the Nd atoms are surrounded by eight O atoms, four at the distance of 2.36 Å, and four at 2.64 Å. The second coordination sphere is occupied by two V atoms at 3.21 Å, followed by four V and four Nd atoms at 4.00 Å, and twelve O atoms at 4.4 Å. The Bi EXAFS model is constructed from the same crystal structure with introduction of Bi on the Nd crystallographic site. All single and multiple scattering paths in the R range up to 4.09 Å were included in the models; in total 4 single scattering and 6 multiple scattering paths. A minimum number of variable parameters were introduced in the fits: a separate Debye-Waller factor ($σ^2$) and a common relative change of distances ($ΔR/R$) for each shell of neighbours, except for the first shell where a separate $ΔR$ was used. The common shift of the energy origin, $ΔE_0$, and the common amplitude reduction factor, S_0^2, were allowed to vary. In both models, the shell coordination

numbers (N) were kept fixed at crystallographic values. The best-fit parameters are given in Table 1 and the quality of the fit is illustrated in Fig. 33 A and B. The error due to the random noise in $\chi(k)$ is $\pm\ 0.5 \cdot 10^{-4}$ and $\pm\ 1\ 10^{-3}$ for Bi and Nd spectrum, respectively. Errors in FT magnitude EXAFS spectra due to the random noise in $\chi(k)$ are estimated at high R values (in the interval from 8–15 Å) and are of the order of $\pm$ $6 \cdot 10^{-3}$ for Bi and $\pm\ 2 \cdot 10^{-2}$ for Nd spectrum.
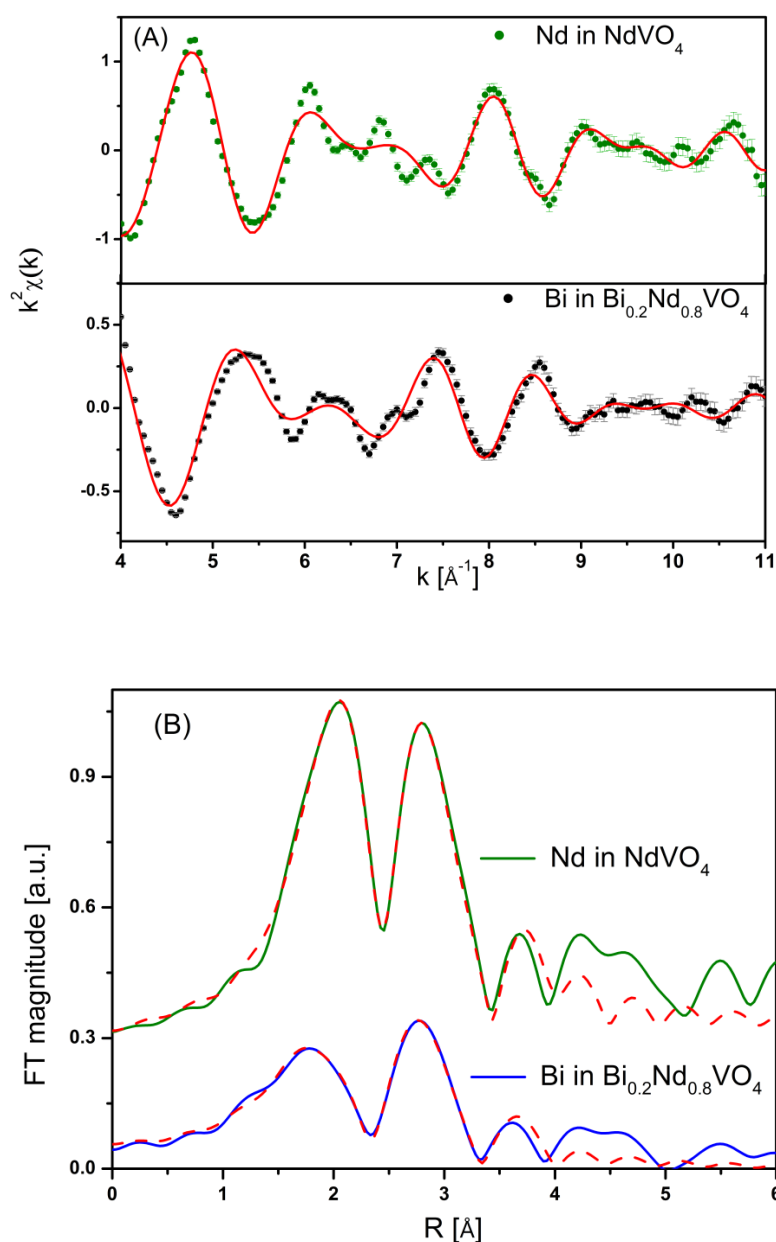
Fig. 33 (A) The k^2-weighted Bi and Nd L_3-edge EXAFS spectra (dots) and best fit EXAFS models (solid line). (B) Fourier transforms magnitude of k^2-weighted Bi L_3-edge EXAFS in $Bi_{0.2}Nd_{0.8}VO_4$ and of Nd L_3-edge EXAFS in $NdVO_4$ (solid lines), compared to their best fit EXAFS models (red dashed line) calculated in the R range = 1–4 Å (spectra are shifted for clarity).

Table 1 Structural parameters of the first coordination shells around Bi atom in $Bi_{0.2}Nd_{0.8}VO_4$ and around Nd in $NdVO_4$, respectively. R = distance and σ^2 = Debye-Waller factor. Uncertainty of the last digit is given in parentheses. The fitting statistics *R-factor* was 0.0018 for the Bi fit and 0.005 for the Nd fit. The amplitude reduction factor was $S_0^2 = 0.98 \pm 0.09$ for Bi and 0.94 ± 0.07 for Nd. The shift of the energy origin, ΔE_0 was -4 ± 1 eV for Bi and 3.7 ± 0.8 eV for Nd.

Neighbour element of		Number of neighbours of		R [Å]		σ^2 [Å²]	
Bi in $Bi_{0.2}Nd_{0.8}VO_4$	Nd in $NdVO_4$	Bi in $Bi_{0.2}Nd_{0.8}VO_4$	Nd in $NdVO_4$	From Bi in $Bi_{0.2}Nd_{0.8}VO_4$ to	From Nd in $NdVO_4$ to	Bi in $Bi_{0.2}Nd_{0.8}VO_4$ to	Nd in $NdVO_4$ to
O			8	2.39(1)	2.44(1)	0.019(1)	0.010(1)
V			2	3.20(1)	3.22(1)	0.008(1)	0.004(1)
Nd			4	3.99(1)	4.00(1)	0.013(1)	0.008(1)
V			4	3.99(1)	4.00(1)	0.016(1)	0.010(1)

From the results of the Bi and Nd EXAFS analysis, we observe that the Bi neighbourhood in $Bi_{0.2}Nd_{0.8}VO_4$ is almost identical to that of Nd in $NdVO_4$. Only a small decrease (~2%) in the closest neighbour distances was found for Bi ions. These findings are consistent with the XRD study (see section 2.3.1.1) that showed a decrease in the unit cell volume of $Bi_xNd_{1-x}VO_4$ with Bi concentration. The smaller unit cell of $Bi_xNd_{1-x}VO_4$ as compared to $NdVO_4$ could be a consequence of the incorporation of Bi^{3+} cation with a stereochemically active lone electron pair.

2.3.1.3 Optoelectronic properties

2.3.1.3.1 Band gap measurements

The diffuse reflectance spectra of $Bi_xNd_{1-x}VO_4$ powders after the Kubelka-Munk treatment are presented in Fig. 34.

The band gap of the single phase $NdVO_4$ was calculated to be 3.53 eV. This value is in the range of values reported in the literature (see Table 2), which significantly differ according to the morphology of the samples. From Table 2 we can see a strong correlation of the particle size and the band gap values; smaller the particle size, smaller the band gap. Our result fits well into this trend. With introduction of Bi onto the A-site of $NdVO_4$, the band gap decreases from initial 3.53 eV to 3.06 eV for $x =$

0.40. In the lower concentration range, the influence of Bi on the band gap reduction is strong but becomes weaker for $x \geq 0.20$.
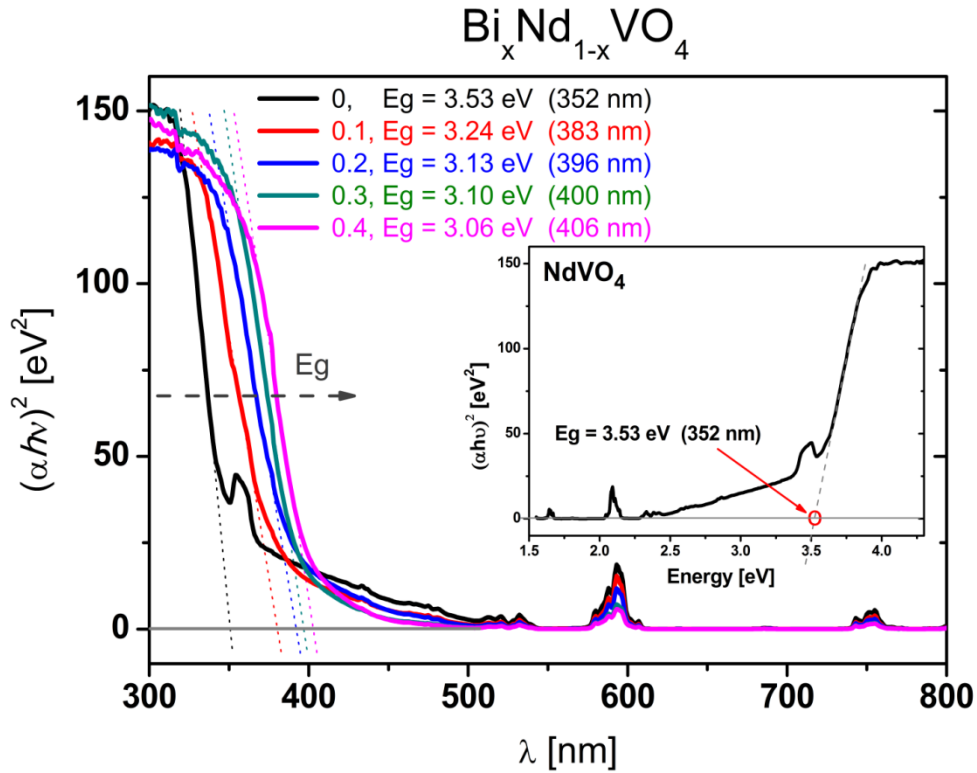
Fig. 34 UV-Vis diffuse reflectance spectra of $Bi_xNd_{1-x}VO_4$ with $x = 0, 0.1, 0.2, 0.3,$ and 0.4. The Kubelka-Munk function is plotted versus the excitation energy. The band gap (E_g) of $NdVO_4$ decreased by Bi-doping. The insert shows the band gap determination of $NdVO_4$.

Table 2 Experimental band-gap energy values for $NdVO_4$.

Paper	Experimental E_g [eV]	Synthesis method and particle size
Panchal et al. [59]	3.72	Single crystals, ~80μm
This work	3.53	Solid-state synthesis, ~1 μm
Mahapatra et al. [195]	2.99	Co-precipitation, 200 nm particles
Xu et al. [212]	2.95	Molten salt method, 100 nm diameter and up to 3 μm length nanowires
Kalai Selvan et al. [213]	2.15	Sonochemical synthesis, 20 nm rods

Taking in consideration the band structure of $BiVO_4$ and $NdVO_4$ [20,21,59], the observed red-shift of the $Bi_xNd_{1-x}VO_4$ band gap could be ascribed to the

hybridization between Bi $6s^2$ and O $2p$ orbitals on the top of the valence band of NdVO$_4$,which results in the up-shift of the valence band. This can be correlated with the colour change that we observed upon Bi doping, from blue-grey of NdVO$_4$ towards more yellowish green for Bi$_x$Nd$_{1-x}$VO$_4$ as the Bi concentration increases.

The UV-Vis spectra of NdVO$_4$ and Bi$_x$Nd$_{1-x}$VO$_4$ also show the presence of two different peaks centred at around 585 nm and 754 nm. These peaks (at the almost the same positions) have already been reported in the literature [212,214] and assigned to the electronic transitions of Nd^{3+} ion, from ^{4}I$_{9/2}$ to ^{4}G$_{5/2}$ and from ^{4}I$_{9/2}$ to ^{4}F$_{7/2}$, respectively.

2.3.1.3.2 Steady-state photoluminescence and lifetime

The PL spectra of Bi$_x$Nd$_{1-x}$VO$_4$ powders are shown in Fig. 35. Due to the electronic transitions inside the rare-earth ion (Nd^{3+}), the NdVO$_4$ spectrum shows a rich structure.
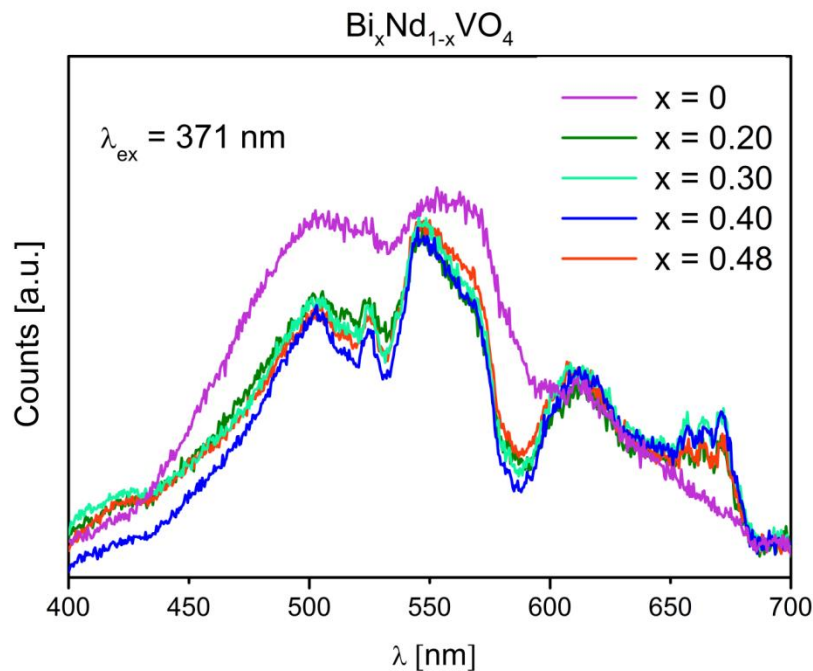
Fig. 35 Room temperature PL spectra of Bi$_x$Nd$_{1-x}$VO$_4$ powders.

In the tetragonal NdVO$_4$, the Nd^{3+} ions are located at the sites that lack the centre of symmetry (D_{2d} symmetry) [215] which make possible the electronic dipole transitions within the Nd^3 4f shells. Calculation of the energy level diagrams for Nd^{3+} in NdVO$_4$ can be found in [215]. The PL properties of NdVO$_4$ upon UV excitation

have so far been reported only for single-crystalline nanorods, measured with an excitation wavelength of 310 nm at room temperature [213]. The sharp emission bands in the wavelength range 350–500 nm, detected on the $NdVO_4$ nanorods, are not present in the PL spectrum that we have recorded on the powders with around 1 μm particle size, but we observe similar emissions in the interval of 500–650 nm as reported in [213,216,217,218]. The emission peaks at ~503, 525, 556, 598, and 605-612 nm were assigned to the $^4G_{11/2} \rightarrow \, ^4I_{11/2}$ [216], $^4G_{7/2} \rightarrow \, ^4I_{9/2}$ [217,218], $^4G_{9/2} \rightarrow \, ^4I_{9/2}$ [217,218], $^4G_{5/2} \rightarrow \, ^4I_{9/2}$ and $^4G_{7/2, \, 9/2} \rightarrow \, ^4I_{11/2, \, 13/2}$ transitions respectively [216]. Figs. 36–40 present the time-resolved photoluminescence spectra of $Bi_xNd_{1-x}VO_4$ powders excited by a 371 nm laser wavelength and monitored at 522 nm. The decay process of $NdVO_4$ sample is shown in Fig. 36. This decay curve could only be simulated by a second-order exponential function with the two lifetimes: a short one $\tau_1 = 1.23$ ns, and a longer one: $\tau_2 = 11.59$ ns. To our best knowledge, the lifetime of the excited carriers in $NdVO_4$ was not described in the literature yet. The decay profiles of the $Bi_xNd_{1-x}VO_4$ (x = 0.1, 0.2, 0.3, 0.48) powders were fitted using Eq. 40 with two exponential terms, which suggests that the decay processes in these powders are dominated by the second order kinetics.
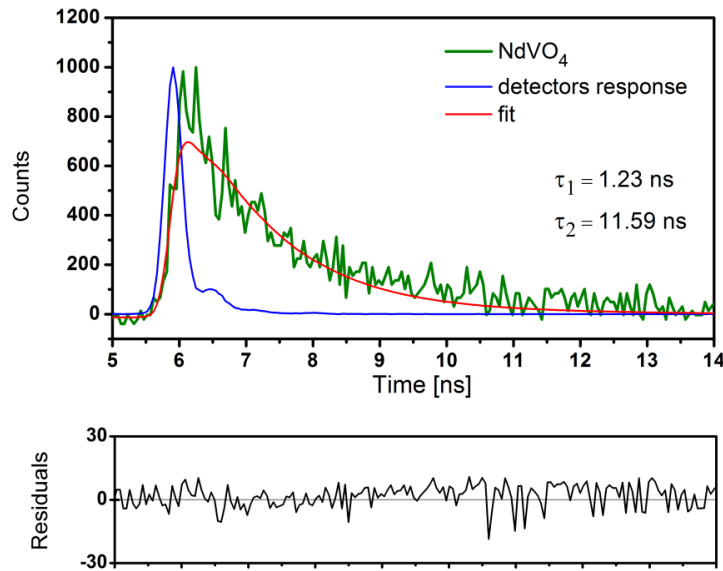
Fig. 36 The green line shows the time-domain intensity decay of $NdVO_4$ powder. $\lambda_{em} = 522$ nm. The red line is the fitting curve and the blue line is the response of the detector. The residuals represent the difference between the fitted curve (red line) and the measured data. The goodness of the fit, χ^2, is 18.870).[4]

---

[4] χ^2 (reduced chi-square) represents the goodness of the fit.
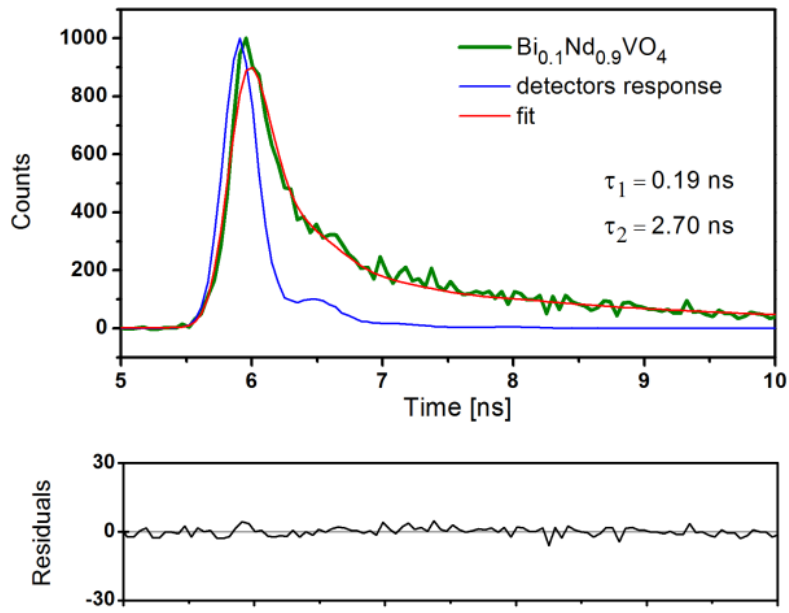
Fig. 37 The green line shows the time-domain intensity decay of $Bi_{0.1}Nd_{0.9}VO_4$ powder. λ_{em} =522 nm. The red line is the fitting curve and the blue line is the response of the detector. The residuals represent the difference between the fitted curve (red line) and the measured data. The goodness of the fit, χ^2, is 2.051.
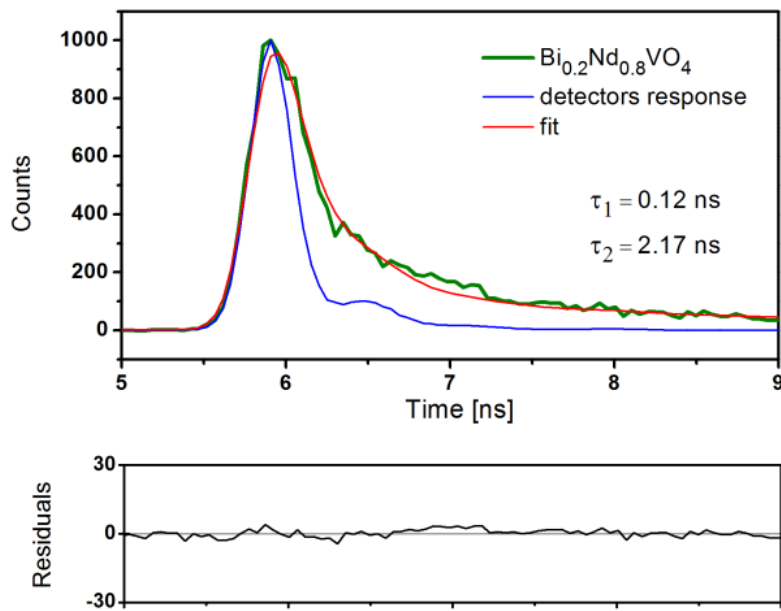
Fig. 38 The green line shows the time-domain intensity decay of $Bi_{0.2}Nd_{0.8}VO_4$ powder. λ_{em} =522 nm. The red line is the fitting curve and the blue line is the response of the detector. The residuals represent the difference between the fitted curve (red line) and the measured data. The goodness of the fit, χ^2, is 5.249.

Fig. 39 The green line shows the time-domain intensity decay of $Bi_{0.3}Nd_{0.7}VO_4$ powder. λ_{em} =522 nm. The red line is the fitting curve and the blue line is the response of the detector. The residuals represent the difference between the fitted curve (red line) and the measured data. The goodness of the fit, χ^2, is 2.290.

Fig. 40 The green line shows the time-domain intensity decay of $Bi_{0.48}Nd_{0.52}VO_4$ powder. λ_{em} =522 nm. The red line is the fitting curve and the blue line is the response of the detector. The residuals represent the difference between the fitted curve (red line) and the measured data. The goodness of the fit, χ^2, is 0.493.

82

Table 3 Fitting parameters of the photoluminescence decay curves of $Bi_xNd_{1-x}VO_4$ powders at room temperature, excited by 371 nm ($\lambda_{em} = 522$ nm).

Sample	Lifetime [ns]	Standard deviation [ns]	χ^2	B1	B2
$NdVO_4$	$\tau_1 = 1.23$ (78.03%) $\tau_2 = 11.59$ (21.97%)	0.01 0.68	18.870	0.13	0.00
$Bi_{0.1}Nd_{0.9}VO_4$	$\tau_1 = 0.19$ (58.32%) $\tau_2 = 2.86$ (41.68%)	0.01 0.06	2.051	0.34	0.02
$Bi_{0.2}Nd_{0.8}VO_4$	$\tau_1 = 0.19$ (44.82%) $\tau_2 = 2.70$ (55.18%)	0.01 0.05	5.249	0.30	0.03
$Bi_{0.3}Nd_{0.7}VO_4$	$\tau_1 = 0.12$ (73.00%) $\tau_2 = 2.17$ (27.00%)	0.01 0.08	2.290	0.48	0.01
$Bi_{0.48}Nd_{0.52}VO_4$	$\tau_1 = 0.12$ (88.02%) $\tau_2 = 1.17$ (11.98%)	0.00 0.09	0.493	0.50	0.01

As it can be seen from Table 3, the lifetime of the photogenerated charges in the $Bi_xNd_{1-x}VO_4$ powders is of the order of nanoseconds, and the samples with a higher amount of Bi exhibit shorter lifetime. Fig. 41 shows the comparison of the decay curves of $Bi_xNd_{1-x}VO_4$ ($x = 0, 0.1, 0.2, 0.3, 0.48$) powders.
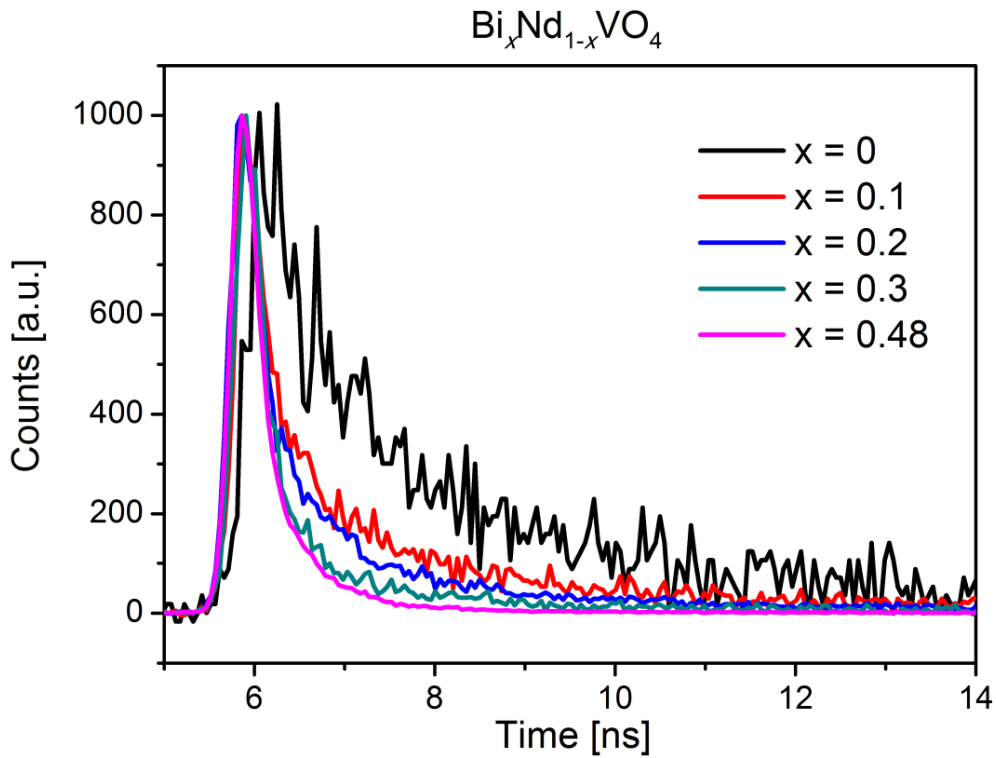
Fig. 41 Time-domain intensity decays of $Bi_xNd_{1-x}VO_4$ powders, plotted for comparison.

2.3.2 $Nd_yBi_{1-y}VO_4$

2.3.2.1 Crystal structure and phase composition

The XRD patterns of $Nd_yBi_{1-y}VO_4$ (y < 0.08) nominal compositions in Fig. 42 show the presence of only the monoclinic $BiVO_4$ phase. For $y > 0.08$, additional peaks of the tetragonal $NdVO_4$-based structure appear in the XRD pattern. The unit cell volume of this $NdVO_4$-based phase corresponds to the end member of the $Bi_xNd_{1-x}VO_4$ solid solution with $x = 0.49(1)$.

Because of very small dopant concentration and the limited sensitivity of the XRD technique, I could not make convincing conclusions about the Nd substitution in $BiVO_4$ even for the $y < 0.08$ samples that appear to be single phase. Therefore, I have performed EXAFS studies to verify whether or not Nd^{3+}, in small concentrations enters the crystal structure of $BiVO_4$.
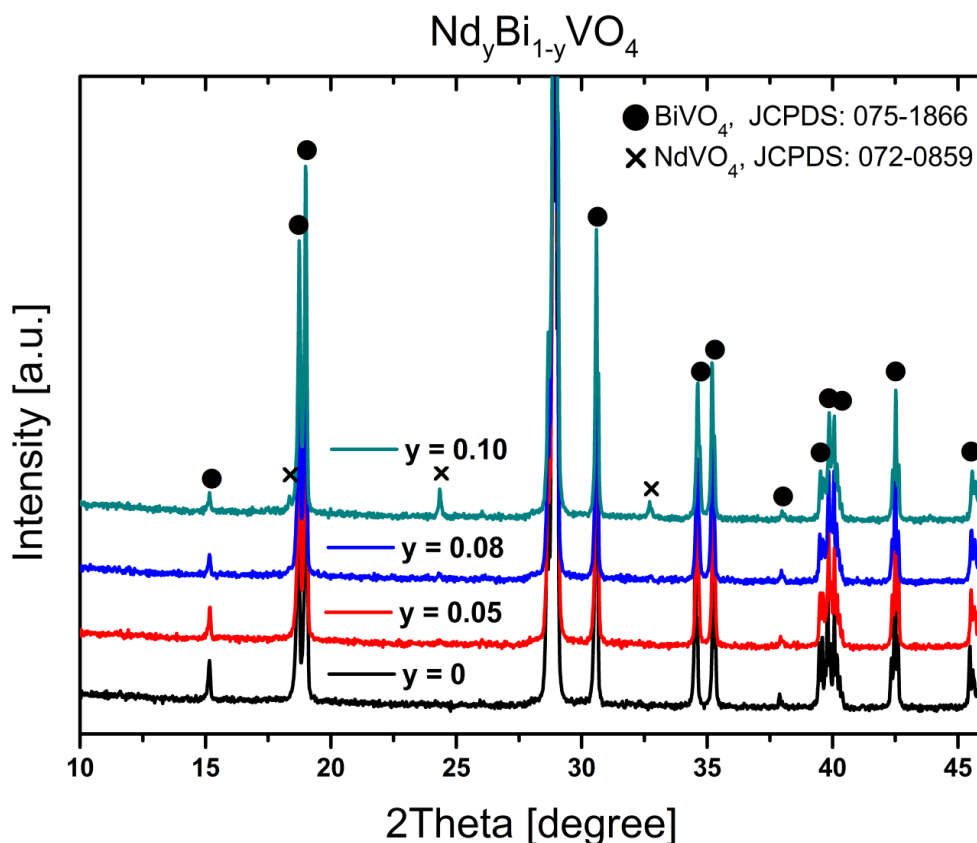
Fig. 42 X-ray diffraction patterns of Nd-doped $BiVO_4$ samples with the nominal stoichiometry $Nd_yBi_{1-y}VO_4$. The tetragonal $NdVO_4$-based phase is marked with the crosses and the monoclinic $BiVO_4$ with the filled circles.

2.3.2.2 EXAFS studies

The XRD pattern of the sample with the nominal composition $Nd_{0.05}Bi_{0.95}VO_4$ corresponds to the single-phase monoclinic $BiVO_4$. I used the EXAFS analysis to determine whether Nd has indeed entered the crystal structure of $BiVO_4$. We measured Nd L_3-edge EXAFS on the $Nd_{0.05}Bi_{0.95}VO_4$ sample and V K-edge and Bi L_3-edge EXAFS on $BiVO_4$ sample. The FT of k^2-weighted Nd, Bi and V EXAFS spectra were calculated over the range of $k = 3.5–10.5$ Å^{-1}. Errors in FT magnitude EXAFS spectra due to the random noise in $\chi(k)$ are estimated at high R values (in the interval from 8–15 Å) and are of the order of $\pm\, 1{\cdot}10^{-3}$ for the Bi, $\pm\, 1{\cdot}10^{-2}$ for the Nd, and $\pm\, 3{\cdot}10^{-3}$ for the V spectrum. The comparison between the measured FT EXAFS signals (Fig. 43) shows significant differences between the three spectra. Neither Bi nor V spectrum is similar to the Nd spectrum. This comparison strongly suggests that Nd in the sample with the nominal composition $Nd_{0.05}Bi_{0.95}VO_4$ does not have the same environment as Bi or V in $BiVO_4$. Therefore, Nd is probably forming a secondary phase with different local structure. Based on the described XRD studies it is reasonable to assume that the secondary phase is the $Bi_xNd_{1-x}VO_4$ end member, i.e., $Bi_{0.49}Nd_{0.51}VO_4$.
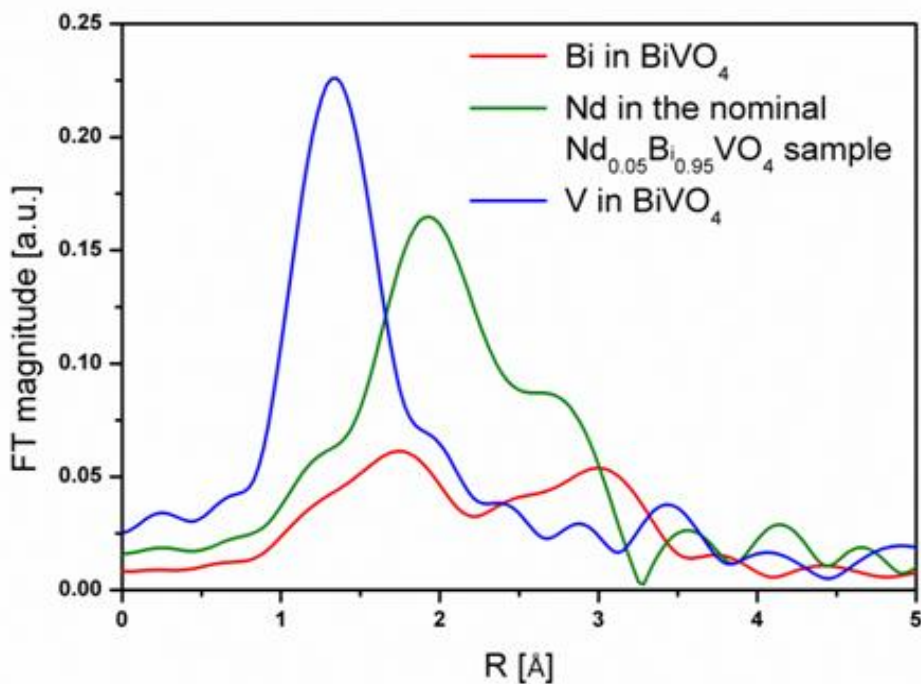
Fig. 43 Fourier transform magnitude of the k^2-weighted Nd L_3-edge EXAFS measured on the sample with the $Bi_{0.05}Nd_{0.95}VO_4$ nominal composition, compared to k^2-weighted Bi L_3-edge and V K-edge FT EXAFS spectra, measured on $BiVO_4$ calculated in the k range of 3.5–10.5 Å^{-1}.

In order to fit the Nd EXAFS spectrum, we constructed Nd model EXAFS functions *ab initio,* from crystallographic data of the $NdVO_4$ reference [211], as described in section 3.3.1.2, but in this case we substituted 50% of Nd neighbour atoms with Bi atoms, to obtain the EXAFS model for the $Bi_{0.5}Nd_{0.5}VO_4$ crystal structure. In the EXAFS model function all single and multiple scattering paths in the R range up to 5.1 Å were included. A minimum number of variable parameters were introduced in the fit: a separate Debye-Waller factor (σ^2) and a common relative change of distances ($\Delta R/R$), for each shell of neighbours, except for the first Nd-O distance and for the Nd-Bi distance where separate ΔR were used. The common shift of the energy origin, ΔE_0, and the common amplitude reduction factor S_0^2 were allowed to vary. The shell coordination numbers (N) were kept fixed at the crystallographic values of the model $Bi_{0.5}Nd_{0.5}VO_4$ structure. A very good fit of the experimental spectrum with the model $Bi_{0.5}Nd_{0.5}VO_4$ structure was obtained for the fitting performed in the *k* range from 3.4 $Å^{-1}$ to 10 $Å^{-1}$, and the *R* range from 1.35 Å to 5.1 Å. A complete list of the best-fit parameters is given in Table 4, and the quality of the fit is illustrated in Fig. 44. The error due to the random noise in χ(k) is $\pm$ $4 \cdot 10^{-3}$; and the error in FT magnitude EXAFS spectrum due to the random noise in χ(k) is estimated at high R values and is of the order of $\pm$ $1 \cdot 10^{-2}$.

Table 4 Structural parameters of the first coordination shells around Nd atom in the $Bi_{0.5}Nd_{0.5}VO_4$ model structure. R = distance and σ^2 = Debye-Waller factor. Uncertainty of the last digit is given in parentheses. The fitting statistics, *R-factor*= 0.007. The amplitude reduction factor $S_0^2 = 0.8 \pm 0.1$, and the shift of the energy origin $\Delta E_0 = 1.3 \pm 1.5$ eV.

Neighbour element of Nd	Number of neighbours	R [Å]	σ^2 [$Å^2$]
O	8	2.43(1)	0.008(1)
V	2	3.15(2)	0.007(2)
Nd	2	3.92(2)	0.003(2)
V	4	3.92(2)	0.011(2)
Bi	2	4.22(3)	0.003(2)
O	12	4.31(2)	0.015(5)
O	8	5.06(7)	0.011(1)
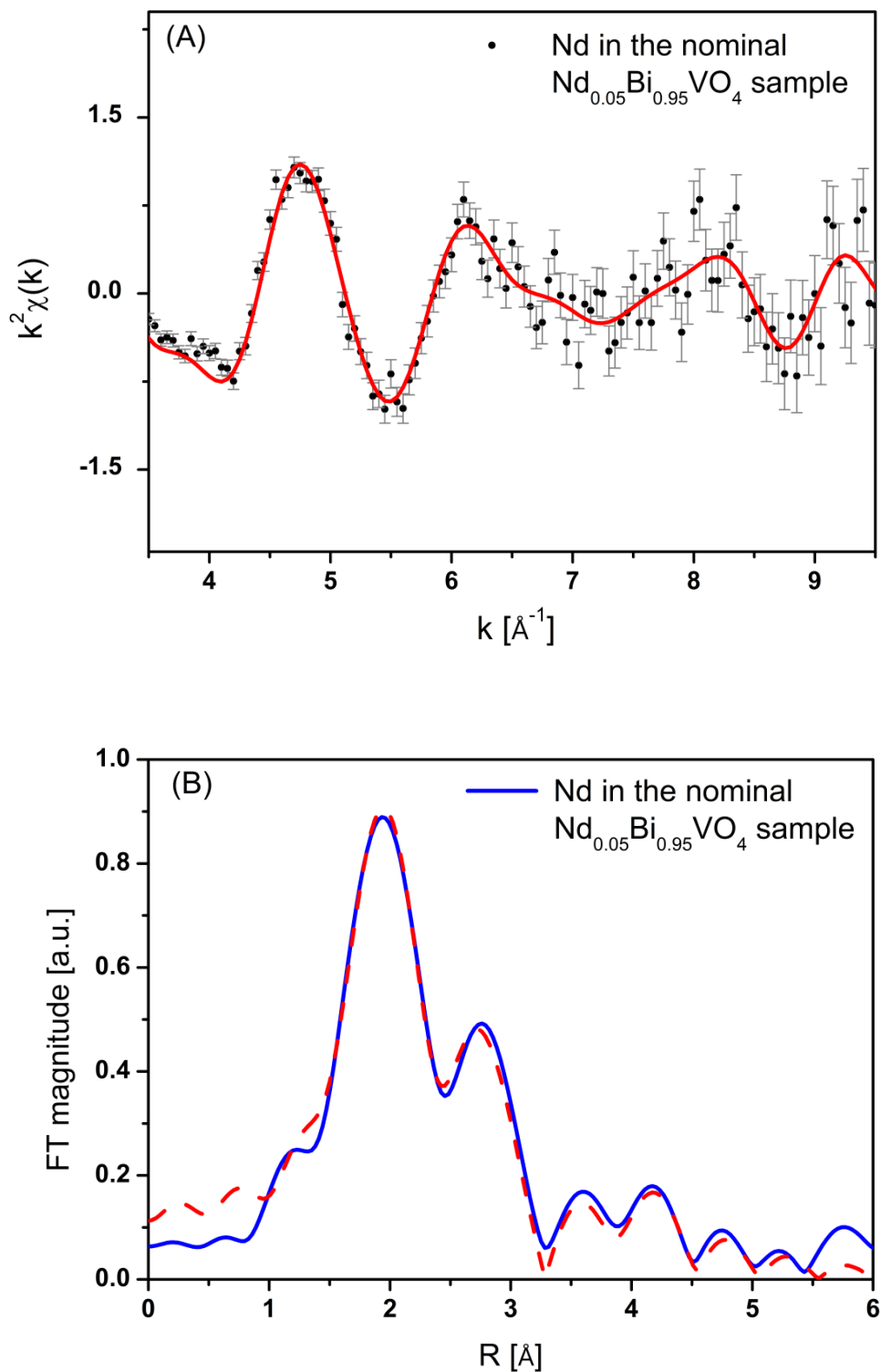
Fig. 44 (A) The k^2-weighted Nd L_3-edge EXAFS spectrum, measured on the sample with the $Nd_{0.05}Bi_{0.95}VO_4$ nominal composition (dots), and its best fit EXAFS model (solid line). (B) Fourier transforms magnitude of the k^2-weighted Nd L_3-edge EXAFS spectrum (solid line), measured on the sample with the $Nd_{0.05}Bi_{0.95}VO_4$ nominal composition, compared to the best fit EXAFS model (dashed line) calculated in the R range = 1.35−5.1 Å.

The results of the EXAFS analysis show that even for the smallest concentrations, Nd did not enter the crystal structure of $BiVO_4$ but it formed, most probably nanocrystalline, secondary $Bi_xNd_{1-x}VO_4$ phase with $x = 0.49(1)$. The fact that Nd did not enter the $BiVO_4$ crystal structure is somewhat surprising, taking into account that the ionic radii of Nd^{3+} and Bi^{3+} are very similar (1.11 Å and 1.17 Å, respectively). The result indicates that for the stabilization of the $BiVO_4$ structure, the specific electron structure of Bi^{3+} is crucial. It appears that the hybridization of the Bi $6s^2$ and O $2p$ orbitals stabilizes the monoclinic $BiVO_4$ structure by distorting the Bi cation environment and adjusting the oxygen coordination sphere correspondingly. The distance of the A-site ion to the first oxygen coordination sphere is shorter in the monoclinic $BiVO_4$ than in the tetragonal $NdVO_4$ (2.35 Å [219] and 2.44 Å, respectively) and, therefore, such cation site cannot be occupied by Nd^{3+} ion without the ability for the hybridization. This also explains why $NdVO_4$ and $BiVO_4$ crystallize in very different crystal structures and no Nd^{3+} can enter the A-site of $BiVO_4$. For the same reason no successful substitution on the A-site of the m-$BiVO_4$ has been reported so far. $NdVO_4$ can adopt the monoclinic $BiVO_4$-type of structure but only under high pressure [59]. Such monoclinic structure with rare earth ions on the A-site is a metastable polymorph, in which, instead of the hybridization, the cation-oxygen distances are reduced by application of the external pressure.

2.3.2.3 Optoelectronic properties

2.3.2.3.1 Band gap

The band gap energy of the m-$BiVO_4$ obtained by us (~2.38 eV) is in a good agreement with values reported in the literature (~2.4 eV [192,194]).

From Fig. 45 can be seen that the band gap of m-$BiVO_4$ varies insignificantly with the nominal Nd concentration, which is consistent with the previous finding that Nd does not enter the crystal structure of $BiVO_4$.

The UV-vis spectra of $Bi_{0.49}Nd_{0.51}VO_4$/$BiVO_4$ composites show the presence of two different peaks centred at around 585 nm and 754 nm, like for the spectra of $Bi_xNd_{1-x}VO_4$ samples. For the assignment of these peaks see section 2.2.1.3.1. This assignment is consistent with the fact that we have observed them for all the samples except for $BiVO_4$.
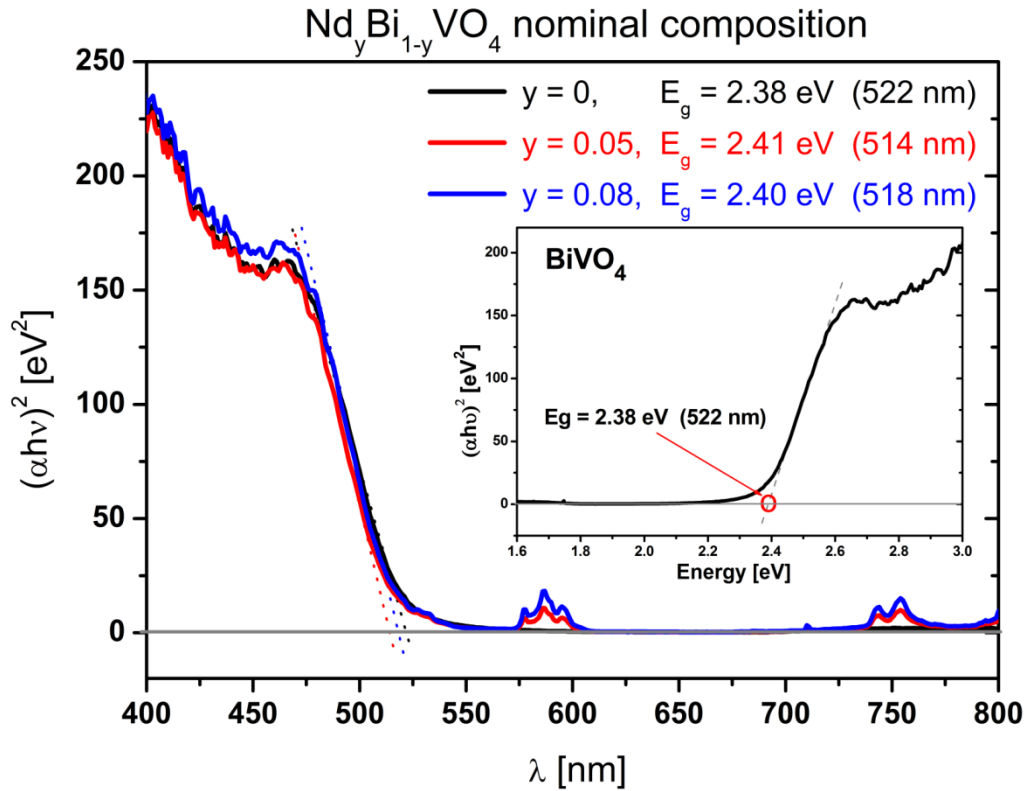
Fig. 45 UV-Vis diffuse reflectance spectra of nominal $Nd_yBi_{1-y}VO_4$ compositions. The Kubelka-Munk function is plotted versus the excitation energy. The E_g of $BiVO_4$ varies insignificantly with Nd concentration. The insert shows the band gap determination of $BiVO_4$.

To obtain the band edge positions of $BiVO_4$, I used a simple theoretical approach, from the absolute (Mulliken) electronegativity (arithmetic mean of the atomic electron affinity and the first ionization energy) of the constituent elements [220,221]. There are other methods to determine the band edge positions, such as experimental photoelectrochemical techniques or theoretical calculations from the first principles.

For a bulk material, the energy of valence band edge, E_{VB}, is a measure of the ionization potential, while the conduction band edge energy, E_{CB}, is a measure of the electron affinity. The Fermi level represents the chemical potential of electrons in a semiconductor, and is the absolute (Mulliken) electronegativity [222]. The conduction band edge of a semiconductor at the point of zero charge can be thus predicted by the equation [220,222]:

$$E_{CB} = X - E^e - 0.5 \cdot E_g \tag{41}$$

89

where X is the Mulliken's (absolute) electronegativity of the semiconductor, expressed as the arithmetic mean of the atomic electron affinity and the first ionization energy [220], or as the geometric mean of the absolute electronegativity of the constituent atoms [222], E^e is the energy of free electrons on the hydrogen scale (~4.5 eV), E_g is the band gap of the semiconductor.

The calculated and previously reported band edge positions of $BiVO_4$ are compared in Table 5.

Table 5 Absolute electronegativity (X) and estimated band gap energy levels of conduction and valence band edge[5] for $BiVO_4$ at the point of zero charge. X was considered to be 6.035 eV [223].

$E_g{}^6$ in eV	Conduction band edge, E_{CB} in eV	Valence band edge, E_{VB} in eV	Reference	Synthesis method
2.38	0.35	2.73	This work	Solid-state synthesis, ~1 μm particles
2.28	0.39	2.67	Long et al. [221]	Aqueous medium, microparticles, several μm size
2.45	0.31	2.76	Jiang et al. [223]	Solution combustion, ~520 nm particles

As it can be seen from Table 5, the band edge positions of $BiVO_4$ obtained by solid state method are in good agreement with the ones reported in the literature.

2.3.2.3.2 Photoluminescence and lifetime

Photoluminescence spectra of the m-$BiVO_4$ have been reported in the literature [18,221,224,225,226,227]. Most of the reported spectra show a broad peak in the range of 490–600 nm but with different intensity and peak position. These differences have been attributed to different synthesis method, particle size, and conditions of measurement (temperature, excitation wavelength, etc). For example, $BiVO_4$ prepared by the ultrasonic method [227] showed a broad band from 490 until

---

[5] Valence band edge was obtained by a summation between the Eg value and CB value.
[6] In all cases, $BiVO_4$ was considered a direct band gap semiconductor.

570 nm, with three maxima. The PL intensity of this sample was higher than the one of $BiVO_4$ obtained by the solid-state method. The sample prepared in an aqueous medium [221] showed a peak centred at about 600 nm with a higher intensity at 77 K than at room temperature, while in [18] no PL signal was observed, even at 83 K. The m-$BiVO_4$, prepared by a liquid-solid reaction, gave a broad PL peak centred at about 715 nm [224]. The spectrum of $BiVO_4$ from this work (Fig. 46) looks similar to the spectrum reported for the ~20 nm sized $BiVO_4$ prepared via an ultrasound irradiation, measured at room temperature [63]. The broad peak in the emission spectrum of the $BiVO_4$ powder was attributed to a radiative recombination of the holes, formed in the O $2p$ – Bi $6s$ of the valence band, with the V $3d^0$ electrons in the conduction band.
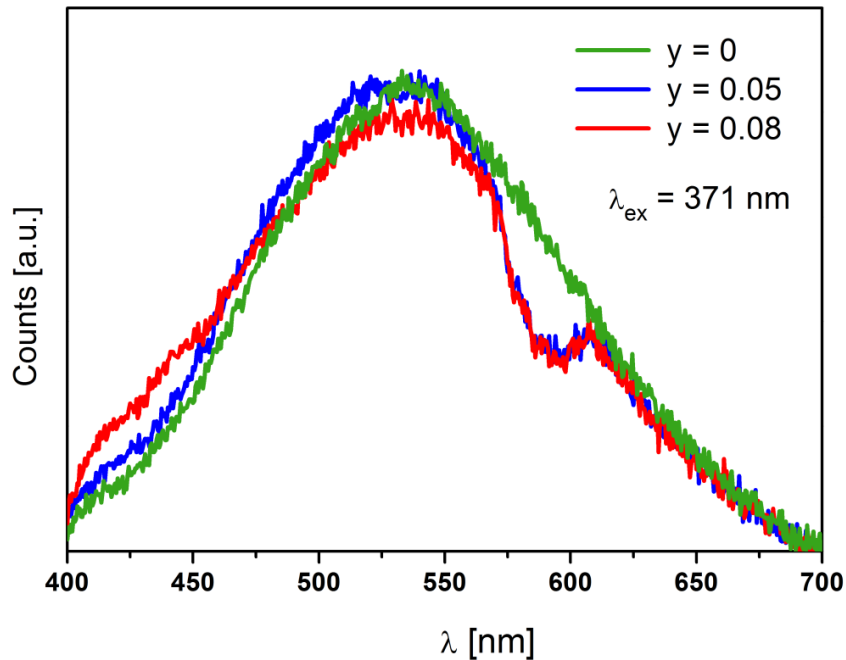
Fig. 46 Room temperature PL spectra of $BiVO_4$ and of nominal $Nd_yBi_{1-y}VO_4$ compositions.

From Fig. 46 we see that the PL spectra of $BiVO_4$ and the nominal $Nd_yBi_{1-y}VO_4$ compositions have similar intensities (which is expected because Nd^{3+} does not enter the $BiVO_4$ structure). In the case of the nominal $Nd_yBi_{1-y}VO_4$ compositions, an additional peak can be observed at ~605 nm which could originate from the Nd^{3+} ion electronic transition (viz. $^4G_{7/2,9/2} \rightarrow {}^4I_{11/2,13/2}$ [216]).

Fig. 47 shows the carrier dynamics of all the powders with the $Nd_yBi_{1-y}VO_4$ (y = 0, 0.05, 0.08) nominal composition, plotted for comparison. From Fig. 47 it can be

seen that the effect of the composition on the lifetime of the photogenearted charges in the $Nd_yBi_{1-y}VO_4$ powders is negligible.

The fitted decay profiles for all three compositions are shown in Figs. 48–50, and the lifetime values together with the fitting parameters are in Table 6. All the decay curves could be fitted only by using two exponential terms, which suggests that the decay processes in the powders with the $Nd_yBi_{1-y}VO_4$ nominal composition are dominated by the second order kinetics. The fitted decay profile of $BiVO_4$ is presented in Fig. 48. To my knowledge, there are no previous reports on the analysis of the decay profile of $BiVO_4$. The decay in $BiVO_4$ that I obtained can be described with two characteristic lifetimes, $\tau_1 = 0.60$ ns and $\tau_2 = 4.42$ ns.
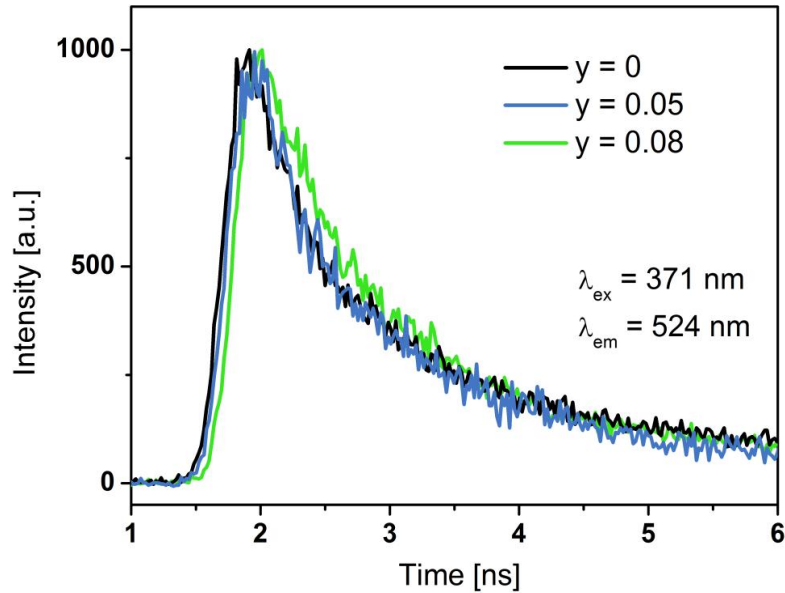
Fig. 47 Time-domain intensity decays of powders with the $Nd_yBi_{1-y}VO_4$ nominal composition, plotted for comparison.

Table 6 Fitting parameters of the photoluminescence decay curves of powders with $Nd_yBi_{1-y}VO_4$ nominal composition, at room temperature, excited by 371 nm ($\lambda_{em}= 524$ nm).

Sample	Lifetime [ns]	Standard deviation [ns]	χ^2	B1	B2
$BiVO_4$	$\tau_1 = 0.60$ (40.61%) $\tau_2 = 4.42$ (59.39%)	0.01 0.04	2.1 10	0.06	0.01
y = 0.05	$\tau_1 = 0.58$ (44.63%) $\tau_2 = 3.37$ (55.37%)	0.01 0.05	4.6 51	0.06	0.01
y = 0.08	$\tau_1 = 0.62$ (46.17%) $\tau_2 = 3.61$ (53.83%)	0.01 0.04	2.4 64	0.07	0.01
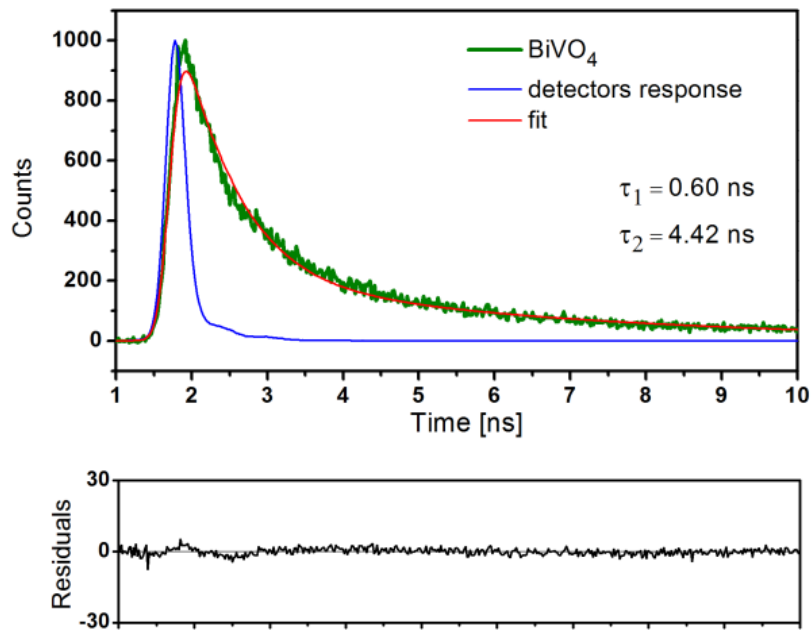
Fig. 48 The green line shows the time-domain intensity decay of $BiVO_4$ powder. $\lambda_{em} = 524$ nm. The red line is the fitting curve and the blue line is the response of the detector. The residuals represent the difference between the fitted curve (red line) and the measured data. The goodness of the fit, χ^2, is 2.110.
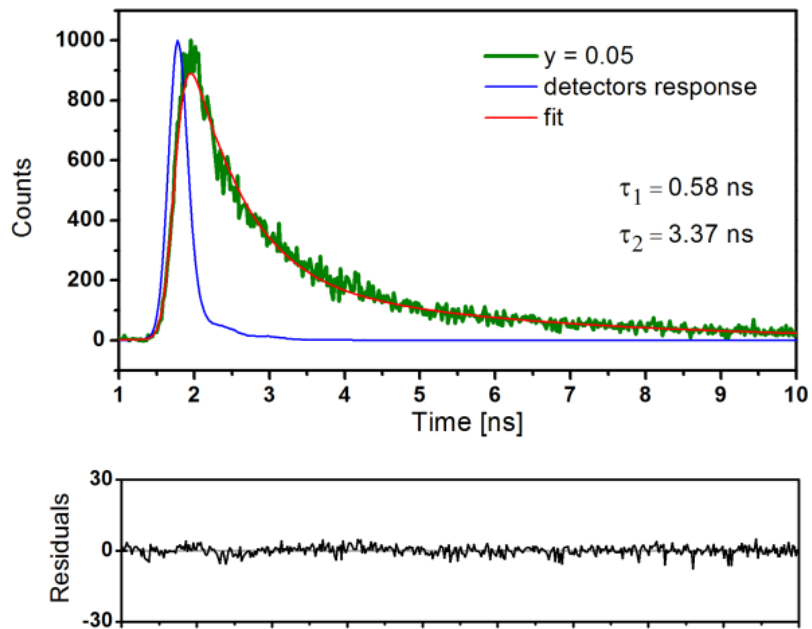
Fig. 49 The green line shows the time-domain intensity decay of $Nd_{0.05}Bi_{0.95}VO_4$ nominal composition. $\lambda_{em} = 524$ nm. The red line is the fitting curve and the blue line is the response of the detector. The residuals represent the difference between the fitted curve (red line) and the measured data. The goodness of the fit, χ^2, is 4.651.
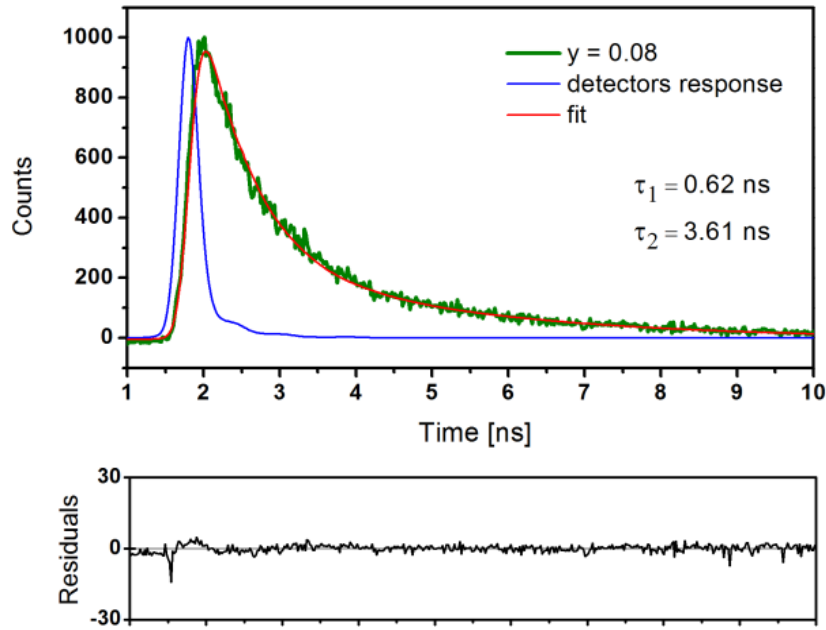
Fig. 50 The green line shows the time-domain intensity decay of $Nd_{0.08}Bi_{0.92}VO_4$ nominal composition. $\lambda_{em} = 524$ nm. The red line is the fitting curve and the blue line is the response of the detector. The residuals represent the difference between the fitted curve (red line) and the measured data. The goodness of the fit, χ^2, is 2.464.

2.4 Conclusions

In this study, the phase relations in the $BiVO_4-NdVO_4$ system and the optoelectronic properties of the present solid solutions have been reported. The findings can be summarized as follows:

- Bi can be incorporated in the tetragonal $NdVO_4$ structure up to 0.49(1) mol %, as the XRD and EXAFS studies indicated. On the other side of the $BiVO_4-NdVO_4$ system, EXAFS study proved that Nd does not substitute neither Bi, nor V in the m-$BiVO_4$ structure.

- The EXAFS study of Bi in the $Bi_xNd_{1-x}VO_4$ ($x = 0.2$) sample showed that the first oxygen atoms around Bi^{3+} are at a smaller distance as it could be expected from their ionic radii, which is a consequence of the hybridization of Bi $6s^2$ and O $2p$ orbitals.

- By the Bi-doping, the absorption of $NdVO_4$ was shifted towards the visible range of the solar spectrum and thus, it enhanced its optical absorption. The decrease of the band gap has been attributed to the Bi $6s^2$ − O $2p$ hybridization at the top of the $NdVO_4$ valence band.

94

- A hybridization of Bi $6s^2$ and O $2p$ orbitals is also suggested from the PL analysis by the appearance of new emission lines in the PL spectra.

- The decay profiles of the $Bi_xNd_{1-x}VO_4$ powders were found to depend on the composition: the lifetime values of the photogenerated charges in $NdVO_4$ decreased with Bi *d*oping. We can conclude that the Bi $6s^2$ − O $2p$ hybridization at the top of the valence band does not only positively influence the absorption properties of $NdVO_4$, but also accounts for the shortening of the exciton lifetime.

- Since $Bi_xNd_{1-x}VO_4$ samples show visible light absorption, it would be interesting to further investigate their photocatalytic properties.

3 Synthesis and optoelectronic characterisation of Bi-doped NdVO₄ nanoparticles

3.1 Background and goals

The dependence of material properties on size and morphology have led scientists towards the synthesis of nanomaterials with controlled shape. Novel optical or electronic properties can be discovered in nanocrystals, compared to their bulk counterparts, due to their large specific surface and quantum size effect.

Recently, rare earth (Y, Sc, and La–Lu)-based nanomaterials are receiving a great attention. Beside their conventional applications (e.g., phosphors, catalysts, or fuel cells) newly discovered properties of the rare earth compounds (such as optical, electrical, or magnetic) make possible new applications. In the last years, rare earth orthovanadate nanocrystals are investigated as multiphoton fluorescent materials, biochemical labels, sensors, fluorescent lamps, displays, light emitting diodes (LEDs), solar cells, and other optoelectronic nanodevices [228,229,230,231,232]. The performance of the rare earth phosphors consisting of micron-size particles is lower than the corresponding nanosized material. Due to the large surface area, the quenching concentration of luminescent dopants in rare earth nanomaterials is higher than for the corresponding bulk phosphors [233]. Initially, the development of the phosphors was focused on the aluminate matrices. The introduction of the rare earth elements led to the important improvement in the performances of these phosphors [234]. But a low absorbance cross-section and a narrow excitation line of Ln^{3+} ($Ln =$ La–Lu) is still the bottleneck in practical applications. The vanadate matrix is a good candidate, because it excites the lanthanide ions via the charge-transfer energy migration. Under the excitation in the UV region they show an absorption band located at about 250–350 nm (due to a charge transfer inside the VO_4 matrix) [235,236]. This facilitates a non-radiative energy transfer from the vanadate matrix to the Ln^{3+} and can significantly enhance the absorption and excitation efficiency. To increase even more the efficiency of the lanthanide emissions and to overcome the low absorption of its parity forbidden $4f$–$4f$ transitions, excitation in the wavelengths >350 nm (in the near UV region) should occur. This can be possible trough

97

sensitization via energy transfer (non-radiative) from a sensitizer (an ion containing a ns^2 lone electron pair) to the V ion (d^0) and then to the Ln (activator) ions. [237,238]. Among other ions with lone-pair ns^2 configuration (e.g., Tl^+, Sn^{2+}, Pb^{2+}, Sb^{3+}), Bi^{3+} has been widely used as a sensitizer for YVO_4:Eu (a typical commercial red-emitting phosphor used in cathode ray tubes), Eu^{3+}/Sm^{3+} doped $LnVO_4$ (Ln = Y, Gd), $GdVO_4$, or $EuVO_4$ [239,240,241,242,243]. Highly efficient tunable red, green, and blue emissions from the Ln^{3+} ions under excitation with longer wavelenghts such as 350–400 nm (so the absorption band is extended to NUV region), can be achieved by Bi^{3+} doping. This is possible due to a metal charge transfer from the Bi $6s^2$ − O $2p$ hybrid orbital to the V $3d^0$ and further to the Ln^{3+} ion (Fig. 51).
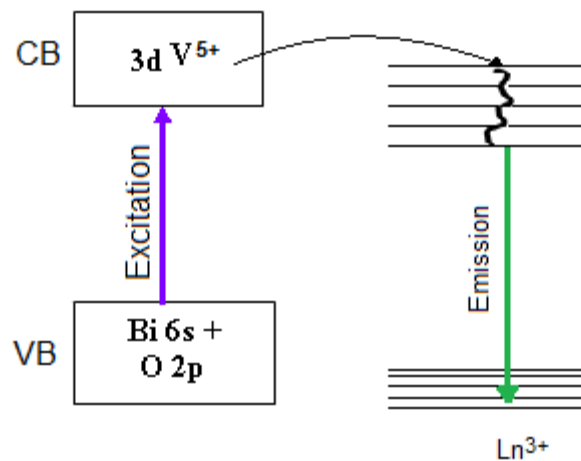
Fig. 51 Scheme illustrating the energy band structure of the Bi-activated $LnVO_4$ phosphors and the energy transfer process.

For instance, the Bi^{3+}-doped Ln^{3+}:YVO_4 (Ln = Eu, Sm, Dy, Ho) nanocrystals (5 nm size) that Chen et al. [239] prepared showed a shifted excitation band from 280 (without Bi) to 345 nm. The emissions of such phosphors were also easily tuned by changing the Ln^{3+} ion. Due to their high stability and high transparency, the rare earth orthovanadates doped with Bi^{3+} are also used as spectral down-shifters for solar cells, which convert near UV to visible light [244,245].

So far, $NdVO_4$ has been also studied as a potential photocatalyst. Nd^{3+} is an important constituent of optical materials and a good candidate for upconversion fluorescence and in solid-state lasers (for which has been recognized as the most efficient rare earth ion). And for these reasons it is expected that $NdVO_4$ should also

show good luminescent properties. Indeed, Wu et al. [246] have reported on blue emissions of $NdVO_4$ nanorods under 310 nm excitation.

The photoluminescence studies (presented in Chapter 2 of this thesis) showed that micrometer-sized $NdVO_4$ emits in the visible spectrum upon UV excitation, but by Bi-doping, no significant influence on the emission spectrum was observed. Yet, it will be interesting to investigate the optoelectronic properties of Bi-doped $NdVO_4$ (Bi-$NdVO_4$) nanoparticles. We expect important luminescent properties due to the Bi^{3+} ion which could act as a sensitizer for the Nd^{3+} ion. This could lead to more efficient/tunable emissions from the Nd^{3+} ion. But the synthesis of Bi-doped $NdVO_4$ (Bi-$NdVO_4$) nanoparticles has not been reported so far. Therefore, the main aims of the study presented in this chapter were:

- to develop a method for the synthesis of Bi-$NdVO_4$ nanoparticles with the composition: $Bi_xNd_{1-x}VO_4$ ($x = 0$, 0.1, 0.2, 0.3, and 0.48). This step is the key importance to the further exploration of the properties of these materials;
- to evaluate the influence of the Bi-doping on the structure, absorption and emission properties of $NdVO_4$ nanoparticles.

3.2 Materials and methods

3.2.1 Fundamental concepts of coprecipitation synthesis

Coprecipitation is a common wet chemical route for preparation of mixed oxides, including rare earth orthovanadates. Several other wet chemical methods are also known: hydrothermal, solvothermal, sonochemical, reversible micelli, metathesis reactions, sol-gel technique, citrate route, etc. The coprecipitation involves precipitation of solids from a supersaturated solution containing the precursors (usually metal salts). The precipitation is triggered by the addition of an agent that has the role to initiate a chemical reaction or reduces the solubility. According to IUPAC nomenclature [247], coprecipitation is the 'simultaneous precipitation of a normally soluble component with a macrocomponent from the same solution by the formation of mixed crystals, by absorption, occlusion, or mechanical entrapment.' By the coprecipitation, amorphous intermediates (that should be thermal treated for oxide formation), or even already crystallized oxides can be obtained.

Beside for the synthesis of pigments, the coprecipitation is also very suitable for preparation of catalysts (such as Al_2O_3, Fe_2O_3, ZrO_2, etc.) because it generates a good chemical homogeneity of catalyst components.

A coprecipitation process involves a number of steps:

1. Precipitation (through physical or chemical means)
2. Ageing
3. Filtering
4. Drying
5. Thermal treatment

1. Precipitation

Precipitation usually implies the mixing of the liquids (precursors) with a precipitating agent. The solid is formed through nucleation of the primary particles and crystal growth. The nucleation is a complex step and it can be of two types: homogeneous (the solid forms in the solution that is initially free of any solid particles) or heterogeneous (nucleation in the presence of seeds of the same material or other solid materials regarded as 'impurities').

For the solid to precipitate from a homogeneous solution, the nuclei must first form [248]. As illustrated in Fig. 52 [2,249,250,251] there is a critical excess free energy, ΔG^*, associated with the critical radius of cluster, r^*. At initial stages, atoms collide to produce small clusters that will grow until a critical size r^* is reached. These small clusters can overcome the critical free energy barrier (ΔG^*) and became thermodynamically stable nuclei. When the radius is smaller than the critical value ($r<r^*$), the system lowers its free energy by dissolving clusters, and at the same time new ones form due to spontaneous collisions. The expressions of critical radius r^* and maximum excess free energy ΔG^* can be found in ref [251].

The nucleation process can be described according to Gibbs free energy. The excess free energy (ΔG_r) contains two competing terms, the surface energy change (ΔG_S) and volume free energy change (ΔG_V) - Fig. 52 . The excess free energy can be defined as:

$$\Delta G_r = 4\pi r^2 \gamma + \frac{4}{3}\pi r^3 \frac{RT lnS}{V_m} \tag{42}$$

Where:

r = the radius of the cluster,

γ = surface free energy per unit area

R = ideal gas constant

V_m = molar volume of bulk crystal

S = ratio between solute concentrations at saturation and equilibrium conditions.
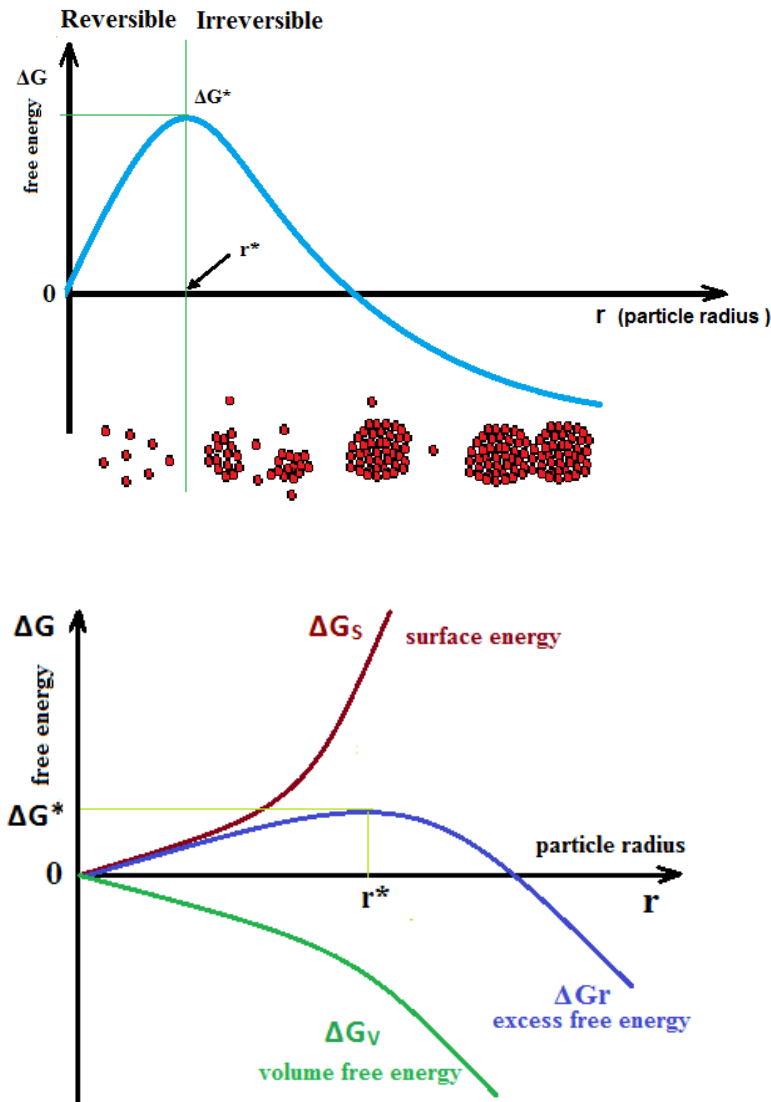
Fig. 52 (top): La Mer diagram describing the dependence of Gibbs free energy on the crystal size. Below r* (critical radius), the process is reversible. (down) nucleation model showing the free energy diagram for nucleation.

The form, shape, and size of a precipitate depend upon the experimental conditions. The particle size distribution of the precipitate depends on the nucleation period: a fast nucleation will lead to a narrow particle size distribution, while a long nucleation period will result in a wide particle size distribution. The final size of the particles will depend on the competition between nucleation, and growth. The size can also be adjusted with stabilizers (usually organic molecules) or by a proper

choice of the solvent. The shape of the crystals is controlled by the surface energy of the particle: the cluster will grow in a geometric arrangement such as to minimize the surface energy, while the shape is determined by the surface energies of the crystal facets. At equilibrium, the crystal will be having the facets giving the minimum total surface energy. With the aid of surfactants, crystals with certain morphologies can be obtained since the surfactant molecules adsorb selectively on certain facets and inhibit their growth [252,253].

The nucleation rate is generally described by the following equation [248,254]:

$$\frac{dN}{dt} \cdot \frac{1}{V} = A \exp(-\frac{\Delta G^*}{kT}) \tag{43}$$

Where:

- N = number of nucleation centres formed per volume unit and time
- A = pre-exponential factor with vales in between 10^{25}–10^{56} $s^{-1}m^{-3}$.

The supersaturation of the solution from which precipitation occurs is the key factor of the precipitation process. A suprasaturated solution has a big free energy which is lowered by forming nucleation centers. The supersaturation can be achieved either by physical or chemical means:

- by cooling the reaction mixture,
- by evaporating the solvent,
- by introducing a precipitating agent in solution that can change the pH of the solution, leading to condensation of the precursors, or can introduce certain ions in solution that make the solubility of the precipitate to be exceeded,
- by a direct reaction between ions,
- by redox reactions, etc.

When dealing with multicomponent systems, knowledge about the relative solubilities of the precipitates is crucial. It is better to work at a high supersaturation level in order to exceed the solubility of all products simultaneously, and thus avoid a sequential precipitation of undesired phases.

2. Ageing

Ageing refers to the time, for which a precipitate is left in the mother solution (precipitation medium) or under different conditions. According to IUPAC nomenclature [247], ageing is the 'time dependent change of the properties of a precipitate, e.g. loss of water, growth of crystals, recrystallization, decrease of the

specific surface, loss of coprecipitated substances or improvement of the filtering properties.' The duration and conditions of ageing have important consequences on the particle size, surface area, pore size distribution, crystallization or the chemical nature of the phase. Particle growth can occur through Ostwald ripening which involves the dissolution of smaller particles (which have a higher solubility than the larger ones) and re-precipitation on the larger particles.

Another process that can occur during ageing is the agglomeration of particles leading to the formation of aggregates - group of particles held randomly together.

Very often, the initial precipitate is amorphous, especially if it is precipitated at a high supersaturation level, and it crystallizes during aging. If the initial precipitate is already a crystalline phase, different phase transitions are also possible.

3. Filtering

After precipitation, the product must be separated from the solution mostly by filtration. Other method to separate the precipitate from the supernatant solution is by spraydrying.

4. Drying

Drying follows the filtration process and is performed for complete removal of the solvent(s) from precipitate. A careful choice of the drying temperature is necessary in order to avoid the decomposition of the product, loss of the product by volatalization or any other changes in its structure.

5. Thermal treatment

Depending on the precursors used, a thermal treatment is in some cases a necessary step for the decomposition of the intermediates to the desired phases or to improve the crystallinity. There are three ways in which the coprecipitation synthesis can occur:

- *in a batch operation* where all parameters except temperature are changing during the precipitation. In the batch operation, the precipitating agent is added to the solution of the precursors in the vessel. This is a simple process, but sometimes, variations of the batch composition can occur.
- *in a batchwise operation* where the precipitating agent and the metal salts solutions are mixed simultaneously at a controlled pH. The ratio between the metal salts and precipitating agent remains constant, but all other parameters

change during this process. Higher homogeneity of the product can be achieved in this case than in the batch operation.

- *in a continuous process* where all the parameters are kept constant or controlled when desired. In this process, the precipitation occurs at low supersaturation and the nucleation occurs heterogeneously, as seeds are already present in the vessel. Such process is used for example for precipitation of catalysts such as $Al(OH)_3$ in the Bayer process.

Several factors such as a concentration and composition of the precursors, the nature of the solvent, temperature or pH affect the properties of the final product. In the preparation of catalysts, the composition and concentration of the starting solutions have impact on the composition and size of the final product. At higher precursor concentrations, high supersaturation can be achieved, which will lead, through homogeneous nucleation, to formation of small particles with high specific surface area. At low concentrations, in order to produce large particles, seeds must be added to the solution.

The most used solvent is water. Organic solvents such as alcohols, aldehydes, esters, are also employed, but the solubility of most metal salts is much lower in organic solvents than in H_2O. A problem that appears when using the organic solvents is the long precipitation time, which can last for days due to the low concentration of the precipitating agent. However, the catalysts precipitated from the organic solvent can be ~50% more active than the ones precipitated in H_2O, due to a higher surface area [255].

3.2.2 Coprecipitation of Bi-doped NdVO$_4$ nanoparticles

Bi-RVO$_4$ compounds are usually prepared by solid state reactions, and only a limited number of studies exist on the wet-chemical synthesis of Bi-RVO$_4$. Bi^{3+}/Ln^{3+} (Ln = Eu, Sm, Dy, Ho) co-doped YVO$_4$ [256] has been prepared by a citrate-assisted solvothermal route while Bi^{3+}; Eu^{3+} co-doped YVO$_4$ have been prepared by the citrate [257] and sol-gel [258] method.

The preparation of Bi-NdVO$_4$ trough a wet chemical synthesis method was not reported so far. While studying the possibility to synthesise Bi-NdVO$_4$ nanoparticles, the doping of Bi into NdVO$_4$ faced some challenges:

- It was difficult to find a solvent that will dissolve simultaneously Bi, Nd, and V salts. While Nd and V salts are soluble in water, Bi^{3+} salts require acidic conditions or special organic solvents.
- It was not possible to obtain a single phase material by hydrothermal or microemulsion synthesis method.

After preliminary studies, the coprecipitation method was in the end adopted as the right method to synthesize Bi-$NdVO_4$ nanocrystals. A typical precipitation route for the rare earth vanadates starts from the soluble salts, containing the cooresponding cations and anions, such as rare earth nitrates, chlorides, and vanadates (ammonium metavanadate, sodium orthovanadate, etc.). The pH value of the initial and final solution plays a crucial role in the process, especially for bismuth and for vanadates because they can exist in different forms at different acidities. For the preparation of rare earth orthovanadate nanocrystals, the optimized pH value of the initial solution was < 1, while the final solution had a pH commonly around 11. The synthesis scheme of Bi-doped $NdVO_4$ nanocrystals is shown in Fig. 53 below.
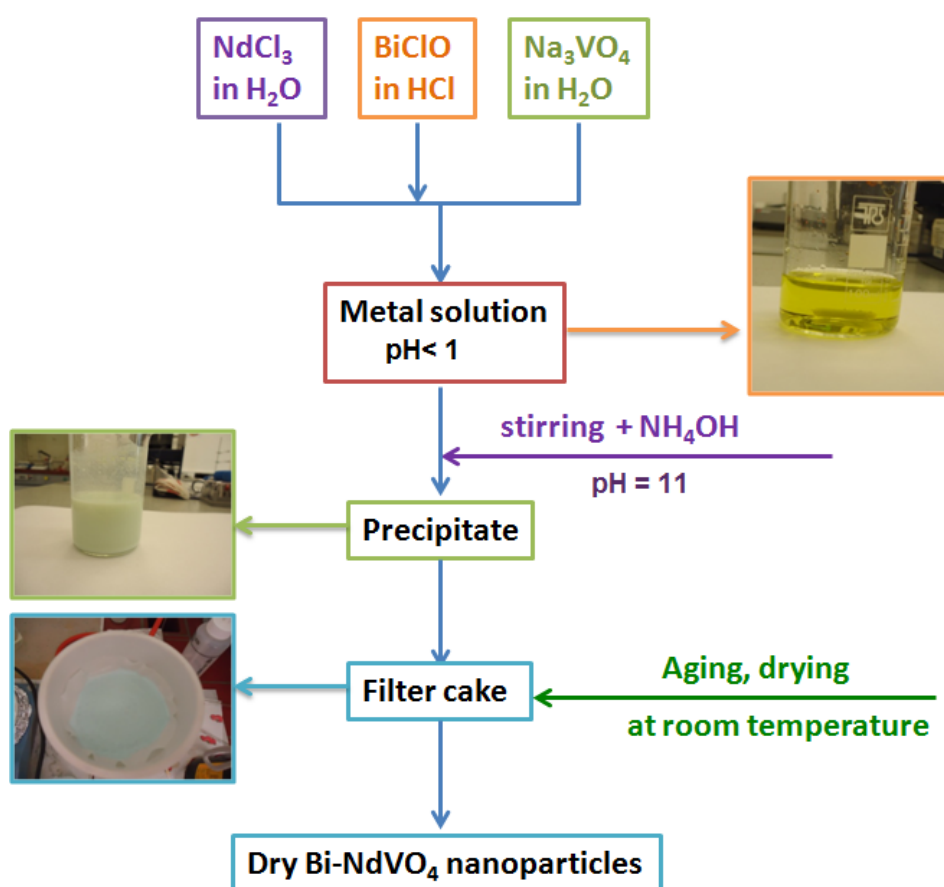
Fig. 53 Scheme of the coprecipitation synthesis of $Bi_x Nd_{1-x} VO_4$ nanoparticles.

In this method, BiOCl (98%, Alfa Aesar), $NdCl_3 \cdot 6H_2O$ (99.9%, Alfa Aesar) and Na_3VO_4 (99.9%, Alfa Aesar) were the precursors, while NH_4OH was the precipitating agent. In a typical synthesis, BiOCl, $NdCl_3 \cdot 6H_2O$, and Na_3VO_4 were weighted according to the molar ratio. Different amounts (corresponding to the molar ratio x) of BiOCl were dissolved in ~9 mL HCl (32%), resulting in a transparent sol. The aqueous Nd solution was prepared by adding $(1-x)$ 0.005 mol $NdCl_3 \cdot 6H_2O$ in 1–2 mL H_2O, while the aqueous solution of Na_3VO_4 (0.05 mol in 2–3 mL H_2O) was prepared by adding 0.05 mol Na_3VO_4 in 2–3 mL H_2O. The Nd solution was added slowly to the Bi solution, and a transparent solution formed. The pH of this solution was < 1. The aqueous solution of Na_3VO_4 was added slowly to the above sol and a yellow sol resulted. NH_4OH solution (25%) was added fast and under vigorous stirring to the above sol until the pH reached the value of ~11. A purple or green to yellowish precipitate formed, the colour depending on the dopant concentration x. The obtained mixture is stirred for 5 more minutes before the precipitate was filtered, washed thoroughly with NH_4OH aqueous solution and then dried at room temperature for 24 hours. The reactions that lead to the formation of $Bi_xNd_{1-x}VO_4$ can be summarized as follows:

$$x\text{BiOCl}_{3(s)} + 2\text{HCl}_{(aq)} + (1-x)\text{NdCl}_{3(aq)} + \text{Na}_3\text{VO}_{4(aq)} \xrightarrow{+NH_4OH} \text{Bi}_x\text{Nd}_{1-x}\text{VO}_4 \downarrow + 3\text{NaCl}_{(aq)}$$

(44)
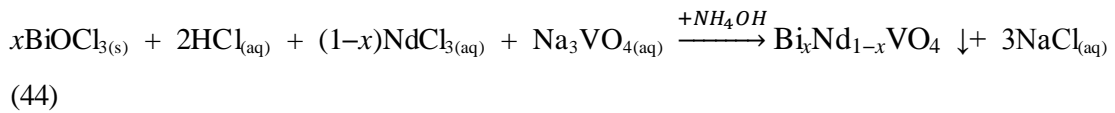
3.2.3   Characterisation

3.2.3.1   XRD

The phase composition of the samples was analyzed by X-ray powder diffraction using a PANalytical X-ray diffractometer with Cu K_α radiation ($\lambda = 0.154$ nm), a step size of $0.017°$ and scan step time of 25.8 s. The diffraction patterns were recorded in the range $2\theta = 15–70°$.

3.2.3.2   SEM

The morphology of the Bi-doped $NdVO_4$ samples was observed by microscopy carried out by a SUPRA 40 field-emission scanning electron microscope (Carl Zeiss AG).

The principle of SEM is based on a high-energy beam of electrons (with an energy ranging from 0.2 keV to 40 keV) that scans the surface of the solid sample. Upon the interaction of the electron beam with the sample, a number of signals will produce a 2D image. The information obtained by the SEM analysis contains not only details about the morphology crystallographic orientation but also about the phase composition.

The power of the scanning electron microscope comes from the wide range of signals that may result from the interaction of the electrons with the sample surface. These include:

- *Secondary electrons* (SE) – the most commonly used signal is derived from these low-energy (< 50 eV) electrons that are ejected from the K-orbitals of the specimen atoms by inelastic scattering interactions with beam electrons. Due to their low energy, these electrons originate within a few nanometers from the sample surface. The brightness of the signal depends on the number of secondary electrons reaching the detector. Steep surfaces and edges tend to be brighter than flat surfaces, which results in images with a well-defined, three-dimensional appearance. Using the signal of secondary electrons, image resolution less than 0.5 nm is possible. SE gives information about the surface of the sample.

- *Backscattered electrons* (BSE) – high energy electrons reflected from the sample by elastic scattering interactions with nucleus of the specimen atoms. BSE are generated from different depth which depends on the experimental conditions. The fraction of the backscattered incident beam depends on the atomic number (Z) of the specimen. It increases with Z. BSE are used to detect contrast between areas with different chemical compositions since heavy elements (with high atomic number) backscatter electrons stronger than light elements (with low atomic number), and thus appear brighter in the image. The backscattered electrons can also be used to form an electron backscatter diffraction (EBSD) image that can be used to determine the crystallographic orientation of the specimen.

- *Characteristic X-rays* are generated by inelastic collisions of the incident electrons with electrons in discrete orbitals (shells) of atoms in the sample. When the excited electrons return to their lower energy states, they yield the

characteristic X-rays are generated. Their wavelength is related to the difference in energy levels of electrons in different shells for a given element. Thus, characteristic X-rays are produced for each element in a mineral that is excited by the electron beam. The X-ray process is not favoured for low atomic number, for which Auger electrons transitions are more probable. The EDS X-ray detector (also called EDS or EDX) measures the number of emitted x-rays versus their energy. EDS is used for elemental analysis of the sample.

The SEM imaging requires the sample to be conductive. So the samples are often carbon or gold coated to become electrically conductive at the surface, to prevent accumulation of electrostatic charges. Nonconductive specimens can be imaged uncoated using low voltage mode of SEM operation (0.3–4 kV). The low-voltage SEM is conducted in an FEG-SEM because FEG (field emission guns) can produce high primary electron brightness and small spot size at low voltage.

3.2.3.3 Raman spectroscopy

Raman spectroscopy is a technique which employs inelastic photon scattering to study the vibrational, rotational, and other lower modes in a system. When radiation consisting of a monochromatic light (usually from a laser, in the visible range) passes through a medium, the species present in the medium scatter a portion of the incident beam in all directions due to interactions of the laser light with sample material. The emitted light is then collected with a lens and sent to the detector. Most of the scattered light is of the same frequency as the incident light, and thus, elastic or Rayleigh scattering. Only a small amount of the scattered light (~10^{-5} % of the incident light) is shifted in energy from the laser frequency due to interactions between the incident electromagnetic waves and vibrational energy levels of the molecules in the sample and will be analyzed. This shift provides information about vibrational, rotational and other low frequency transitions in molecules, and it is called *Raman shift*.

Infrared spectroscopy yields similar but complementary information with Raman spectroscopy. Indian scientist C. V. Raman was the first to observe this phenomenon in liquids in 1928 for which he received the Nobel Prize in 1938. But due to its very low scattering efficiency, Raman spectroscopy did not become popular until

powerful laser systems were available after 1960s. Now, Raman spectroscopy has become one of the most popular approaches to study the vibrational structures of molecules together with infrared spectroscopy.

Fig. 54 depicts a qualitative picture of the sources of Raman and Rayleigh scattering.
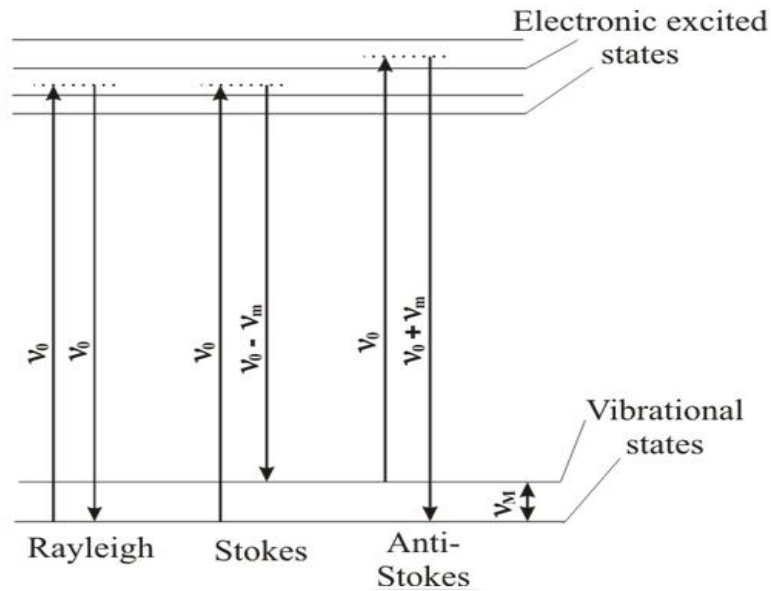
Fig. 54 The energy level diagram showing the basic transitions involved in the spontaneous Raman scattering.

Assuming a beam of radiation, with an electric field E, incident upon the sample, the electric field of the radiation will interact with the electron cloud of the bonds in the sample, inducing a dipole moment m in the bond. *m* is given by the relation

$$m = \alpha E \qquad (45)$$

where α is the polarizability of the bond and is a measure of the deformability of the bond in an electric field [259]. In order for the bond to be Raman active, the polarizability must vary with the distance between nuclei according to the equation [259]:

$$\alpha = \alpha_0 + (r\text{-}r_{eq})\left(\frac{\partial \alpha}{\partial r}\right) \qquad (46)$$

where α_0 is the polarizability of the bond at the equilibrium internuclear distance r_{eq}, while *r* is the internuclear distance at any moment. A complete description of the Raman scattering can be found in ref [259].

The Raman spectrum of the sample results from plotting the intensity of this shifted light versus frequency. In general, Raman spectra are plotted with respect to the laser frequency such that the Rayleigh bands lies at 0 cm^{-1}. On this scale, the band positions will lie at frequencies that correspond to the energy levels of different functional group vibrations. Atoms in solids vibrate at frequencies of approximately 10^{12}–10^{13} Hz [260]. Thus, vibrational modes can be excited to higher energy states by radiation in this frequency range. Raman scattering is a very important vibrational spectroscopic technique, largely used to characterize the vibrational modes of solids, being very useful in identifying vibrating complexes in different materials and in characterizing structural changes in solids [260]. It is sensitive to ordering arrangements of crystal structures. Ordering atoms onto specific lattice sites in the parent structure often forms derivative structures having different space groups. The new symmetry leads to relaxed selection rules, which in turn lead to new Raman lines or to the splitting of the lines of the parent structure. Raman spectra of solid solutions, crystals with lattice defects, and systems having other types of structural disorder usually exhibit a pronounced line broadening in comparison with ordered structures [260].

In this study, Raman spectroscopy was used for identification and structural characterisation of the Bi-NdVO$_4$ nanoparticles. Room temperature Raman spectra were collected in a 180° backscattering geometry, after 10 recordings, on a powder sample with a microprobe Raman system type Horiba Jobin-Yvon Lab RAM HR spectrometer equipped with a holographic notch filter and a CCD detector, using a 632.81 nm excitation line of a 25 mW He Ne laser, after 10 recordings. The samples were placed and oriented on an Olympus BX 40 microscope equipped with 15×, 50× and 100x objective and recorded at a resolution of 1cm^{-1} in the range of 50−1200 cm^{-1}. The spectra were recorded on different areas of the same sample.

3.2.3.4 Diffuse reflectance spectroscopy

To obtain band gap energies, diffuse reflectance spectra were recorded in the range 250−800 nm with a UV-Vis spectrophotometer (Perkin Elmer, model λ 650S) equipped with a 150 mm integrated sphere and using spectralon as a reference material. The diffuse reflectance data were converted to absorbance coefficients

according to Kubelka-Munk theory - more details can be found in Chapter 2, section 2.2.4.

3.2.3.5 Photoluminescence and lifetime

The PL emission and excitation spectra were collected with the same instrument described in Chapter 2, section 2.2.5. Room temperature excitation spectra monitored for the 524 nm emission line were collected in the range of 350–450 nm, while the emission spectra were collected in the range of 400–700 nm with an excitation wavelength of 371 nm (λ_{exc} = 371 nm).

The time-resolved PL spectra were recorded at room temperature on a Picosecond diode laser EPL 375 with an excitation wavelength of 371 nm (λ_{em} = 524 nm), and a blue sensitive high speed photomultiplier detector – Hamamatsu H5773-03. The time range was 0–50 ns. The analysis of the fluorescence decays were performed using the F900 analysis software. This procedure was described in detail in Chapter 2, section 2.2.5.2.

3.3 Results and discussion

3.3.1   Powder characterisation

3.3.1.1 XRD

Fig. 55 shows the XRD patterns of $Bi_xNd_{1-x}VO_4$ (x = 0, 0.1, 0.2, 0.3, and 0.48) samples. All the samples can be indexed as the tetragonal $NdVO_4$ phase with the space group $I4_1/amd$. No impurities were detected.

3.3.1.2 SEM analysis

The morphology and size of the particles were determined with SEM. The SEM images of Bi-doped $NdVO_4$ samples are shown in Figs. 56–60. The $NdVO_4$ particles prepared in this study by the coprecipitation method have an acicular shape, with the length of about 50 nm and the diameter of ~10 nm (Fig. 56), but form agglomerates. The morphologies of the Bi-$NdVO_4$ particles become more irregular as the Bi concentration increases. For the $Bi_{0.1}Nd_{0.9}VO_4$ sample, the SEM image (Fig. 57) shows small aggregates composed of irregular smaller crystallites with an average

length of 80 nm. By increasing the Bi content to $x \geq 0.48$, the particles become more spherical and agglomerated (Figs. 58–60). The average crystallite size determined by SEM is 50 nm.
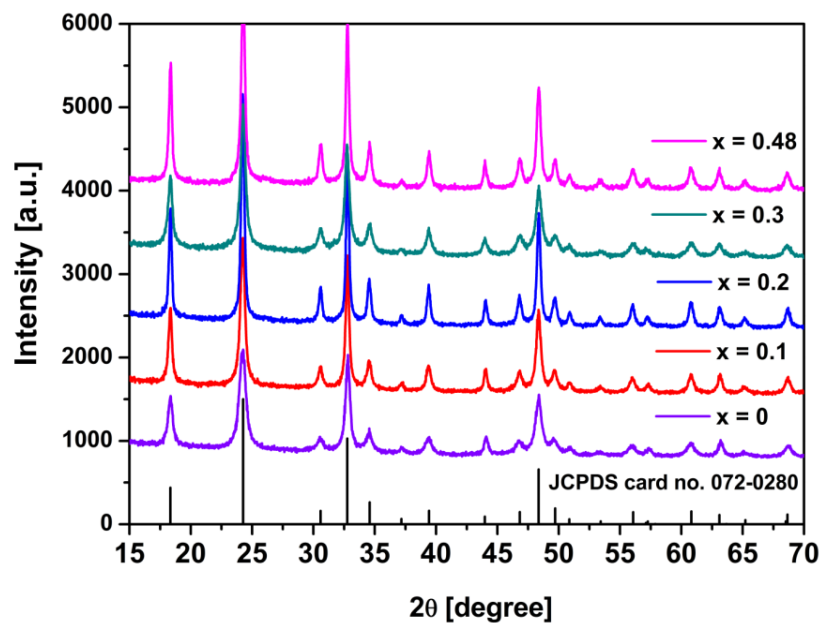
Fig. 55 XRD patterns of $Bi_xNd_{1-x}VO_4$ ($x = 0, 0.1, 0.2, 0.3,$ and 0.48) nanopowders.
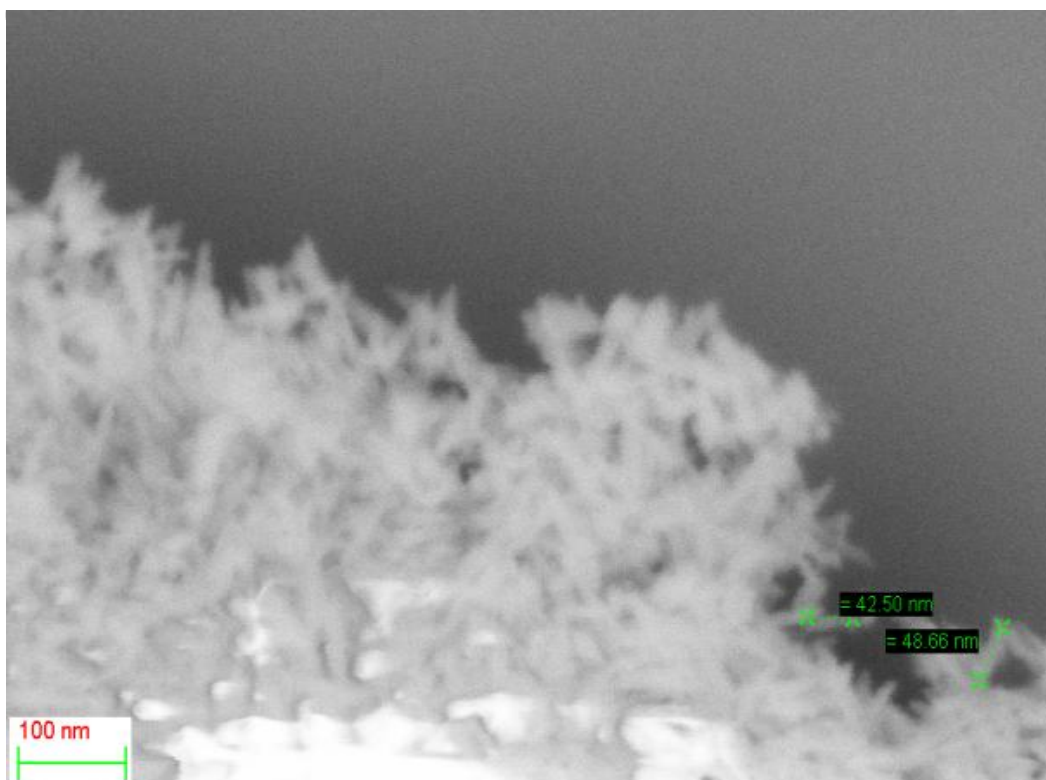
Fig. 56 SEM image of NdVO$_4$ sample.

112
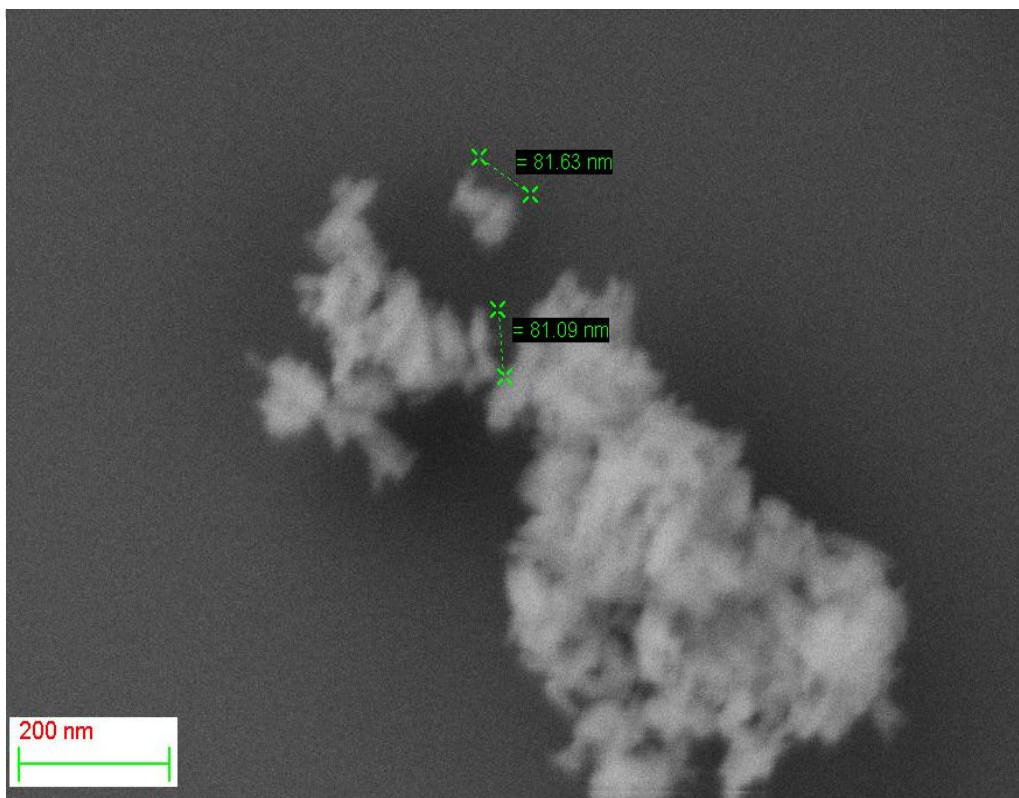
Fig. 57 SEM image of $Bi_{0.1}Nd_{0.9}VO_4$ sample.
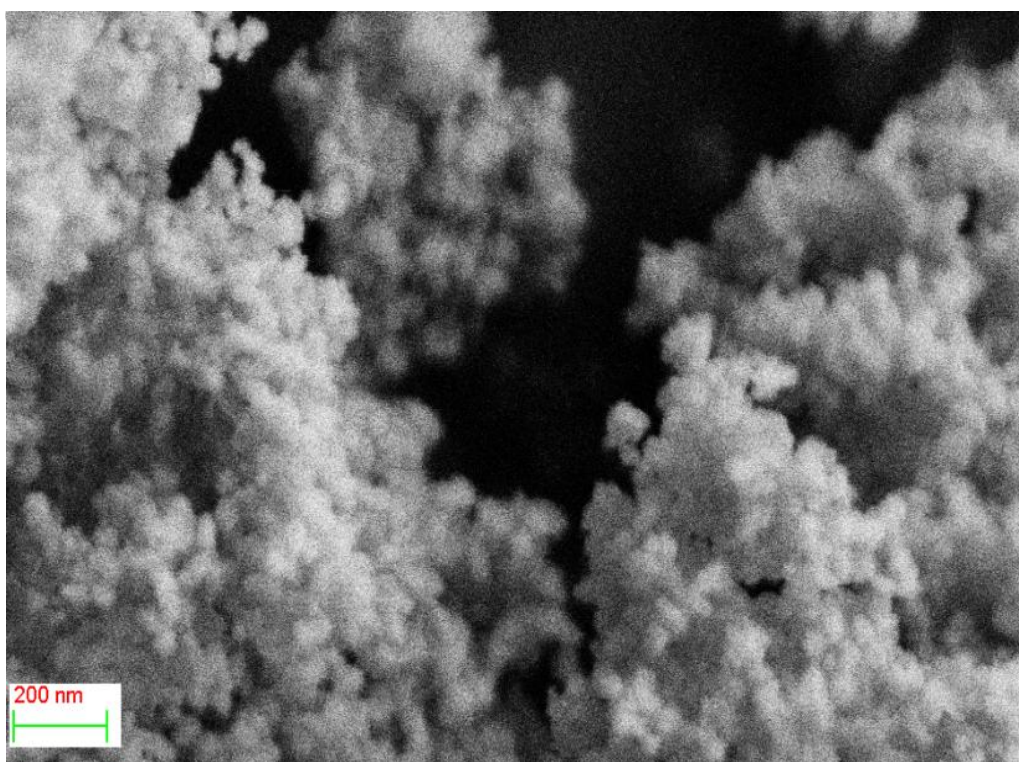
Fig. 58 SEM image of $Bi_{0.2}Nd_{0.8}VO_4$ sample.

113
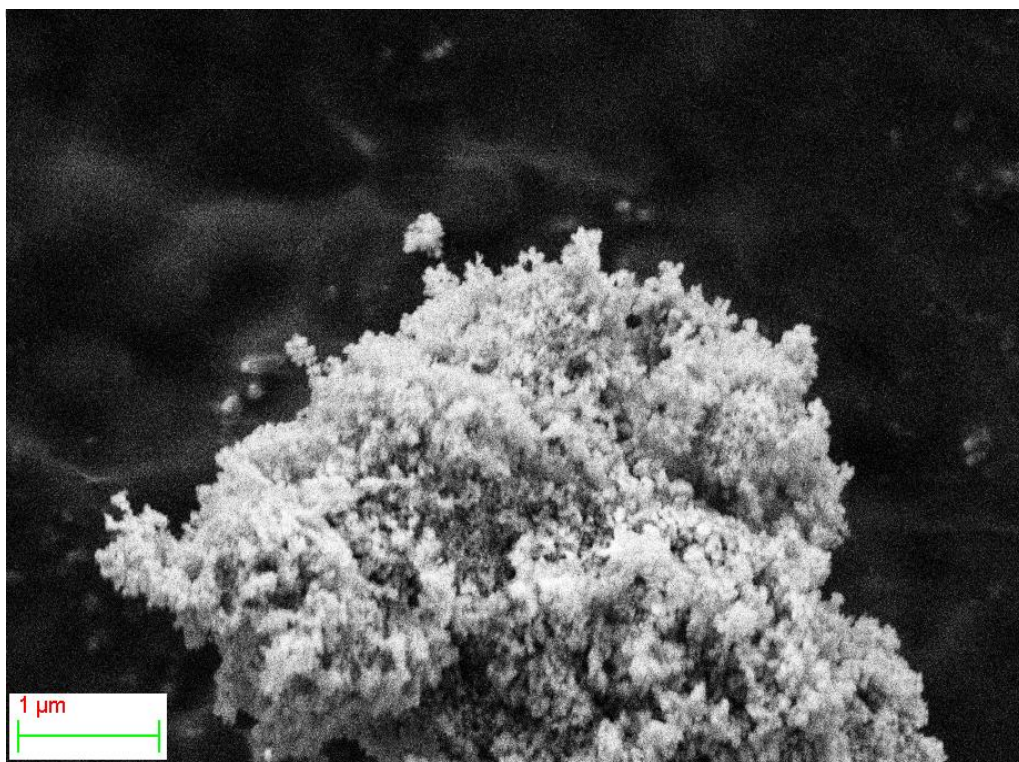
Fig. 59 SEM image of $Bi_{0.3}Nd_{0.7}VO_4$ sample.
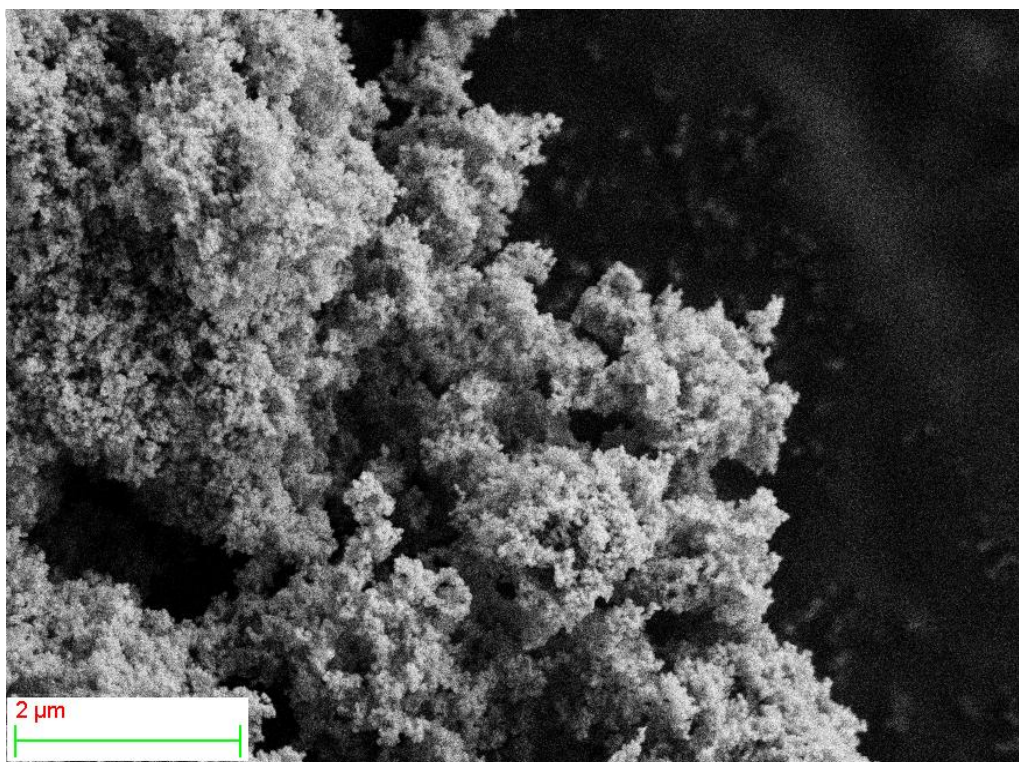
Fig. 60 SEM image of $Bi_{0.48}Nd_{0.52}VO_4$ sample.

3.3.1.3 Raman spectroscopy study

As XRD results suggested, $NdVO_4$ and Bi-doped $NdVO_4$ samples are adopting the zircon structure (space group $I4_1/amd$, $Z = 4$). From group theory considerations [261], it is known that $NdVO_4$ has 12 Raman active modes: $2A_{1g}$, $4B_{1g}$, B_{2g}, and $5E_g$. From these 12 modes, 7 are internal modes associated with internal vibrations in the VO_4 structural unit ($2A_{1g}$, $2B_{1g}$, $1B_{2g}$, $2E_g$) and external vibrations ($3E_g$, $2B_{1g}$) in the Nd sublattice.

The Raman spectra of $NdVO_4$ compound have been measured so far on single crystals and polycrystalline samples by several researchers:

- Jandl et al. [262] at 10 K using the excitation line of 632.8 nm like in our case, on single crystals with an average size $3x2x1$ mm^3 and elongated in the direction of the crystallographic c axis of the tetragonal structure.
- Nguyen et al. [263] on single crystals of $NdVO_4$ ($1 \times 1 \times 6$ mm) at both -268 and 0 °C using the 488 nm excitation line, in a 90° configuration.
- Fidancev et al. [215] measured the room temperature spectrum of polycrystalline $NdVO_4$.
- Santos et al. [261] on a single crystal $NdVO_4$ under 514.5 nm excitation line.

Fig. 61 shows the Raman spectrum of nanosized $NdVO_4$ sample obtained by coprecipitation synthesis, over the range of 150–1200 cm^{-1}. Table 7 presents the comparison of our results with the literature reports.
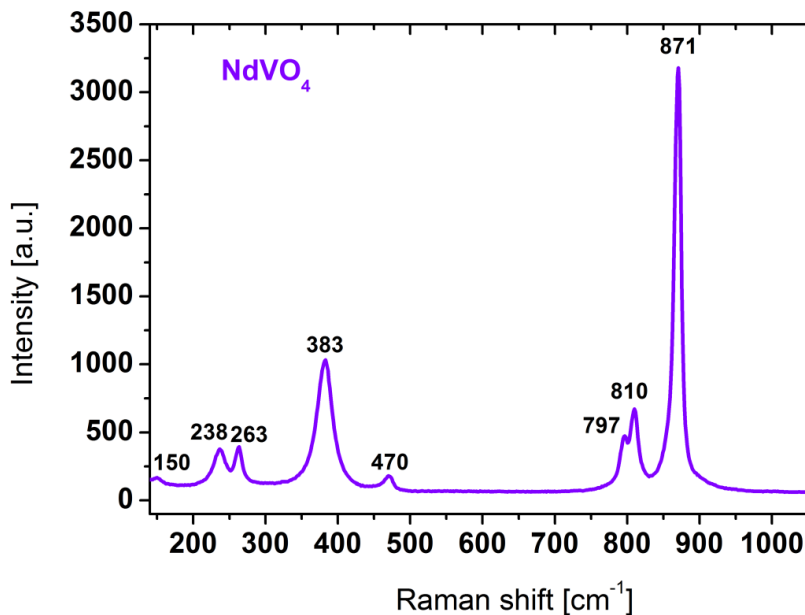
Fig. 61 Raman spectrum of the $NdVO_4$ nanopowder.

Table 7 The comparison of the NdVO$_4$ Raman modes reported in the literature and the ones found in this study for NdVO$_4$ nanoparticles prepared by coprecipitation.

Study	Peak position [cm^{-1}]									Measured:
This study	871	810	797	470	383	-	263	238	150	At room temperature
Santos et al. [261]	871	808	795	472	381	375	260	237	148	At room temperature
Jandl et al. [262]	873	810	797	472	381	-	259	242	151	At 10 K
Nguyen et al. [263]	871	808	795	472	381	375	260	237	148	At 297 K
	873	810	797	473	380	378	259	242	151	At 4.2 K
Antic-Fidancev et al. [215]	868	805	790	471	380	375	262	235	151	At room temperature

From Table 7 it can be seen that our results are in a good agreement with the literature. In the 150–900 cm^{-1} region, our Raman spectrum of NdVO$_4$ shows 8 modes separated in two regions. Firstly, there is a high-energy region between 700 and 900 cm^{-1} and secondly, are the modes below 500 cm^{-1}. The high frequency region includes the internal modes in the VO$_4$ units, while the external modes occur at lower frequency and correspond to translational or rotational motions of the Nd−O in a NdO$_8$ dodecahedron. So, the modes observed, are[7]:

a) 5 internal modes in the VO$_4$ units:

871 cm^{-1}: A$_{1g}$ (ν_1) symmetric stretching mode,

810 cm^{-1}: E$_g$ (ν_3) antisymmetric stretching mode,

797 cm^{-1}: B$_{1g}$ (ν_3) translational stretching mode,

470 cm^{-1}: B$_{1g}$ (ν_4) asymmetric bending mode,

383 cm^{-1}: A$_{1g}$ (ν_2) symmetric bending mode,

b) 3 external modes:

263 cm^{-1}: B$_{1g}$ mode,

238 cm^{-1}: E$_g$ mode,

150 cm^{-1}: E$_g$ mode.

---

[7] The symmetry annotations were made in accordance with the previous results reported in the literature [261,262].

Fig. 62 shows the Raman spectra of the Bi-doped $NdVO_4$ samples in the 150–1000 cm^{-1} range. The use of the Raman spectrometer coupled with a microscope allowed us to obtain spectra within a 1 mm spot focus over different regions of each sample. Spectra recorded on different areas of a specific sample were identical, allowing us to confirm that the samples were homogeneous. The data on Raman frequency shift in the Bi-doped $NdVO_4$ and $NdVO_4$ samples together with the observed Raman lines assignments are summarized in Table 8.
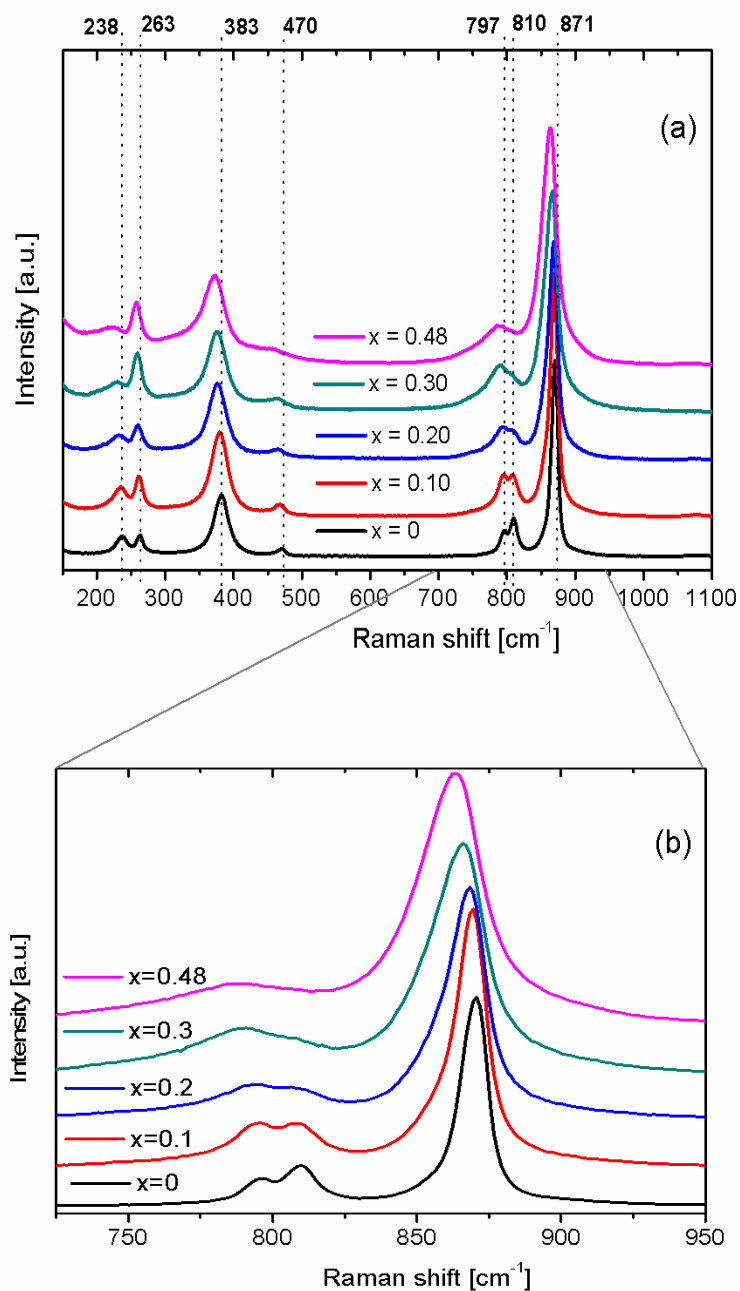
Fig. 62 (a) Raman spectra of the $Bi_xNd_{1-x}VO_4$ ($x = 0, 0.1, 0.2, 0.3,$ and 0.48) nanopowders. (b) 700–950 cm^{-1} zone where the increase in the band widths with the Bi concentration is evident.

117

Table 8 Assignations of the Raman modes observed for the $Bi_xNd_{1-x}VO_4$ ($x = 0, 0.1, 0.2, 0.3,$ and 0.48) nanopowders, measured at room temperature. The 151 cm^{-1} peak assigned for $NdVO_4$ was out of scale and I did not include it here.

Peak [cm^{-1}]					Suggested assignement
$x = 0$ $NdVO_4$	$x = 0.10$	$x = 0.20$	$x = 0.30$	$x = 0.48$	
871	870	868	866	864	A_{1g} (ν_1)
810	808	806	788	785	E_g (ν_3)
797	795	794	788	785	B_{1g} (ν_3)
470	468	466	468	457	B_{1g} (ν_4)
383	379	378	377	372	A_{1g} (ν_2)
263	261	260	259	258	B_{1g}
238	235	233	230	223	E_g

With the Bi doping, a continuous shift of the $NdVO_4$ Raman modes to lower wavenumbers is observed, especially for the strongest peaks positioned at 871 and 383 cm^{-1}. An increase in the full width half maximum (FWHM) values is also clearly visible from Fig. 62 b. Generally, the change of composition in the solid solution will lead to so-called one - or two-mode behaviour for long wavelength optical phonons [264]. In the one-mode behaviour the Raman shift frequency varies continuously and approximately linearly with the dopant concentration, x. In the two-mode behaviour, two sets of optical modes will be present. These modes correspond nearly to those of the two end compositions of the solid solution, and they may persist very close to the end compositions ($x = 0$ and $x = 1$). In our case, the Bi-$NdVO_4$ samples showed the one-mode behaviour with Bi addition - Fig. 62.

Also, studies of Duyckaerts [265] and Liu et al. [266] showed that there is a mass effect on Raman's mode frequency. A heavier dopant will cause the modes to shift to lower frequencies. Therefore, a change of the average cation radius in a Bi-$NdVO_4$ crystal could be the reason of the decrease of the Raman mode frequencies. This phenomenon suggests that indeed Bi was incorporated in the $NdVO_4$ crystal structure, in line with the XRD results.

While Raman band positions are sensitive to the short range order, the widths are more sensitive to the degree of crystallinity, disorder, defects, particle size and aggregation of the particles. In our case, an increase in the band widths with the Bi doping could suggest some modifications in the $NdVO_4$ structure due to Bi incorporation (some bond lengths become increasingly irregular with the Bi concentration). These changes with the Bi incorporation can also be related to the

modification of V−O bonds in the VO_4 tetrahedron. Therefore the local structure of vanadium in the VO_4 tetrahedron by using Raman spectroscopy was also investigated. Hardcastle *et al.* [267] proposed an empirical relationship to connect the symmetric stretching frequency A_{1g} (v_1) to the V−O bond length and the Raman shift, in which the lower frequency of stretching vibrational Raman band corresponds to the longer bond length:

$$v \, [cm^{-1}] = 21349 exp(-1.9176 \cdot R \, [Å] \,) \qquad (47)$$

This relation assumes that if the V−O bond can be modelled as a harmonic oscillator, then the stretching frequency is direct proportional to the square root of the force constant [267].

The strongest peak observed at 871 cm^{-1}, associated with the symmetric stretching vibration of VO_4 tetrahedron in $NdVO_4$, moves to lower frequencies with Bi doping. The moving of the V−O bond stretching frequency from 871 cm^{-1} to lower frequencies with Bi concentration suggests an increase in the V−O bond length in the VO_4 tetrahedron. Using Eq. 47, we calculated the V−O bond length for $NdVO_4$ and Bi-$NdVO_4$. The results are shown in Table 9, while Fig. 63 presents the variation on the V−O bond length with the Bi concentration. As x increases, the V−O stretching frequency decreases, and V−O bond length becomes longer.

Table 9 Calculated V−O bond lengths as a function of the V−O stretching frequencies in $Bi_xNd_{1−x}VO_4$ (x = 0, 0.1, 0.2, 0.3, and 0.48) compounds.

Compound $Bi_xNd_{1−x}VO_4$	Calculated V−O bond length (Å)	Observed frequency $[cm^{-1}]$
$x = 0$ ($NdVO_4$)	1.6683	871
$x = 0.1$	1.6689	870
$x = 0.2$	1.6701	868
$x = 0.3$	1.6713	866
$x = 0.48$	1.6725	864

With increasing the Bi doping concentration, the Raman spectra of Bi-$NdVO_4$ nanoparticles look more close to the Raman spectrum of zircon $BiVO_4$ – see Fig. 64 [268] rather than to the one of the zircon $NdVO_4$ nanoparticles. The 810 cm^{-1} mode present in the $NdVO_4$ spectrum gradually decreases with the Bi concentration, and it

almost vanishes at a doping concentration of 48% Bi. A similar trend can be seen for the 263 and 238 cm^{-1} modes. The 238 cm^{-1} mode of $NdVO_4$ gradually decreases in intensity with Bi concentration, becoming almost undetectable for 48% Bi, while the 263 cm^{-1} [1] mode increases with x. The 470 cm^{-1} mode decreases with the Bi doping. For $x = 0.48$, the lineshape of the Raman spectrum of Bi-$NdVO_4$ sample looks more similar to the spectrum of tetragonal $BiVO_4$ [268] than $NdVO_4$.
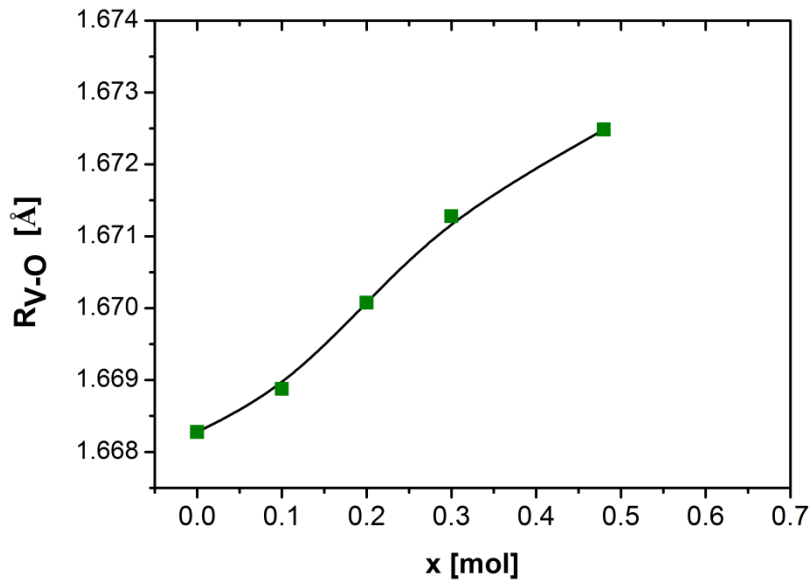
Fig. 63 Variation of the V−O bond length with the Bi content in the $Bi_xNd_{1-x}VO_4$ compounds.
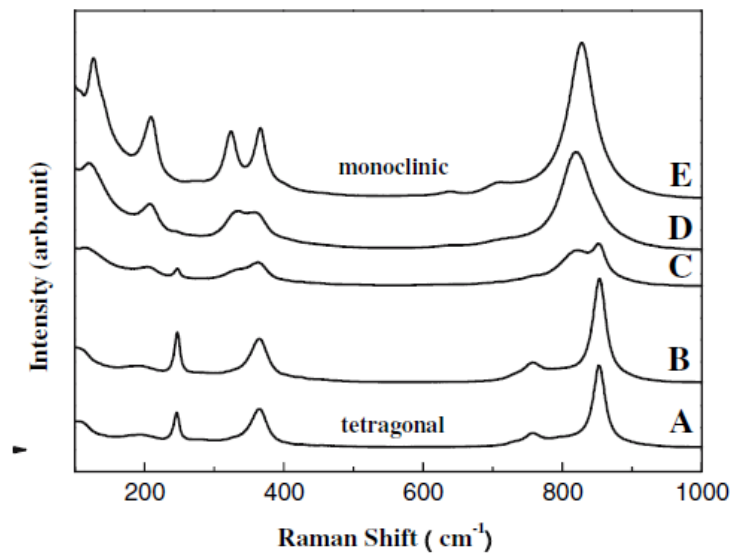
Fig. 64 Raman spectra of $BiVO_4$ sample A (pure tetragonal), B, C, D, and E (pure monoclinic) in the 100–1000 cm^{-1} region. The graph was taken from Zhang et al. [268].

3.3.2 Optoelectronic properties

3.3.2.1 Optical absorption

Fig. 65 shows the UV-Vis diffuse reflectance spectrum of $NdVO_4$ nanopowder. Light absorption of $NdVO_4$ powder, prepared by a coprecipitation method, starts at a wavelength of about 770 nm, continues with an absorption peak centered at about 615 nm and increases sharply at about 357 nm (3.48 eV) reaching a maximum at about 280 nm (originating from $O^{2-}-V^{5+}$ charge transfer within the VO_4^{3-} group) [235,236]. The sharp increase at about 357 nm corresponds to the band gap transition in $NdVO_4$.
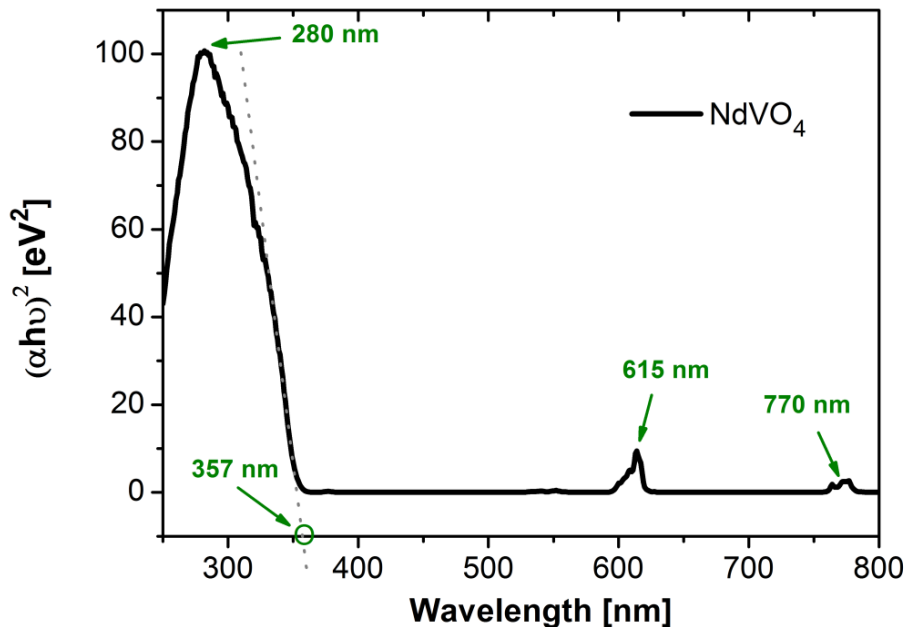
Fig. 65 The UV-Vis diffuse reflectance spectrum of $NdVO_4$ nanopowder.

Fig. 66 shows the UV-Vis diffuse reflectance spectra of $Bi_xNd_{1-x}VO_4$ ($x = 0$, 0.1, 0.2, 0.3, and 0.48) samples. Besides the main absorption peak, located at 280 nm, the $Bi_xNd_{1-x}VO_4$ samples exhibit an additional peak at around 360 nm. In comparison with $NdVO_4$, the main absorption edge of Bi-$NdVO_4$ samples is positioned at higher wavelengths and is red shifted with the Bi concentration. The magnitude of the shift is larger for lower concentrations and gets smaller with further increase in the concentration. It is about 20 nm for $x = 0.1$ and 50 nm for the whole solid solubility range to $x = 0.48$. The main absorption edge of $Bi_{0.48}Nd_{0.52}VO_4$ is located at 410 nm (3.03 eV), that is already in the visible region of the electromagnetic spectrum.

These results are similar to results obtained for samples prepared by solid-state reactions, where the main absorption edge of Bi-NdVO$_4$ powders is also red-shifted with the Bi concentration, so that for $x = 0.48$, the absorption edge is located in the visible region. The red shift of the absorption edge with the Bi concentration can be explained with an extra absorption involving the Bi^{3+} ions and the host lattice. In NdVO$_4$, the main absorption edge is due to the electron transition from the O $2p$ on the top of the VB to the V $3d$ empty levels situated at the bottom of the CB. In Bi-NdVO$_4$, the red shift of the absorption edge can be assigned to the charge transfer from the Bi $6s$ – O $2p$ antibonding state [21] situated at the top of the Bi-NdVO$_4$ VB to the V $3d$ (with some contribution of Bi $6p$) at the bottom of the CB - Fig. 67.
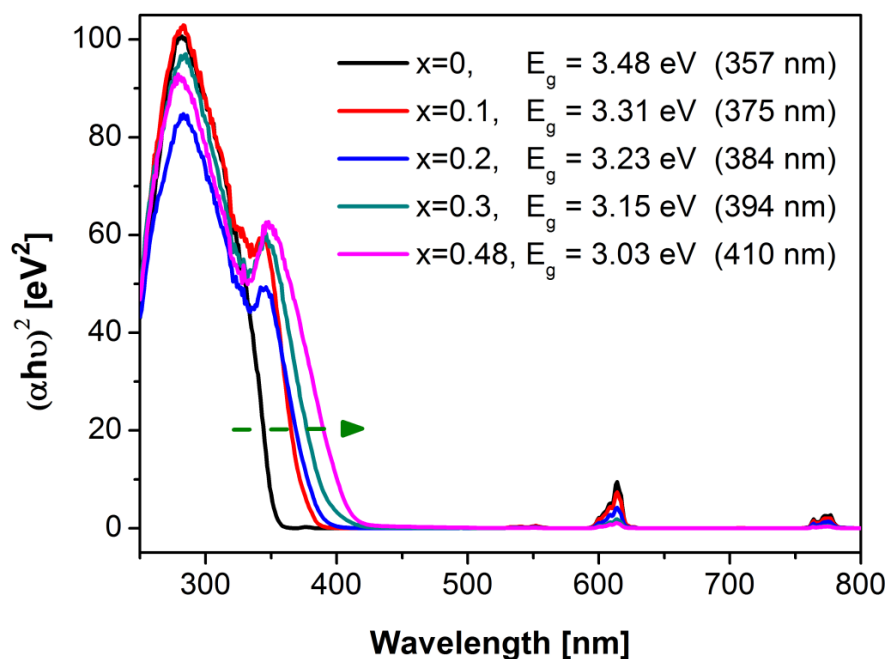
Fig. 66 The UV-Vis diffuse reflectance spectra of Bi$_x$Nd$_{1-x}$VO$_4$ ($x = 0$, 0.1, 0.2, 0.3, and 0.48) nanopowders.
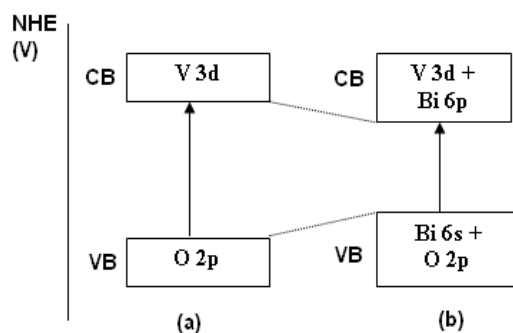
Fig. 67 Schematic energy band diagram for (a) NdVO$_4$ and (b) Bi-NdVO$_4$

The additional absorption peaks observed in the UV-Vis spectrum of $NdVO_4$ at about 615 and 770 nm have also been described in the literature - as it can be seen in Table 10. These peaks are also present in the $Bi_xNd_{1-x}VO_4$ spectra ($x \geq 0.1$) but their intensity decreases with Bi concentration. The peak at about 520-530 nm is usually a weak peak rarely observed in the $NdVO_4$ absorption spectra.

Table 10 Peaks in the experimental UV-Vis absorption spectrum of $NdVO_4$ observed in the region 500–800 nm.

Peak position [nm]			Synthesis method and particle size	Study	Comments/ Assignement
(1)	(2)	(3)			
-	615	775	Co-precipitation, acicular particles of .~50 nm length and 10 nm diameter	This study	From $^4I_{9/2}$ to: (1) / , (2) $^4G_{5/2}$ and (3) $^4F_{7/2}$
-	590	750	Solid-state reactions, ~1µm.	Chapter 2 of this thesis	(1) / , (2) $^4I_{9/2}$ to $^4G_{5/2}$, (3) $^4I_{9/2}$ to $^4F_{7/2}$
532	582	744	A sol-gel in a AAO template Nanotubes with the diameter of about 40 nm	Peng et al. [218]	(1) $^4G_{7/2}$ and $^4G_{9/2}$ (2) $^4G_{7/2}$, (3) $^4F_{7/2}$ and $^4S_{3/2}$
538	590	752	Nanowires, 100 nm diameter and 3µm length	Xu et al. [269]	From $^4I_{9/2}$ to: (1) $^2G_{7/2}$, (2) $^4G_{5/2}$, (3) $^4F_{7/2}$
~525 (very low int.)	593	753	Hydrothermal, nanorods, rectangular cross section: 30 × 30 nm^2 to 100 × 200 nm^2, length: 400–700 nm.	Wu et al. [246]	(1) / , (2) $^4I_{9/2}$ to $^4G_{5/2}$, (3) $^4F_{7/2}$

3.3.2.2 PL and lifetime

Fig. 68 shows the emission bands (excited at λ_{exc} =371 nm) of $Bi_xNd_{1-x}VO_4$ (x = 0, 0.1, 0.2, 0.3, and 0.48) samples. Under the UV excitation, $NdVO_4$ nanoparticles shows green, yellow, and orange emissions. The $NdVO_4$ spectrum consists of a broad peak centred at about 500 nm with three small shoulders, at about 523, 545, and 600 nm. The photoluminescence spectra of nanosized $NdVO_4$ particles (excited with UV light) have already been reported in the literature. Wu et al. [246] reported the PL emission spectra of single crystalline nanorods (of ~200 nm in diameter and 400–700 nm in length) λ_{exc} = 310 nm. Their spectrum shows a strong emission around 490 nm followed by two less intense peaks at ~525 and 550 nm, and a triplet at 600–615 nm. The $NdVO_4$ nanoparticles prepared in this thesis by a co-precipitation method show

similar peak positions. Similar results were also obtained for the 1 μm NdVO$_4$ particles prepared by a solid-state method and described in Chapter 2, section 2.3.1.3.2. Briefly, the emission at about 500 nm can be assigned to the $^4G_{11/2} \rightarrow {}^4I_{11/2}$ transition, the shoulders, at about 525, 545, and 600 nm to the $^4G_{7/2} \rightarrow {}^4I_{9/2}$, $^4G_{7/2} \rightarrow {}^4I_{9/2}$, and $^4G_{5/2} \rightarrow {}^4I_{9/2}$ transitions, respectively.
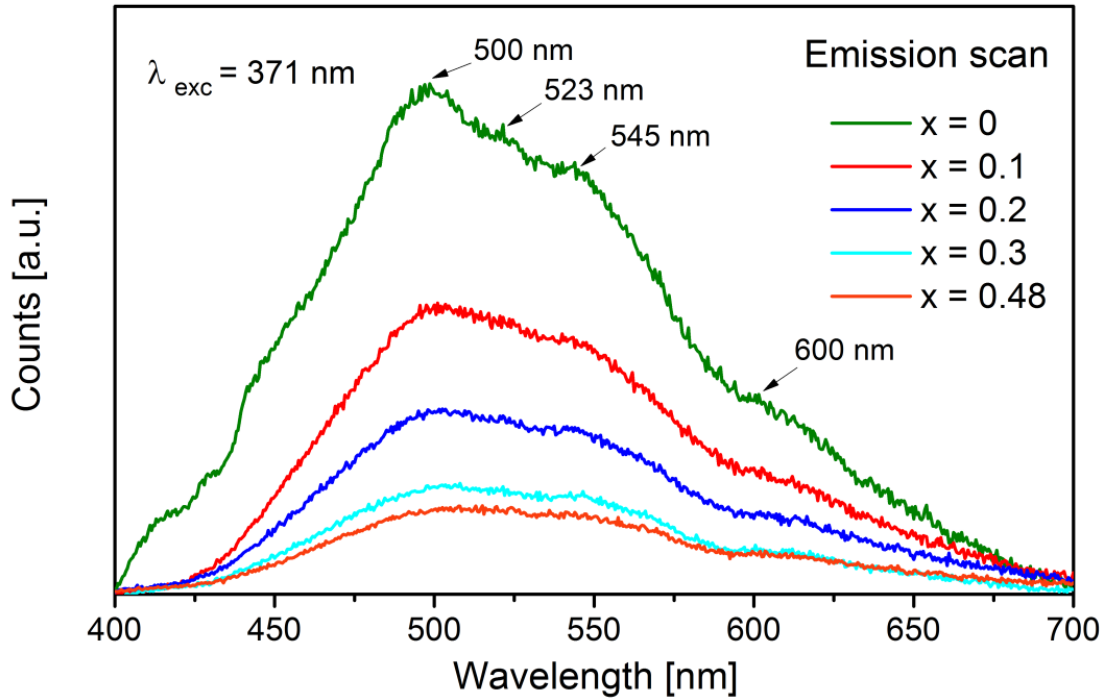
Fig. 68 The emission spectra of Bi$_x$Nd$_{1-x}$VO$_4$ samples, with λ_{exc} = 371 nm.

Fig. 69 presents the room temperature excitation spectra of Bi$_x$Nd$_{1-x}$VO$_4$ (x = 0, 0.1, 0.2, 0.3, and 0.48) nanopowders.

The room temperature excitation spectrum of NdVO$_4$, monitored for the 524 nm emission peak, consists of a prominent peak centred at 371 nm. For the Bi$_x$Nd$_{1-x}$VO$_4$ powders ($x \geq 0.1$), this peak becomes less intense and broader with Bi concentration. The most significant change is noticed for x = 0.1, but it become insignificant for $x \geq$ 0.3. For $x \geq 0.1$, the peak position is also slightly shifted to a lower energy compared to the NdVO$_4$ samples (from 371 to 372 nm). Fig. 70 shows the carrier dynamics of all the Bi$_x$Nd$_{1-x}$VO$_4$ powders. It can be seen that the effect of the composition on the lifetime of the Bi$_x$Nd$_{1-x}$VO$_4$ powders is negligible.
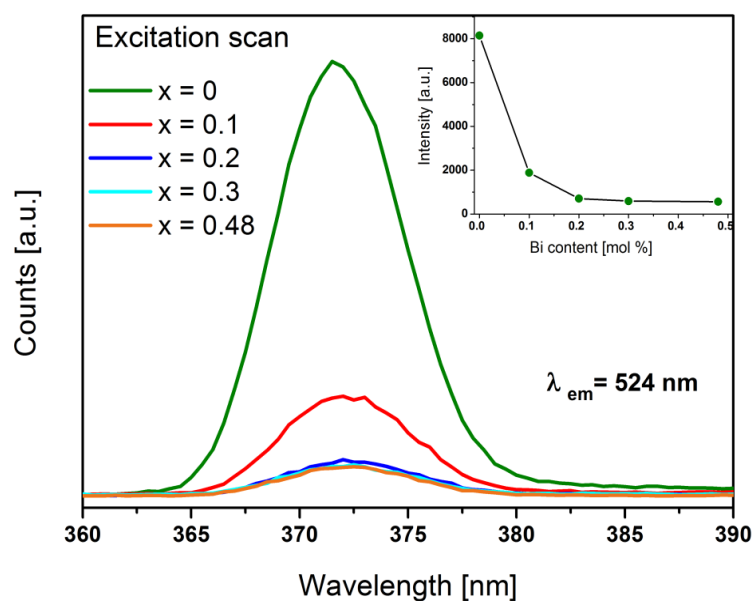
Fig. 69 The excitation curves of $Bi_xNd_{1-x}VO_4$ ($x = 0$, 0.1, 0.2, 0.3, and 0.48) samples monitored at 500 nm and collected in the range of 350–450 nm. The inset shows the variation of the excitation band with the Bi content.
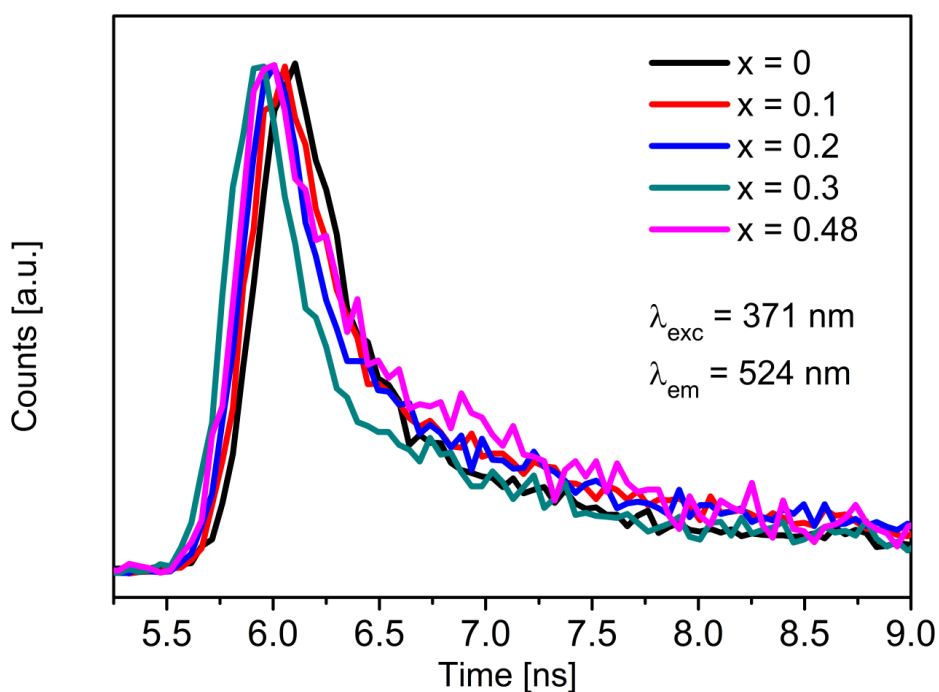
Fig. 70 Time-domain intensity decays of $Bi_xNd_{1-x}VO_4$ powders.

Figs. 71–75 present the time-resolved photoluminescence spectra of $Bi_xNd_{1-x}VO_4$ powders excited by a 371 nm laser wavelength and monitored at 524 nm. The decay process of $NdVO_4$ sample is shown in Fig. 71. This decay curve could only be

125

simulated by a third-order exponential function with the three lifetimes: $\tau_1 = 0.16$ ns, $\tau_2 = 1.70$ ns, and $\tau_3 = 4.74$ ns. Compared to the $NdVO_4$ obtained by solid state method, this sample exhibits a shorter lifetime for the green emission.
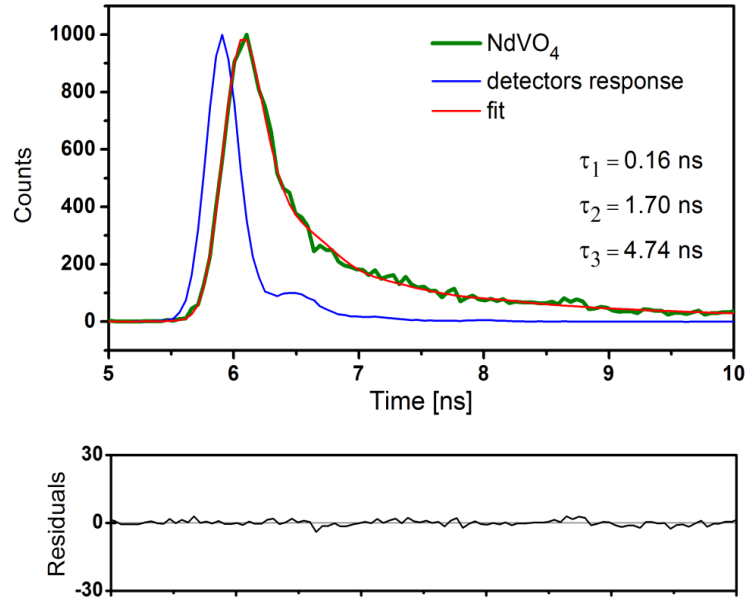
Fig. 71 The green line shows the time-domain intensity decay of $NdVO_4$ nanopowder. $\lambda_{em} = 524$ nm. The red line is the fitting curve and the blue line is the response of the detector. The residuals represent the difference between the fitted curve (red line) and the measured data. The goodness of the fit, χ^2, is 1.418.
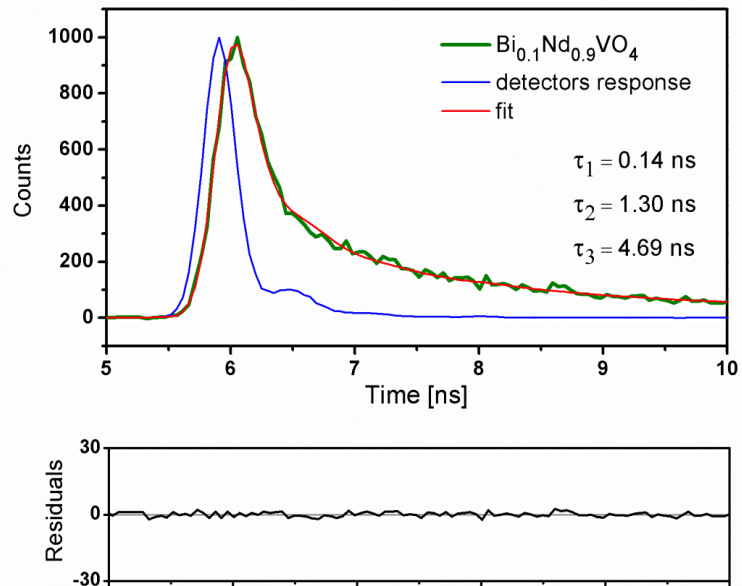
Fig. 72 The green line shows the time-domain intensity decay of $Bi_{0.1}Nd_{0.9}VO_4$ nanopowder. $\lambda_{em} = 524$ nm. The red line is the fitting curve and the blue line is the response of the detector. The residuals represent the difference between the fitted curve (red line) and the measured data. The goodness of the fit, χ^2, is 1.652.
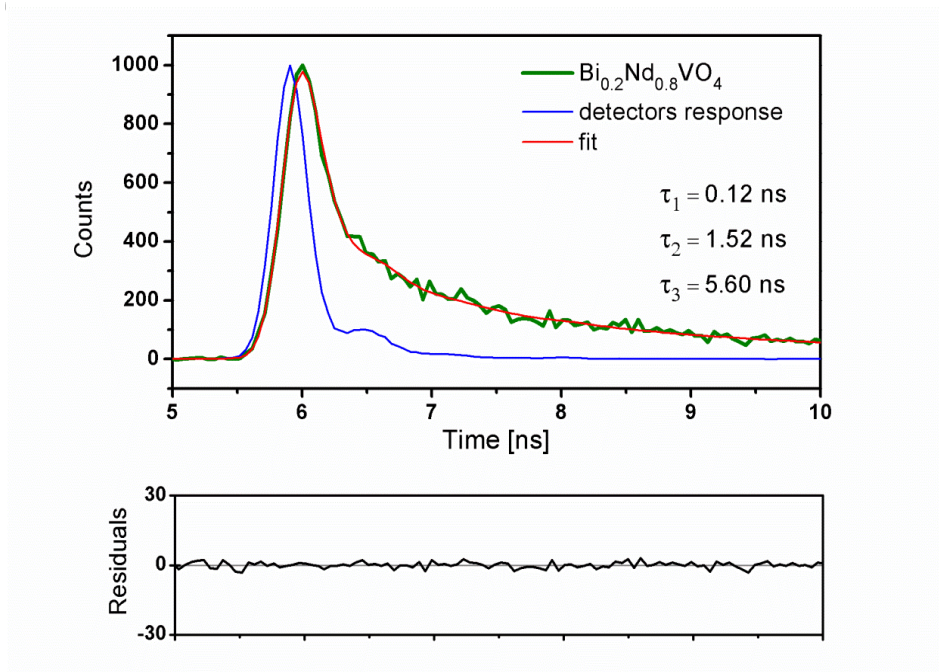
Fig. 73 The green line shows the time-domain intensity decay of $Bi_{0.2}Nd_{0.8}VO_4$ nanopowder. λ_{em} =524 nm. The red line is the fitting curve and the blue line is the response of the detector. The residuals represent the difference between the fitted curve (red line) and the measured data. The goodness of the fit, χ^2, is 2.465.
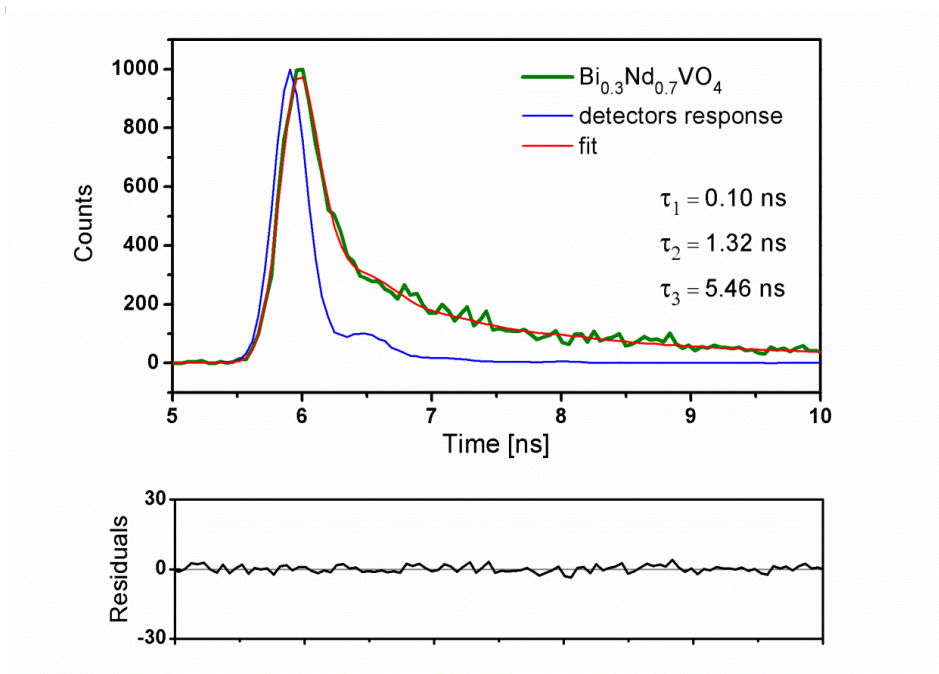
Fig. 74 The green line shows the time-domain intensity decay of $Bi_{0.3}Nd_{0.7}VO_4$ nanopowder. λ_{em} =524 nm. The red line is the fitting curve and the blue line is the response of the detector. The residuals represent the difference between the fitted curve (red line) and the measured data. The goodness of the fit, χ^2, is 2.524.

127
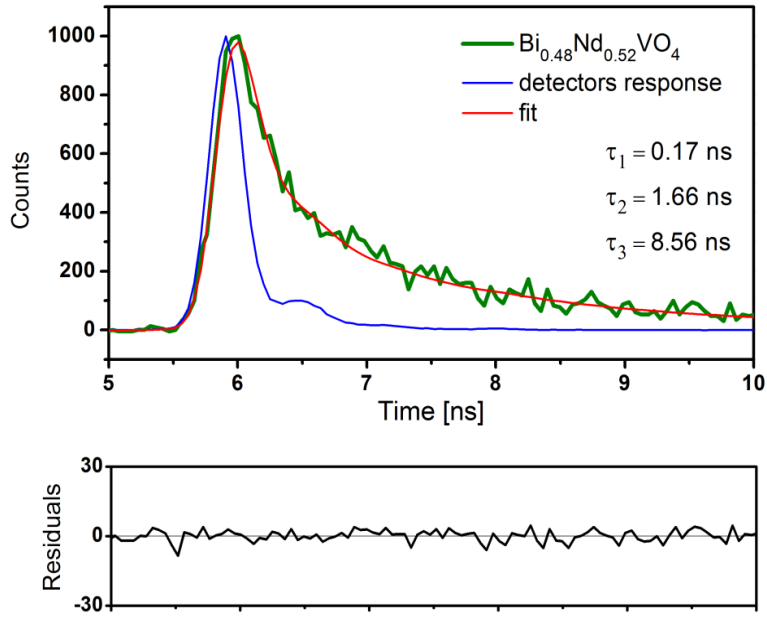
Fig. 75 The green line shows the time-domain intensity decay of $Bi_{0.48}Nd_{0.52}VO_4$ nanopowder. $\lambda_{em} = 524$ nm. The red line is the fitting curve and the blue line is the response of the detector. The residuals represent the difference between the fitted curve (red line) and the measured data. The goodness of the fit, χ^2, is 6.505.

Table 11 Fitting parameters of the photoluminescence decay curves of the nanopowders with $Bi_xNd_{1-x}VO_4$ composition. ($\lambda_{ex} = 371$ nm, $\lambda_{em} = 524$ nm).

Sample	Lifetime [ns]	Standard deviation [ns]	χ^2	B1	B2	B3
$NdVO_4$	$\tau_1 = 0.16$ (50.61%) $\tau_2 = 1.70$ (30.64%) $\tau_3 = 4.74$ (18.75%)	0.01 0.15 0.59	1.418	0.35	0.03	0.00
$Bi_{0.1}Nd_{0.9}VO_4$	$\tau_1 = 0.14$ (33.23%) $\tau_2 = 1.30$ (26.99%) $\tau_3 = 4.69$ (39.78%)	0.01 0.13 0.27	1.652	0.36	0.03	0.01
$Bi_{0.2}Nd_{0.8}VO_4$	$\tau_1 = 0.12$ (31.42%) $\tau_2 = 1.52$ (33.92%) $\tau_3 = 5.60$ (34.66%)	0.01 0.11 0.34	2.465	0.40	0.03	0.01
$Bi_{0.3}Nd_{0.7}VO_4$	$\tau_1 = 0.10$ (38.53%) $\tau_2 = 1.32$ (31.89%) $\tau_3 = 5.46$ (29.58%)	0.01 0.10 0.45	2.524	0.46	0.03	0.01
$Bi_{0.48}Nd_{0.52}VO_4$	$\tau_1 = 0.17$ (35.06%) $\tau_2 = 1.66$ (54.33%) $\tau_3 = 8.56$ (10.61%)	0.00 0.06 1.50	6.505	0.50	0.01	0.01

As it can be seen from Table 11, no significant influence of the Bi doping on the lifetime is observed, except for the sample with $x = 0.48$ which exhibits a slightly longer lifetime: 8.56 ns. Nevertheless, these lifetime values are still shorter than for the bulk samples, which is not favourable for the photocatalytic reactions.

3.4 Conclusions

The main conclusions of this study are:

- Bi-NdVO$_4$ nanocrystals have been obtained for the first time by aqueous coprecipitation reaction under ambient temperature and pressure, without further thermal treatment. This is a facile route that also saves energy.

- XRD analysis showed the successful incorporation of Bi in the structure of NdVO$_4$ nanoparticles, i.e., no secondary phases were detected.

- The morphology of the Bi-NdVO$_4$ nanoparticles was observed by SEM. The NdVO$_4$ particles prepared by the coprecipitation method have acicular shape, with the length of about 50 nm and the diameter of ~10 nm and form agglomerates. The morphologies of the Bi-doped NdVO$_4$ nanoparticles become more irregular as the Bi concentration increases. For the Bi$_{0.1}$Nd$_{0.9}$VO$_4$ sample, aggregates composed of irregular smaller crystallites with an average length of 80 nm are observed. By increasing the Bi content to $x \geq 0.48$, the particles become more spherical and agglomerate even more.

- The Bi-NdVO$_4$ nanoparticles exhibited 7 Raman active modes in the range 200−1000 cm^{-1}.

- The results of Raman spectroscopy have further proved that the Bi-NdVO$_4$ nanoparticles are chemically homogeneous. With the Bi doping, a continuous shift of the NdVO$_4$ Raman modes to lower wavenumbers is observed, especially for the strongest peaks (positioned at 871 and 383 cm^{-1}). An increase in the full width half maximum (FWHM) values is also clearly visible. As the Bi concentration increases, the V−O stretching frequency decreases, and V−O bond length becomes longer.

- The DRS studies showed that in comparison with NdVO$_4$, the main absorption edges of Bi-NdVO$_4$ samples are positioned at higher wavelengths. For the Bi$_{0.48}$Nd$_{0.52}$VO$_4$ sample, the absorption edge is located at 410 nm (3.03 eV), which is well in the visible region of the electromagnetic spectrum.

- The $NdVO_4$ nanoparticles absorb near UV light and emit green, yellow, and orange colours, as the PL study revealed. This composition also shows the highest PL intensity of all compositions.

- Doping with Bi does not influence the lifetime of the excitons for the green emission of $NdVO_4$, except for the sample with the composition $Bi_{0.48}Nd_{0.52}VO_4$ which showed the slowest decay rate.

- Since the intensity of PL is a measure of the recombination of the electro-hole pairs, the lower PL intensity of the $Bi-NdVO_4$ nanoparticles might imply better photocatalytic properties than that of $NdVO_4$. The lower PL intensity suggests a lower recombination rate and this could lead to higher photcoatalytic efficiency for the $Bi-NdVO_4$ nanoparticles.

4 Photocatalytic activity of Bi-doped NdVO₄ nanoparticles for dye degradation

4.1 Motivation of the study

One of today's environmental problems is the large amount of organic dyes discharged into wastewaters from the textile or other industrial processes such as pharmaceuticals, cosmetics, paper manufacturing, etc. The demand for the dyes has increased even more in the last years. The organic dyes used in the textile industry nowadays have high chemical and photolytic stability and the conventional textile effluent treatment does not efficiently degrade them. Their degradation is a necessity because these dyes or their intermediates are potential carcinogenic and/or mutagenic for water and soil microorganisms [270,271]. They can also induce allergies, skin, lung, brain or respiratory diseases to human body [272,273]. It is estimated that over 7×10^5 tons of about 10,000 different dyes and pigments are produced annually worldwide and about 10−15% of the dye is lost during the dyeing [273,274,275,276].

From structural point of view, the organic dyes contain two key components: chromophores and auxochromes. The chromophores are light absorbing groups in the molecule and represent delocalized electron systems with conjugated double bonds. According to IUPAC nomenclature [277], a chromophore is 'the part (atom or group of atoms) of a molecular entity in which the electronic transition responsible for a given spectral band is approximately localized'. The molecule can absorb certain wavelengths from the visible spectrum (and appears coloured) only if the energy difference between two molecular orbitals is in the visible range. Examples of chromophores are: –C=C, –N=N–, –NO₂, quinoid rings, etc. The auxochromes are functional groups of atoms attached to a chromophoric group. According to IUPAC nomenclature [277], an auxochrome is 'an atom or group which, when added to or introduced into a chromophore, causes a bathochromic shift and/or a hyperchromic effect in a given band of the chromophore, usually in that of lowest frequency'. So the auxochromes are essential constituents of dyes; they do not produce the colour by themselves, but they have the role to modify the ability of the chromophore to absorb light. If they are in a direct conjugation with the π-system of the chromophore, they may intensify the colour, but if situated in a meta position, they do not have any

influence on the colour. Some examples of the auxochrome groups are: hydroxyl group –OH, amino group –NH$_2$, aldehyde group –CHO, sulfonate group –SO$_3$H, etc.

Dyes can be classified by the chemical structure or the method, by which they are applied to the substrate. The Colour Index (CI) [278] classifies the dyes according to their application. There are:

- *Acidic dyes* (water soluble anionic dyes): sodium salts of phenols and carboxylic dyes that ionize in solution to produce negatively charged ions. They find application in dyeing fabrics like wool, silk, modified acrylic or nylon. The adsorption to the fibers occurs through the attachment of the anionic groups of the dye to the cationic groups in the fiber. The acidic dyes are: antraquinone, azo, azine, xanthenes, nitro compounds. Examples: Eosin and Aniline Blue.

- *Basic dyes*: water soluble cationic compounds used to dye acid-group containing fibers such as nylon, modified polyesters, polyacrylonitrile, and sometimes for wood or silk, but also to colour the paper. Azo, diarylmethane, triarylmethane, anthraquinone compounds are examples of the basic dyes (e.g. Malachite Green, Aniline Yellow).

- *Direct dyes:* form the second largest dye class with high affinity for cellulose fibres. They are water soluble anionic dyes used to dye cotton, paper, wool, nylon, leather. Most of these dyes are azo compounds. Examples: Congo Red, Martius Yellow.

- *Vat dyes*: water insoluble dyes used in an alkaline media in order to bind to the fiber. Indigo is an example of the vat dye.

- *Mordant dyes*: dyes that require a mordant to fix to the fibres. The mordant act as a binder between the dye and the fibres. They are used for dyeing wool, silk, paper and cellulose fibres. Compounds such as azo, oxazine or triarylmethane are mordant dyes. Example: Alizarin (Turkey Red).

- *Dispersive dyes*: insoluble in water and are used to colour synthetic fibres such as polyester, polyamide, acryl, etc. They are the third largest group of dyes in the CI (colour index). They are azo or metal complex azo compounds, and antraquinones compounds. Examples: Disperse Yellow 3, Disperse Blue 39, Disperse Violet 4.

- *Reactive dyes*: dyes with reactive groups that form a covalent bond between a carbon atom of the dye and the –OH, –NH, or –SH groups in fibres such as

cotton, silk, nylon. They are among the most permanent dyes and can be applied at room temperature. Examples: Reactive Red 1, Reactive Blue 19.

- *Azoic dyes*: insoluble dyes applied to the fibre by reaction of a diazoic salt and a coupling component. They are used to colour cotton, cellulose, polyester, etc. The colour is controlled by the choice of the diazoic and coupling components. Due to the toxicity of the chemicals this dyeing procedure is losing importance. Examples of azoic coupling components are: Naphthol AS, Naphthol AS-G [279]. Diazo components are: Fast Red B base, Fast Scarlet G base, Fast Garnet GBS base, etc.

- *Sulfur dyes*: dyes which have heterocyclic S-containing groups and are mainly used for cotton. They give the dark black colour. One example of the sulphur dyes is the Sulfur Black 1 - the largest selling dye by volume.

By the nature of the chromophore, the dyes can be classified in different groups [280]: antraquinone dyes (Alizarin RedS, Vat Orange 15), acridine dyes (Basic orange 15), arylmethane dyes (Basic Green 4), azo dyes (Mordant Yellow 1), diazonium dyes (Fast Blue B, Azoic Diazo 5), nitro dyes (Acid yellow 1, Acid black 1), phtalocyanine dyes (Alcian blue 8GX), quinone (Azocarmine B), thiazole (Basic Yellow 1, Primuline), xanthene dyes (Rhodamine B, Solvent Green 4) and others.

The unfixed dyes after the dyeing process cannot be recovered and reused because it has lost the bonding. Mainly they are released in nature. These dyes are recalcitrant to the nature and their removal from the wastewaters is a big challenge as the conventional treatments are not efficient (economically or ecofriendly) [281]. Therefore, new methods must be developed and applied to treat/degrade these organic pollutants. Conventional methods to eliminate these compounds from the wastewaters are [275,282]:

a) separation processes such as sedimentation, centrifugation, filtration, activated carbon adsorption, etc.;

b) partial or complete mineralization using biological or chemical processes [283,284].

An alternative to these conventional methods are the advanced oxidation processes AOPs. AOPs are applied for the chemical treatment of the contaminated ground water, industrial waste water, but also to purify the air [285,286,287] – see Chapter 1, section 1.3.2 for more details. Based on the use of a photocatalyst and UV or Visible light radiation, heterogeneous photocatalysis has been successfully employed to

eliminate various organic pollutants including some of the dyes. Compounds such as TiO_2, ZnO, $BiVO_4$, or Bi_2WO_6, etc, were able to photochemicaly oxidate the dyes to low weight organic molecules, or even to CO_2 and H_2O.

With the aim to examine the photoactivity of the Bi-$NdVO_4$ nanopowders, Rhodamine B (RhB) was employed in this study as the model of a persistent organic pollutant of the wastewaters. RhB (also named Basic Violet 10, C.I. 45170) is an important representative of xanthene dyes with $C_{28}H_{31}ClN_2O_3$ molecular formula and four N-ethyl groups at the either sides of the xanthenes ring (see Fig. 76). It is a fluorescent dye, widely used to dye paper, textiles, in cosmetics, as a staining fluorescent dye and in other biotechnology applications such as fluorescence microscopy, fluorescence correlation spectroscopy, etc. [288,289,290].
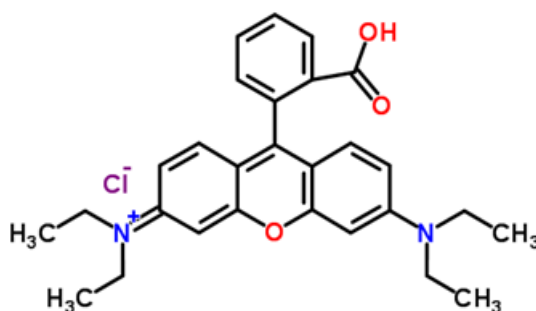
Fig. 76 The chemical structure of RhB.

The review of the European Food Safety Authority [291] classifies Rhodamine B as 'potentially genotoxic and carcinogenic'. So far, many studies focused on the photocatalytic degradation of RhB with TiO_2 [292,293], $BiVO_4$ [294], ZnO [295,296], Bi_2WO_6, [297,298], Pr-NO_3-TiO_2 [299], $LiNbO_3$ [300] or other materials using UV or Visible light irradiation.

4.2 Electrochemical properties of Bi-doped $NdVO_4$ nanoparticles

The redox ability of Bi-doped $NdVO_4$ nanoparticles is assessed by determining the energy positions of its valence and conduction bands. The VB and CB positions are important parameters in determination of the electrochemical properties of a photocatalyst. Generally, the more positive the potentials of the VB maximum are, the stronger the oxidation capacity of the holes; and the more negative the potentials

of the CB minimum, the stronger the reduction ability of the electrons. Based on the results of the diffuse reflectance from Chapter 3, section 3.3.2.1. of this thesis, the band gap values of $Bi_xNd_{1-x}VO_4$ nanoparticles are:

3.03 eV (409 nm) for $x = 0.48$ ($Bi_{48}Nd_{0.52}VO_4$)

3.15 eV (393 nm) for $x = 0.3$ ($Bi_{0.3}Nd_{0.7}VO_4$)

3.23 eV (383 nm) for $x = 0.2$ ($Bi_2Nd_{0.8}VO_4$)

3.31 eV (375 nm) for $x = 0.1$ ($Bi_{0.3}Nd_{0.7}VO_4$)

3.48 eV (356 nm) for $x = 0$ ($NdVO_4$)

Using Mulliken electronegativities (see details in Chapter 2, section 2.3.2.3.1), the band edge positions of $NdVO_4$ nanoparticles were calculated and the results are presented below:

$$E_{CB} = X - E^e - 0.5 \cdot E_g$$

where X = the absolute electronegativity of $NdVO_4$, E^e is the energy of free electrons on the hydrogen scale (ca. 4.5 eV).

$$X_{NdVO_4} = (\chi_{Nd}\, \chi_V \cdot \chi_O^4)^{1/6}$$

Where χ_{Nd}, χ_V, and χ_O are the absolute electronegativities of the Nd, V, and O atoms [301].

$$\chi_{Nd} = \frac{(Ei + Ea)}{2} = \frac{(0.515 + 5.525)}{2} = 3.0215 \text{ eV}$$

$$\chi_V = \frac{(Ei + Ea)}{2} = \frac{(0.526 + 6.74615)}{2} = 3.6361 \text{ eV}$$

$$\chi_O = \frac{(Ei + Ea)}{2} = \frac{(1.4611 + 13.618)}{2} = 7.5395 \text{ eV}$$

$$X_{NdVO_4} = (\chi_{Nd} \cdot \chi_V \cdot \chi_O^4)^{1/6} = (3.0215 \cdot 3.63605 \cdot 7.53957^4)^{1/6} = 5.7328 \text{ eV}$$

$$E_{CB} = X - E^e - 0.5 \cdot E_g = 5.7328 - 4.5 - 0.5 \cdot 3.48 = -0.51 \text{ V}$$

$$E_{VB} = E_g + E_{CB} = 3.48 - 0.507 = 2.97 \text{ V}$$

Using same procedure, the E_{CB} and E_{VB} of Bi-NdVO$_4$ were also calculated. A schematic representation of their positions is shown in Fig. 77. The VB maximum potential of Bi-NdVO$_4$ (at pZC) are at a more positive than O$_2$/H$_2$O (1.23 V), H$_2$O$_2$/H$_2$O (1.77 V) and O$_3$/H$_2$O (2.07 V) - Fig. 77. Therefore, Bi-NdVO$_4$ could oxidize H$_2$O to produce O$_2$ and decompose many organic pollutants.
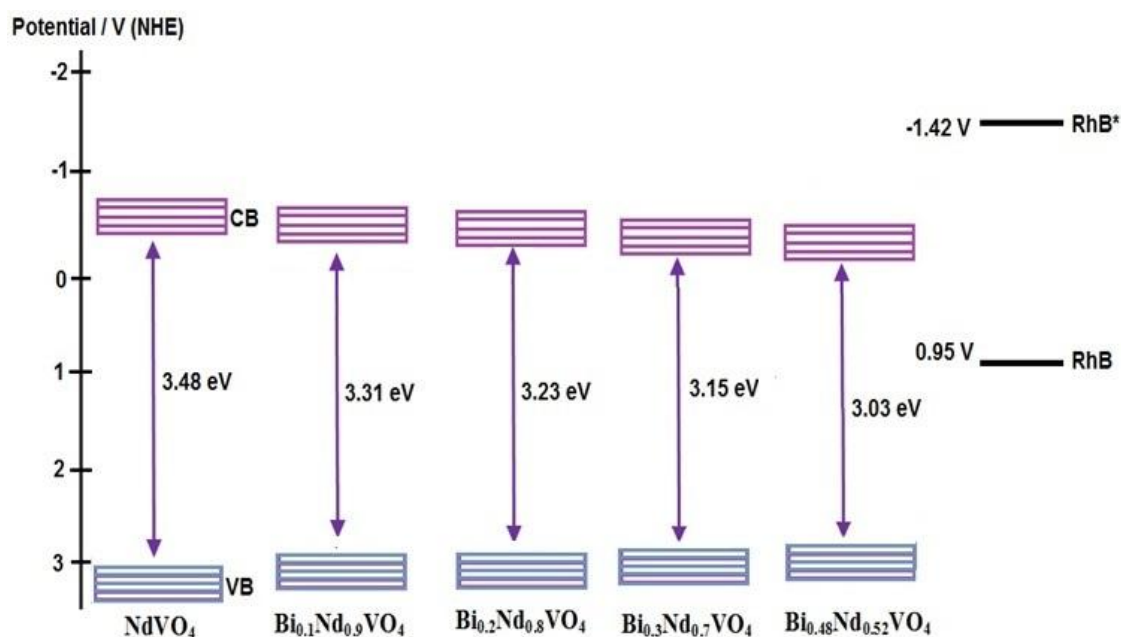
Fig. 77 Schematic band structures of NdVO$_4$ and Bi-NdVO$_4$ nanopowders prepared in this study by coprecipitation method. The redox potentials of Rhodamine B (0.95 and -1.42 V vs. NHE [302]) are also marked.

4.3 Experimental

4.3.1 Photocatalytic reactor set-up and light source

The photocatalytic experiments were performed in a photoreactor that was specially constructed for this purpose. Six low pressure mercury lamps were used as a UVA radiation source (black light) - 6 × 18 W, 590 × 26 mm, Osram, with a broad maximum at 370 nm.

The reactor was also equipped with Visible light source made from 4 lamps, 500 × 30 mm, Linestra Special 1604 60 W 230 V S14s, Osram, with a broad maximum at 642 nm. The lamps were positioned circularly around the periphery of the photoreactor and a reflective surface of polished aluminium was placed behind them.

The photocatalytic cell that consists of a borosilicate glass tube with double walls (300 mm in length, inner diameter of 25 mm, and outer diameter of 35 mm) was positioned in the centre of the reactor. In the water jacket cold water was circulating, maintaining the reaction temperature constant. The powder was kept in suspension and stirred by a magnetic stirrer placed under the reactor cell. The light spectra (relative irradiance) of the lamps were measured with a minispectrometer model Tristan USB 30-106-331 and are shown in Fig. 79 below. The band gaps values of Bi-NdVO$_4$ nanopowders are also marked.
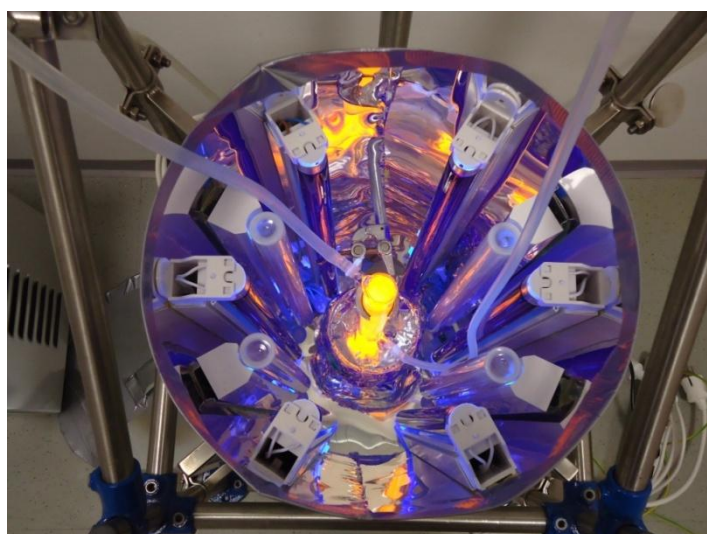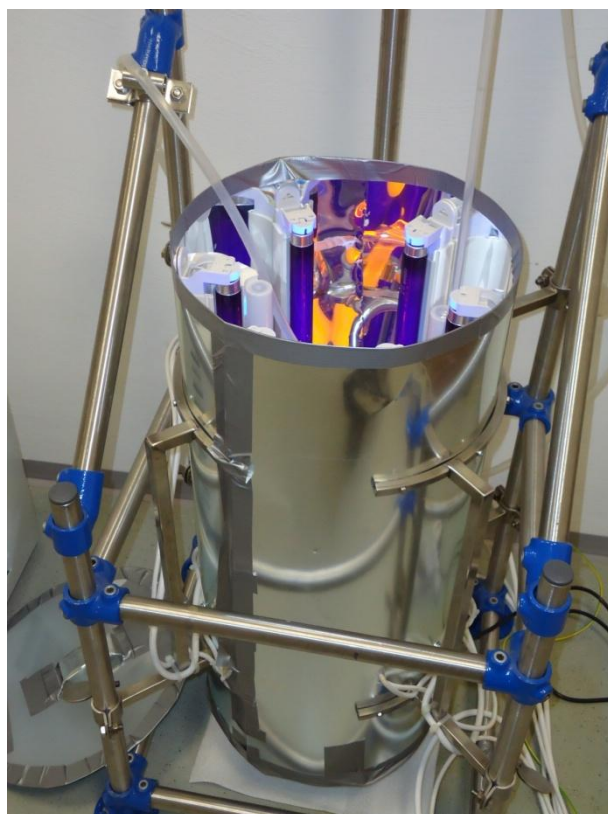
Fig. 78 The photocatalytic reactor. View: (a) from the side and (b) view from the top.
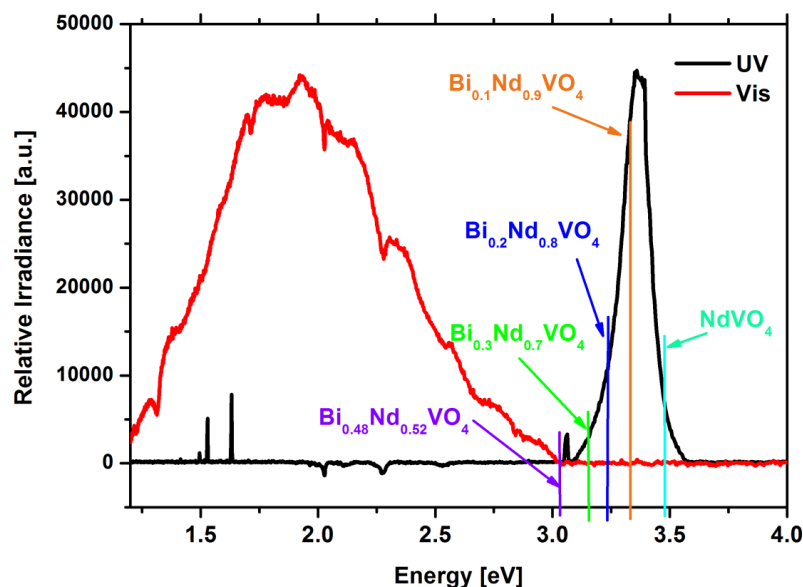
Fig. 79 The spectra of the UV and Vis lamps from the photocatalytic reactor.

4.3.2 Experimental procedures

In a typical experiment, 75 mL of $5 \cdot 10^{-3}$ mol$\cdot$L^{-1} aqueous solution of RhB, (Alfa Aesar, 98%) and 0.075 g Bi-NdVO$_4$ nanopowder were placed in the reactor vessel. Prior to irradiation, the dispersion was magnetically stirred in the dark for 30 min to ensure the adsorption/desorption equilibrium. At different time intervals, an aliquot solution of 3 mL was sampled and centrifuged (at 1200 rot/min, 5 min). The filtrates were further analysed with an UV-Vis spectrophotometer, model PerkinElmer, model Lambda 35, to measure the absorption of RhB. The temperature of the system was kept constant at 21 ^{o}C by water cooling. The extent of photodegradation of RhB by Bi-NdVO$_4$ was determined by monitoring the absorbance maximum in the UV-Vis spectra of RhB, which is located at 554 nm.

4.4 Results and Discussions

4.4.1 Photocatalytic degradation of RhB at pH = 6.5

From Fig. 79 it is obvious that only the UVA lamps can produce photons with energy higher than E_g of the synthesized compositions. Therefore, the photocatalytic evaluation of the Bi-NdVO$_4$ nanoparticles was firstly carry out under UVA

irradiation at a natural pH of 6.5. The photodegradation of RhB solution in the presence of UVA light illumination at pH 6.5 is shown in Figs. 80–85 below.
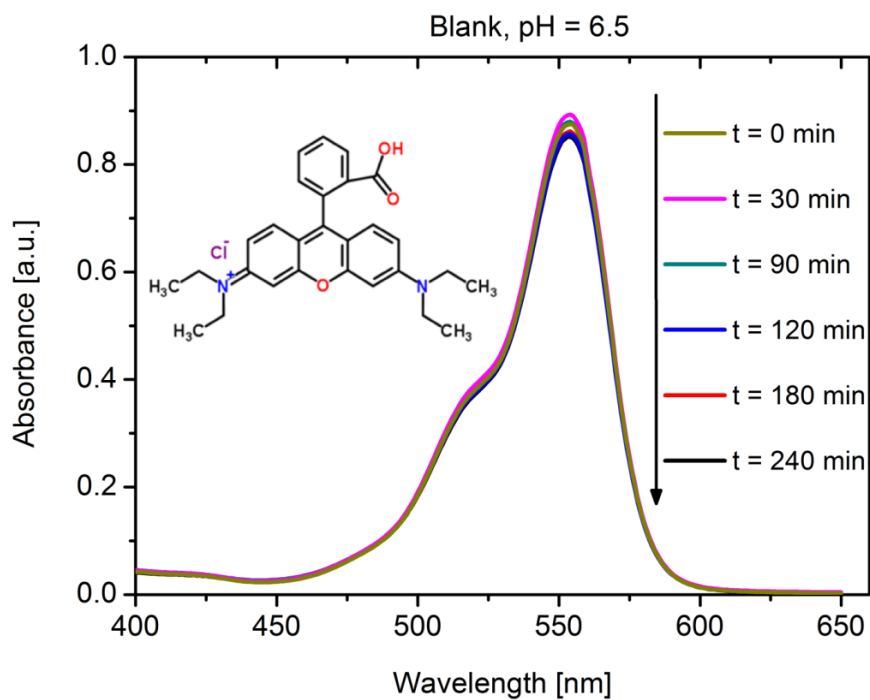
Fig. 80 UV-Vis absorption spectra of rhodamine B solution, in the absence of photocatalyst, under UVA light, at natural pH.
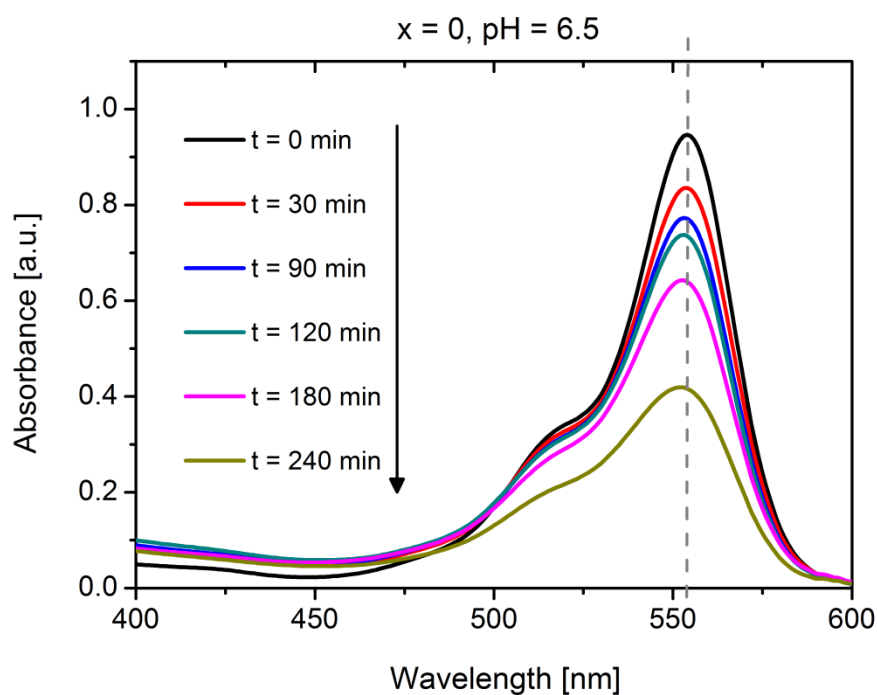
Fig. 81 UV-Vis absorption spectra of RhB before and after UVA radiation in the presence of NdVO$_4$ nanopowder at a natural pH of 6.5.

Under similar conditions, the UVA light irradiating on the $Bi_{0.1}Nd_{0.9}VO_4$/RhB dispersion (Fig. 82) led to a decrease in absorption for almost 47%, but no peak shift was noticed.
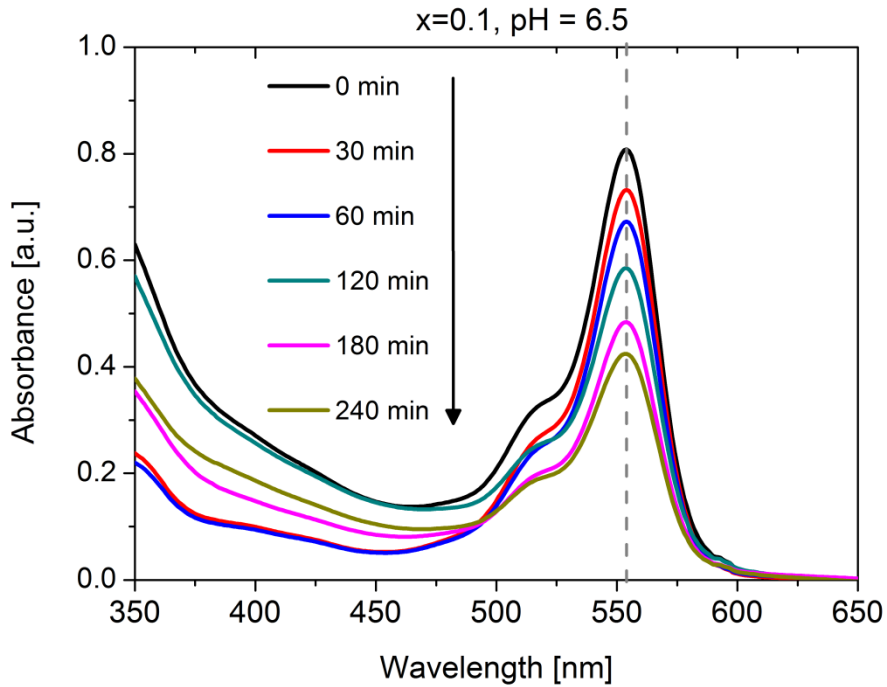
Fig. 82 UV-Vis absorption spectra of rhodamine B before and after UVA radiation in the presence of $Bi_{0.1}Nd_{0.9}VO_4$ nanopowder, at natural pH of 6.5.
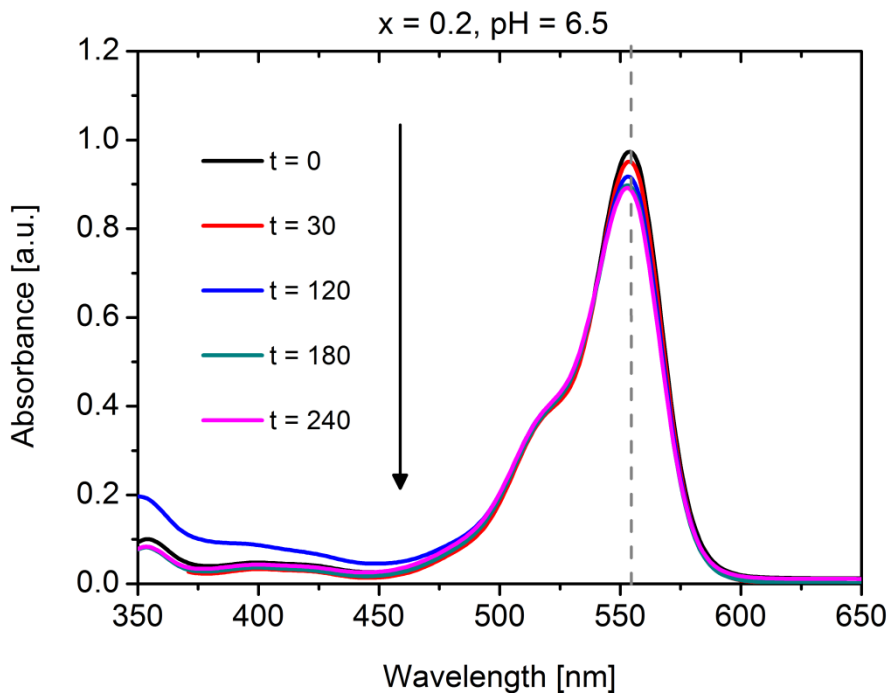
Fig. 83 UV-Vis absorption spectra of rhodamine B before and after UVA radiation in the presence of $Bi_{0.2}Nd_{0.8}VO_4$ nanopowder, at natural pH of 6.5.
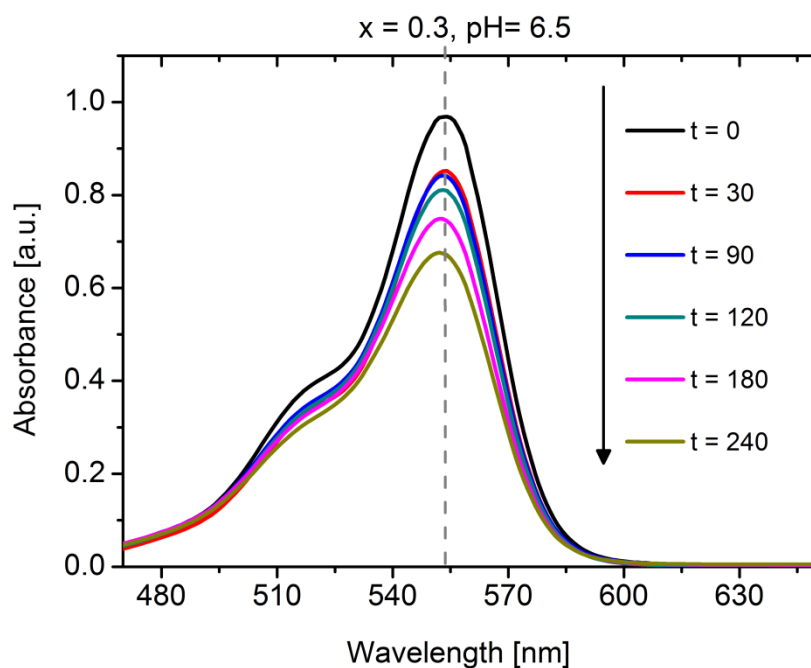
Fig. 84 UV-Vis absorption spectra of rhodamine B before and after UVA radiation in the presence of $Bi_{0.3}Nd_{0.7}VO_4$ nanopowder, at natural pH of 6.5.
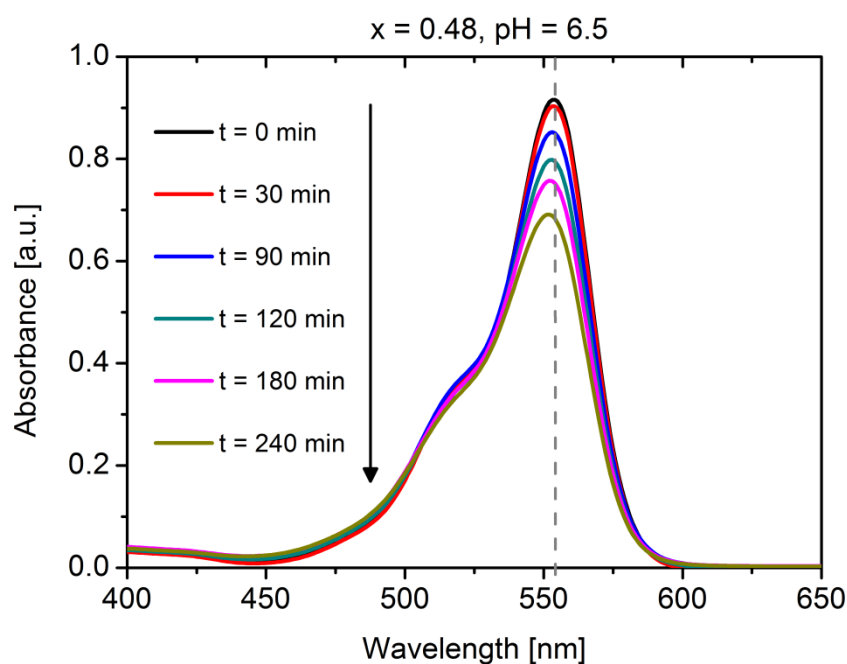
Fig. 85 UV-Vis absorption spectra of rhodamine B before and after UVA radiation in the presence of $Bi_{0.48}Nd_{0.52}VO_4$ nanopowder, at natural pH of 6.5.

The temporal evolution of the RhB alone under UVA light irradiation is shown in Fig. 80. The tetra-ethylated RhB shows a major absorption at 554 nm, followed by a small shoulder at about 517 nm. UVA light irradiation of the aqueous RhB solution

does not lead to any decrease of the absorption, which indicates that RhB alone did not undergo the photolysis process.

UVA light irradiation of the $NdVO_4$/RhB aqueous dispersion (Fig. 81) led to a decrease in the absorption intensity of the main absorption peak and a small blue shift. After 240 min of irradiation, the loss in absorption is about 50%, while the absorption peak shift was from 554 to 551 nm.

For the $Bi_{0.2}Nd_{0.8}VO_4$/RhB dispersion (Fig. 83), after 240 min of UVA light irradiation, no significant decrease in the absorption maximum was detected.

The $Bi_{0.3}Nd_{0.7}VO_4$ sample (Fig. 84) showed a higher photodegradation rate compared to the $Bi_{0.2}Nd_{0.8}VO_4$. After 240 min, 30% of RhB solution was photodegraded, and the absorption maximum was shifted to 552 nm.

In the presence of $Bi_{0.48}Nd_{0.52}VO_4$ nanoparticles and UVA light (Fig. 85), 25% RhB was photodegraded in 240 min. The main absorption band is shifted to 552 nm.
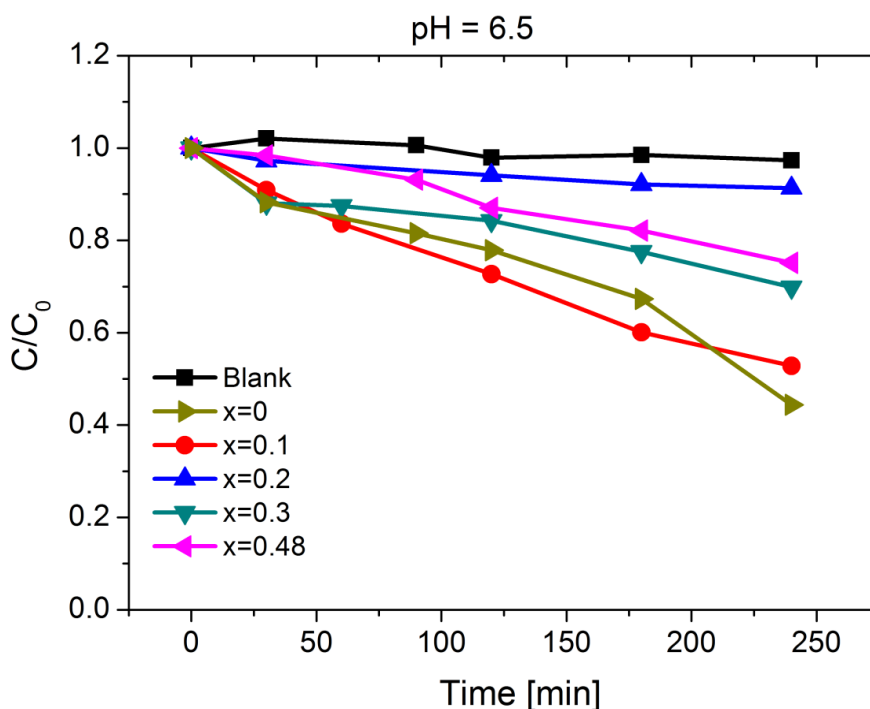
Fig. 86 Temporal course of photocatalytic degradation of rhodamine B with and without $Bi_xNd_{1-x}VO_4$ nanopowders, at natural pH of 6.5 under UVA light.

Almost for all the compositions, the decrease in the RhB absorption intensity at 554 nm is accompanied by a slight blue shift (hypsochromic shift). This indicates that the degradation pathway might be going through processes such as chromophore cleavage, ring-opening and/or mineralization, and only a very small percentage of

de-ethylation of the RhB molecule. The degradation of rhodamine B by *N*-de-ethylation and the destruction of conjugated structure are the main competitive processes mentioned in the literature. Mechanistic studies of RhB degradation were reported by Qu et al. [303] Chen et al. [304], Wu et al. [292], He et al. [298]. The de-ethylation of RhB yields intermediate products such as: N,N-diethyl-N'-ethyl-rhodamine, N,N-diethyl-rhodamine, N-ethyl-N'-ethyl-rhodamine, N-ethyl-rhodamine and fully de-ethylated RhB molecule with absorption band maxima at 541, 525, 529, 514, 506 nm, respectively. In our case, the degradation intermediates might include carboxylic acids, dicarboxylic acids, amines and/or other compounds of these types which do not absorb in the visible region, because we did not observe additional absorption peaks in the investigated interval of 400–650 nm. One of the mechanistic scheme that might take place during the photocatalytic degradation of RhB under UVA light irradiation in the presence of Bi-NdVO$_4$ photocatalyst is the following:

$$\text{Bi-NdVO}_4 + h\nu \text{ (UVA)} \rightarrow \text{Bi-NdVO}_4 \, (h_{VB}^+ + e_{CB}^-) \tag{48}$$

$$\text{Bi-NdVO}_4 \, (h_{VB}^+) + \text{H}_2\text{O} \rightarrow \text{Bi-NdVO}_4 + \text{OH}\cdot + \text{H}^+ \tag{49}$$

$$\text{OH}\cdot + \text{RhB} \rightarrow \text{P}\cdot \text{ (degradation intermediates)} \tag{50}$$
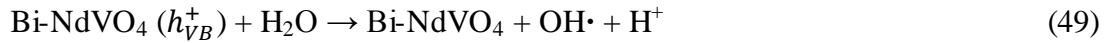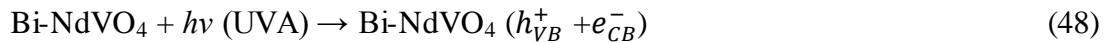
Under UVA light irradiation (with energy $>$ E$_g$ of the material), electron-hole pairs are generated in Bi-NdVO$_4$. They dissociate and diffuse to the surface of the semiconductor. By reaction of the holes with the water molecules on the surface of the photocatalyst, $\cdot$OH radicals are formed. Further, these hydroxyl radicals react with RhB to yield oxidized intermediates, P$\cdot$, which could be further transformed to CO$_2$ and H$_2$O by a complete mineralization process.

The oxygen adsorbed on the photocatalyst surface might as well participate in the redox reaction by the following reactions:

$$\text{Bi-NdVO}_4 \, (e_{CB}^-) + \text{O}_2 \rightarrow \text{Bi-NdVO}_4 + \text{O}_2\cdot^- \tag{51}$$

The O$_2\cdot^-$ radical can also transform into H$_2$O$_2$:

$$\text{O}_2\cdot^- + \text{H}^+ \rightarrow \cdot\text{OOH} \tag{52}$$

$$\cdot\text{OOH} + \cdot\text{OOH} \rightarrow \text{H}_2\text{O}_2 + \text{O}_2 \tag{53}$$
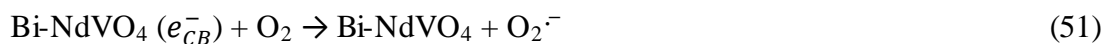
H_2O_2 can act as a direct electron acceptor, which leads to formation of $\cdot OH$ radicals:

$$H_2O_2 + O_2{}^{\cdot -} \rightarrow \cdot OH + OH^- + O_2 \tag{54}$$

The hydroxyl radicals will react with RhB to produce oxidation intermediates, $P\cdot$ according to Eq. 50.

4.4.2 Photocatalytic degradation of RhB at pH = 5 using hydrogen peroxide

Hydrogen peroxide is largely used in AOPs where it produces $\cdot OH$ radicals trough homolytic photolysis under UV irradiation [305,306,307]. Recently, it also started to be used as an electron scavenger in heterogeneous photocatalysis. H_2O_2 has been proven to greatly improve the degradation efficiency of RhB and other pollutants [296,308,309]. In the present study, H_2O_2 was used as an electron scavenger for the Bi-NdVO$_4$/RhB system. Addition of 0.46 M of H_2O_2 into the photocatalytic reactor prior to irradiation resulted into a decrease of pH to a value of ca. 5. The effect of the electron accepting agent (H_2O_2) on the degradation of RhB is shown in Fig. 87 and Figs. 89–92.

Fig. 87 shows the control reaction without photocatalyst, only with RhB and H_2O_2. In the absence of the Bi-NdVO$_4$ photocatalyst, the RhB solution was degraded up to 35% after 60 min of UVA light irradiation. This indicates that H_2O_2 itself decomposes the dye in the absence of the photocatalyst. The blank test in the absence of H_2O_2 did not show any change in the absorption spectra of RhB. We believe that photolysis of H_2O_2 is less probable to occur because only a very small fraction of the UVA light (with the wavelengths of 350–400) could be absorbed by H_2O_2, since the extinction coefficient of hydrogen peroxide is very low at wavelengths > 300 nm [307,310] - Fig. 88. Thus, the decrease in absorption for the blank test with H_2O_2 might be caused by other process such as a direct oxidation of the dye by H_2O_2.

In the presence of H_2O_2 and NdVO$_4$ (Fig. 89), the dye was degraded up to 53% after 60 min of UVA irradiation. In the Bi$_{0.1}$Nd$_{0.9}$VO$_4$/H$_2$O$_2$ system, RhB was degraded only 30%, while in the Bi$_{0.48}$Nd$_{0.52}$VO$_4$/H$_2$O$_2$ system (Fig. 90), 87% of the RhB was degraded. In the Bi-NdVO$_4$/H$_2$O$_2$ system and under UVA irradiation, RhB

could be degraded by a combination of different processes, which could be the reason why RhB is more rapidly degraded.
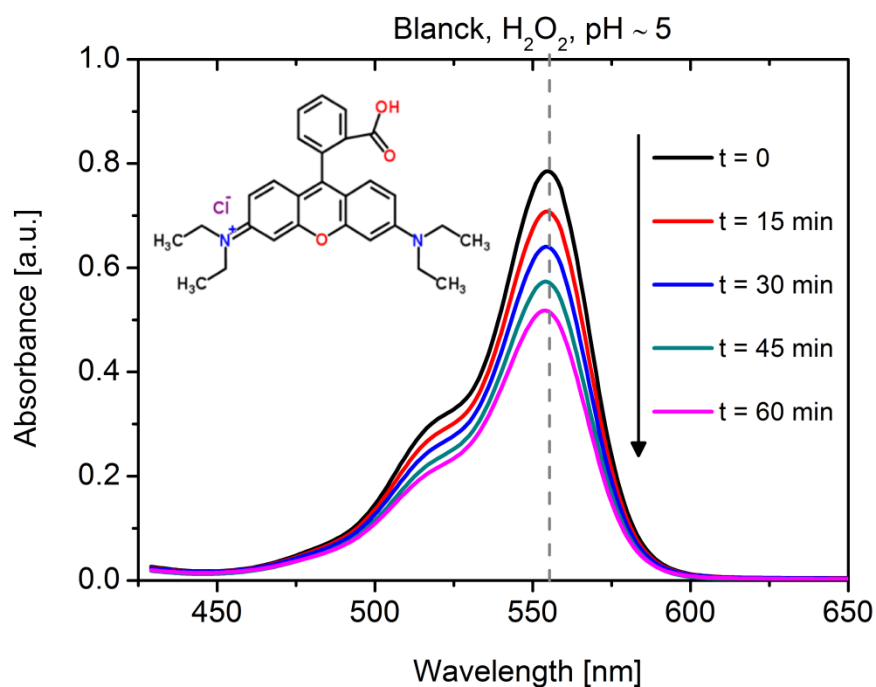
Fig. 87 UV-Vis spectra changes of RhB (5 mM, pH = 5) in the presence of H_2O_2, under UVA light irradiation.
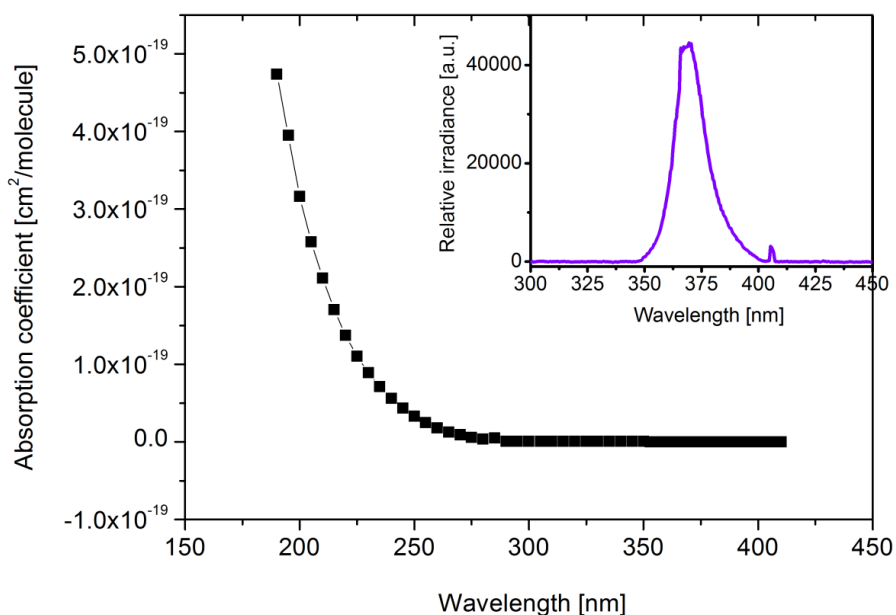
Fig. 88 Literature room-temperature absorption cross sections for H_2O_2 from 190 to 410 nm. The data displayed here were taken from the Mainz Spectral Database [310]. The inset shows the emission spectrum of the UVA lamps used in this study for the photocatalytic tests.
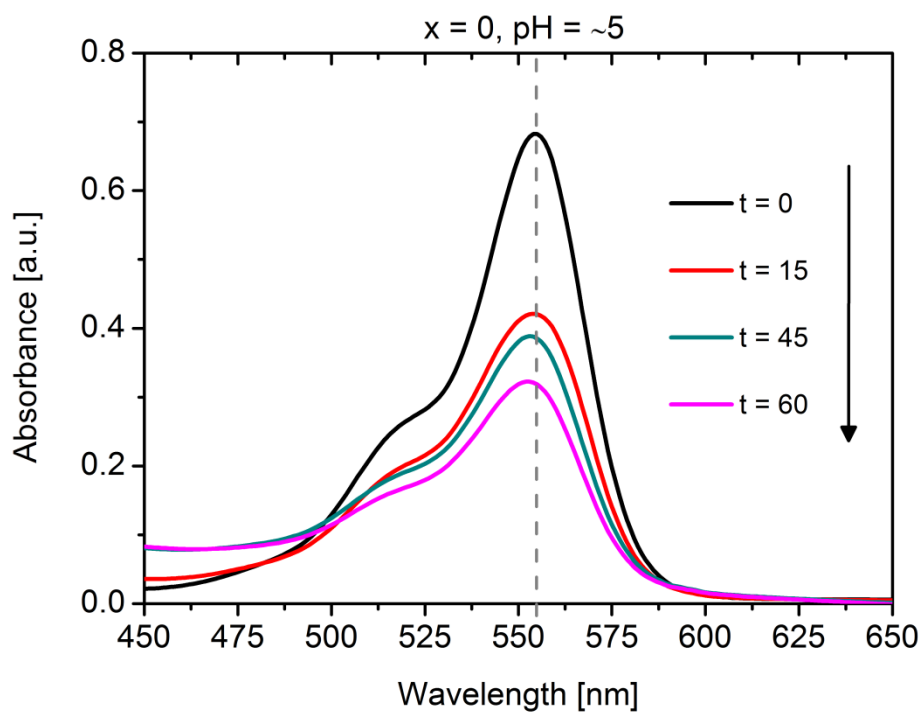
Fig. 89 UV-Vis absorption spectra of rhodamine B before and after UVA radiation in the presence of NdVO$_4$ nanopowder at pH of 5.
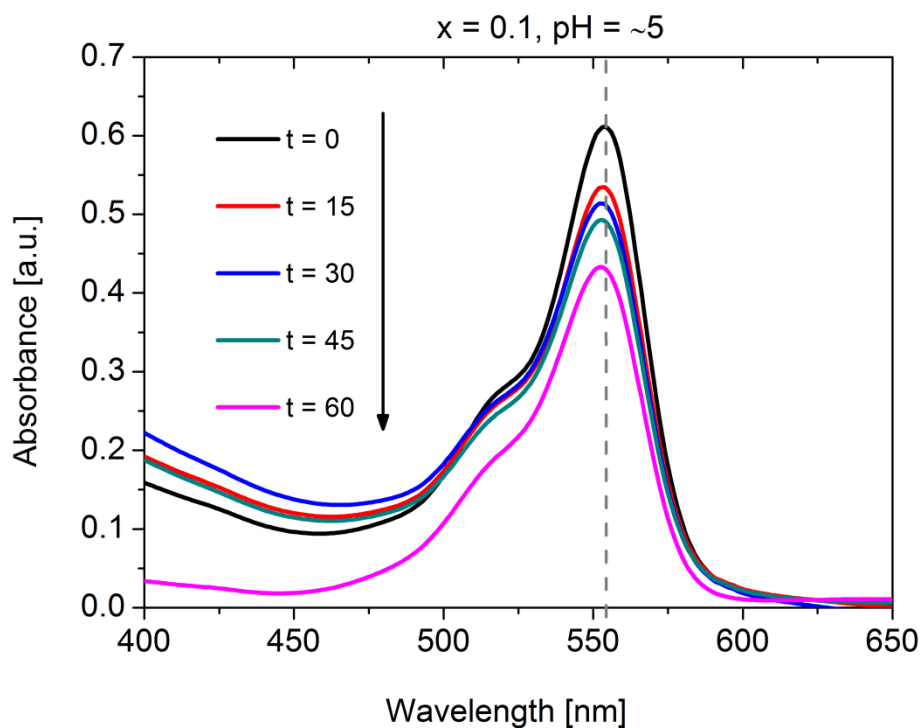
Fig. 90 UV-Vis absorption spectra of rhodamine B before and after UVA radiation in the presence of Bi$_{0.1}$Nd$_{0.9}$VO$_4$ nanopowder at a pH of 5.
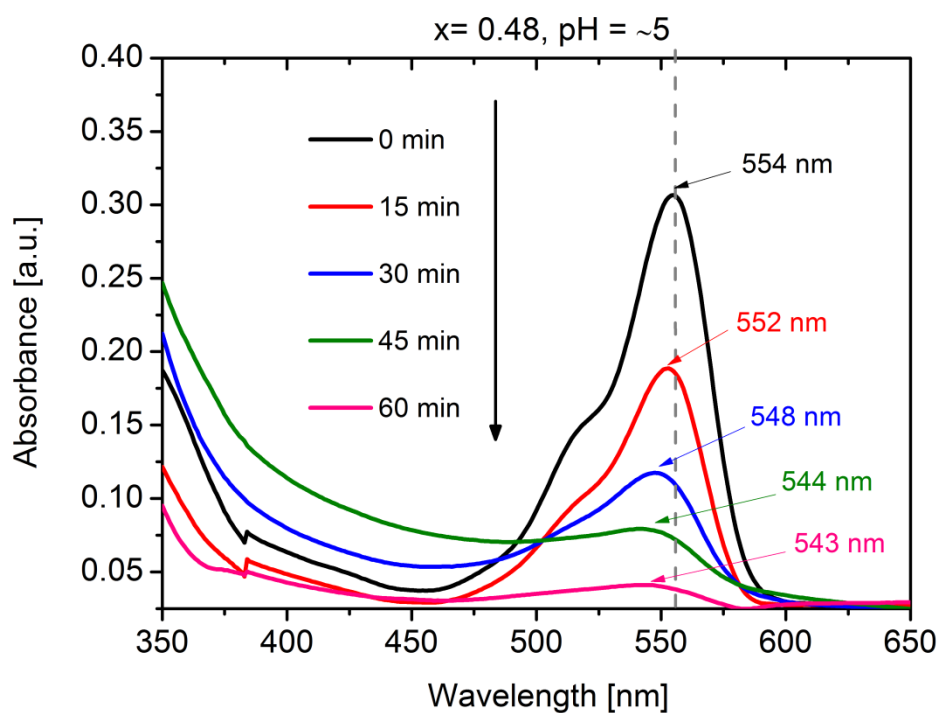
Fig. 91 UV-Vis absorption spectra of rhodamine B before and after UVA radiation in the presence of $Bi_{0.48}Nd_{0.52}VO_4$ nanopowder at a pH of 5.
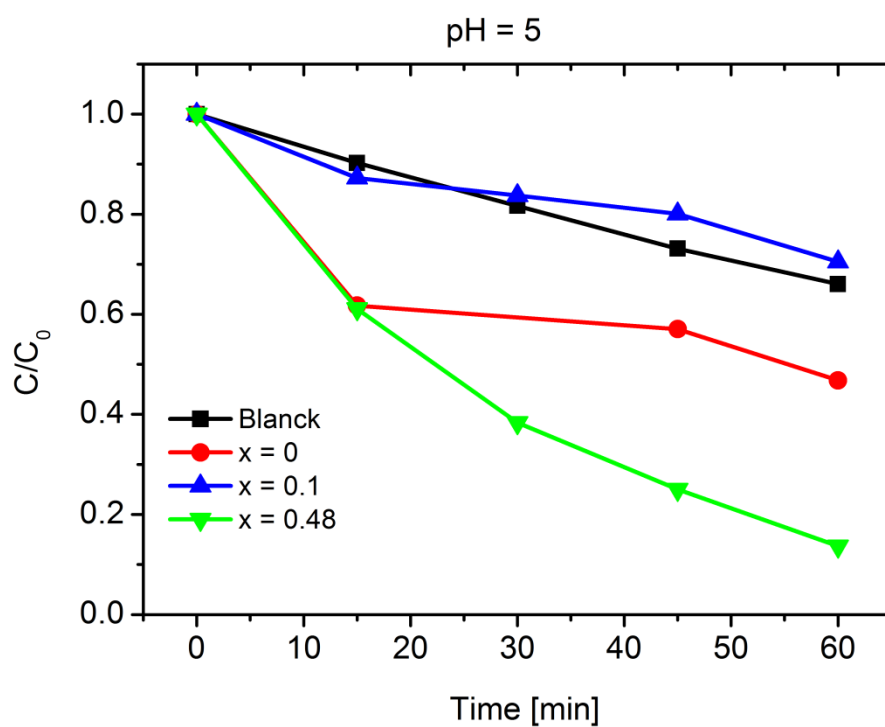
Fig. 92 Temporal course of photocatalytic degradation of rhodamine B without and in the presence of $Bi_xNd_{1-x}VO_4$ nanopowders, at a pH of 5, under UVA light.

4.4.3 Kinetics of the RhB degradation

The photocatalytic rate was inspected and the resulted plots of the irradiation time (t) versus $\ln(C_0/C)$ show on a nearly linear dependence (Fig. 93 and Fig. 94).
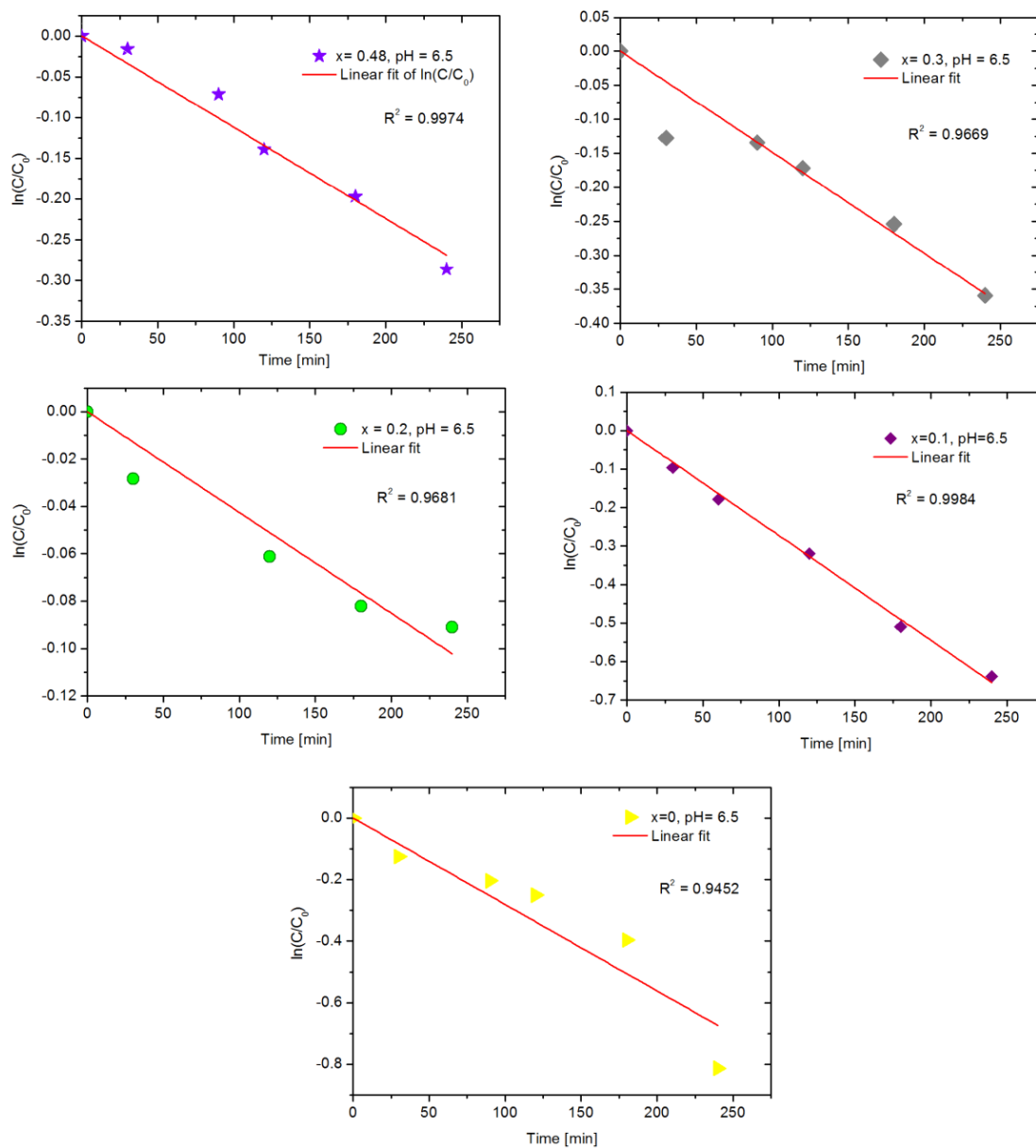
Fig. 93 First-order plots for the photodegradation of RhB byBi-NdVO$_4$ nanoparticles at pH = 6.5.
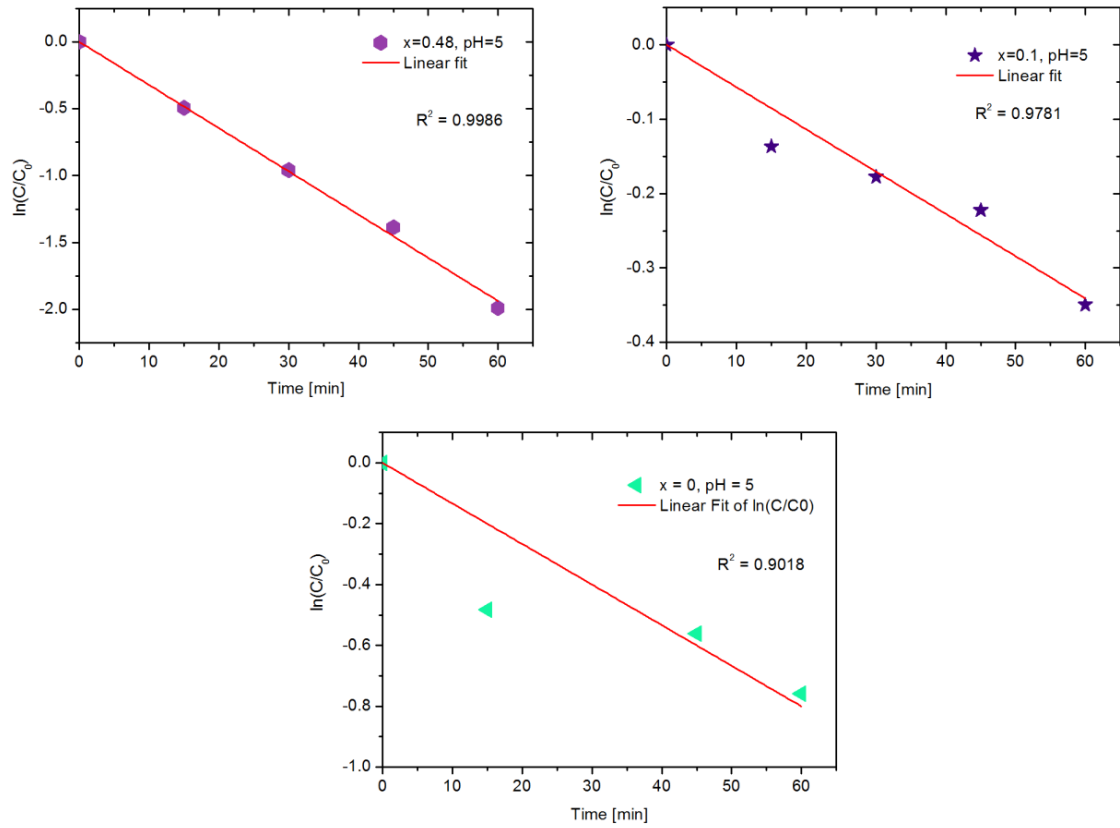
Fig. 94 First-order plots for the photodegradation of RhB by Bi-NdVO$_4$ nanoparticles at pH = 5.

Thus, the reactions of photocatalytic degradation of RhB by Bi-NdVO$_4$ under the experimental conditions applied seem to follow the first-order order kinetics of the Langmuir-Hinshelwood (L-H) model. The L-H model is well describing the photocatalytic degradation of various dyes when the concentration of pollutants is low [311,312]:

$$r = \frac{-dC}{dt} = \frac{k_r K C}{1 + KC} \tag{55}$$

where k_r is reaction rate constant, K is the adsorption coefficient of the reactant, and C is the reactant (RhB) concentration. For very small C values, the product KC becomes negligible with respect to unity ($KC \ll 1$), so that the Eq. 55 describes a first order kinetics. For $t = 0$, the equation becomes:

$$-\ln\left(\frac{C}{C_0}\right) = kt \tag{56}$$

where k is the first order reaction constant, and C_0 is the initial concentration. k is obtained from the gradient of the graph of $\ln(C/C_0)$ as a function of time.

The reaction rate constants together with the correlation coefficient R^2 are presented in Table 12.

Table 12 Kinetic parameters of the degradation process of RhB with Bi-NdVO$_4$ nanoparticles. x represents the amount of Bi in Bi-NdVO$_4$, k is the kinetic constant, and R^2 is the correlation coefficient.

x [mol]	k [min^{-1}]		R^2	
	pH = 6.5	pH = 5	pH = 6.5	pH = 5
0	0.00281	0.00133	0.94521	0.90180
0.1	0.00270	0.00568	0.99830	0.97812
0.2	$4.2553 \cdot 10^{-4}$	-	0.96812	-
0.3	0.00149	-	0.96686	-
0.48	0.00122	0.03228	0.99740	0.99866

The influence of the composition on the photocatalytic rate was also investigated, and the results are shown in Fig. 95. It was observed that, upon increasing the Bi concentration, the decolorization rate of RhB by Bi-NdVO$_4$ nanoparticles decreases when the pH of the solution was 6.5 and in the absence of H$_2$O$_2$. The reaction rate constant seems to linearly decrease with the Bi concentration, except for the $x = 0.2$ composition, which showed an out of trend behaviour and a rate constant ten times smaller than that of NdVO$_4$, which degrades RhB the fastest, with a reaction rate of 0.00281 min^{-1}. On the other hand, when H$_2$O$_2$ was present in the system, doping with Bi resulted in an almost 30 time increase of the decolorization rate, from 0.00133 min^{-1} to 0.0323 min^{-1}.
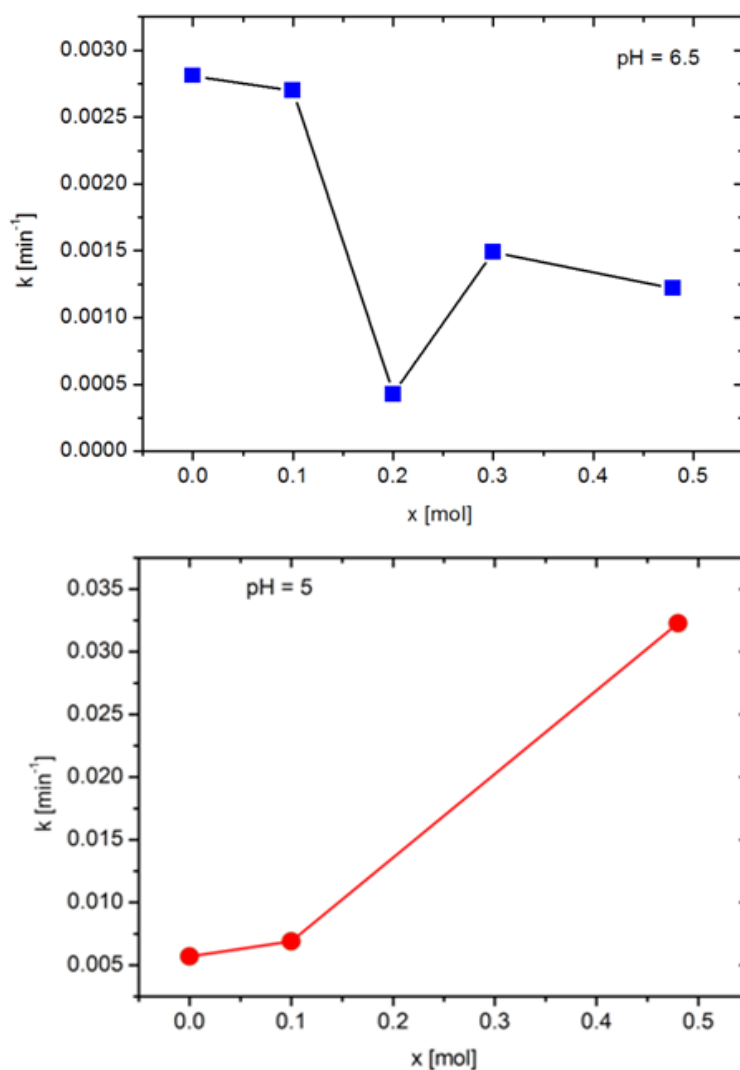
Fig. 95 Influence of the Bi concentration x over the photocatalytic degradation kinetic rate constant of RhB, at pH =6.5 (up) and at pH = 5(down).

4.5 Conclusions

The following conclusions can be drawn from the results reported in this work:

- We have found that the photocatalytic activity of the $Bi_xNd_{1-x}VO_4$ nanopowders, which was tested for the degradation of rhodamine B under UVA light irradiation at natural pH 6.5 and at pH = 5 (by addition of H_2O_2) shows different performances.

- At pH 6.5, the photocatalytic activity depends on the composition, i.e. Bi concentration with $NdVO_4$ sample, decreasing with x. The highest

degradation rate was achieved for $NdVO_4$, with about 50% degradation after 240 min of UVA light irradiation.

- With both catalysts and H_2O_2 additive (pH = 5) but under the same experimental conditions, the rate of RhB degradation by Bi-$NdVO_4$ nanoparticles significantly increased.

- The $Bi_{0.48}Nd_{0.52}VO_4$ sample showed the highest degradation rate, being able to decompose about 87% of the dye after 60 min of UVA light irradiation.

- The reaction of the photocatalytic degradation of RhB by Bi-$NdVO_4$ seems to follow a pseudo-first order kinetics of the Langmuir-Hinshelwood model due to the low concentration of RhB.

- The rate constant k was found to depend on the composition and pH. At pH = 6.5, k decreased almost by half with x, while a decrease of the pH to a value of 5 resulted in a thirty-fold increase of the k.

5 Structural stability and synthesis peculiarities of BiVO$_3$ perovskite

5.1 Background and goals

In the last years, the interest in the Bi-based compounds, especially perovskites, have further escalated due to their potential as:

1. lead-free piezoelectrics - BiAlO$_3$, BiScO$_3$, BiFeO$_3$, BiCoO$_3$, BiGaO$_3$ and modified versions of these compounds [313,314,315,316,317],

2. photocatalysts (BiFeO$_3$, Ga-doped BiFeO$_3$,) [318,319,320], and

3. multiferroics (BiFeO$_3$, BiMnO$_3$, BiCoO$_3$, BiCrO$_3$) [321,322,323,324,325,326,327].

As a consequence, these compounds have been thoroughly investigated and significant amount of knowledge has been accumulated. Also for other Bi-perovskites (such as BiNiO$_3$) interesting properties have been discovered such as negative thermal expansion and the giant magneto-optical Kerr effect [328,329].

In addition to the mentioned compounds, there is a group of simple Bi-perovskites that has not been synthesized yet. There is no information available in the literature about the existence of BiVO$_3$, BiTiO$_3$ or BiCuO$_3$ [330]. It would be wrong to assume that the lack of the literature reports on these compounds indicates that they are not stable. For instance, BiAlO$_3$ has not been synthesized for a long time but only after an *ab initio* computational study predicted its thermodynamic stability and promising piezoelectric properties, enough experimental efforts have been invested to synthesize it [313,331].

By analogy to similar BiFeO$_3$ and BiMnO$_3$ systems, BiVO$_3$ could be a promising photocatalytic and/or multiferroic material. In photocatalysis, finding a chemically stable visible light active metal oxide semiconductor with a band gap < 3.1 eV (and so with improved efficiency by harvesting the broadest portion of the solar spectrum) is still a challenge (see Chapter 1, section 1.3 for more details). Beside simple oxides such as TiO$_2$, WO$_3$ or Fe$_2$O$_3$, also perovskite compounds with ABO$_3$ structure (simple, complex or doped perovskites) such as SrTiO$_3$, LiNbO$_3$, KNbO$_3$, KTaO$_3$, NaTaO$_3$, BiFeO$_3$, etc [332,333,334,335,336,337], are known to be promising photocatalytic materials. One reason is the compositional versatility of the ABO$_3$

structure. ABO_3 structure can accommodate many metallic elements in the periodic table and thus, it offers the possibility to control the electronic band structures by adjusting the elemental composition. The control of the band structure is an effective way to tune the light response range of a photocatalytic material. In addition, Bi-based ABO_3 are considered good candidates as photocatalysts also due to the $6s^2$ lone electron pair of Bi^{3+} which hybridizes with the O $2p$ orbital creating a Bi-O orbital that is located at a lower energy than O $2p$ orbital alone. This is the reason why the Bi-based oxide semiconductors exhibit untypically low band gaps (e.g., the band gaps of $Bi_2Ti_2O_7$ [338] $BiFeO_3$ [339] or $BiVO_4$ [340] are 2.8, 2.5, and 2.4 eV, respectively). Therefore, a new compound such as $BiVO_3$ could exhibit a narrow band gap and better harvesting of the solar spectrum. The narrower band gap could lead to higher photocatalytic efficiencies and make the process of hydrogen evolution through photocatalytic water splitting economically viable.

In addition to the positive effects of Bi^{3+}, $BiVO_3$ contains also vanadium – a typical transitional metal which can also contribute to the absorption in the visible spectrum [341,342,343]. In plus, vanadium is also a very abundant element on Earth, so from the point of view of elemental strategy, photocatalytic compounds based on V are a good choice.

By analogy with $BiFeO_3$, $BiVO_3$ $BiVO_3$ could also present multiferroic properties. Multiferroic materials[8] are of high fundamental importance for material scientists as well as of high applied value for modern technologies. They find applications in many fields such as multiple state memory elements where data are stored both in the electric and the magnetic polarizations, high-sensitivity magnetic field sensors, electrically tuneable microwave devices, etc. There is a possibility that in $BiVO_3$ both ferroelectricity and ferromagnetism would co-exist and be coupled: a distortion of the Bi coordination environment could result in ferroelectricity, while the partially filled d orbitals of V^{3+} are available to induce ferromagnetism.

Although these promising properties are anticipated for $BiVO_3$ perovskite, no successful synthesis of this compound has been reported so far. In addition, nobody has yet reported on the fundamental reasons for the problems with the synthesis or (in)stability of this compound. Also, no Bi_2O_3–V_2O_3 phase diagram or any

---

[8] Multiferroics are materials in which ferroelctricity, ferromagnetism and ferroelasticity coexist and are coupled in the same phase.

information regarding the interactions between these two oxides is available in the literature at the time this study was performed. Therefore, the main aim of this chapter is to perform these studies and obtain an insight into characteristics of the synthesis and stability of $BiVO_3$ perovskite.

A study of the $BiVO_3$ structure with SPuDS, a software that predicts structure of perovskites using the bond valence concept, has been performed first. I will also present empirical relationships such as tolerance factor and octahedral factor which were employed to estimate the stability of $BiVO_3$ perovskite. Further on, several approaches to synthesize $BiVO_3$ are will be described. The identification of the obtained phases was performed by X-ray powder diffraction and X-ray absorption spectroscopy. The analysis of the reaction intermediates and final products in dependence of the synthesis conditions has enabled me to conclude on the fundamental reasons that make the high-temperature synthesis of $BiVO_3$ unsuccessful.

5.2 Structure prediction and stability of $BiVO_3$

Due to the lack of the crystal structure information, we used a structure prediction software, SPuDS, to predict the crystal structure of $BiVO_3$ [344,345]. The input data are elemental composition with the oxidation states of the ions. SPuDS calculates the optimal structure in ten different Glazer tilt systems for single site B cations. The calculation is performed by distorting the structure to minimize the global instability index (*GII*) while maintaining the octahedral undistorted (six equivalent B-O distances and all O−B–O angles equal to 180 degrees). This restriction was made to simplify the calculations, because usually most distorted perovskites show very little distortion of the BX_6 octahedra [345].

According to Sanchez et al. [346], the stability of a crystal structure can be judged by its global instability index, *GII*. Usually, the *GII* with the lowest value indicates the most stable structure. *GII* is the difference between the calculated bond valence sum and the formal valence of each ion:

$$GII = \{[\sum_{i=1}^{N}(d_i^2)]/N\}^{1/2} \tag{57}$$

Where:

- d_i is the discrepancy factor (a measure of the lattice strains present in the compound. $d_i = V_{i(ox)} - V_{i(calc)}$ where $V_{i(ox)}$ is the formal valence and $V_{i(calc)}$ is the calculated bond-valence sum for the ith ion.
- N is the number of atoms in the asymmetric unit.

Table 13 shows possible symmetries for $BiVO_3$ generated by SPuDS along with their *GII*s.

Table 13 Results of the SPuDS calculations for $BiVO_3$.

Coordination geometry (Glazer tilt system)	Tilt system number	Global Instability Index (GII)	Space group
$a^+a^+a^+$	No. 3	0.22430	*Im–3*
$a^+a^+c^-$	No. 5	0.09279	*P42/nmc*
$a^-b^+a^-$	No. 10	0.00879	*Pnma*
$a^-a^-a^-$	No. 14	0.00048	*R–3c*
$a^-b^-b^-$	No. 13	0.18702	*C2/c*
$a^0b^+b^+$	No. 16	0.25380	*I4/mmm*
$a^+b^0c^-$	No. 17	0.15048	*Cmcm*
a^0b^-b-	No. 20	0.02606	*Imma*
$a^0a^0c^-$	No. 21	0.09085	*P4/mbm*
$a^0a^0c^-$	No. 22	0.09084	*I4/mcm*
$a^0a^0a^0$	No. 23	0.69608	*Pm–3m*

From Table 13 it can be seen that at temperature of 20 °C, SPuDS predicted the lowest *GII* (0.00048) for the *R–3c* space group that has the octahedra tilted out of phase in all three axial directions. Despite *R-3c* space group resulted in the lowest *GII,* it is not necessarily the $BiVO_3$ will really adopt this structure [347]. This is because the *GII* is just an indication of the relative structural stability, but does not contain information regarding the bonding or unrealistically short bond distances. Due to the large tilting angles, very short and unfavourable A–O bonds can result for the *R–3c* structure. Below a certain threshold value of the *GII* any tilt system may be stable and additional factors need to be considered, such as the A–O bonding [347].

A more symmetric environment of the A cation can be achieved in *Pnma* which is the next structure (with an orthorhombic symmetry) with the lowest *GII* (0.00879). A

very recent study on the structural stability of $BiVO_3$ confirmed that indeed, the *Pnma* structure is the one most likely to be adopted by $BiVO_3$ [348]. In the *Pnma* structure, the VO_6 octahedra are tilted in phase along the *b* axis (+) and out of phase (−) along the *a* and *c* axis directions ($a^-b^+c^-$).
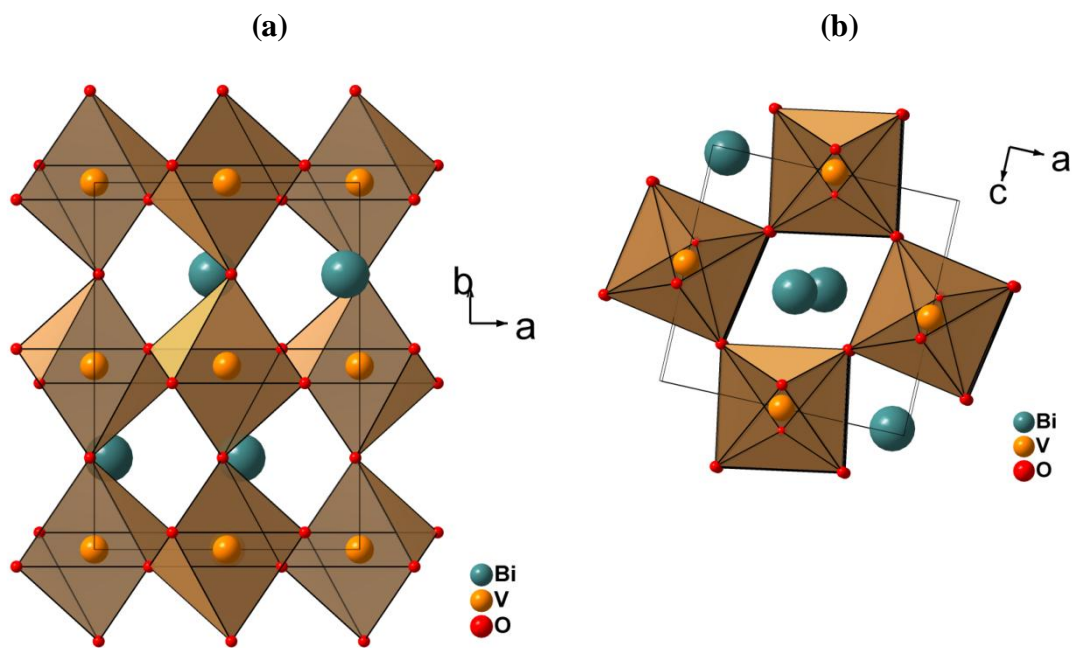
Fig. 96 *Pnma* structure of $BiVO_3$ predicted by SPuDS. (a) projection along the *c*-axis; (b) projection along the *b*-axis.

A parameter often used to estimate the stability of perovskites is the Goldschmidt tolerance factor, *t*. A tolerance factor of 1 corresponds to an ideal cubic perovskite. For $t < 1$, the A cation is too small for its site and this results in a tilting of the BO_6 octahedra and lowering of the symmetry (e.g., the orthorhombic distortion). $t > 1$ implies that the A-site cations are too large, which results in formation of hexagonal perovskites. The tolerance factor for a stable perovskite structure should be in the range of 1.05–0.78 [349] for ionic radii reported by Shannon [76]. With a calculated Goldschmidt tolerance factor of 0.892, the *t* value of $BiVO_3$ falls well within the stability limit.

For the stability of the perovskites, the octahedral factor (r_B/r_O) is as important as the tolerance factor. For $BiVO_3$ this value was found to be 0.457, which again falls within the stability range of the perovskites, which lies between 0.414–0.732 [350].

Although these numbers and calculations predict for $BiVO_3$ a stable perovskite–type structure (orthorhombic distortion), no successful synthesis of $BiVO_3$ has been

157

reported yet. Only two unsuccessful attempts have been reported so far. In the 1970`s N. Ramadass et al. [351] fired the stoichiometric mixture of Bi_2O_3 and V_2O_3 in a sealed evacuated silica tube. The product was not the $BiVO_3$ perovskite but described as having a cubic defect pyrochlore structure with a composition of $Bi_2V_2O_{7-y}$. Unfortunately, the report on the structural analysis of this pyrochlore is very deficient and does not allow us to judge on the correctness of their conclusions. Very recently, A. Belik [330] briefly mentioned $BiVO_3$ as 'an unresolved problem'. His attempt to synthesise $BiVO_3$ perovskite at high pressure–high temperature conditions (6 GPa) resulted in the formation of $Bi_4V_3O_{12}$ as a main phase. No other information was reported.

5.3 Study of the synthesis of $BiVO_3$ perovskite

In the present study, the attempts to synthesize $BiVO_3$ included:
  A. thermal reduction of $BiVO_4$,
  B. study of incorporation of Bi in the crystal structure of $NdVO_3$ perovskite,
  C. solid state reactions between Bi_2O_3 and V_2O_3 at atmospheric pressure and in vacuum.

5.3.1 Experimental part

5.3.1.1 Thermal reduction of $BiVO_4$

$BiVO_4$ was first prepared by solid state reactions. The stoichiometric mixtures of Bi_2O_3 (Alfa Aesar, 99.975% purity) and V_2O_5 (Alfa Aesar, 99.6% purity) were homogenized in a planetary mill using ethanol as a homogenizing medium. The powders were dried, pressed into pellets and calcinated at 800 ^{o}C for 10 h. The thermal reduction of $BiVO_4$ pellets was performed at temperatures between 500−800 °C at atmospheric pressure, in a reducing atmosphere with the following composition: 3% H_2 and 97% Ar. The phase identification and crystallographic characterisation was carried out with X-ray powder diffraction using a PANalytical X-ray diffractometer with Cu K$_\alpha$ radiation (λ = 0.154 nm), a step size of 0.017° and scan step time of 25.8 s. The diffraction patterns were recorded in the range 2θ = 15−80°. Phase quantification was performed using the PANalytical X'pert HighScore Plus software.

5.3.1.2 Study of the Bi incorporation into the NdVO₃ structure

Solid-state reaction technique was employed for the synthesis of the samples with the $Bi_xNd_{1-x}VO_4$ nominal composition (x = 0, 0.03, 0.05, 0.08, and 0.10). The stoichiometric amounts of Bi_2O_3 (Alfa Aesar, 99.975% purity), V_2O_5 (Alfa Aesar, 99.6% purity) and Nd_2O_3 (Alfa Aesar, 99.6% purity, pre-dried for 10 hr in air at 1000 ℃ for the removal of the moisture and carbonates), were homogenized in a planetary mill using ethanol as homogenizing medium. The powders were dried and pressed into pellets. The pellets were calcinated in air in two steps, at 700 ℃ for 3 h, and 800℃ for 3 h, with intermediate grinding. The reduction was carried out in an atmosphere consisting of 35% H_2 in Ar (99.999%) at 900 ℃, for 10 hr.

Because of relatively low sensitivity of the XRD technique (could be up to few percents of the phase), we used X-ray Absorption Near Edge Structure spectroscopy (XANES) to further check the incorporation of Bi^{3+}. With XANES, the valence state of metal cations can be deduced from the energy position of the absorption edge of the selected element (a shift to higher energies means a higher valence state) and from the pre-edge absorption features [200] – different environments of the cation with different site symmetries leads to different Bi L_3-edge profiles. We have measured Bi L_3-edge XANES spectra of the sample with the nominal composition $Bi_{0.03}Nd_{0.97}VO_3$, and two standard references: $Bi_{0.03}Nd_{0.97}VO_4$ where Bi is in +3 oxidation state, and Bi metallic foil. The X-ray absorption spectra in the energy region of the Bi L_3-edge were measured in transmission detection mode at room temperature at HASYLAB synchrotron facility at DESY in Hamburg, Germany. The station was equipped with a Si(311) double-crystal monochromator with ~1.5 eV resolution at the Bi L_3-edge (13419 eV). Higher-order harmonics were efficiently eliminated by detuning the monochromator crystals to 60% of the rocking curve maximum using a beam stabilization feedback control. The samples were prepared in the form of homogeneous pellets with absorption thickness of about 2 above the Bi absorption edge. They were prepared from micronised powder homogeneously mixed with micronised BN powder. The intensity of the X-ray beam was measured by three consecutive 10 cm long ionization detectors, the first filled with 360 mbar of Ar, and the second and third with 1000 mbar of Kr (for the Bi L_3-edge). The samples were placed between the first two detectors. The exact energy calibration was obtained by an absorption measurement on Bi metal foil (Bi L_3-edge 13419 eV),

inserted between the second and the third ionization detector. The absorption spectra were measured within the interval from –250 eV to 1000 eV relative to the absorption edge. In the edge region the equidistant energy steps of 0.3 eV were used, while for the EXAFS region the equidistant k-steps ($\Delta k \approx 0.03$ Å^{-1}) were used with an integration time of 1 s/step. The XANES spectra were further analysed with the IFEFFIT program package ATHENA [203].

5.3.1.3 Solid state reactions

5.3.1.3.1 Solid-state reactions at atmospheric pressure

In this approach, the stoichiometric mixture of the starting reagents, Bi_2O_3 (Alfa Aesar, 99.975%) and V_2O_3 (Alfa Aesar, 97%), was homogenized dry in an agate mortar. The homogenized mixture was pressed into pellets and heat-treated at temperatures ranging from 300–900 ^oC in a sealed tube furnace under N_2 (99.999%) atmosphere. Reference samples consisting of only Bi_2O_3 or V_2O_3, were heat-treated separately at the same conditions as the stoichiometric mixtures.

5.3.1.3.2 Solid state reactions in vacuum

In a separate experiment, the stoichiometric mixture was inserted into quartz ampoules and vacuum sealed at a pressure of $\sim 10^{-6}$ bar[9]. The sealed quartz ampoules were heated at temperatures ranging from 300 to 900 ^oC. Reference samples consisting of only Bi_2O_3 or V_2O_3, were also heated separately at the same conditions as the stoichiometric mixtures.
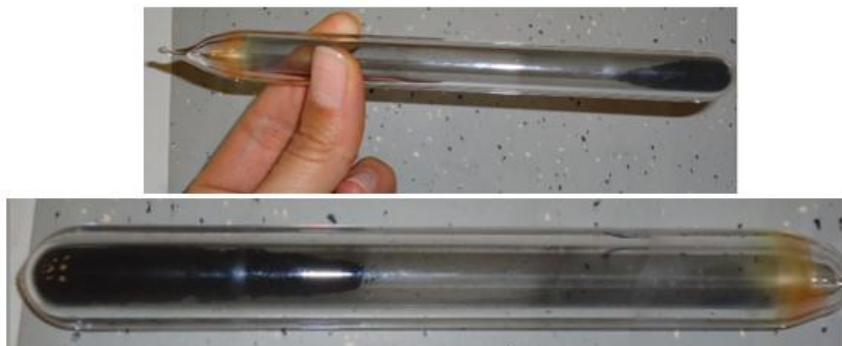
Fig. 97 Quartz ampoules used for the solid-state reactions between Bi_2O_3 and V_2O_3 performed at low pressure.

---

[9] This part of the experiment was performed at Jozef Stefan Institute, Ljubljana, Slovenia.

5.3.2 Results and discussion

5.3.2.1 Thermal reduction of BiVO$_4$

So far, AVO$_3$ compounds (where A = Y, La, Gd, or Nd, etc., with both V and A in +3 oxidation state) having a perovskite-type structure were reported to be prepared only by hydrogen reduction of AVO$_4$ compounds (where V is in +5 oxidation state) [84,352]. The reduction of V^{+5} to V^{+3} results in AVO$_3$ compounds according to the reaction:

$$AVO_4 + H_2 \xrightarrow{\Delta} AVO_3 + H_2O \qquad (58)$$
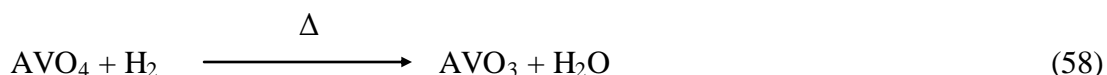
The AVO$_4$ compounds can be synthesised by different wet chemistry routes such as coprecipitation, sol-gel, hydrothermal synthesis and similar. Therefore, an easy and straightforward way to obtain BiVO$_3$ could be by thermal reduction of BiVO$_4$. Under thermal treatment in a reducing atmosphere, V^{+5} could be reduced to V^{+3} to yield BiVO$_3$. In this study, BiVO$_4$ was first synthesized by the solid state reactions; its XRD pattern confirms the presence of single phase monoclinic BiVO$_4$ as shown in Fig. 98.
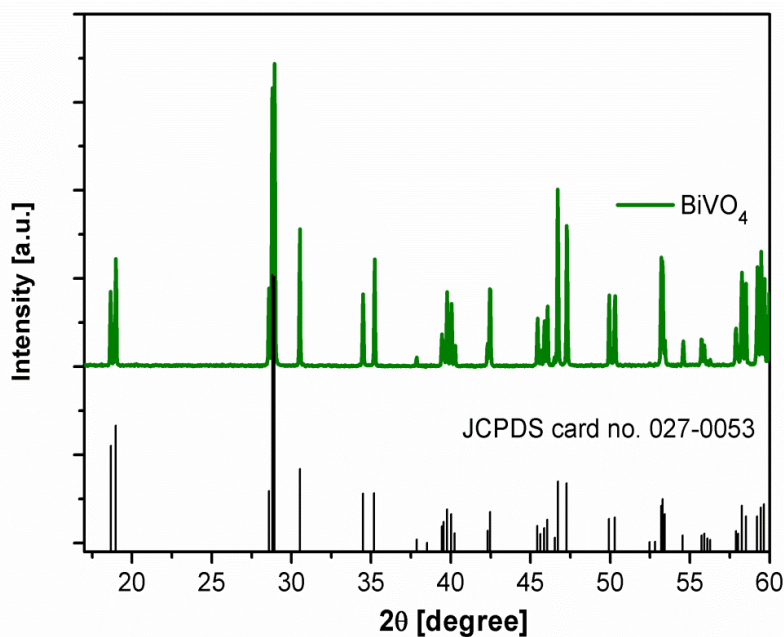
Fig. 98 X-ray diffraction patterns of BiVO$_4$, synthesized by the solid state method (green line) and the database record for monoclinic BiVO$_4$, JCPDS card no. 027-0053 (black line).

After the synthesis, BiVO$_4$ samples were heated in a reducing atmosphere composed

of 3% H_2 in Ar, for 8 h, at 500, 700, and 800 °C, respectively. The products of the reduction as well as the oxidation state of Bi and V in the resulted phases are shown in Table 14.

Table 14 Conditions of the thermal reduction of $BiVO_4$ and resulting phase composition.

No.	Thermal treatment	Resulted phases	Quantification [%]	Oxidation state of Bi	Oxidation state of V
1.	500 °C, 8h	Bi^0	32.1%	0	-
		Bi_2O_3	8.2 %	+3	-
		$Bi_{1.62}V_3O_{16}$	31.3%	+3	+4.5
		$Bi_4V_2O_{11}$	28.4%	+3	+5
2.	700 °C, 8h	Bi^0	22.4%	0	-
		Bi_2O_3	29.6%	+3	-
		V_2O_3	32%		+3
		$Bi_4V_2O_{11}$	16%	+3	+5
3.	800 °C, 8h	Bi^0	13.5%	0	-
		Bi_2O_3	18.4%	+3	-
		V_2O_3	68.1%	-	+3

The XRD patterns of the $BiVO_4$ samples after the thermal reduction are shown in Fig. 99.
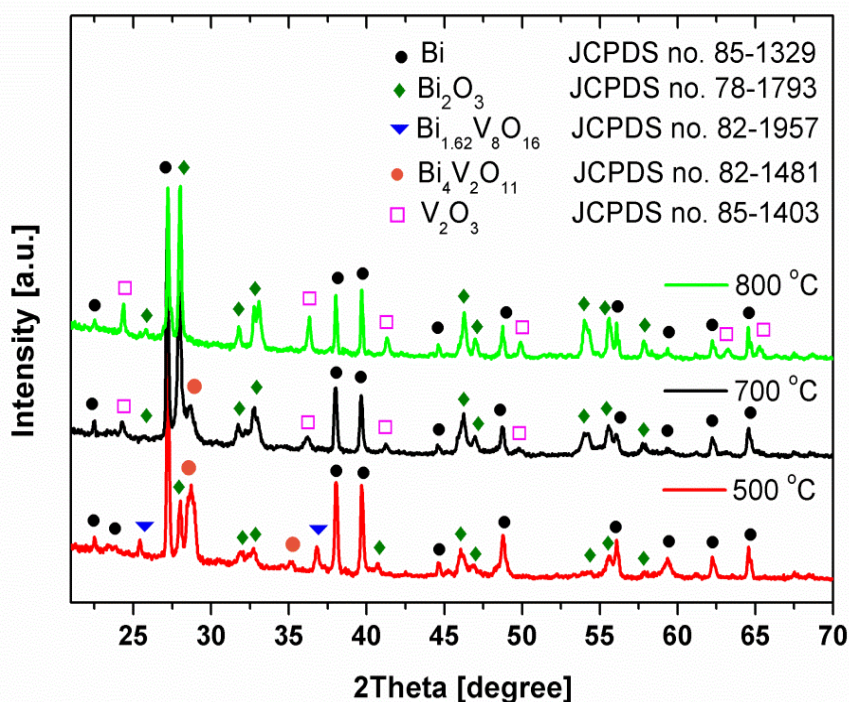
Fig. 99 X-ray diffraction patterns of $BiVO_4$ samples after the thermal reduction in the gas mixture of 3% H_2 in Ar.

The thermal reduction of $BiVO_4$ did not yield the $BiVO_3$ perovskite, as expected, but the $BiVO_4$ compound decomposed to metallic Bi, Bi_2O_3, V_2O_3 and/or mixed Bi–V phases. Bi^0 and Bi_2O_3 appeared independently of the firing temperature, while $Bi_{1.62}V_3O_{16}$ and $Bi_4V_2O_{11}$ phases were detected only at temperature ≤ 700 ^oC. At 800 ^oC, all vanadium was reduced to +3 valence state.

The results presented above suggested showed that via thermal reduction of $BiVO_4$ we could not stabilize and further obtain the $BiVO_3$ perovskite. Therefore, new approaches needed to be explored. Its stabilization could be initiated by forming solid solutions with a stable and well-known perovskite (such as $NdVO_3$). Whether new $Bi_xNd_{1-x}VO_3$ solid solutions can form and/or $BiVO_3$ could be obtained by this approach is shown in the following section of this chapter.

5.3.2.2 Bi^{3+} incorporation into the $NdVO_3$ crystal structure

The stability of the $BiVO_3$ perovskite can be promoted by forming solid solutions with a stable perovskite such as $NdVO_3$. The substitution of Nd^{3+} in the $NdVO_3$ with Bi^{3+} is expected due to similar ionic radii of Nd^{3+} and Bi^{3+} (1.109 and 1.17 Å, respectively [76]).

The synthesis of $Bi_xNd_{1-x}VO_3$ perovskite was conducted as a two step process. First step was to synthesize $Bi_xNd_{1-x}VO_4$ phase, which was in the second step reduced in order to be convert into $Bi_xNd_{1-x}VO_3$ perovskites.

5.3.2.2.1   XRD study

The study of the phase relations in the $NdVO_4$–$BiVO_4$ system (Chapter 2) showed that Bi can enter the crystal structure of $NdVO_4$ up to $x = 0.49(1)$. Therefore, the doping concentrations used in this study ($x \leq 0.1$), are below the solubility limit. The XRD patterns in Fig. 100 showed on the successful incorporation of Bi in $NdVO_4$; for all $Bi_xNd_{1-x}VO_4$ ($x = 0.03, 0.05, 0.08, 0.1$) compositions only the $NdVO_4$-based phase with the tetragonal structure (space group $I4_1/amd$) was identified.

Fig. 101 shows the XRD patterns of the samples after the thermal reduction of the $Bi_xNd_{1-x}VO_4$ samples. All the Bi-doped samples after the thermal reduction contain $NdVO_3$ phase (JCPDS card no: 25-0547) and a small amount of metallic Bi (JCPDS no. 85-1331). The presence of Bi^0 suggests that the reduction process of

$Bi_xNd_{1-x}VO_4$ did not yield the $Bi_xNd_{1-x}VO_3$ perovskite phase but rather resulted in $NdVO_3$ perovskite-type phase and metallic Bi. However, based on only XRD analysis we cannot convincingly conclude that no Bi was incorporated into $NdVO_3$ perovskite-type.

To support the XRD studies the XANES analysis on Bi L_3-absorption edge has also been performed.
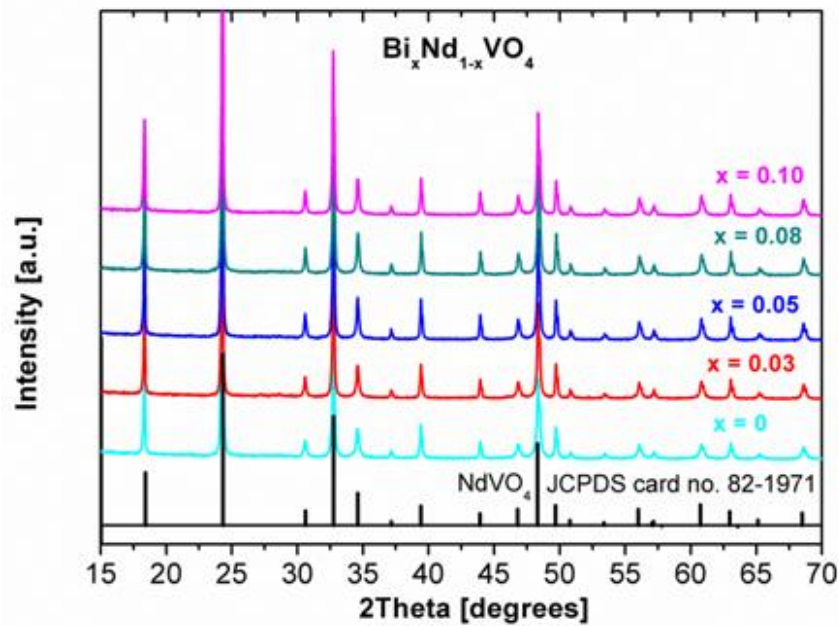
Fig. 100 X-ray diffraction patterns for $Bi_xNd_{1-x}VO_4$ samples, $0 \le x \le 0.10$ prepared by solid state reactions.
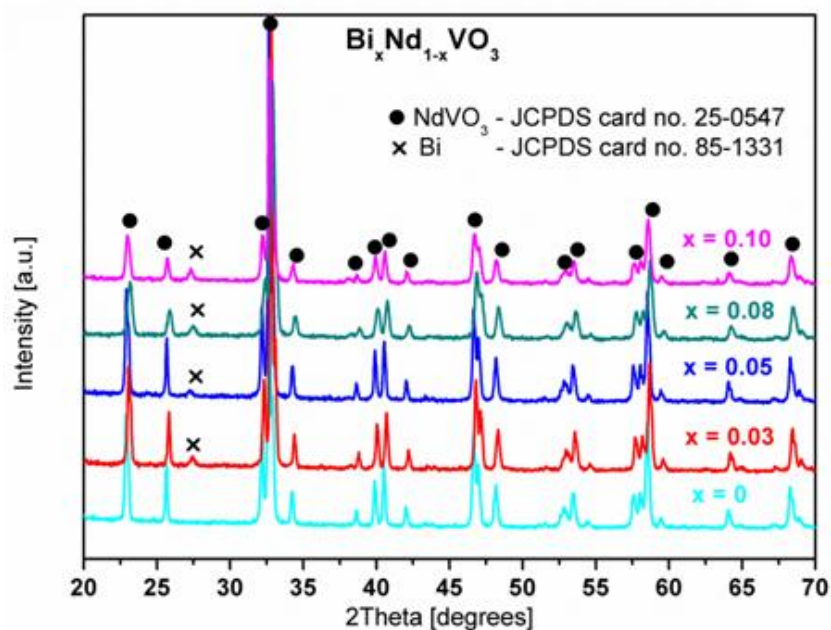
Fig. 101 X-ray diffraction patterns for the $Bi_xNd_{1-x}VO_4$ samples $0 \le x \le 0.10$ reduced with a the gas mixture consisting of 3% H_2 in Ar, at 900 °C, for 10 h.

164

5.3.2.2.2 XANES study

XANES study was performed to more precisely analyze if some of the Bi^{3+} was incorporated into the $NdVO_3$ structure. The normalized Bi L_3-edge spectra from the sample with the $Bi_{0.03}Nd_{0.97}VO_3$ nominal composition and two references ($Bi_{0.03}Nd_{0.97}VO_4$ and Bi metallic foil) with known valence state and local symmetry of the Bi atom neighborhood are shown in Fig. 102.
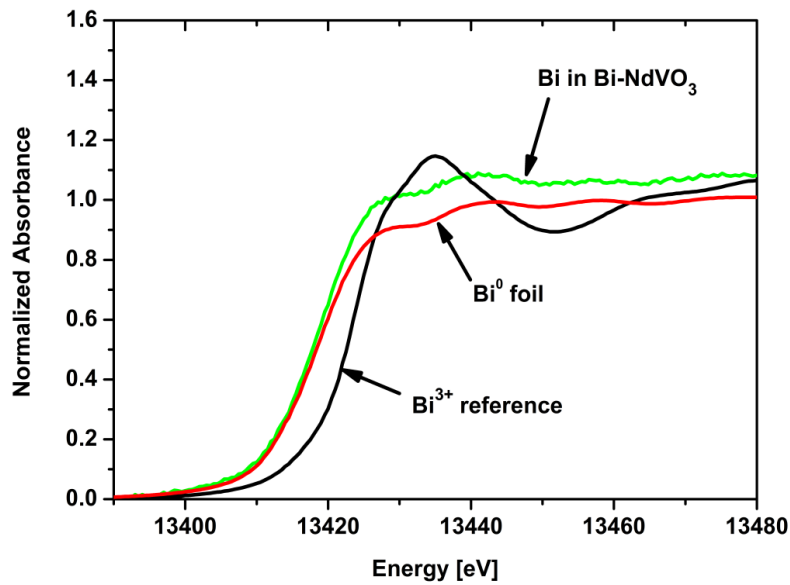
Fig. 102 Bi XANES spectra of the Bi L_3-edge in the samples with $Bi_{0.03}Nd_{0.97}VO_3$ nominal composition, Bi metallic foil and $Bi_{0.03}Nd_{0.97}VO_4$ sample.
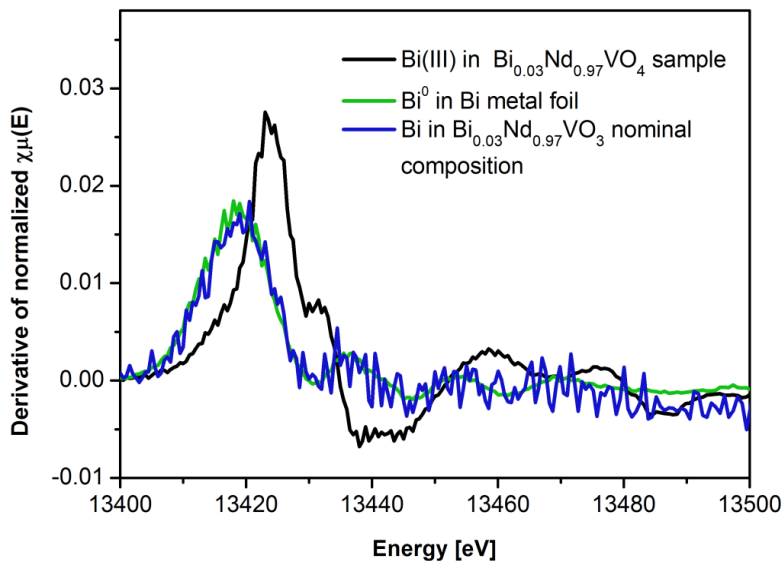
Fig. 103 Derivative of normalized $\chi\mu(E)$.

165

Fig. 103 shows the derivatives of the Bi L_3-edge profiles, where the edge inflection point (which is used as a marker of the energy position of the edge) appears as the tip of the peak.

From the comparison of the three spectra from Fig. 102 and Fig. 103, we can clearly see that Bi in $Bi_{0.03}Nd_{0.97}VO_3$ is in metallic form. The shape of the Bi L_3-edge and its derivative in the nominal $Bi_{0.03}Nd_{0.97}VO_3$ sample looks almost identical to the Bi in metallic foil, with the same edge and energy position. Also, it is much different than the shape of Bi L_3-edge in $Bi_{0.03}Nd_{0.97}VO_4$. In $Bi_{0.03}Nd_{0.97}VO_4$, the edge is shifted to higher energies what indicates a higher valence state for Bi and probably oxygen atoms as the nearest neighbours. This analysis of the XANES spectra clearly shows that no Bi^{3+} entered the structure of $NdVO_3$ perovskite.

The approach discussed in this section as well as the previous attempts did not lead to the formation of $BiVO_3$ perovskite, but resulted in phases with bismuth and vanadium in different oxidation states, even if a special care has been taken regarding the atmosphere where the experiments were performed. Therefore, the further aim of this work was to identify the chemical processes and interactions that prevent the formation of $BiVO_3$ at elevated temperatures. In this sense, solid state reactions between Bi_2O_3 and V_2O_3 have been performed in oxygen free atmosphere. At the moment when this study was performed, nobody has been reported on the fundamental reasons for the problems with the synthesis or (in)stability of $BiVO_3$. Also, no Bi_2O_3−V_2O_3 phase diagram or any information regarding the interactions between these two oxides was available in the literature.

A first insight into the characteristics of the synthesis and stability of $BiVO_3$ perovskite is described in the next section of the present chapter.

5.3.2.3   Solid state reactions between Bi_2O_3 and V_2O_3

Solid state reactions of Bi_2O_3 and V_2O_3 were performed at atmospheric and low pressure. The reactions yielded similar products for the both cases, and thus will be treated together. Firstly, two reference samples, Bi_2O_3 and V_2O_3, have been separately heat treated in N_2 at atmospheric pressure and in the vacuumed quartz ampoules. The XRD analysis after the thermal treatment has showed partial oxidation of the V_2O_3 to VO_2 and partial amorphisation (see Fig. 104). The partial oxidation of the V_2O_3 phase could have been caused by the residual oxygen in the atmosphere and/or oxygen species adsorbed on the surface of the V_2O_3 oxide. In the

case of Bi_2O_3, no chemical changes have been noticed after the heat treatment (see Fig. 105).
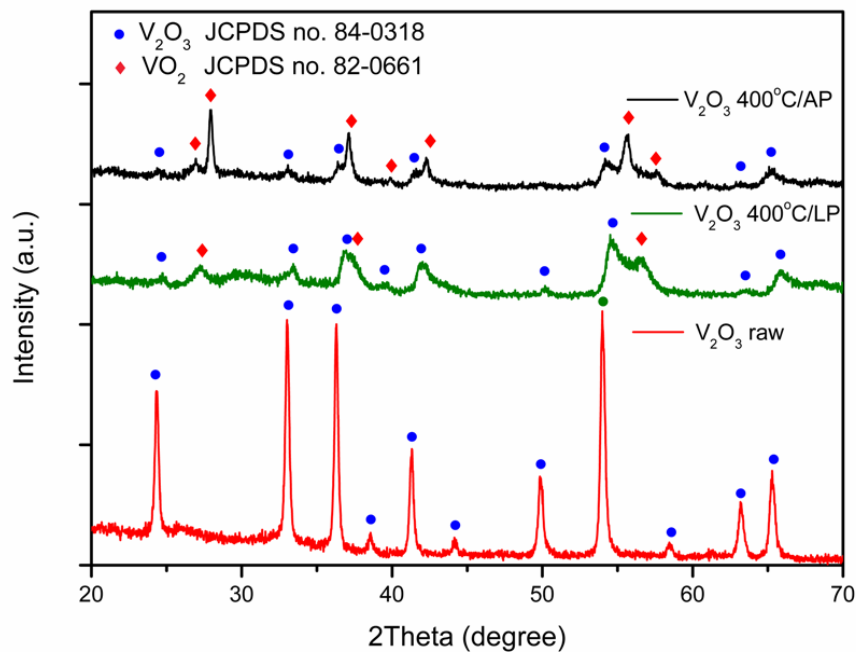
Fig. 104 X-ray diffraction patterns of V_2O_3 before and after thermal treatment at 400 °C
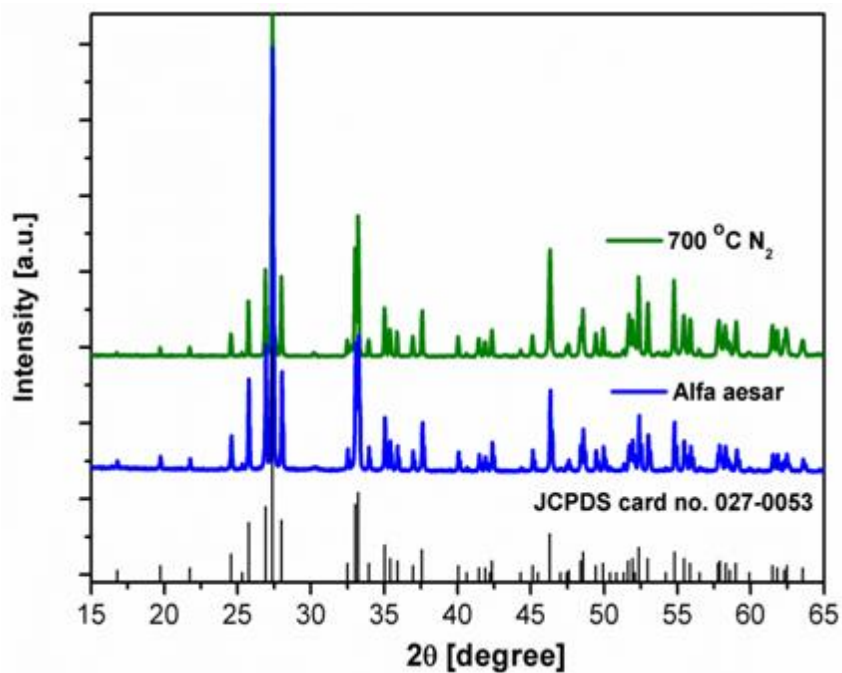
Fig. 105 X-ray diffraction patterns of Bi_2O_3 before and after thermal treatment at 700 °C, in N_2 atmosphere.

Further experiments were performed on the equimolar mixtures of V_2O_3 and Bi_2O_3

which were heated at different temperatures between 300–900 $^{\circ}$C. The experiments have again been performed in N_2 and vacuum; however, no significant influence of the atmosphere has been detected. At 300 $^{\circ}$C, no interaction between the two oxides has been observed. The product consisted of some VO_2 in accordance to the reference experiment. At 400 $^{\circ}$C, the first interaction between both phases has been observed (see Fig. 106).
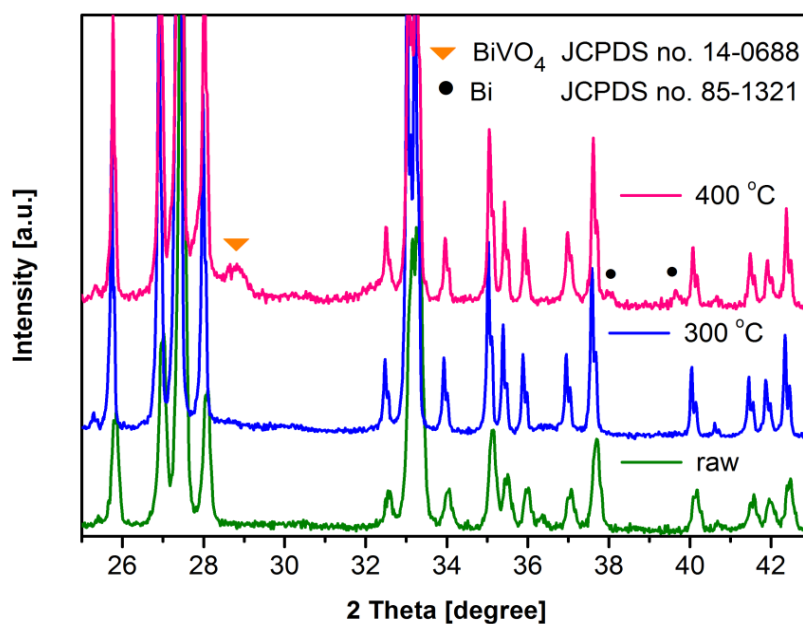
Fig. 106 X-ray diffraction patterns of the equimolar Bi_2O_3–V_2O_3 sample heated at 800 and 900 $°$C.

The new phases that have formed were Bi^0 and $BiVO_4$. At the same conditions of the thermal treatment, the reference Bi_2O_3 sample has not been reduced to metal Bi (Fig. 105), but in the presence of V_2O_3, metal Bi appeared as a reaction product. In addition, the reaction has yielded $BiVO_4$ phase with vanadium in +5 oxidation state. This indicates that the direct reaction between Bi_2O_3 and V_2O_3 with the formation of $BiVO_3$ does not occur. The reaction is sequential, initially induced by an electron transfer from V^{3+} onto Bi^{3+}, i.e., solid-state redox reaction that yields Bi^0 and V^{5+}:

$$2/3Bi_2O_3 + V_2O_3 \rightarrow 4/3Bi^0 + V_2O_5 \tag{59}$$

At these conditions, V_2O_5 reacts further with unreduced Bi_2O_3 to yield the $BiVO_4$ phase:

$$V_2O_5 + Bi_2O_3 \rightarrow 2BiVO_4 \tag{60}$$

Bi_2O_3 oxidizes V_2O_3, but competitively also reacts with newly formed V_2O_5. As a consequence, the redox reaction stops before all V-oxides are consumed. Unfortunately, the low electron density and the consequent low X-ray scattering factors for V-oxides compared to Bi compounds, make the XRD analysis of small concentrations of the V-oxides difficult. So, in these cases we have not been able to reliably detect and identify the remaining V-oxide phases.

At temperatures above 500 ^{o}C, other bismuth vanadates appear (see Fig. 107): predominantly $Bi_{1.62}V_8O_{16}$ and polymorphs of $Bi_4V_2O_{10.5}$, in which V is again in the oxidation state lower than +5. As we have seen, Bi_2O_3 and VO_2/V_2O_3 do not react directly into the binary compounds but rather undergo the described redox process; therefore, the only reaction path that can yield the binary Bi-vanadates with V^{3+} or V^{4+} must go through the reduction of V^{5+} from $BiVO_4$:

$$5.62\ BiVO_4 + 4.38\ VO_x \xrightarrow{\ T > 600\ ^{o}C\ } Bi_4V_2O_{10.5} + Bi_{1.62}V_8O_{16} \tag{61}$$
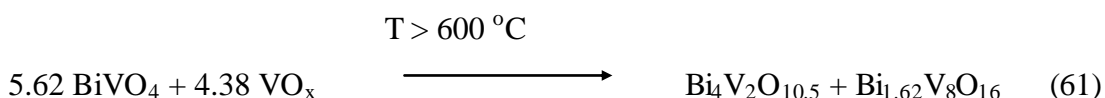
The coefficients in the Eq. 61 are approximate as the V-oxides were not quantitatively determined.
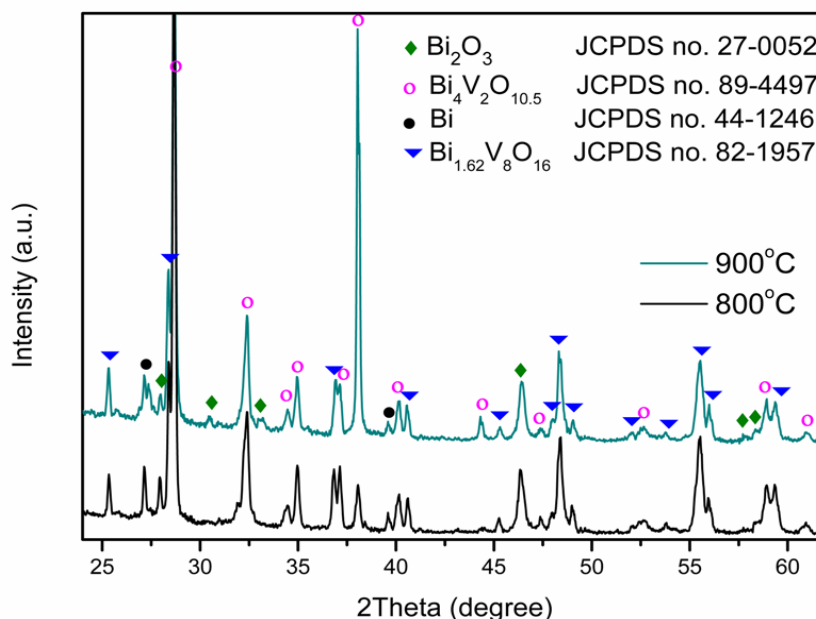
Fig. 107 X-ray diffraction patterns of the equimolar Bi_2O_3–V_2O_3 sample heated at 800 and 900 ^{o}C.

The experiments show that the reduction-oxidation reaction occurs between Bi^{3+} and V^{3+} already at very low temperature, around 400 ^{o}C. This solid-state redox reaction is a consequence of tendency for covalent bonding between the Bi^{3+}, V^{3+} cations and oxygen. To stabilize the $BiVO_3$ structure and facilitate the short Bi–O bonds (calculated by ab-initio modeling to be ~2.2 Å [348]), a strong orbital interaction between Bi^{3+} and VO_6 octahedra is necessary. This reduces the activation energy and facilitates a charge transfer between V^{3+} and Bi^{3+} at fairly low temperatures. The situation is different in the hollandite-type $Bi_{1.62}V_8O_{16}$ phase [353] (with Bi in +3 and V in +3 and +4 oxidation state) wherein the electron transfer between Bi^{3+} and V^{3+} does not take place even at high temperatures (800 ^{o}C). This indicates higher activation energy for the reduction of Bi^{3+} to the metallic state, probably because in the hollandite-type structure [353] the Bi cations occupy much larger channels (Fig. 108) and interact with the VO_6 octahedra only weakly and with much less covalent contribution to the bonding (here the Bi–O distance is 2.5 Å [354]).
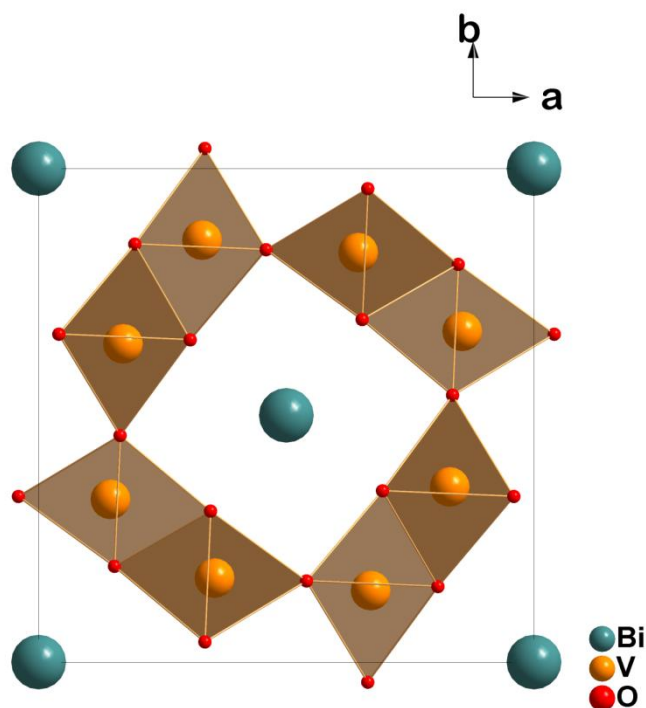
Fig. 108 The $Bi_xV_8O_{16}$ hollandite structure projected along the c axis. The VO_6 octahedra share an edge with other VO_6 octahedra (with V in +3 and +4 oxidation state). Such double octahedra share corners with other double octahedra to form the $[V_8O_{16}]$ framework. The framework contains large tunnels parallel to the tetragonal c axis. Bi cations are positioned in the center of the tunnels.

5.4 Conclusions

The main conclusions of this study can be summarized as follows:

- The structure of a new possible compound, $BiVO_3$ perovskite, was calculated with SPuDS. According to SPuDS calculations, $BiVO_3$ could adopt an orthorhombic structure (*Pnm*a space group).

- The stability of $BiVO_3$ was discussed based on empirical relationships. The $BiVO_3$ tolerance factor (*t)* of 0.892 and octahedral factor of (*r_B/r_O*) of 0.457 fall well into the stability range of perovskites.

- Attempts to synthesize $BiVO_3$ by the thermal reduction of $BiVO_4$ were performed. $BiVO_4$ compound was first prepared by the solid state reactions and further thermal treated in a reducing atmosphere to convert it to $BiVO_3$. The reaction did not yield $BiVO_3$ but rather Bi^0, Bi_2O_3, V_2O_3, $Bi_{1.62}V_3O_{16}$, and $Bi_4V_{32}O_{11}$ phases.

- Attempts to stabilize $BiVO_3$ structure by forming solid solutions with $NdVO_3$ were also performed. The intermediary Bi-$NdVO_4$ compounds were synthesized and then thermal treated in reducing atmosphere to form Bi-doped $NdVO_3$. However, the XRD and XANES analysis confirmed that Bi^{3+} was not incorporated in $NdVO_3$ structure, but was reduced to Bi^0.

- Solid state reactions between Bi_2O_3 and V_2O_3 at atmospheric and low pressure have also been performed in order to obtain an insight into the processes that occur during the attempts to synthesise $BiVO_3$. A reduction-oxidation reaction between Bi^{3+} and V^{3+} has been identified as the process that averts the formation of $BiVO_3$ perovskite. At the processing temperatures (> 400 ^{o}C), the activation energy for the electron transfer from V to Bi was exceeded and the structure was destabilized. The interaction yielded metallic Bi and V_2O_5 instead of $BiVO_3$. However, the above result does not necessarily disprove the stability of $BiVO_3$ or the possibility of its formation by lower temperatures synthesis methods (such as hydro(solvo)thermal or ammonothermal) were the activation energy for the reduction-oxidation process would not be exceeded.

6 Summary and Conclusions

The Bi_2O_3–Nd_2O_3–VO_x system already contains compounds such as $BiVO_4$, $NdVO_4$ and $NdVO_3$ with interesting electronic properties, but has not been fully investigated. Thus, the principle aim of the thesis was to revise this system and search for new compounds/solid solutions which could show similar or even more attractive properties than the existing phases.

I first started with the investigation of the phase relations in the $BiVO_4$–$NdVO_4$ system. Using the solid-state method, I synthesized Bi-doped $NdVO_4$ samples with a nominal stoichiometry of $Bi_xNd_{1-x}VO_4$ ($x \leq 0.60$) and Nd-doped $BiVO_4$ with a nominal stoichiometry of $Nd_yBi_{1-y}VO_4$ ($y \leq 0.10$)]. Further on, I analyzed their structure and optoelectonic properties with XRD, EXAFS, DRS, and PL techniques. XRD analysis showed that the solid solubility limit for substitution of Nd with Bi in tetragonal $Bi_xNd_{1-x}VO_4$ is $x = 0.49(1)$. On the other side of the $BiVO_4$–$NdVO_4$ system, EXAFS, DRS, and PL studies proved that Nd does not substitute neither Bi nor V in the m-$BiVO_4$ structure, but forms the secondary tetragonal $NdVO_4$–based phase. XRD, EXAFS, DRS, and PL analyses of the $Bi_xNd_{1-x}VO_4$ samples indicated on the hybridization of Bi $6s^2$ and O $2p$ orbitals, which was the reason for:

- the decrease of the unit cell with the Bi concentration,
- the shortening of the distance between Bi^{3+} and the first oxygen coordination shell,
- the red shift of the absorption of $NdVO_4$ towards the visible range of the solar spectrum (from 3.53 to 3.1 eV for $x = 0.48$),
- the aparition of new emission lines in the PL spectra,
- the decrease of the lifetime of the photoexcited carriers.

Therefore, except for tetragonal $Bi_xNd_{1-x}VO_4$ is $x = 0.49(1)$, no other phases in the $BiVO_4$–$NdVO_4$ system were detected.

As many materials show disting properties at the nano level, also the properties of the $Bi_xNd_{1-x}VO_4$ nanoparticles could be different that the μ-sized ones. Thus, the synthesis of Bi-$NdVO_4$ nanoparticles was performed next and their structure and electronic properties were further investigated. Bi-$NdVO_4$ nanocrystals have been obtained for the first time by aqueous coprecipitation reaction under ambient

temperature and pressure, without further thermal treatment. This is a facile route that also saves energy. Using XRD and Raman analyses, I first confirmed the successful incorporation of Bi in $NdVO_4$ at the nanolevel. Further structural characterisation showed that the Bi-$NdVO_4$ nanoparticles have a tetragonal structure and are chemically homogeneous. With the Bi-doping, a continuous shift of all the $NdVO_4$ Raman modes to lower wavenumbers together with an increase in their FWHM values was clearly visible. As the Bi concentration, x, increases, the V−O stretching frequency decreases and (calculated) V−O bond length becomes longer. The morphology of the Bi-$NdVO_4$ nanoparticles was investigated by SEM analysis. $NdVO_4$ particles have acicular shape, with the length of about 50 nm and the diameter of ~10 nm, but with the increasing Bi concentration, they become spherical and form agglomerates. As the DRS analysis suggested, the main absorption edge of the Bi-$NdVO_4$ nanopowders was located in the visible part of the solar spectrum, at 410 nm (3.03 eV), while the one of $NdVO_4$ nanoparticles was located at 3.53 eV. The PL intensity of the Bi-$NdVO_4$ nanoparticles was lower than that of $NdVO_4$ which suggests a lower recombination rate and possibly a higher photocatalytic efficiency of the Bi-$NdVO_4$ nanoparticles than $NdVO_4$ alone.

Later on, I examined the photocatalytic activity of the Bi-$NdVO_4$ nanopowders and used RhB as the model of a persistent organic pollutant of the wastewaters. The redox ability of Bi-$NdVO_4$ nanoparticles was assessed by determining the energy positions of their valence and conduction bands and the results showed that they can oxidize H_2O to produce O_2 and decompose many organic pollutants. The photocatalytic tests were further conducted at pH 6.5 and pH 5 (with the addition of H_2O_2). I observed that at a pH of 6.5, the photocatalytic activity depended on the composition, i.e., Bi concentration. $NdVO_4$ showed the highest degradation, about 50% after 240 min of UVA light irradiation, while the photocatalytic rate decreased almost two-fold with the Bi concentration. At pH of 5, with both catalysts and H_2O_2 additive, the rate photodegradation of RhB significantly increased. The $Bi_{0.48}Nd_{0.52}VO_4$ sample showed the highest degradation rate, degrading about 87% of the dye after 60 min of UVA light irradiation, and also resulted in a thirty-fold increase of the kinetic rate.

Furthermore, I studied the synthesis possibility of a new compound, $BiVO_3$. Firstly, its structure was calculated with SPuDS and found to be orthorhombic, within the *Pnm*a space group. With a tolerance factor of 0.892 and octahedral factor

174

of 0.457, $BiVO_3$ falls well into the stability range of perovskites. The experimental work onthe synthesis of $BiVO_3$ resulted in the following conclusions:

- Thermal reduction from $BiVO_4$ did not yield $BiVO_3$ but rather Bi^0, Bi_2O_3, V_2O_3, $Bi_{1.62}V_3O_{16}$, and $Bi_4V_{32}O_{11}$ phases.

- An investigation of the stabilization of $BiVO_3$ with $NdVO_3$ by forming solid solutions showed on the reduction of Bi^{3+} to Bi^0, as the XRD and XANES analysis indicated.

- A reduction-oxidation reaction between Bi^{3+} and V^{3+} has been identified as the process that averts the formation of $BiVO_3$ perovskite.

- At high processing temperatures (> 400 ^{o}C), when the activation energy for the electron transfer from V to Bi was exceeded and the structure was destabilized, the interaction yielded metallic Bi and V_2O_5 instead of $BiVO_3$.

In the end, I propose that a successful synthesis of $BiVO_3$ might be accomplished by low-temperature synthesis methods (such as hydro(solvo)thermal or ammonothermal) were the activation energy for the reduction-oxidation process would not be exceeded.

7 Scientific contributions

Part of the work presented in Chapter 2 was partially published as:

- M. Dragomir, I. Arčon, S. Gardonio, M. Valant. Phase relations and optoelectronic characteristics in the $NdVO_4$–$BiVO_4$ system. *Acta Mat*er. **61** (2013) 1126–1135.

Part of the work presented in Chapter 5 was partially published as:

- M. Dragomir, M. Valant. Synthesis peliculiarities of the $BiVO_3$ perovskite. *Ceram. Int*. **39** (2013) 5963–5966.

8 Bibliography

1   H. Iwahara, T. Esaka, T. Sato, T. Takahashi. Formation of high oxide ion conductive phases in the sintered oxides of the system Bi_2O_3–Ln_2O_3 (Ln=La–Yb). J. *Solid State Chem.* **39** (1981) 173–180.

2   R. Horyn, M. Wolcyrz, A. Wojakowski. Synthesis and crystallographic characterisation of the $Bi_3RE_5O_{12}$–type phases. *J. Solid State Chem.* **116** (1995) 68–71.

3   Y. C. Lan, X. L. Chen, J. Q. Li. Structure of $Bi_2Nd_4O_9$ monoclinic phase. *J. Solid State Chem.* **153** (2000) 30–33.

4   Y. Sun, G. Rao, J. Yang, W. Tang et al. Subsolidus phase relations of Bi_2O_3-Nd_2O_3-CuO. *J. Alloys Compd.* **248** (1997) 106–111.

5   N. P. Smolyaninov, I. N. Belyaev. *Russ. J. Inorg. Chem.* **8** (1963) 632–634.

6   Ya. N. Blinovskov, A. A. Fotiev. The Bi_2O_3–V_2O_5 system. *Russ. J. Inorg. Chem.* **32** (1987) 254–256.

7   M. Touboul, C. Vachon. The Bi_2O_3–V2O5 system and crystal data about some bismuth vanadates. *Thermochim. Acta* **133** (1988) 65–66.

8   S. Sorokina, R. Enjalbert, P. Baules, A. Castro, J. Galy. Continuous structural evolution of $(Bi_2O_2)_2V_{2y}O_{4y+2}$ ($1 \leq y \leq 4$) Aurivillius phases in the Bi_2O_3–VO_2 system. *J. Solid State Chem.* **125** (1996) 54–62.

9   H. Brusset, F. Madaule-Aubry, B. Blanck, J. P. Glaziou, J. P. Laude. Study of mixed oxides of vanadium(V) and lanthanides. *Can. J. Chem.* **49** (1971) 3700–3707 (in French).

10   K. Kitayama, C. Mizokuchi, T. Katsura. Phase equilibria in the Nd_2O_3–V_2O_3–V_2O_5 system at 1200 °C. *Bull. Chem. Soc. Jpn.* **56** (1983) 695–669.

11   T. Shinike, T. Sakai, T. Sakai, G. Adachi, J.Shiokawa. Spectroscopic studies on the rare-earth vanadites. *Mater. Res. Bull.* **12** (1977) 685–688.

12   G. J. McCarthy, C.A. Sipe, K.E. McIlvried. Crystal chemistry of $ReVO_3$ phases (Re = La–Lu, Y). *Mater. Res. Bull.* **9** (1974) 1279–1284.

13   A. K. Bhattacharya, K. K. Mallick, A. Hartridge. Phase transition in $BiVO_4$. *Mater. Lett.* **30** (1997) 7–13.

14   M. W. Stoltzfus, P. M. Woodward, R. Seshadri, J. H. Klepeis, B. Bursten. structure and bonding in $SnWO_4$, $PbWO_4$, and $BiVO_4$: lone pairs vs inert pairs. *Inorg. Chem.* **46** (2007) 3839–3850.

15   S. Tokunaga, H. Kato, A. Kudo. Selective preparation of monoclinic and tetragonal $BiVO_4$ with scheelite structure and their photocatalytic properties. *Chem. Mater.* **13** (2001) 4624–4628.

16   Z. Zhao, Z. Li, Z. Zou. Electronic structure and optical properties of monoclinic clinobisvanite $BiVO_4$. *Phys. Chem. Chem. Phys.* **13** (2011) 4746–4753.

17 A. W. Sleight, H. Y. Chen, A. Ferretti, and D. E. Cox. Crystal growth and structure of BiVO₄. *Mater. Res. Bull.* **14** (1979) 1571–1581.

18 A. Kudo, K. Omori, H. Kato. A novel aqueous process for preparation of crystal form-controlled and highly crystalline BiVO₄ powder from layered vanadates at room temperature and its photocatalytic and photophysical properties. *J. Am. Chem. Soc.* **121** (1999) 11459–11467.

19 W. J. Jo, J.-W. Jang, K.-J. Kong, H. J. Kang, J. Y. Kim et al. Phosphate doping into monoclinic BiVO₄ for enhanced photoelectrochemical water oxidation activity. *Angew. Chem. Int. Ed.* **51** (2012) 3147–3151.

20 A. Walsh, Y. Yan, M. N. Huda, N. M. Al-Jassim, S. H.Wei. Band edge electronic structure of BiVO₄ elucidating the role of the Bi s and V d orbitals. *Chem Mater* **21** (2009) 547–51.

21 D. J. Payne, M. Robinson, R. G. Egdell, A. Walsh, J. McNulty et al. The nature of electron lone pairs in BiVO₄. *Appl. Phys. Lett.* **98** (2011) 212110 – 3 pp.

22 R. S. Roth, J. L. Waring. Synthesis and stability of bismuthotantalite, stibiotantalite and chemically similar ABO₄ compounds. *Am. Miner*al. **48** (1963) 1348–1356.

23 J. F. Li, A. S. Bhalla, L. E. Gross. Temperature sensitivity of the optical constants of BiVO₄. *Opt. Commun.* **92** (1992) 115–118.

24 H. Luo, A.H. Mueller, T.M. McCleskey, A.K. Burrell, E. Bauer et al. Structural and photoelectrochemical properties of BiVO₄ thin films. *J. Phys.* Chem. C **112** (2008) 6099–6102.

25 G. Xi, J. Ye. Synthesis of bismuth vanadate nanoplates with exposed {001} facets and enhanced visible-light photocatalytic properties. *Chem. Commun.* **46** (2010) 1893–1895.

26 L. Zhang, D. Chen, X. Jiao. Monoclinic structured BiVO₄ Nanosheets: hydrothermal preparation, formation mechanism, and coloristic and photocatalytic properties. *J. Phys. Chem. B* **110** (2006) 2668–2673.

27 J. D. Bierlein, A.W. Sleight. Ferroelasticity in BiVO₄. *Solid State Comm.* **16** (1975) 69–70.

28 K. Aizu. Possible species of 'ferroelastic' crystals and of simultaneously ferroelectric and ferroelastic crystals. *J. Phys. Soc, Japan* **27** (1969) 387–396.

29 W. I. F. David. Ferroelastic phase transition in BiVO₄: III. Thermodynamics. *J. Phys. C: Solid State Phys.* **16** (1983) 5093–5118.

30 R. van de Krol, M. Gräetzel. Photoelectrochemical hydrogen roduction. Springer (2012) Berlin.

31 J. Yu, A. Kudo. Effects of structural variation on the photocalytic performance of hydrothermally synthesised BiVO₄. *Adv. Funct. Mater.* **16** (2006) 2163–2169.

32 F. Wang, M. Shao, Liang Cheng, J. Hua, X. Wei. The synthesis of monoclinic bismuth vanadate nanoribbons and studies of photoconductive, photoresponse, and photocatalytic properties. *Mat. Res. Bull.* **44** (2009) 1687–1691.

33   D. Ke, T. Peng, L. Ma, P. Cai, K. Dai. Effects of hydrothermal temperature on the microstructures of $BiVO_4$ and its photocatalytic O_2 evolution activity under visible light. *Inorg. Chem.* **48** (2009) 4685–4691.

34   H. B. Li, G. C. Liu, X. C. Duan. Monoclinic $BiVO_4$ with regular morphologies: hydrothermal synthesis, characterisation and photocatalytic properties. *Mater. Chem. Phys.* **115** (2009) 9–13.

35   M. Han, X. Chen, T. Sun, O. Kiang Tan, M. S. Tsea. Synthesis of mono-dispersed m-$BiVO_4$ octahedral nano-crystals with enhanced visible light photocatalytic properties. *Cryst. Eng. Comm.* **13** (2011) 6674–6679.

36   L. Chen, S.-F. Yin, R. Huang, Q. Zhang, S.-L. Luo et al. Hollow peanut-like m-$BiVO_4$: facile synthesis and solar-light-induced photocatalytic property. *Cryst. Eng. Comm.* **14** (2012) 4217–4222.

37   A. M.-de la Cruz, U. M. G. Perez. Photocatalytic properties of $BiVO_4$ prepared by the co-precipitation method: degradation of rhodamine B and possible reaction mechanisms under visible irradiation. *Mater. Res. Bull.* **45** (2010) 135–141.

38   J. Yu, Y. Zhang, A. Kudo. Synthesis and photocatalytic performances of $BiVO_4$ by ammonia co-precipitation proces. *J. Solid State Chem.* **182** (2009) 223–228.

39   M. Wang, Q. Lin, H. Luan, Y. Han. Preparation, pharacterization and photocatalytic property of $BiVO_4$ photocatalyst by sol-gel method. *Appl. Mech. Mater.* **99–100** (2011) 1307–1311.

40   M. Wang, Q. Liu, Y. Che, L. Zhang, D. Zhang. Characterisation and photocatalytic properties of N-doped $BiVO_4$ synthesized via a sol-gel method. *J. Alloys Compd.* **548** (2013) 70–76.

41   W. Liu, L. Cao, G. Su, H. Liu et al. Ultrasound assisted synthesis of monoclinic structured spindle $BiVO_4$ particles with hollow structure and its photocatalytic property. *Ultrason. Sonochem.* **17** (2010) 669–674.

42   H. M. Zhang, J B. Liu, H. Wang, W. X. Zhang, H. Yan. Rapid microwave-assisted synthesis of phase controlled $BiVO_4$ nanocrystals and research on photocatalytic properties under visible light irradiation. *J Nanopart Res.* **10** (2008) 767–774.

43   Y. K. Kho, W. Y. Teoh, A. Iwase, L. Madler et al. Flame Preparation of Visible-Light-Responsive $BiVO_4$ Oxygen Evolution Photocatalysts with Subsequent Activation via Aqueous Route. *Appl. Mater. Interfaces* **3** (2011) 1997–2004.

44   C.-Y. Chung, C.-H. Lu. Reverse-microemulsion preparation of visible-light-driven nano-sized $BiVO_4$. *J. Alloys Compd.* **502** (2010) 1–5.

45   Y. Liu, J. Ma, Z. Liu, C. Dai et al. Low-temperature synthesis of $BiVO_4$ crystallites in molten salt medium and their UV-vis absorption. *Ceram. Int.* **36** (2010) 2073–2077.

46   G. P. Nagabhushana, G. Nagarajuband, G. T. Chandrappa. Synthesis of bismuth vanadate: its application in H_2 evolution and sunlight-driven photodegradation. *J. Mater. Chem. A* **1** (2013) 388–394.

47 A. Rabenau. The role of hydrothermal synthesis in preparative chemistry. *Angew. Chem. Int. Ed. Engl.* **24** (1985) 1026–1040.

48 L. Ren, L. Jin, J.-B. Wang, F. Yang et al. Template-free synthesis of $BiVO_4$ nanostructures: I. Nanotubes with hexagonal cross sections by oriented attachment and their photocatalytic property for water splitting under visible light. *Nanotechnology* **20** (2009) 115603 - 9 pp.

49 S. Liu, K. Yin, W. Ren, B. Cheng, and J. Yu. Tandem photocatalytic oxidation of Rhodamine B over surface fluorinated bismuth vanadate crystals. *J. Mater. Chem.* **22** (2012) 17759–17767.

50 J-Q Li, D.-F. Wang, H. Liu, et al. Nanosheet-based $BiVO_4$ hierarchical microspheres and their photocatalytic activity under visible light. *Phys. Status Solidi A* **209** (2012) 248–253.

51 F. Schuth, M. Hesse, K. K. Unger. Precipitation and Coprecipitation in Handbook of Heterogeneous Catalysis (editors G. Ertl, H. Kniizinger, J. Weitkamp) Vol. 2, Wiley-VCH (2008) Germany.

52 M. Lok. Coprecipitation, in Synthesis of Solid Catalysts (editors K. P. de Jong), Wiley-VCH Verlag GmbH & Co. KGaA, Weinheim, (2009) Germany.

53 J. A. Baglio, O. J. Sovers. Crystal structures of the rare earth orthovanadates. *J. Solid State Chem.* **3** (1971) 458–465.

54 C.-T. Au, W.-D. Zhang. Oxidative dehydrogenation of propane over rare-earth orthovanadates. *J. Chem. Soc., Faraday Trans.* **93** (1997) 1195–1204.

55 X. Wu, Y. Tao, L. Dong, J. Zhu, Z. Hu. Preparation of single-crystalline $NdVO_4$ nanorods, and their emissions in the ultraviolet and blue under ultraviolet excitation. *J. Phys. Chem. B* **109** (2005) 11544–11547.

56 S. Mahapatra, G. Madras, T. N. G. Row. Structural and photocatalytic activity of lanthanide (Ce, Pr, Nd) molybdovanadates. *J. Phys. Chem. C* **111** (2007) 6505–6511.

57 Y. Ni, J. M. Hughes. Crystal chemistry of the monazite and xenotime structures. *Am. Mineral.* **80** (1995) 21–26.

58 J. Zhang, J. Shi, J. Tan, X. Wang ,M. Gong. Morphology-controllable synthesis of tetragonal $LaVO_4$ nanostructures. *Cryst. Eng. Comm.* **12** (2010) 1079–1085.

59 V. Panchal, D. Errandonea, A. Segura, P Rodriguez-Hernandez et al. The electronic structure of zircon-type orthovanadates: Effects of high-pressure and cation substitution. *J. Appl. Phys.* **110** (2011) 043723-10 pp.

60 R.A. Fields, M. Birnbaum, C. L. Fincher. Highly efficient Nd: YVO_4 diode-laser end-pumped laser. *Appl. Phys. Lett.* **51** (1987) 1885 - 2 pp.

61 H. Zhang, H. Kong, S. Zhao, J. Jiu et al. Growth of new laser crystal Nd:$LuVO_4$ by the Czochralski method. *J. Cryst. Growth* **256** (2003) 292–297.

62 S. Mahapatra, G Madras, T. N. G. Row. Synthesis, characterisation and photocatalytic activity of lanthanide (Ce, Pr and Nd) orthovanadates. *Ind. Eng. Chem. Res.* **46** (2007) 1013–1017.

63   A. Di Paola, E. Garcia-Lopez, G. Marci, L. Palmisano. A survey of photocatalytic materials for environmental remediation. *J. Hazard. Mater.* **211–212** (2012) 3–29.

64   S. Mahapatra, S. K. Nayak, G. Madras, T. N. G. Row. Micowave synthesis and photocatalytic activity of nanolanthanide (Ce,Pr, and Nd) oryhovanadates. *Ind. Eng. Chem. Res.* **47** (2008) 6509–6516.

65   J. Liu, Y. Li. General synthesis of colloidal rare earth orthovanadates nanocrystals. *J. Mater. Chem.* **17** (2007) 1797–1803.

66   Z. Xu, C. Li, Z. Hou, C. Peng, J. Lin. Morphological control and luminescence properties of lanthanide orthovanadate $LnVO_4$ (La-Lu) nano-/microcrystals via hydrothermal process. *CrystEngComm* **13** (2011) 474–482.

67   M. Jang, K.M. Doxsee. Synthesis of anhydrous yttrium and rare earth vanadium oxides from aqueous solution. *CrystEngComm.* **13** (2011) 1210–1214.

68   R. Kalai Selvan, A. Gedanken, P. Anilkumar, G. Manikandan, C. J. Karunakaran. Synthesis and characterisation of rare earth orthovanadate (RVO_4; R=La, Ce, Nd, Sm, Eu&Gd) nanorods/nanocrystals/nanospindles by a facile sonochemical method and their catalytic properties. *J. Cluster. Sci.* **20** (2009) 291–305.

69   W. Fana, W. Zhaoa, L. You, X. Songa et al. Simple method to synthesize single-crystalline lanthanide orthovanadate nanorods. *J. Solid State Chem.* **177** (2004) 4399–4403.

70   J. Xu, C. Hu, G. Liua, H. Liu et al. Synthesis and visible-light photocatalytic activity of $NdVO_4$ nanowires. *J. Alloys Compd.* **509** (2011) 7968–7972.

71   R. S. Roth. Classification of perovskite and other ABO_3-type compounds. *J. Res. Natl. Bur. Stand. (U. S.)* **58** (1957) 75–88.

72   M. A. Pena, J. L. Fierro. Chemical structures and performance of perovskite oxides. *Chem. Rev.* **101** (2001) 1981–2017.

73   A. S. Bhalla, R. Guo, R. Roy. The perovskite structure- a review of its role in ceramic science and technology. *Mat. Res. Innovat.* **4** (2000) 3–26.

74   V. M. Goldschmidt. Die Gesetze der Krystallochemie ('The laws of Cristallochemistry'). *Die Naturwissenschaften* **14** (1928) 477–485 (In German).

75   C. A. Randall, A. S. Bhalla, T. R. Shrout, L. E. Cross. Classification and consequences of complex lead perovskite ferroelectrics with regard to B-Site Cation Order. *J. Mater. Res.* **5** (1990) 829–834.

76   R. D. Shannon. Revised Effective Ionic Radii and Systematic Studies of Interatomic Distances in Halides and Chaleogenides. *Acta Crystallogr., Sect. A: Cryst. Phys., Diffr., Theor. Gen. Crystallogr.* **32** (1976) 751–767.

77   Z. L. Wang, Z. C. Kang. Perovskites and Related Systems, pp. 93–149 in Functional and Smart Materials: Structural Evolution and Structure Analysis, Kang Plenum Publishing (1998) New York.

78   A. M. Glazer. The classification of tilted octahedra in perovskites. *Acta Cryst. B* **28** (1972) 3384–3392.

79   H. A. Jahn, E. Teller. Stability of polyatomic molecules in degenerate electronic states. I. Orbital Degeneracy. *Proc. R. Soc. Lond. A* **161** (1937) 220–235.

80   R. G. Pearson. Concerning Jahn-Teller effects. *Proc. Nat. Acad. Sci. USA* **72** (1975) 2104–2106.

81   H. L. Yakel. On the structures of some compounds of the perovskite type. *Acta Cryst.* **8** (1955) 394–398.

82   S. Geller. Crystallographic studies of perovskite-like compounds. IV. Rare earth scandates, vanadites, galliates, orthochromites. *Acta Cryst.* **10** (1957) 243–248.

83   H. P. Wijn. Perovskites II, Oxides with Corundum, Ilmenite and Amorphous Structures Landolt-Börnstein - Group III Condensed Matter. Volume 27 F3, 1994, pp 46–55.

84   M. H. Sage, G.R. Blake, C. Marquina, T. T. M. Palstra. Competing orbital ordering in RVO_3 vompounds: High-resolution x-ray diffraction and thermal expansion. *Phys. Rev. B* **76** (2007) 195102 - 9 pp.

85   J. Fujioka, T. Yasue, S. Miyasaka, Y. Yamasaki et al. Critical competition between two distinct orbital-spin ordered states in perovskite vanadates,.*Phys. Rev. B* **82** (2010) 14425 - 12 pp.

86   S. Miyasaka, Y. Okimoto, M. Iwama, Y. Tokura. Spin-orbital phase diagram of perovskite-type RVO_3 (R = rare-earth ion or Y). *Phys. Rev. B* **68** (2003) 100406 - 4pp.

87   R. M. Bozorth, H.J. Williams, D. E. Walsh. Magnetic Properties of Some Orthoferrites and cyanides at low temperatures. *Phys. Rev.* **103** (1956) 572–578.

88   Y. Kimishima, M. Uehara, T. Saitoh. Ca-doping effects on N-type ferrimagnetism of $NdVO_3$. *Solid State Commun.* **133** (2005) 559–564.

89   L. D Tung, M. R. Lees, G. Balakrishnan, D. McK Paul. Magnetization reversal in orthovanadate RVO_3 compounds (R = La, Nd, Sm, Gd, Er, and Y): Inhomogeneities caused by defects in the orbital sector of quasi-one-dimensional orbital system. *Phys. Rev. B* **75** (2007) 104404 - 8 pp.

90   L. Néel. Propriétés magnétiques des ferrites. Ferrimagnétisme et antiferromagnétisme. *Ann. Phys.* **3** (1948) 137–198 (In French).

91   M. J. Martinez-Lope, J.A. Alonso, M. Retuerto, M. T. Fernandez-Diaz. Evolution of the Crystal Structure of RVO_3 (R = La, Ce, Pr, Nd, Tb, Ho, Er, Tm, Yb, Lu, Y) Perovskites from Neutron Powder Diffraction Data. *Inorg. Chem.* **47** (2008) 2634–2640.

92   D. Saha, S. Mahapatra, T. N. G. Row, G. Madras. Synthesis, structure and photocatalytic activity in Orthorhombic Perovskites $LnVO_3$ and $Ln_{1-x}Ti_xVO_3$ (Ln = Ce, Pr and Nd). *Ind. Eng. Chem. Res.* **48** (2009) 7489–7497.

93   D. Khomskii. Classifying multiferroics: mechanisms and effects. *Physics* **2** (2009) 20.

94   N. A. Hill. Why are there so few magnetic ferroelectrics? *J. Phys. Chem. B* **104** (2000) 6694–6709.

95   P. Royen, K. Swars, Das System Wismutoxyd– Eisenoxyd im Bereich von O bis 55 mol. % Eisenoxyd. *Angew. Chem.* **69** (1957) 779 (in German).

96   F. Kubel, H. Schmid: Structure of a ferroelectric and ferroelastic monodomain crystal of the perovskite $BiFeO_3$. *Acta Crystallogr. B* **46** (1990) 698–702.

97   C. Michel, J.-M. Moreau, G. D. Achenbach, R. Gerson, W. J. James: The atomic structure of $BiFeO_3$. *Solid State Commun.* **7** (1969) 701–703.

98   J. B. Neaton, C. Ederer, U. V. Waghmare, N. A. Spaldin, K. M. Rabe: Firstprinciples study of spontaneous polarization in multiferroic $BiFeO_3$. *Phys. Rev. B* **71** (2005) 014113.

99   J. Iniguez, L. Bellaiche, D. Vanderbilt. First-principles study of $(BiScO_3)_{1-x}$ – $(PbTiO_3)_x$ alloys. *Phys. Rev. B* **67** (2003) 224107.

100   K. M. Rabe, C. H. Ah, J.-M. Triscone. Physics of ferroelectrics. A modern perspective. Springer-Verlag (2007) Berlin Heidelberg, Germany.

101   S. V. Kiselev, R. P. Ozerov, G. S. Zhdanov. Detection of magnetic order in ferroelectric $BiFeO_3$ by neutron diffraction. *Sov. Phys. Dokl.* **7** (1963) 742–744.

102   Wang, J. B. Neaton, H. Zheng, V. Nagarajan, S.B. Ogale et al. Epitaxial $BiFeO_3$ multiferroic thin film hetrostructures. *Science* **299** (2003) 1719–1721.

103   G. Xu, J. Li, D. Viehland. Ground state monoclinic (M_b) phase in $(110)_c$ $BiFeO_3$ epitaxial thin films. *Appl. Phys. Lett.* **89** (2006) 222901–222904.

104   R. J. Zeches, M. D. Rossell, J. X. Zhang, A. J. Hatt, Q. He et al., A strain-driven morphotropic phase boundary in $BiFeO_3$. *Science* **326** (2009) 977–980.

105   A. Belik. Polar and polar phases of $BiMO_3$: a review. *J. Solid State Chem.* **195** (2012) 32–40.

106   T. Atou, H. Chiba, K. Ohoyama, Y. Yamaguichi, Y. Syono: Structure determination of ferromagnetic perovskite $BiMnO_3$. *J. Solid State Chem.* **145** (1999) 639–642.

107   P. Baettig, R. Seshadri, N. Spaldin. Anti-polartiy in ideal $BiMnO_3$. *J. Am. Chem. Soc.* **129** (2007) 9854–9855.

108   V. Goian, S. Kamba, M. Savinov, D. Nuzhnyy et al. Absence of ferroelectricity in $BiMnO_3$ ceramics. *J. Appl. Phys.* **112** (2012) 074112.

109   H. Jeen, G. Singh-Bhalla, P. R. Mickel, K. Voigt et al. Growth and characterisation of multiferroic $BiMnO_3$ thin films. *J. Appl. Phys.* **109** (2011) 074104.

110   F.Sugawara, S. Iiida, Y. Syono, S. Akimoto. Magnetic properties and crystal distortions of $BiMnO_3$ and $BiCrO_3$. *J. Phys. Soc. Jpn.* **25** (1968) 1553–1558.

111   V. Samuel, S. C. Navale, A. D. Jadhav, A. B. Gaikwad, V. Ravi. Synthesis of ultrafine $BiMnO_3$ particles at 100 °C. *Mater. Lett.* **61** (2007) 1050–1051.

112   G. Catalan, J. F. Scott. Physics and applications of bismuth ferrite. *Adv. Mater.* **21** (2009) 2463–2485.

113   M. Valant, A.-K. Axelsson, N. Alford. Peculiarities of a Solid-State Synthesis of Multiferroic Polycrystalline $BiFeO_3$. *Chem. Mater.* **19** (2007) 5431–5436.

114   H. Bea, M. Bibes, A. Barthelemy, K. Bouzehouane et al. Influence of parasitic phases on the properties of $BiFeO_3$ epitaxial thin films. *Appl. Phys. Lett.* **87** (2005) 072508.

115   http://www.fujitsu.com/ca/en/news/pr/fma_20060802.html. Accessed on 12.03.2013.

116   T.-J. Park, G. C. Papaeftymiou, A. J. Viescas, A. R. Moodenbaugh, S. S. Wong. Size-Dependent magnetic properties of single-crystalline multiferroic $BiFeO_3$ Nanoparticles. *Nano Lett.* **7** (2006) 766–722.

117   J. T. Richardson, W. O. Milligan. Magnetic properties of colloidal nickelous oxide. *Phys. Rev.* **102** (1956) 1289–1294.

118   J. T. Richardson, D. I. Yiagas, B. Turk, K. Forster, M. V. Twigg. Origin of superparamagnetism in nickel oxide. *J. Appl. Phys.* **70** (1991) 6977–6983.

119   S. Li, Y.-H. Lin, B.-P. Zhang, Y. Wang, C-W. Nan. Controlled fabrication of $BiFeO_3$ uniform microcrystals and their magnetic and photocatalytic behaviours. *J. Phys. Chem. C* **114** (2010) 2903–2908.

120   H. Zheng, X. Liu, C. Diao, Y. Gu, W. Zhang. A separation mechanism of photogenerated charges and magnetic properties for $BiFeO_3$ microspheres synthesized by a facile hydrothermal method. *Phys. Chem. Chem. Phys.* **14** (2012) 8376–8381.

121   J. Luo, P. A. Maggard. Hydrothermal synthesis and photocatalytic activities of $SrTiO_3$ coated Fe_2O_3 and $BiFeO_3$. *Adv. Mater.* **18** (2006) 514–517.

122   L. Xiaomeng, X. Jimin, S. Yuanzhi, L. Jiamin. Surfactant-assisted hydrothermal preparation of submicrometer-sized two-dimensional $BiFeO_3$ plates and their photocatalytic activity. *J. Mater. Sci.* **42** (2007) 6824–6827.

123   C. M. Cho, J. H. Noh, I.-S. Cho, J.-S. An, K. S. Hong. Low-temperature hydrothermal synthesis of pure $BiFeO_3$ nanopowders using triethanolamine and their applications as visible-light photocatalysts. *J. Am. Ceram. Soc.* **91** (2008) 375–3755.

124   J.-T. Han, Y.-H. Huang, X.-J. Wu, C.-L. Wu et al. Tunable synthesis of bismuth ferrites with various morphologies. *Adv. Mater.* **18** (2006) 2145–2148.

125   U. A. Joshi, J. S. Jang, P. H. Borse, J. S. Lee. Microwave synthesis of single-crystalline perovskite $BiFeO_3$ nanocubes for photoelectrode and photocatalytic applications. *Appl. Phys. Lett.* **92** (2008) 242106 - 3 pp.

126   F. Gao, X. Chen, K. Yin, S. Dong, Z. Ren et al. Visible light photocatalytic properties of weak magnetic $BiFeO_3$ nanoparticle. *Adv. Mater.* **19** (2007) 2889–2892.

127   W. Luo, L. Zhu, N. Wang, H. Tang, M. Cao. Efficient removal of organic pollutants with magnetic nanoscaled $BiFeO_3$ as are usable heterogeneous fenton-like catalyst. *Environ. Sci. Technol.* **44** (2010) 1786–1791.

128   R. Guo, L. Fang, W. Dong, F. Zheng, M. Shen. Enhanced photocatalytic activity and ferromagnetism in Gd doped $BiFeO_3$ nanopraticles. *J. Phys. Chem. C* **114** (2010) 21390–21396.

129   J. Deng, S. Banerjee, S. K. Mohapatra, Y. R. Smith, M. Misra. Bismuth iron oxide nanoparticles as phtocatalyst for solar hydrogen generation from water. *J Fund. Renew. En. Appl.* **1** (2011) 101204.

130   C. Hengky, X. Moya, N. D. Mathur, S. Dunn. Evidence of high rate visble light photochemical decolorisation of Rhodamine B with $BiFeO_3$ nanoparticles associated with $BiFeO_3$ photocorrosion. *RSC Advances* **2** (2012) 11843–11749.

131   T. Xian, H. Yang, J. F. Dai, Z. Q. Wei, W. J. Feng. Photocatalytic properties of $BiFeO_3$ nanoparticles with different sizes. *Mater. Lett.* **65** (2011) 1573–1575.

132   C. M. Cho, J. H. Noh, I-S. Cho, J.-S. An, K. S. Hong. Low-temperature hydrothermal synthesis of pure $BiFeO_3$ nanopowders using triethanolamine and their applications as visible-light photocatalysts. *J. Am. Ceram. Soc.* **91** (2008) 3753–3755

133   S. Farhadi, M. Zaidi. Bismuth ferrite ($BiFeO_3$) nanopowder prepared by sucrose-assisted combustion method: A novel and reusable heterogeneous catalyst for acetyletion of amines, alcohols and phenols under solvent-free consitions. *J. Mol. Catal. A: Chem.* **299** (2009) 18–25.

134   S. Y. Yang, L. W. Martin, S. J. Byrnes, T. E. Conry et al. Photovoltaic effects in $BiFeO_3$. *Appl. Phys. Lett.* **95** (2009) 062909 - 3 pp.

135   M. Stock, S. Dunn. Influence of the Ferroelectric nature of lithium niobate to drive photocatalytic dye decolorization under artificial solar light. *J. Phys. Chem. C*. **116** (2012) 20854–20859.

136   www.census.gov/population/popclockworld.html. Accesed on 15.01.2013.

137   www.census.gov/population/international/data/worldpop/table_population.php. Accessed on 15. 01. 2013.

138   BP Statistical Review of World Energy, June 2012. Available from: www.bp.com. Accessed on 15.01.2013.

139   M. I. Hoffert, K. Caldeira, G. Benford, D. R. Criswell et al. Advanced Technology Paths to Global Climate Stability: Energy for a Greenhouse Planet. *Science* **298** (2002) 981–987.

140   J. Hansen, M. Sato, P. Kharecha, D. Beerling, R. Berner, et al. Target atmospheric CO_2: Where should humanity aim? *Open Atmos. Sci. J.* **2** (2008) 217–231.

141   www1.eere.energy.gov/hydrogenandfuelcells/mypp/pdfs/production.pdf (2011 Interim Update Hydrogen Production Multi-Year Research, Development and Demonstration Plan). Accessed on 15. 01. 2013.

142   N. S. Lewis, G. Crabtree. Basic Research Needs for Solar Energy Utilization: report of the Basic Energy Sciences Workshop on Solar Energy Utilization. April 18-21, 2005. US Department of Energy, Office of Basic Energy Science, Washington DC (2005). Available at: www.science.energy.gov.

143 O. Legrini, E. Olivieros, A.M. Braun. Photochemical processes for water treatment. *Chem. Rev.* **93** (1993) 671–698.

144 J.-M. Herrmann. Heterogeneous photocatalysis: fundamentals and applications to the removal of various types of aqueous pollutants. *Catalysis Today* **53** (1999) 115–129.

145 M. R. Hoffmann, S. T. Martin, W. Choi, D. W. Bahnemann. Environmental applications of semiconductor photocatalysis. *Chem. Rev.* **95** (1995) 69-96.

146 H. Helmholtz. On Some Laws of the Distribution of Electrical Currents in Material Conductors with Application to Experiments in Animal Electricity. *Pogg. Ann.* **89** (1853) 211.

147 L. G. Gouy. Sur la constitution de la charge électrique à la surface d'un électrolyte. *J. Phys. Theor. Appl.* **9** (1910) 457–468. Available at: http://electrochem.cwru.edu/estir/hist/hist-21-Gouy-1.pdf.

148 D. L. Chapman. A contribution to the theory of electrocapillarity. *London, Edinburgh Dublin Philos. Mag. J. Sci.* **25** (1913) 475–481. Available at: http://electrochem.cwru.edu/estir/hist/hist-25-Chapman.pdf.

149 R. Parson. The electrical double layer: recent experimental and theoretical developments. *Chem. Rev.* **90** (1990) 813–826.

150 Craig A. Grimes, Omman K. Varghese, Sudhir Ranjan. Light, Water, Hydrogen: The Solar Generation of Hydrogen by Water Photoelectrolysis. Springer (2008) U.S.A.

151 L. E. Brus. A simple model for the ionization potential, electron affinity, and aqueous redox potentials of small semiconductor crystallites. *J. Chem. Phys.* **79** (1983) 5566–5571.

152 A. Hagfeldtt, M. Gratzel. Light-Induced Redox Reactions in Nanocrystalline Systems. *Chem. Rev.* **95** (1995) 49–68.

153 A. Henglein. Q-particles: Size quantization effects in colloidal semiconductors. *Prog. Colloid Polym. Sci.* **73** (1987) 1–4.

154 F. E. Osterloh. Inorganic nanostructures for photoelectrochemical and photocatalytic water splitting. *Chem. Soc. Rev.* **42** (2013) 2294–2320.

155 C. Kornmann, D. W. Bahnemann, M.R. Hoffmann. Preparation and characterisation of quantum-size titanium dioxide. *J. Phys. Chem.* **92** (1988) 5196–5201.

156 M. Anpo, T. Shima, S. Kodama, Y. Kubokawa. Photocatalytic Hydrogenation of CH_3CCH with H_2O on Small-Particle TiO_2: size quantization effects and reaction intermediates. *J. Phys. Chem.* **91** (1987) 4305–4310.

157 R. F. Howe. Recent developments in photocatalysis. *Dev. Chem. Eng. Mineral Process.* **6** (1998) 55–84.

158 A. J. Hoffman, E. R. Carraway, M. R. Hoffmann. Photocatalytic production of H_2O_2 and organic peroxides on quantumsized semiconductor colloids. *Environ. Sci. Technol.* **28** (1994) 776–785.

159 J. P. Lepore, C. H. Langford, J. Vichovl, A. Vleek, Jr. Photochemistry and picosecond absorption spectra of aqueous suspensions of a polycrystalline

titanium dioxide optically transparent in the visible spectrum. *J. Photocltem. Photobiol. A: Chetn.* **75** (1993) 67–75.

160　Z. Zhang, J. T. Yates, Jr. Band Bending in Semiconductors: Chemical and Physical Consequences at Surfaces and Interfaces. *Chem. Rev.* **112** (2012) 5520−5551.

161　C.-C. Wang, Z. Zhang, J. Y. Ying. Photocatalytic decomposition of halogenated organics over nanocrystalline titania. *Nanostruct. Mater.* **9** (1997) 583–586.

162　Z. Zhang, C.-C. Wang, R. Zakaria, J. Y. Ying. Role of particle Size in nanocrystalline TiO_2-Based photocatalysts. *J. Phys. Chem. B* **102** (1998) 10871−10878.

163　H. Zhang, G. Chen, D. W. Bahnemann. Photocatalytic materials for environmental applications. *J. Mater. Chem.* **19** (2009) 5089–5121.

164　ASTM (2003) Standard Tables for Reference Solar Spectral Irradiances: Direct Normal and Hemispherical on 37 Tilted Surface. Standard G173-03, American Society for Testing and Materials, West Conshohocken, PA. Available from: http://www.astm.org/Standards/G173.htm.

165　R. van de Krol, Y. Liang, J. Schoonman. Solar hydrogen production with nanostructured metal oxides. *J. Mater. Chem.* **18** (2008) 2311–2320.

166　K. Sivula, F. Le Formal, M. Grätzel. Solar water splitting: progress using hematite (α-Fe_2O_3) photoelectrodes. *ChemSusChem* **4** (2011) 432–449.

167　A. Fujishima, K. Honda. Electrochemical photolysis of water at a semiconductor electrode. *Nature* **238** (1972) 37–38.

168　F. Steinbach. Influence of metal support and ultraviolet irradiation on the catalytic activity of nickel oxide. *Nature* **221** (1969) 657–658.

169　X. Chen, S. S. Mao. Titanium dioxide nanomaterials: synthesis, properties, modifications, and applications. *Chem. Rev.* **107** (2007) 2891–2959.

170　X. Liu, F. Wang, Q. Wang. Nanostructure-based WO_3 photoanodes for photoelectrochemical water splitting. *Phys. Chem. Chem. Phys.* **14.** (2012) 7894–7911.

171　F. T. Wagner, G. A. Somorjai. Photocatalytic hydrogen production on Pt-free $SrTiO_3$ in alkali hydroxide solutions. *Nature* **285** (1980) 559–560.

172　J. Sato, N. Saito, Y. Yamada, K. Maeda, T. Takata et al. RuO_2-Loaded *α*-Ge_3N_4 as a non-oxide Photocatalyst for overall water splitting. *J. Am. Chem. Soc.* **127** (2005) 4150–4151.

173　N. Arai, N. Saito, H. Nishiyama, Y. Inoue et al.. Overall water splitting by RuO_2-dispersed divalent-ion-doped GaN photocatalysts with d^{10} electronic configuration. *Chem. Lett.* **35** (2006) 796–797.

174　K. Maeda, T. Takata, M. Hara, N. Saito, et al. GaN:ZnO Solid Solution as a Photocatalyst for Visible-Light-Driven Overall Water Splitting. *J. Am. Chem. Soc.* **127** (2005) 8286–8287.

175　A. Kudo, Y. Miseki. Heterogeneous photocatalyst materials for water splitting. *Chem. Soc. Rev.* **38** (2009) 253–278.

176   Y. Inoue. Photocatalyic water splitting by RuO$_2$-loaded metal oxides and nitrides with d^0- and d^{10} - related electronic configurations. *Energy Environ. Sci.* **2** (2009) 364–386.

177   H. Nishiyama, H. Kobayashi, Y. Inoue. Effects of distortion of metal-oxygen octahedra on photocatalytic water splitting performance of RuO$_2$-loaded niobium and tantalum phosphate bronzes. *ChemSusChem* **4** (2011) 208–215.

178   M. Kohno, S. Ogura, K. Sato, Y. Inoue. Reduction and oxidation of BaTi$_4$O$_9$ with a pentagonal tunnel structure. Effects on radical formation upon UV irradiation and on the activity of RuO$_2$/BaTi$_4$O$_9$ photocatalyst for water decomposition. *J. Chem. Soc., Faraday Trans.* **93** (1997) 2433–2437.

179   S. Ogura, M. Kohno, K. Sato, Y. Inoue. Effects of RuO$_2$ on activity for water decomposition of a RuO$_2$/Na$_2$Ti$_3$O$_7$ photocatalyst with a zigzag layer structure. *J. Mater. Chem.* **8** (1998) 2335–2337.

180   A. Kudo, H. Kato, S. Nakagawa. Water splitting into H$_2$ and O$_2$ on new Sr$_2$M$_2$O$_7$ (M= Nb and Ta) photocatalysts with layered perovskite structures: factors affecting the photocatalytic activity. *J. Phys. Chem. B* **104** (2000) 571–575.

181   Y. Sasaki, H. Nemoto, K. Saito, A. Kudo. Solar water splitting using powdered photocatalysts driven by Z-schematic interparticle electron transfer without an electron mediator. *J. Phys. Chem. C* **113** (2009) 17536–17542.

182   M. Long, W. Cai, J. Cai, B. Zhou, X. Chai. Y. Wu. Efficient photocatalytic degradation of phenol over Co$_3$O$_4$/BiVO$_4$ composite under visible light irradiation. *J Phys. Chem. B* **110** (2006) 20211–20216.

183   J.Yu, A. Kudo. Effects of structural variation on the photocatalytic performance of hydrothermally synthesized BiVO$_4$. *Adv. Func. Mater.* **16** (2006) 2163–2169.

184   L. Ge. Novel visible-light driven Pt/BiVO$_4$ photocatalyst for efficient degradation of methyl orange. *J. Mol. Catal. A: Chem.* **282** (2008) 62–66.

185   S. W. Cao, Z. Yin, J. Barber, F. Y. C. Boey, S. C. J. Loo et al. Preparation of Au-BiVO$_4$ heterogeneous nanostructures as highly efficient visible-light photocatalysts. *ACS Appl. Mater. Interfaces* **4** (2012) 418–423.

186   B. Zhou, X. Zhao, H. Liu, J. Qu, C. P. Huang. Synthesis of visible-light sensitive m-BiVO$_4$ (M = Ag, Co, and Ni) for the photocatalytic degradation of organic pollutants. *Sep. Purif. Technol.* **77** (2011) 275–282.

187   B. Zhou, X. Zhao, H. Liu, J. Qu, C. P. Huang. Visible-light sensitive cobalt-doped BiVO$_4$ (Co-BiVO$_4$) photocatalytic composites for the degradation of methylene blue dye in dilute aqueous solutions. *Appl. Catal., B* **99** (2010) 214–221.

188   L. Liang, X. Luo, X. Lin, C. Xu, Z. Zhao. Preparation and characterisation of Fe-doped BiVO$_4$. *Mater. Sci. Forum* **620–622** (2009) 655–658.

189   A. Zhang, J. Zhang. Syntheses and activities of visible light driven Cu/BiVO$_4$ composite photocatalysts. *Acta Phys. -Chim. Sin.* **26** (2010) 1337-1342.

190   Y. Weifeng, I. Hideo, Y. Jinhua. Effects of molybdenum substitution on the photocatalytic behavior of BiV0$_4$. *Dalton Trans.* **11** (2008) 1426–1430.

191 Y. Liang, T. Tsubota, L. P. A. Mooij, R. van de Krol. Highly improved quantum efficiencies for thin film $BiVO_4$ photoanodes. *J. Phys. Chem. C* **115** (2011) 17594–17598.

192 W. J. Jo, W. J. Jang, K. Kong, H. J. Kang, J. Y. Kim et al. Phosphate doping into monoclinic $BiVO_4$ for enhanced photoelectrochemical water oxidation activity *Angew Chem., Int. Ed.* **51** (2012) 3147–3151.

193 J. Bi, J. Li, L. Wu, H. Zheng, W. Su. Effects of aluminum substitution on photocatalytic property of $BiVO_4$ under visible light irradiadiation. *Mater. Res. Bull.* **47** (2012) 850–855.

194 W. Yao, J. J. Ye. Photophysical and photocatalytic properties of Ca1-xBixVxMo1-xO4 solid solutions. *J. Phys. Chem. B* **110** (2006) 11188–11195.

195 S. Mahapatra, G Madras, T. N. G. Row. Synthesis, characterisation and photocatalytic activity of lanthanide (Ce, Pr and Nd) orthovanadates. *Ind. Eng. Chem. Res.* **46** (2007) 1013–1017.

196 S. Mahapatra, S. K. Nayak, G. Madras, T. N.G. Row. Microwave Synthesis and Photocatalytic Activity of Nano Lanthanide (Ce, Pr, and Nd) Orthovanadates. *Ind. Eng. Chem. Res.* **47** (2008) 6509–6516.

197 S. Mahapatra, R. Vinu, T. N. G. Row, G. Madras. Kinetics of photoconversion of cyclohexane and benzene by $LnVO_4$ and $LnMo_{0.15}V_{0.85}O_4$ (Ln = Ce, Pr and Nd). *Appl. Catal., A* **351** (2008) 45–53.

198 P. P. Ewald. Fifty Years of X-Ray Diffraction. International Union of Crystallography, The Netherlands, 1962. Available at: http://www.iucr.org/publ/50yearsofxraydiffraction.

199 V. K. Pecharsky, P. Y. Zavalij. Fundamentals of Powder Diffraction and Structural Characterisation of Materials, 2nd Ed., Kluwer Academic Publishers (2006) U.S.A.

200 A. Kodre, I. Arčon, J. Padežnik Gomilšek. X-ray absorption spectroscopy and related techniques. *Acta Chim. Slov.* **51** (2004) 1–10.

201 N. Novak Tušar, N. Zabukovec Logar, G. Vlaic, I. Arčon et al. Local environment of manganese incorporated in mesoporous MCM-41. *Microporous Mesoporous Mater.* **82** (2005) 129–136.

202 D.C. Koningsberger, R. Prins, X-ray Absorption, Principles, techniques of EXAFS, SEXAFS and XANES, John Wiley & Sons (1988) New York.

203 Ravel B, Newville M. ATHENA, ARTEMIS, HEPHAESTUS: data analysis or X-ray absorption spectroscopy using IFEFFIT. *J. Synchrotron Radiat.* **12** (2005) 537–541.

204 P. Kubelka, F. Munk. Ein beitrag zur optik der farbanstriche zeitschr. *F. Techn Physik* **12a** (1931) 593–601 (in German).

205 M. A. Butler. Photoelectrolysis and physical properties of the semiconducting electrode WO_3. *J. Appl. Phys.* **48** (1977) 1914.

206 R. Lakowicz Joseph. Principles of Fluorescence Spectroscopy, 3rd edition (2006) Springer US.

207 http://cnx.org/content/m38357/latest/?collection=col10699/latest. Accesed on 08.05.2013.

208 http://www.edinburghphotonics.com/files/file/brochures/FLS920-Brochure.pdf. Accessed on 8. 05. 2013.

209 Manual of the fluorescence lifetime. Edinburgh Instruments (2000) UK.

210 J. H. Rehr, R. C. Albers, S. I. Zabinsky. High-order multiple-scattering calculations of X-ray-absorption fine structure. *Phys. Rev. Lett.* **69** (1992) 3397–3400.

211 W. O. Milligan, L. W. Vernon. Crystal structure of heavy metal orthovanadates. *J. Phys. Chem.* **56** (1952) 145–148.

212 J. Xu, C. Hu, G. Liu, H. Liu, G. Du et al. Synthesis and visible-light photocatalytic activity of $NdVO_4$ nanowires. *J. Alloys Compd.* **509** (2011) 7968–7972.

213 R. Kalai Selvan, A. Gedanken, P. Anilkumar, G. Manikandan, C. Karunakaran. Synthesis and characterisation of rare earth orthovanadate (RVO_4, R = La, Ce, Nd, Sm, Eu&Gd) nanorods/nanocrystals/nanospindles by a facile sonochemical method and their catalytic properties. *J. Cluster Sci.* **20** (2009) 291–305.

214 X. Wu, Y. Tao, L. Dong, J. Zhu, Z. Hu. Preparation of single-crystalline $NdVO_4$ banorods, and their emissions in the ultraviolet and blue under ultraviolet excitation. *J. Phys. Chem. B* **109** (2005) 11544–11547.

215 E. Antic-Fidancev, J. Holsa, M. Lemaitre-Blaise, P. Porcher. Simulation of the energy level scheme of Nd^{3+} and Eu^{3+} ions in rare-earth orthovanadates and phosphates. *J. Phys: Condens. Matter.* **3** (1991) 6829–6843.

216 R. Balda, J. Fernandez, E. E. Nyein, U. Hommerich. Infrared to visible upconversion of Nd^{3+} ions in KPb_2Br_5 low phonon crystal. *Opt. Express* **14** (2006) 3993–4004.

217 H. Deng, S. Yang, S. Xiao, H. M. Gong, Q. Q. Wang. Controlled synthesis and upconverted avalanche luminescence of cerium(III) and neodymium(III) orthovanadate nanocrystals with high uniformity of size and shape. *J. Am. Chem. Soc.* **130** (2008) 2032–2040.

218 X. N. Peng, X. Zhang, L. Yu, L. Zhou. Preparation and photoluminescence properties of $NdVO_4$ nanotubes in AAO template. *Mod. Phys. Lett. B* **23** (2009) 2647–2653.

219 A. W. Sleight, H. Chen, A. Ferretti. Crystal growth and structure of $BiVO_4$. *Mater. Res. Bull.* **14** (1979) 1571–1581.

220 M. A. Butler, D. S. Ginley. Prediction of flatband potentials at semiconductor-electrolyte interfaces from atomic electronegativities. *J. Electrochem. Soc.* **125** (1978) 228–232.

221 M. Long, W. Cai, J. Cai, B. Zhou, X. Chai. Y. Wu. Efficient photocatalytic degradation of phenol over $Co_3O_4/BiVO_4$ composite under visible light irradiation. *J Phys. Chem. B* **110** (2006) 20211–20216.

222 Y. Xu, M. A. A. Schoonen. The absolute energy positions of conduction and valence bands of selected semiconducting minerals. *Am. Mineral.* **85** (2000) 543–556.

223 H. Jiang, H. Endo, H. Natori, M. Nagai, K. Kobayashi. Fabrication and photocatlytic activity of spherical-shaped $BiVO_4$ photocatalysts through solution combustion synthesis method. *J. European Ceram. Soc.* **28** (2008) 2955–2962.

224 Y. Sasaki, H. Nemoto, K. Saito, A. Kudo. Solar water splitting using powdered photocatalysts driven by Z-schematic interparticle electron transfer without an electron mediator. *J. Phys. Chem. C* **113** (2009) 17536–17542.

225 W. Liu, Y. Yu, L. Cao, G. Su, X. Liu et al. Synthesis of monoclinic structured $BiVO_4$ spindly microtubes in deep eutectic solvent and their application for dye degradation. *J. Hazard. Mater.* **181** (2010) 1102–1108.

226 C. Yu, K. Yang, C. J. Yu, F. Cao, X. Zhou. Fast fabrication of Co_3O_4 and $CuO/BiVO_4$ composite photocatalysts with high crystallinity and enhanced photocatalytic activity via ultrasound irradiation. *J. Alloys. Compd.* **509** (2011) 4547–4552.

227 M. Shang, W. Wang, L. Zhou, S. Sun, W. Yin. Nanosized $BiVO_4$ with high visible-light-induced photocatalytic activity: Ultrasonic-assisted synthesis and protective effect of surfactant. *J. Hazard. Mater.* **172** (2009) 338–344.

228 Y. Liu, D. Tu, H. Zhuab, X. Chen. Lanthanide-doped luminescent nanoprobes: controlled synthesis, optical spectroscopy, and bioapplications. *Chem. Soc. Rev.*, 2013, Advance Article. DOI: 10.1039/C3CS60060B.

229 C. Yao, Y. Tong. Lanthanide ion-based luminescent nanomaterials for bioimaging. *TrAC, Trends Anal. Chem.* **39** (2012) 60–71.

230 X. Huang, S. Han, W. Huang, X. Liu. Enhancing solar cell efficiency: the search for luminescent materials as spectral converters. *Chem. Soc. Rev.* **42** (2013) 173—201.

231 C. Che Lin, Ru-Shi Liu. Advances in Phosphors for Light-emitting Diodes. *J. Phys. Chem. Lett.* **2** (2011) 1268–1277.

232 C. Sun, H. Liab, L. Chen. Nanostructured ceria-based materials: synthesis, properties, and applications. *Energy Environ. Sci.* **5** (2012) 8475–8505.

233 Handbook on the Physics and Chemistry of Rare Earths, Volume 41, chapter 251 (edited by Karl A. Gschneidner, Jean-Claude G. Bünzli and Vitalij K. Pecharsky) (2011) North Holland, The Netherlands.

234 T. Matsuzawa, Y. Aoki, N. Takeuchi, Y. Murayama. A New Long Phosphorescent Phosphor with High Brightness, $SrAl_2O_4:Eu^{2+},Dy^{3+}$. *J. Electrochem. Soc.* **143** (1996) 2670–2673.

235 Y.-S. Chang, F.-M. Huang, Y.-Y. Tsai, L.-G. Teoh. Synthesis and photoluminescent properties of $YVO_4:Eu^{3+}$ nano-crystal phosphor prepared by Pechini process. *J. Lumin.* **129** (2009) 1181–1185.

236 N. Shanta Singh, R. S. Ningthoujam, G. Phaomei, S. Dorendrajit Singh, et al. Re-dispersion and film formation of $GdVO_4$: Ln^{3+} (Ln^{3+} = Dy^{3+}, Eu^{3+}, Sm^{3+},

Tm $^{3+}$) nanoparticles: particle size and luminescence studies. *Dalton Trans.* **41** (2012) 4404–4412.

237 G. Blasse, A. Bril. Investigation on Bi^{3+} activated phosphors. *J. Chem. Phys.* **48** (1968) 217–222.

238 G. Blasse, A. Bril. Luminescence of Phosphors Based on Host Lattices ABO$_4$ (A is Sc, In; B is P, V, Nb). *J. Chem. Phys.* **48** (1969) 2974–2980.

239 D. Chen, Y. Yu, P. Huang, H. Lin, Z. Shan et al. Color-tunable luminescence for Bi^{3+}/Ln^3+:YVO$_4$ (Ln = Eu, Sm, Dy, Ho) nanophosphors excitable by near-ultraviolet light. *Phys. Chem. Chem. Phys.* **12** (2010) 7775–7778.

240 S. Neeraj, N. Kijima, A. K. Cheetham. Novel red phosphors for solid state lighting; the system Bi$_x$Ln$_{1-x}$VO$_4$; Eu^{3+}/Sm^{3+} (Ln = Y, Gd). *Solid State Commun.* **131** (2004) 65–69.

241 Z. Xia, D. Chen, Min Yang, T. Ying. Synthesis and luminescent properties of YVO$_4$:Eu^{3+}, Bi^{3+} phosphor with enhanced photoluminescence by Bi^{3+} doping. *J. Phys. Chem. Solids* **71** (2010) 175–180.

242 B. N. Mahalley, S. J. Dhole, R. B. Pode, G. Alexander. Photoluminescence in GdVO$_4$:Bi^{3+}, Eu^{3+} red phosphor. *Appl. Phys. A: Mater. Sci. Process* **70** (2000) 39–45.

243 L. Chen, K.-J. Chen, S.-F. Hud, R.-S. Liu. Combinatorial chemistry approach to searching phosphors for white light-emitting diodes in (Gd-Y-Bi-Eu)VO$_4$ quaternary system. *J. Mater. Chem.* **21** (2011) 3677–3685.

244 X. Y. Huang, J. X. Wang, D. C. Yu, S. Ye et al. Spectral conversion for solar cell efficiency enhancement using YVO$_4$:Bi^{3+}, Ln^{3+}(Ln = Dy, Er, Ho, Eu, Sm, and Yb) phosphors. *J. Appl. Phys.* **109** (2011) 113526 - 7 pp.

245 S. Takeshita, K. Nakayama, T. Isobe, T. Sawayama, Seiji Niikura. Optical Properties of Transparent Wavelength-Conversion Film Prepared from YVO$_4$:Bi^{3+},Eu^{3+} Nanophosphors. *J. Electrochem. Soc.* **156** (2009) J273–J277.

246 X. Wu, Y. Tao, L. Dong, J. Zhu, Z. Hu. Preparation of single-crystalline NdVO$_4$ nanorods, and their emissions in the ultraviolet and blue under ultraviolet excitation. *J. Phys. Chem.* **B** 109 (2005) 11544–11547.

247 Recommendations on nomenclature for contamination phenomena in Precipitation from aqueous solution. *Pure Appl. Chem.* **37** (1975) 463.

248 F. Schuth, M. Hesse, K. K. Unger. Precipitation and Coprecipitation in Handbook of Heterogeneous Catalysis (editors G. Ertl, H. Kniizinger, J. Weitkamp). Wiley-VCH (2008) Germany.

249 V. Lamer, R. Dinegar. Theory, production and mechanism of formation of monodispersed hydrosols. *J. Am. Chem. Soc.* **72** (1950) 4847–4854.

250 E. Matjevic. Monodispersed metal (hydrous) oxides-a fascinating field of colloid science. *Acc. Chem. Res.* **14** (1981) 22–29.

251 J. Zeng, X. Wang, J. G. Hou (2011). Colloidal Hybrid Nanocrystals: Synthesis, Properties, and Perspectives, Nanocrystal (edited by dr. Yoshitake Masuda) InTech. Available from:

http://www.intechopen.com/books/nanocrystal/colloidal-hybrid-nanocrystals-synthesis-properties-andperspectives.

252 C. Herring. Some theorems on the free energies of crystal surfaces. *Phys. Rev.* **82** (1951) 87–93.

253 Controlled Nanofabrication: Advances and Applications. (edited by Ru-Shi Liu) Pan Stanford Publishing (2013) USA.

254 M. Lok. Coprecipitation, in Synthesis of Solid Catalysts (editor K. P. de Jong), Wiley-VCH Verlag GmbH & Co. KGaA, Weinheim (2009) Germany.

255 M. J. Desmond, M. A. Pepera, US Patent 4686 203 (1987) (Standard Oil Company).

256 D. Chen, Y. Yu, P. Huang, H. Lin, Z. Shan et al. Color-tunable luminescence for Bi^{3+}/Ln^{3+}:YVO_4 (Ln = Eu, Sm, Dy, Ho) nanophosphora excitable by near-ultraviolet light. *Phys. Chem. Chem. Phys.* **12** (2010) 7775–7778.

257 S. Takeshita, T. Isobe, S. Niikura. Low-temperature wet chemical synthesis and photoluminescence properties of YVO_4:Bi^{3+}, Eu^{3+} nanophosphors. *J. Lumin.* **9** (2008) 1515–1522.

258 Z. Xia, D. Chen, M. Yang, T. Ying. Synthesis and luminescence properties of YVO_4:Eu^{3+}, Bi^{3+} phosphor with enhanced photoluminescence by Bi doping. *J. Phys. Chem. Solids.* **71** (2010) 175–180.

259 D. A. Skoog, F. J. Holler, T. A. Nieman. Chapter 18 in Principles of Instrumental analysis, fifth edition. Saunders College Publishing. (1998) U.S.A.

260 J. Garcia, L.E. Bausa, D. Jaque. An introduction to the Optical Spectroscopy of inorganic solids. John Wiley&Sons (2008) U.S.A.

261 C. C. Santos, E. N. Silva, A. P. Ayala, I. Guedes, P. S. Pizani et al. Raman investigations of rare earth orthovanadates. *J. Appl. Phys.* **101** (2007) 053511 - 5pp.

262 S. Jandl, Y. Lévesque, V. Nekvasil, M. Bettinelli. Raman active phonon and crystal-field studies of Yb^{3+} doped $NdVO_4$. *Opt. Mater.* **32** (2010) 1549–1552.

263 A.-D. Nguyen, K. Murdoch, N. Edelstein, L. A. Boatner, M. M. Abraham. Polarization dependence of phonon and electronic Raman intensities in $PrVO_4$ and $NdVO_4$. *Phys. Rev. B* **56** (1997) 7974–7987.

264 T.-T. Kang, A. Hashimoto, A. Yamamoto. Raman scattering of indium-rich $Al_xIn_{1-x}N$: Unexpected two-mode behavior of $A_1(LO)$. *Phys. Rev. B* **79** (2009) 033301 - 4 pp.

265 M. Lieoeois-Duyckaerts, P. Vibrational studies of molybdates, tungstates and related compounds-II. New Raman data and assignments for the scheelite-type compounds. *Spectrochim. Ac*ta **28A** (1972) 2037–2061.

266 H. Liu, J. Yuan, Z. Jiang, W. Shangguan, H. Einagac et al. Novel photocatalyst of V-based solid solutions for overall water splitting. *J. Mater. Chem.* **21** (2011) 16535–16543.

267 F. D. Hardcastle, I. E. Wachs. Determination of vanadium-oxygen bond distances and bond orders by Raman spectroscopy. *J. Phys. Chem.* **95** (1991) 5031–5041.

268 H. M. Zhang, J. B. Liu, H. Wang, W. X. Zhang, H. Yan. Rapid microwave-assisted synthesis of phase controlled $BiVO_4$ nanocrystals and research on photocatalytic properties under visible light irradiation. *J. Nanopart. Res.* **10** (2008) 767–774.

269 J. Xu, C. Hu, G. Liu, H. Liu, G. Du et al. Synthesis and visible-light photocatalytic activity of $NdVO_4$ nanowires. *J Alloys Compd.* **509** (2011) 7968– 7972.

270 J. W. Weaver, E. B. Jeroski, I. S. Goldstein. Toxicity of dyes and related compounds to wood-destroying fungi. *Appl. Environ. Microbiol.* **7** (1959) 145–149.

271 M. Gunay. Eco-friendly textile dyeing and finishing. InTech, Croatia. http://dx.doi.org/10.5772/3436. A free online edition was obtained at: http://www.intechopen.com/books/eco-friendly-textile-dyeing-and-finishing. Accessed on 24.06.2013.

272 L. C. Edwards, H. S. Freeman. Synthetic dyes based on environmental considerations. Part 3: Aquatic toxicity of iron-complexed azo dyes. *Color. Technol.* **121** (2005) 265–270.

273 H. Zollinger. Color Chemistry: Syntheses, Properties, and Applications of Organic Dyes and Pigments. VCHA (2003) Switzerland.

274 A. A. Vaidya, K. V. Datye. Environmental pollution during chemical processing of synthetic fibers. *Colourage* **14** (1982) 3–10.

275 T. Robinson, G. McMullan, R Marchant, P. Nigam. Remediation of dyes in textile effluent: a critical review on current treatment technologies with a proposed alternative. *Bioresour. Technol.* **77** (2001) 247–255.

276 I. H. Cho, K. D. Zoh. Photocatalytic degradation of azo dye (Reactive Red 120) in TiO_2/UV system: Optimization and modeling using a response surface methodology (RSM) based on the central composite design. *Dyes and Pigments* **75** (2007) 533–543.

277 IUPAC. Compendium of Chemical Terminology, 2nd ed. (the "Gold Book"). Compiled by A. D. McNaught and A. Wilkinson. Blackwell Scientific Publications, Oxford (1997). XML on-line corrected version: http://goldbook.iupac.org (2006) created by M. Nic, J. Jirat, B. Kosata; updates compiled by A. Jenkins. Accessed on 02. 07. 2013.

278 Colour Index International 2013. Society of Dyers and Colourists and American Association of Chemists and Colourists. Available online at: www.colour-index.com. Accessed on 03. 07. 2013.

279 http://www.gzchem.com/product/Dyestuff/AZOIC%20DYES.htm Accessed on 24. 06. 2013.

280 http://stainsfile.info/StainsFile/dyes/class/dyeclass.htm. Accessed on 24. 06. 2013.

281 M. C Venceslau, S. Tom, J. J. Simon. Characterisation of textile wastewater-a review. *Environ. Technol.* **15** (1994) 917–929.

282 C. Zaharia Carmen, D. Suteu Textile Organic Dyes – Characteristics, Polluting Effects and Separation/Elimination Procedures from Industrial Effluents – A Critical Overview, Organic Pollutants Ten Years After the Stockholm Convention - Environmental and Analytical Update. Editor Dr. Tomasz Puzyn, InTech (2012). Available from: http://www.intechopen.com/books/organic-pollutants-ten-yearsafter-the-stockholm-convention-environmental-and-analytical-update/textile-organic-dyes-characteristicspolluting-effects-and-separation-elimination-procedures-from-in. Accessed on 24. 06. 2013.

283 A. B. Dos Santos, F. J. Cervantes, J. B Van Lier. Azo dye reduction by thermophilic anaerobic granular sludge, and the impact of the redox mediator AQDS on the reductive biochemical transformation. *Appl. Microbiol. Biotechnol.* **64** (2004) 62–69.

284 U. Wiesmann, I. S. Choi, E. M. Dombrowski. Fundamentals of Biological Wastewater Treatment. Wiley-VCH Verlag GmbH&Co. (2007) Weinheim, Germany.

285 R. S. Thakur, R. Chaudhary, C. Singh. Fundamentals and applications of the photocatalytic treatment for the removal of industrial organic pollutants and effects of operational parameters: A review. *J. Renewable Sustainable Energy* **2** (2010) 042701 – 37 pp.

286 N. Azbar, T. Yonar, K. Kestioglu. Comparison of various advanced oxidation processes and chemical treatment methods for COD and color removal from a polyester and acetate fiber dyeing effluent. *Chemosphere* **55** (2004) 35–43.

287 Taner Yonar (2011). Decolorisation of Textile Dyeing Effluents Using Advanced Oxidation Processes. Advances in Treating Textile Effluent, Prof. Peter Hauser (Ed.), ISBN: 978-953-307-704-8, InTech, DOI: 10.5772/18908. Available from: http://www.intechopen.com/books/advances-in-treating-textile-effluent/decolorisation-of-textile-dyeing-effluents-using-advanced-oxidation-processes. Accesed on 02. 07. 2013.

288 http://www.chemspider.com/Chemical-Structure.6439.html. Accessed on 24. 06. 203.

289 C. Hsu, Y. Liu. Rhodamine B-anchored silica nanoparticles displaying white-light photoluminescence and their uses in preparations of photoluminescent polymeric films and nanofibers. *J. Colloid Interface Sci.* **350** (2010) 75–82.

290 J. Rodriguez-Ramos Fernandez, T. E. Rocke. Use of Rhodamine B as a biomarker for oral plague vaccination of Prairie Dogs. *J. Wildl. Dis.* **47** (2011) 765–768.

291 http://www.efsa.europa.eu/en/efsajournal/doc/263.pdf. Accessed on 24. 06. 2013.

292 T. Wu, G. Liu, J. Zhao, H. Hidaka, N. Serpone. Photoassisted degradation of dye Pollutants. Self-photosensitized oxidative transformation of rhodamine B under visible light irradiation in aqueous TiO_2 dispersions. *J. Phys. Chem. B* **102** (1998) 5845–5851.

293 H. Zhong, Y. Shaogui, J. Yongming, S. Chen. Microwave photocatalytic degradation of rhodamine B using TiO_2 supported on activated carbon: mechanism implication. *J. Environ. Sci. (Beijing, China)* **21** (2009) 268–272.

294 L. Ren, L. Ma, L. Jin, J. Wang et al. Template-free synthesis of $BiVO_4$ nanostructures: II. Relationship between various microstructures for monoclinic $BiVO_4$ and their photocatalytic activity for the degradation of rhodamine B under visible light. *Nanotechnology* **20** (2009) 405602 - 9 pp.

295 B. Li, H. Cao. ZnO@graphene composite with enhanced performance for the removal of dye from water. *J. Mater. Chem.* **21** (2011) 3346–3349.

296 W. Sun, J. Li, G. Mele, Z. Zhang, F. Zhang. Enhanced photocatalytic degradation of rhodamine B by surface modification of ZnO with copper(II) porphyrin under both UV-vis and visible light irradiation. *J. Mol. Catal. A: Chem.* **366** (2013) 84–91.

297 H. Fu, C. Pan, W. Yao, Y. Zhu. Visible-light-induced degradation of rhodamine B by nanosized Bi_2WO_6. *J. Phys. Chem. B* **109** (2005) 22432–22439.

298 Z. He, C. Sun, S. Yang, Y. Ding, et al. Photocatalytic degradation of rhodamine B by Bi_2WO_6 with electron accepting agent under microwave irradiation: Mechanism and pathway. *J. Hazard. Mater* **162** (2009) 1477–1486.

299 W. Su, J. Chen, L. Wu, X. Wang et al. Visible light photcatalysis on praseodymium(III)-nitrate-modified TiO_2 prepared by an ultrasonic method. *Appl. Catal., B* **77** (2008) 264–271.

300 M. Stock, S. Dunn. Influence of the ferroelectric nature of lithium niobate to drive photocatalytic dye decolorization under artificial decolorization under artificial solar light. *J. Phys. Chem.* **116** (2012) 20854–20859.

301 http://www.knowledgedoor.com/2/elements_handbook/oxygen.html. Accessed on 02. 07. 2013.

302 T. Shen, Z.-G. Zhao, Q. Yu, H.-J. Xu. Photosensitized reduction of benzil by heteroatom-containing anthracene dyes. *J. Photochem. Photobiol.* **47** (1989) 203–212.

303 P. Qu, J. Zhao, H. Hidaka. TiO_2-assisted photodegradation of dyes: A study of two competitive primary processes in the degradation of rhodamine B in an aqueous TiO_2 colloidal solution. *J. Mol. Catal. A: Chem.* **129** (1998) 257–268.

304 F. Chen, J. Zha, H. Hidaka. Higly selective deethylation of rhodamine B: Adsorption and photooxidation of the dye on the TiO_2/SiO_2 composite photocatalyst. *Int. J. Photoenergy* **5** (2003) 209–217.

305 F. H. Al Hamedi, M. A. Rauf, S. Salman Ashraf. Degradation studies of Rhodamine B in the presence of UV/H_2O_2. *Desalination* **239** (2009) 159–166.

306 M. Y.Ghaly, G Hartel, R. Mayer, R. Haseneder. Photochemical oxidation of p-chlorophenol by UV/H_2O_2 and photo-Fenton process. A comparative study. *Waste Manag.* 21 (2001) 41–47.

307 S. Goldstein, D. Aschengrau, Y. Diamant, J. Rabani. Photolysis of aqueous H_2O_2: quantum yield and applications for polychromatic UV actinometry in photoreactors. *Environ. Sci. Technol.* **41** (2007) 7486–7490.

308 R. Su, J. Sun, Y. Sun, K. Deng et al. Oxidative degradation of dye pollutants over a broad pH range using hydrogen peroxide catalyzed by FePz(dtnCl$_2$)$_4$. *Chemosphere* **77** (2009) 1146–1151.

309 D. D. Dionysion, M. T. Suidan, I. Baudiu, J. M. Lane. Effect of hydrogen peroxide on the destruction of organic contaminants-synergism and inhibition in a continous mode photocatalytic reactor. *Appl. Catal. B* **50** (2004) 259–269.

310 Keller-Rudek, H. Moortgat, G. K. MPI-Mainz-UV−VIS Spectral Atlas of Gaseous Molecules. Available at: www.atmosphere.mpg.de/spectral-atlas-mainz . Accessed on 24.06.2013.

311 H. Fu, C. Pan, W. Yao, Y. Zhu. Visible-light-induced degradation of rhodamine B by nanosized Bi$_2$WO$_6$. *J. Phys. Chem.* B **109** (2005) 22432–22439.

312 V. A. Sakkas, I. M. Arabatzis, I.K. Konstantinou, A. D. Dimou et al. Methalochlor photocatalytic degradation using TiO$_2$ photocatalysts. *Appl. Catal., B* **49** (2004) 195–205.

313 P. Baettig, C. F. Schelle, R. Le Sar, U. V. Waghmare, N. A. Spaldin. Theoretical Prediction of New High-Performance Lead-Free Piezoelectrics. *Chem. Mater.* **17** (2005) 1376–1380.

314 J. Zylberberg, A. A. Belik, E. Takayama-Muromachiand, Z. Ye. Bismuth Aluminate: A New High-T$_C$ Lead-Free Piezo-/Ferroelectric. *Chem. Mater.* **19** (2007) 6385–6390.

315 T. Zou, X. Wang, H. Wang, C. Zhong, L. Li, I-Wei Chen. Bulk dense fine-grain 1$_{-x}$BiScO$_{3-x}$PbTiO$_3$ ceramics with high piezoelectric coefficient. *Appl. Phys. Lett.* **93** (2008) 192913 - 3pp.

316 K. Oka, M. Azuma, W.T. Chen, A.A. Belik et al. Pressure-induced spin-state transition in BiCoO$_3$. *J. Am. Chem. Soc.* **134** (2010) 9438–9443.

317 K. Ujimoto, T. Yoshimura, A. Ashida, N. Fujimura. Direct piezoelectric properties of (100) and (111) BiFeO$_3$ epitaxial thin films. *Appl. Phys. Lett.* **100** (2012) 102901 - 3pp.

318 Y. Zhang, A. M. Schultz, P. A. Salvador, G. S. Rohrer et al. Spatially selective visible light photocatalytic activity of TiO$_2$/BiFeO$_3$ heterostructures. *J. Mater. Chem.* **21** (2011) 4168–4174.

319 S. Li, Y.-H. Lin, B.-P. Zhang, Y. Wang, C.-W. Nan. Controlled Fabrication of BiFeO$_3$ Uniform Microcrystals and Their Magnetic and Photocatalytic Behaviors. *J. Phys. Chem. C* **114** (2010) 2903–2908.

320 R. Guo, L. Fang, W. Dong, F. Zheng, M. Shen. Enhanced Photocatalytic Activity and Ferromagnetism in Gd Doped BiFeO$_3$Nanoparticles. *J. Phys. Chem. C* **114** (2010) 21390–21396.

321 J. Wang, J. B. Neaton, H. Zheng, V. Nagarajan, et al. Epitaxial BiFeO$_3$ Multiferroic Thin Film Heterostructures. *Science 299* (2003) 1719–1722.

322 G. Catalan, J.F. Scott. Physics and applications of bismuth ferrite. *Adv. Mater.* **21** (2009) 2463−2485.

323 Z. H. Chi, C. J. Xiao, S. M. Feng, F. Y. Li et al. Manifestation of

ferroelectromagnetism in $BiMnO_3$. *J. Appl. Phys.* **98** (2005) 103519 - 5pp.

324 N. A. Hill, K. R. Rabe. First-principles investigation of ferromagnetism and ferroelectricity in bismuth manganite. *Phys. Rev. B* **59** (1999) 8759–8769.

325 R. Ramesh, N. A. Spaldin. Multiferroics: progress and prospects in thin films. *Nat. Mater.* **6** (2007) 21–29.

326 A. A. Belik, S.Iikubo, K. Kodama, N. Igawa et al. Neutron Powder Diffraction Study on the Crystal and Magnetic Structures of $BiCoO_3$. *Chem. Mater.* **18** (2006) 798–803.

327 N. A. Hill, First Principles Search for Multiferroism in $BiCrO_3$. *J. Phys. Chem. B* **106** (2002) 3383–3388.

328 M. Azuma, W. Chen, H. Seki, M. Czapski et al. Colossal negative thermal expansion in $BiNiO_3$ induced by intermetallic charge transfer. *Nat. Commun.* **2** (2011) 1–5.

329 M. Q. Cai, X. Tan, G. W. Yang, L. Q. Wen et al. Giant Magneto-Optical Kerr Effects in ferromagnetic perovskite $BiNiO_3$ with half-metallic state. *J. Phys. Chem. C* **112** (2008) 16638–16642.

330 A. A. Belik, Polar and non polar phases of $BiMO_3$. A review. *J. Solid State Chem.* **195** (2012) 32−40.

331 A. A. Belik, T. Wuernisha, T. Kamiyama, K. Mori et al. High-Pressure Synthesis, Crystal Structures, and Properties of Perovskite-like $BiAlO_3$ and Pyroxene-like $BiGaO_3$. *Chem. Mater.* **18** (2006) 133–139.

332 F. T. Wagner, G. A. Somorjai. Photocatalytic hydrogen production from water on Pt-free $SrTiO_3$ in alkali hydroxide solutions. *Nature* **285** (1980) 559–560.

333 M. Stock, S. Dunn. Influence of the Ferroelectric nature of lithium niobate to drive photocatalytic dye decolorization under artificial solar light. *J. Phys. Chem. C.* **116** (2012) 20854–20859.

334 P. D. Kanhere, J. Zheng, Z. Chen. Site specific optical and photocatalytic properties of Bi-doped $NaTaO_3$. *J. Phys. Chem. C* **115** (2011) 11846–11853.

335 C. Hengky, X. Moya, N. D. Mathur, S. Dunn. Evidence of high rate visble light photochemical decolorisation of Rhodamine B with $BiFeO_3$ nanoparticles associated with $BiFeO_3$ photocorrosion. *RSC Advances* **2** (2012) 11843–11749.

336 C. C. Hu, H. Teng. Influence of structural features on the photocatalytic activity of $NaTaO_3$ powders from different synthesis methods. *Appl. Catal., A* **331** (2007) 44–50.

337 H. Kato, A. Kudo. Water splitting into H_2 and O_2 on alkali tantalate Photocatalysts $ATaO_3$ (A = Li, Na, and K). *J. Phys. Chem. B* **105** (2001) 4285–4292.

338 S. Murugesan, M. N. Huda, Y. Yan, M. M. Al-Jassim, V. Subramanian. Band-Engineered Bismuth Titanate Pyrochlores for Visible Light Photocatalysis. *J. Phys. Chem. C* **114** (2010) 10598–10605.

339 Y. Zhang, A. M. Schultz, P. A. Salvador, G. S. Rohrer. Spatially selective visible light photocatalytic activity of $TiO_2/BiFeO_3$ heterostructures. *J. Mater. Chem.* **21** (2011) 4168–4174.

340 A. Kudo, K. Omori, H. Kato. A Novel Aqueous Process for Preparation of Crystal Form-Controlled and Highly Crystalline $BiVO_4$ Powder from Layered Vanadates at Room Temperature and Its Photocatalytic and Photophysical Properties. *J. Am. Chem. Soc.* **121** (1999) 11459–11467.

341 S. Liu, T. Xie, Z. Chen, J. Wu. Highly active $V–TiO_2$ for photocatalytic degradation of methyl orange. *Appl. Surf. Sci.* **255** (2009) 8587–8592.

342 R. Slama, F. Ghribi, A. Houas, C. Barthou, L. El Mir. Visible light photocatalytic properties of vanadium doped zinc oxide aerogel nanopowder. *Thin Solid Films* **519** (2011) 5792–5795.

343 N. Serpone, D. Lawless, J. Disdier, J.-M. Herrmann. Spectroscopic, photoconductivity, and photocatalytic studies of TiO_2 colloids: naked and with the lattice doped with Cr^{3+}, $Fe^{3}+$, and V^{5+} cations. *Langmuir* **10** (1994) 643–652.

344 http://www.unf.edu/~michael.lufaso/spuds/. Accessed on 12. 06. 2013.

345 M. W. Lufaso, P. M. Woodward. Prediction of the crystal structures of perovskites using the software program SPuDS. *Acta Crystallogr., Sect. B: Struct. Sci.* **57** (2001) 725–738.

346 A Salinas-Sanchez. J. L Garcia-Muñoz, J. Rodriguez-Carvajal, R. Saez-Puche, J. L. Martinez. Structural characterisation of R_2BaCuO_5 (R = Y, Lu, Yb, Tm, Er, Ho, Dy, Gd, Eu and Sm) oxides by X-ray and neutron diffraction. *J. Solid State Chem.* **100** (1992) 201–211.

347 http://www.unf.edu/~michael.lufaso/spuds/manual.pdf. Accessed on 14. 05. 2013.

348 C. S. Praveen. Ab-initio calculations on the modulation of electric band gap of photocatalytic semiconductors. *Ph.D. Dissertation.* University of Nova Gorica, 2012.

349 C. A. Randall, A.S. Bhalla, T.R. Shrout, and L.E. Cross, Classification and consequences of complex lead perovskite ferroelectrics with regard to B-Site Cation Order. *J. Mater. Res.* **5** (1990) 829–834.

350 Z. L. Wang and Z. C. Kang. Functional and Smart Materials: Structural Evolution and Structure Analysis. Kang Plenum Publishing (1998) New York.

351 N. Ramadass, T. Palanisamy, J. Gopalakrishnan, G. Aravamudan, M. V. C. Sastri. Some ABO_3 oxides with defect pyrochlore structure. *Solid State Commun.* **17** (1975) 545–547.

352 T. Palanisamy, J. Gopalakrishnan, M. V. C. Sastri. Studies on some thernary oxides of AVO_3 composition. *Z. Anorg. Allg. Chem.* **415** (1975) 275–284.

353 F. Abraham, O. Mentre. $Bi_{1.7}V_8O_{16}$: The first Bi-hollandite type compound. *J. Solid State Chem.* **109** (1994) 127–133.

354 O. Mentre, A.-C. Dhaussy, F. Abraham. Crystal chemistry of mixed $Bi^{3+}–A^{n+}$ (A^{n+}=Na^+, K^+, Sr^{2+}, Ba^{2+},Tl^+, Pb^{2+}) vanadium hollandite materials. *J. Mater. Chem.* **9** (1999) 1023–1027.